

THE RADIO INFLUENCE CHARACTERISTICS
OF HIGH-VOLTAGE ELECTRICAL DISCHARGES

by

WILLIAM HERBERT HUGGINS

A THESIS

submitted to the
OREGON STATE COLLEGE

in partial fulfillment of
the requirements for the
degree of

MASTER OF SCIENCE

June 1942

APPROVED:

[REDACTED]

Professor of Electrical Engineering in Charge of Major

[REDACTED]

Acting Head of Department of Electrical Engineering

[REDACTED]

Chairman of School Graduate Committee

[REDACTED]

Chairman of State College Graduate Council

PREFACE

The development of practical theories regarding radio interference has lagged far behind the development of those pertaining to radio signal transmission. Thus, at present, the problem of radio interference is treated largely in an experimental and empirical manner whereas the treatment of signal-transmission phenomena is expedited through use of the well-known theories applying to tuned circuits, transmission lines, directional antennas, side-band filters, etc. This development is entirely normal since, after all, the problem of interference arises directly from the signal-transmission problem. Actually, the radio-interference problem is somewhat more complicated than the phenomenon of signal transmission. In the latter case all signals commonly used today may be classified into three general types, viz.; amplitude-modulated, frequency-modulated, or phase-modulated waves; whereas radio interference because of its usual random nature cannot be so grouped.

Several authors have published theoretical treatments of the interference arising from random disturbances, but unfortunately, because of the general method of attack, these treatments have been highly mathematical and have but little meaning to anyone not acquainted with the mathematics involved. In the sections to follow an attempt will be made to apply these theories in analyzing the radio interference arising from high-voltage electrical discharges. While no attempt will be made to secure a high degree of mathematical rigor, as many of the mathematical steps as necessary to clearly show the development of theory will be given in the various appendices.

On the basis of the physical mechanism involved in a high-voltage electrical discharge a rational theory will be developed regarding the radio-influence characteristics of these discharges. Radio interference predicted from this theory will be found in excellent accord with experimental measurements. It is hoped that the material summarized here will be of aid to others who are investigating radio-interference phenomena, and that it will help to place the entire subject of radio interference arising from point discharges on a more substantial foundation.

--W. H. Huggins

Oregon State College

ACKNOWLEDGMENTS

The investigation reported upon herein was supervised by Professor E. C. Starr, who suggested many of the topics which were studied and, through several dark hours, guided the work with patience and foresight toward a worthwhile objective. His guidance and constructive criticism have been invaluable.

Also, the suggestions and contributions of Professor F. O. McMillan, Head of the Department of Electrical Engineering at this college, have been of great assistance in interpreting the high-voltage phenomena studied. If it were not for his generosity in providing a special laboratory and making available the complete facilities of the Department of Electrical Engineering, the investigations could not have been successfully completed.

The Department of Mechanical Engineering loaned the air supercharger used for making the wind tests; the American Phenolic Corporation furnished without charge the co-axial cable which was incorporated in the interference measuring circuit; and the Canadian Radium and Uranium Company provided the radio-active dischargers discussed herein. Thanks are also given to R. H. George of Purdue University for permission to reproduce in Figures 17 and 18 oscillograms from his "Report on a Laboratory Investigation of 'Precipitation Static' Interference as Encountered on Aircraft," C. A. A. Technical Development Report Number 29.

Acknowledgement is also made of the assistance given by Leo E. Chaffin and John J. Wittkopf, seniors in electrical engineering in the construction of laboratory equipment, obtaining of experimental data, preparation of many of the figures in this and other reports, and the reading of proof.

Finally, the author wishes to acknowledge the kind guidance of a personal God who has chosen to partially disclose some of the laws of His handiwork.

W. H. Huggins

Oregon State College

TABLE OF CONTENTS

PART I. RADIO-INFLUENCE CHARACTERISTICS OF HIGH-VOLTAGE
ELECTRICAL DISCHARGES

<u>Chapter</u>	<u>Page</u>
I. Introductory Summary	3
II. Laboratory Equipment and Methodology	3
High-Voltage Power Supply - Synchronization-Voltage Injector Circuit - Radio-Interference-Measuring Circuit - Current and Voltage Measuring Equipment - Other Equipment	
III. High-Voltage-Discharge Phenomena	13
Electric Field Around a Point - Positive-Point Discharge Mechanism - Negative-Point Discharge Mechanism - Comparison of Positive- and Nega- tive-Point Discharges - Effect of Air Movement and Radiation on Point Discharge - Equivalent Circuit for Voltage-Induction Effects - Limita- tions of Equivalent Circuit	
IV. Statistical Current-Frequency Spectrum of Positive and Negative Electrical Discharges	23
Summary of Theory - Calibration of Noise-Measuring Equipment by Shot- Effect Noise Currents - Effect of Diode Detector on Noise Measurements - Frequency Spectrum of Positive Corona Streamers - Effect of Variations in Wave Shape of Elemental Disturbances - Experimental Results - Prob- able Positive-Streamer-Current Wave Shape - Frequency of Negative-Point Corona Pulses	
V. Radio Interference in Complicated Networks	38
Theory - Effect of an Inductor in Series with a Discharge Point - Effect of a Resistor in Series with a Discharge Point	
VI. Shock Excitation of Radio Receivers	45
Summary - Response of Tuned Circuit to Double-Exponential Impulse - Im- pulse Excitation of Cascade Tuned Circuits	
VII. Noise Reduction by Nonlinear Circuit Elements and Other Schemes	50
Noise Reduction by Detuning - Carson's "Irreducible Minimum of Interfer- ence" - Nonlinear Circuit Elements for Further Noise Reduction - Noise Reduction by Audio Limiters - Intermediate-Frequency Limiters - Limiters in the Antenna Circuit - Noise Reduction by "Damper" Circuits	
PART II. THE DEVELOPMENT OF A PRACTICAL CHARGE DISSIPATOR	
VIII. Introductory Summary	63
IX. Point and Fine-Wire Dischargers	63
Comparison of Fine Wire Discharger with the Bendix Discharger	
X. Radio Activated Discharge Devices	68
Theory of Operation - Description of Radio-Activated Cup Discharger - Summary of Tests Made - Discharge Characteristic of Radio Active Cup Only - Characteristics of Radio-Activated Needle-Point Discharges - Dis- charge Characteristics of Needle Points Only - Conclusion	

Chapter	Page
XI. Flame Dischargers Summary - Theory of the Stationary Flame - Combustion Processes in an Electric Field - Desirable Properties of the Discharger Flame - Still- Air Characteristics of Flame Discharger - Effective Flame Center of Positive and Negative Flames - Effect of Space Charge on Flame Dis- charger - Thermal Ionization - Design of a Practical Flame Discharger	85

APPENDICES

Appendix

I. Electric Field Around a Paraboloidal Point Derivation of Paraboloidal Coordinates - The Differential Geometry of Paraboloidal Coordinates - Solution of Laplace's Equation for Arbitrary Potential Distribution over Point - Solution of Laplace's Equation for Equipotential Point - Capacitance Between Confocal Paraboloidal Shells	117
II. Determination of Equivalent-Circuit Parameters Calculation of Capacitance - Calculation of Conductance	122
III. Analysis of Equivalent Network Classification of the Network - Invariant Solution of General Network - Solution of Specific Network - Evaluation of the Operational Solution	123
IV. Frequency Spectrum of Random Impulses Theory - Frequency-Spectrum of Double-Exponential Transients - Effect of Variation of Parameters on Energy-Frequency Spectrum	127
V. Receiver Band-Width and Radio Interference Receiver Effective Band-Width - Relation between Circuit "Q" and Effec- tive Band-Width - Influence of Effective Band-Width on Radio Interfer- ence - Radio Interference Produced by Corona Streamers - Shot-Effect Noise in Temperature-Limited Diode	130
VI. Influence of Exterior Circuit on Radio Interference Theoretical Considerations - Effect on the Radio Interference of a Resonant Circuit Placed Between a Discharge Point and Radio Interfer- ence - Effect on the Radio Interference of a High Resistance Placed Between a Discharge Point and Radio Receiver	135
VII. Shock Oscillations in Tuned Circuits General Theory - Envelope of Shock Oscillations - Epoch and Value of Maximum Amplitude of Shock Oscillations	138
VIII. Comments on Use of AVC voltage for Noise-Measurement Comparisons Methodology - Theoretical Determination of Γ - Sample Calculations for HRO Receiver - Experimental Determination of Γ .	141

LIST OF FIGURES

<u>Figure</u>	<u>Page</u>
1. Circuit Diagram of High-Voltage Power Supply	5
2. Photograph of High-Voltage Power Supply	6
3. Block Diagram of Radio-Interference Measuring Circuit	7
4. Calibrating and Noise-Measuring Equivalent Circuits and Equipment Data	8
5. Schematic Diagram of Selector Circuits and Vacuum-Tube Voltmeter	10
6. Photograph of Measuring Equipment	11
7. Part A. Photograph of Vacuum Chamber	12
Part B. Photograph of Supercharger	12
8. Plot of Paraboloidal Field Configuration Used in Calculations	14
8A. Ratio of Streamer-Current to Total-Current for a Positive-Point Discharge	17
9A. Equivalent Circuit for Voltage Induction Effects	20
9B. Starr's Oscillograms of Voltages Induced by a Positive-Point Streamer	20
10. Calculated Induced Voltages Resulting from Point Discharge	21
11. Frequency Spectrum of Shot-Effect Noise	25
12. Calculated and Experimental Form-Factors of Shock-Oscillations at Second Detector of Radio Receiver	27
13. Effect of Random Variation in Impulse Shapes on Noise-Frequency Spectrum	29
14. Theoretical Noise Spectrum of Random Double-Exponential Transients	30
15. Experimental Noise-Frequency Spectrum of Positive-Point Discharge	32
16. Probable Streamer-Current Wave-Form and Space-Charge Development	33
17. Voltage across a Resistor in Series with 44-Kilovolt, Positive-Needle-Point Discharge	34
18. Voltage Across a Resistor in Series with 44-Kilovolt, Positive-Needle-Point Discharge	36
19. Frequency of Corona Discharges from a Negative Needle Point	37
20. Proposed Resonant Circuit for Termination of Trailing Antenna	39
21. Radio-Interference Spectrum for Inductance in Series with Positive-Point Discharger	41
22. Radio-Interference Spectrum for 50-Megohm Resistor in Series with Positive-Point Discharger	42
23. Radio-Interference Spectrum for a 0.5 Megohm Resistor in Series with Positive Point Discharger	44
24. Impulse-Excitation of 200-Kilocycle Antenna Transformer	48
25. Envelope of Shock Oscillation after First, Third, and Sixth Tuned Circuits	49
26. Improvement in Impulse-Noise-to-Signal Ratio by Additional Tuned Circuits	51

PRECIPITATION-STATIC-REDUCTION RESEARCH

<u>Figure</u>	<u>Page</u>
27. Frequency Spectrum of Damped Oscillations	53
28. Effect of Audio Limiter on Signal-to-Noise Ratio	55
29. Signal-to-Noise Ratio of Amplitude- and Frequency-Modulated Systems	56
30. Point and Fine-Wire Radio Interference as a Function of Current	65
31. Experimental Comparison of Positive-Discharges	66
32. Experimental Comparison of Negative-Discharges	67
33. Discharge Current as Function of Pressure (Radio-Active Cup Discharger)	71
34. Radio Interference as a Function of Current from Positive, Radioactivated Discharge Cup	72
35. Radioactivated Cup Discharger Current as a Function of Voltage. Positive Polarity	74
36. Radioactivated Cup Discharger Current as a Function of Voltage. Negative Polarity	75
37. Pressure at Current Maxima as a Function of Voltage. Radioactivated Discharger	76
38. Corona on Negative Cup Discharger	77
39. Corona on Positive Cup Discharger	78
40. Effect of Radioactive Material on Negative-Needle-Point Discharge	79
41. Effect of Radioactive Material on Positive-Needle-Point Discharge	81
42. Radioactivated-Positive-Point-Discharge Radio Interference as a Function of Discharge Current	82
43. Unactivated-Positive-Point-Discharge Radio Interference as a Function of Discharge Current	83
44. Positive-Needle-Point-Discharge Radio Interference as a Function of Discharge Current	84
45. Diagram of Bunsen-Burner Flame	87
46. Effect of Electric Field on Positive Flame	89
47. Characteristic V-I Curves for 2.5-Inch Positive Oxyacetylene Flame	95
48. Characteristic V-I Curves for 2.5-Inch Negative Oxyacetylene Flame	96
49. Positive Flame Conduction Coefficient as a Function of Flame Length	98
50. Positive Flame Conduction Coefficient as a Function of Burner Spacing	99
51. Positive Flame Conduction Coefficient as a Function of Flame Spacing	100
52. Negative Flame Conduction Coefficient as a Function of Flame Length	101
53. Negative Flame Conduction Coefficient as a Function of Burner Spacing	102
54. Negative Flame Conduction Coefficient as a Function of Flame Spacing	103
55. Second Flame-Conduction Coefficient as Function of Effective-Flame-Center Spacing	104
56. Calculated Potential along Central Axis for Imposed Space Charge Distribution	109
57. Thermal Ionization in Oxy-Acetylene Flame	111
58. Positive Flame Discharge Characteristic in Wind Stream	112
59. Negative Flame Discharge Characteristic in Wind Stream	113

PART I

RADIO-INFLUENCE CHARACTERISTICS OF HIGH-VOLTAGE
ELECTRICAL DISCHARGES

RADIO-INFLUENCE CHARACTERISTICS OF HIGH-VOLTAGE

ELECTRICAL DISCHARGES

I. INTRODUCTORY SUMMARY

The radio interference resulting from high-voltage electrical discharges is influenced by three things: the nature of the electrical discharge itself, the characteristics of the associated electrical network, and the radio receiver. It has been found that, in general, the associated electrical network has but little influence on the characteristic nature of the electrical discharge. Accordingly, each of these three factors may be studied separately, and a measure of each in its contribution to radio interference thus obtained. The various phases of the problem to be considered are as follows:

1. Physical discharge mechanism of high-voltage electrical discharges.
2. Approximate equivalent circuit for studying voltage-induction effects arising from corona discharges.
3. Theoretical and experimental determinations of the statistical current-frequency spectrum of the positive-streamer discharge and the determination therefrom of the current-burst shape.
4. Determination of pulse rate of negative point corona.
5. Calculation of radio interference in complicated networks.
6. Effect of receiver detection systems on measured interference.
7. Shock excitation of circuits and the relationship between effective band-width and circuit decrement.
8. Noise-reduction by the use of nonlinear circuit elements.

As a result of these studies, it is concluded that the interference arising from corona discharges can be considered as a radio-frequency noise-current spectrum of noise currents distributed over the entire radio frequency spectrum. Calculations of interference based on this noise spectrum agree remarkably well with experimental observations

From these studies it is apparent that if radio interference is to be reduced beyond that which can be done with simple filters and tuned circuits, the frequency band of the signal must be reduced with respect to the signal. This can only be accomplished by non-linear circuits which discriminate between the signal and noise on the basis of their different wave forms. Such discrimination is not possible in linear networks.

Because of this fact, it is concluded that the engineer's last best hope for greatly improved radio reception must lie in a more universal adoption and wise application of nonlinear circuit elements incorporated in radio receiver design.

II. LABORATORY EQUIPMENT AND METHODOLOGY

High-voltage Power Supply

To supply the large direct-voltages needed to produce electrical discharges at atmospheric pressure, the power supply shown in Figure 1 was constructed. The principal advantage of the half-wave voltage-doubling circuit employed is that the maximum inverse voltage appearing across either high-vacuum tube is the same as the output potential and, furthermore, it is only necessary to use a transformer having a voltage rating of about half the output voltage.

The power supply was designed to be corona-free for all voltages up to 200,000 volts. Copper pipe of $1\frac{1}{2}$ -inch diameter was used for the conducting system and all fittings were carefully ground and polished before installation. The capacitor rack, visible in Figure 2, was constructed so that its leakage paths would form a natural, voltage divider to equalize the voltages across the series filter condensers. The protective resistors shown in the circuit diagram simply replace appropriate sections of the copper conductors.

The output voltage of the power supply is controlled by an induction regulator in the primary circuit of the high-voltage transformer. For low-voltage operation, up to 50 kilovolts, two smaller high-voltage rectifiers, with filament power supplied through two ac-operated filament transformers, may be plugged in parallel with the larger rectifier tubes whose filaments, because of the high-voltage insulation requirements, are battery-powered.

Synchronization-voltage Injector Circuit

Also shown in Figure 1 between the dotted lines is the circuit by means of which an oscillating voltage of several thousand volts and of any frequency between 100 and 4000 cycles per second may be superimposed upon the direct potential delivered by the high-voltage power supply. The "feeding" condenser is comprised of 8, 0.5 microfarad, 25,000-volt condensers connected in series-parallel. In addition to injecting a synchronizing voltage when desired, this circuit also serves as an additional filter section to the power supply to reduce still further any 60-cycle ripple in the output voltage, and remove other disturbance resulting from the corona discharge. However, because of the voltage limitation of the capacitors, the circuit can only be used at voltages less than 100 kilovolts.

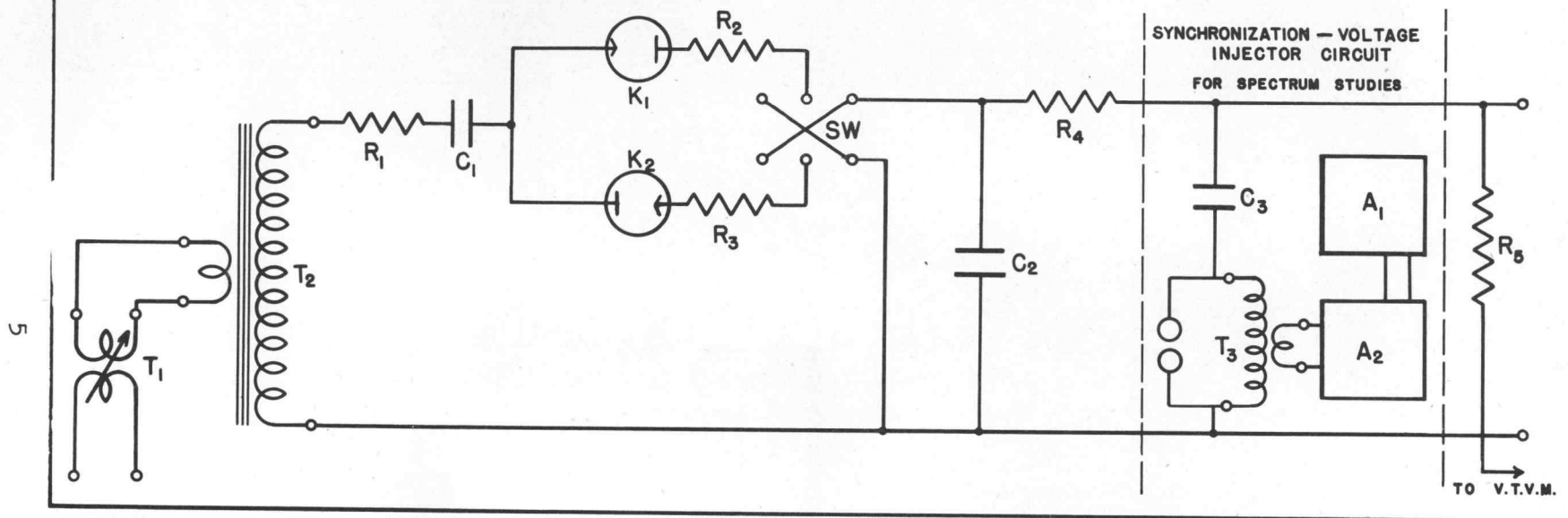
Radio-interference-measuring Circuit

A substitution method was employed to measure the magnitude of the radio interference at any particular frequency. Figure 3 shows a block diagram of the circuit used to measure the radio interference and the currents and voltages at the discharge electrode. The entire measuring equipment was arranged in a grounded metal cage and was connected to the discharge electrode under test by a coaxial cable 22 feet long. A similar cable of identical length connected the standard-signal generator to the remaining portion of the measuring circuit. By means of a three-position master-selector switch, the radio receiver could either be connected to the cable leading to the discharge electrode or to the standard signal generator. In both of these positions, the avc voltage developed in the receiver was indicated on a vacuum-tube volt-meter.

When the master-selector switch was turned to the third position the same vacuum-tube voltmeter was calibrated to read discharge currents ranging from 0.005 to 5,000 microamperes, and output voltages delivered by the DC-power supply between the values of 5 to 200,000 volts. A push-button selector switch conveniently placed at the end of a flexible cable was used to select any of the five current ranges and six voltage ranges between the above limits.

To measure the radio interference at any particular frequency to which the standard-signal generator had been set, the master selector switch was first turned to the position connecting the receiver to the standard signal generator and the radio receiver tuned for maximum response to the standard signal. The master selector switch was then turned to connect the radio receiver to the discharge electrode under test. After the receiver gain control had been adjusted to give an avc voltage of about three volts (the gain setting of course depending upon the magnitude of the radio interference), the standard signal generator was again substituted for the discharge point, and the output voltage of the standard signal generator adjusted to obtain the same avc voltage. The open-circuit output voltage delivered by the signal generator could then be read directly upon its calibrated attenuator dial.

FIG. I. HIGH-VOLTAGE DIRECT-CURRENT POWER SUPPLY CIRCUIT



LEGEND:

- T_1 INDUCTION REGULATOR
 T_2 100 KV. HIGH VOLTAGE TRANSFORMER
 T_3 110-3000/1500 V. TRANSFORMER
 SW POLARITY CHANGING SWITCH
 K_1, K_2 KENOTRONS FP-92 (0-50 KV)
 KR-5 (0-200 KV)
 $R_1, R_2, R_3, R_4,$ 0.35 MEGOHMS, PROTECTIVE RESISTORS
 R_5 400 MEGOHM, VOLTMETER MULTIPLIER RESISTOR

- C_1 0.25 MFD., 100 KV. BLOCKING CAPACITOR
 C_2 TWO 0.25 MFD., 100 KV. CAPACITORS IN SERIES
 C_3 EIGHT 0.5 MFD., 25 KV. CAPACITORS IN SERIES-PARALLEL
 TO GIVE 0.25 MFD., 100 KV.
 A_1 HEWLETT-PACKARD 200-C AUDIO OSCILLATOR
 A_2 50-WATT, 2000-VOLT AMPLIFIER

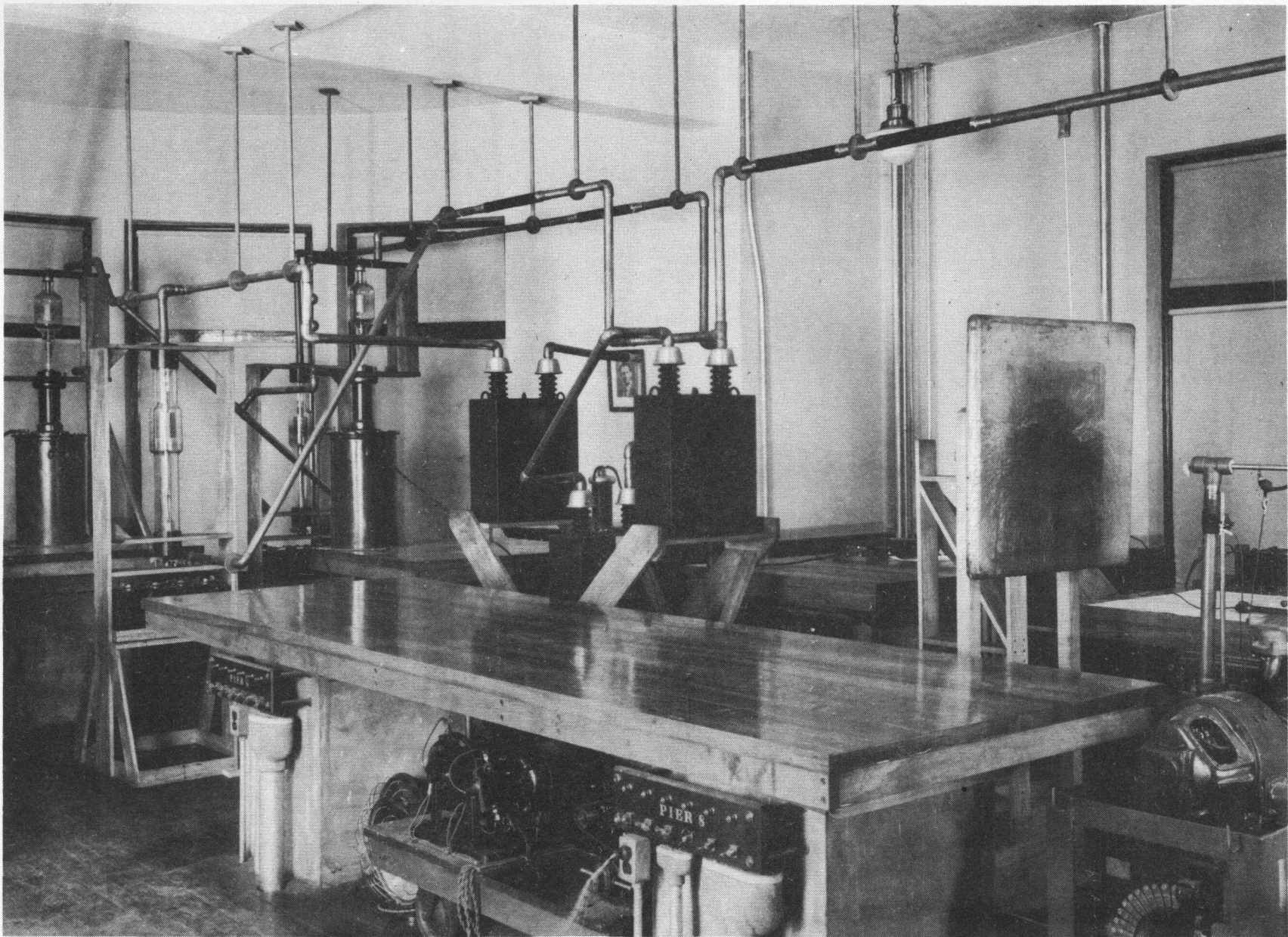
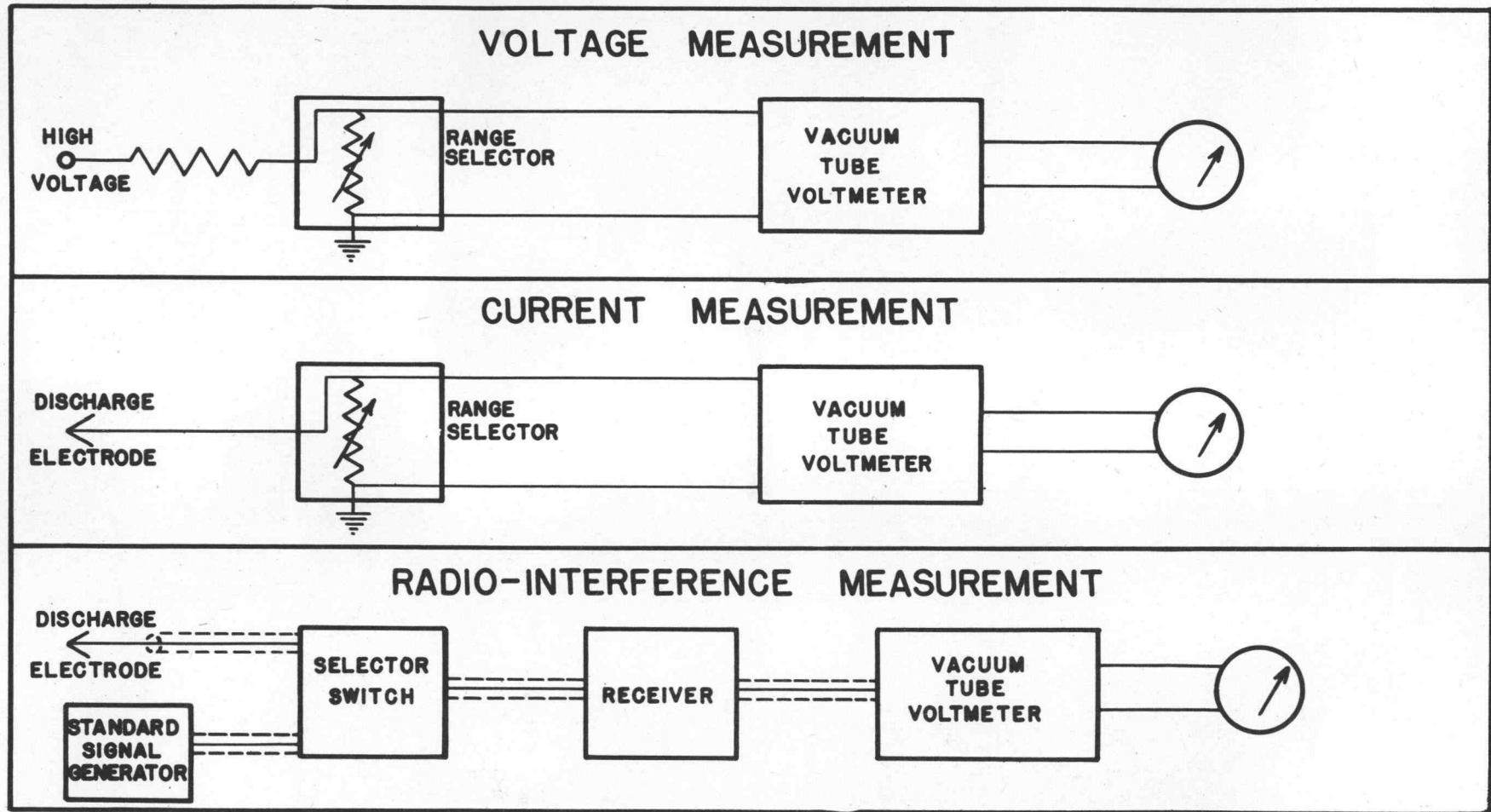


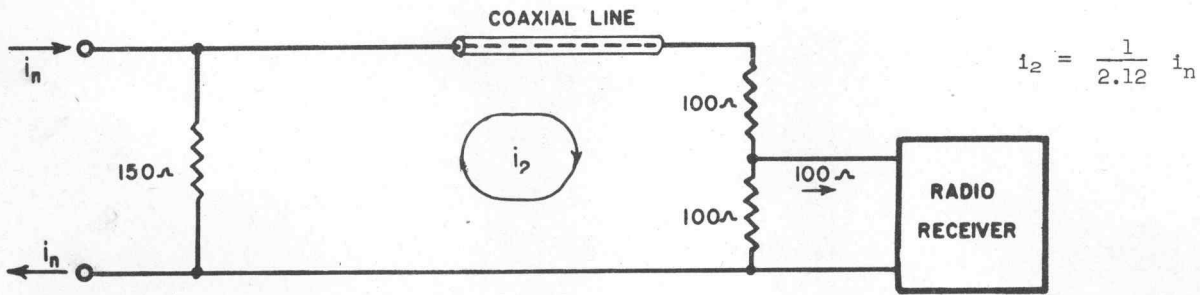
Figure 2. High-Voltage Power Supply

FIGURE 3.
BLOCK DIAGRAMS OF MEASURING CIRCUITS

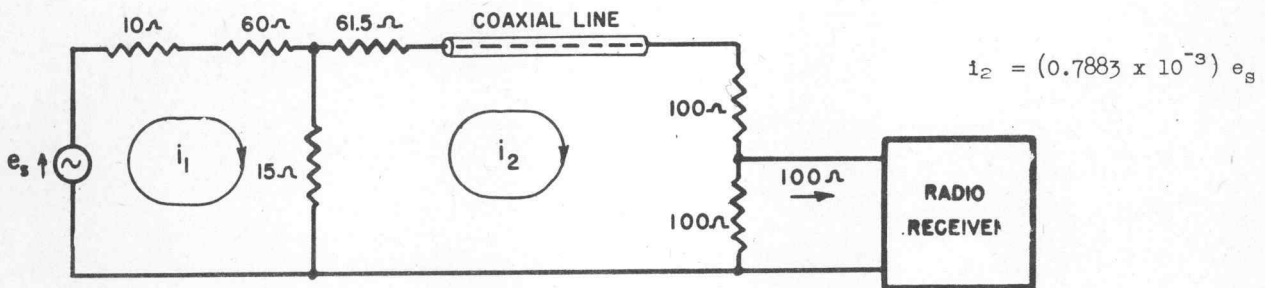


7

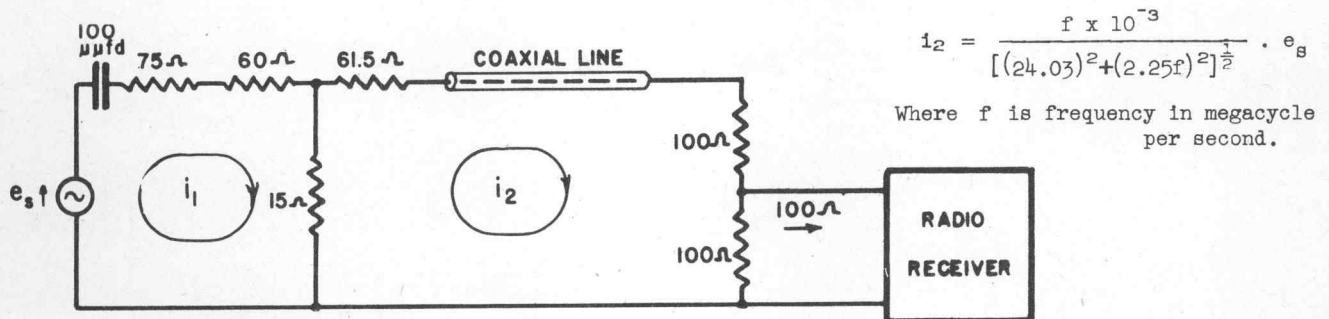
Figure 4. Calibrating and Noise-Measuring Equivalent Circuits and Equipment Data



(A) Equivalent Noise-Measuring Circuit. (50 Kc - 30 Mc)



(B) Equivalent Calibrating Circuit (50 Kc - 30 Mc)



(C) Equivalent Calibrating Circuit (28 Mc - 148 Mc)

Coaxial Line, All Circuits

Amphenol type 72-24, Length: 22 feet, Characteristic Impedance: 150 ohms.

Radio Receivers

Circuit b, National Type HRO (50kc - 30 mc), serial no. 6290.

Circuit c, Hallicrafters UHF Communications Receiver, Type S-27, (28mc - 148 mc.), Serial no. H-150851.

Signal Generators:

Circuit b. General Radio Standard Signal Generator, Type 605-B, Serial no. 1663.

o Circuit c. General Radio, UHF Signal Generator, Type 804-B, Serial no. 332.

Attenuation Insertion Unit, Circuits B and C.

General Radio, Type 774-X1.

RADIO-INFLUENCE CHARACTERISTICS

It was necessary to establish the relationship between this open-circuit voltage and the current reaching the radio receiving equipment. The calibrating and noise-measuring equivalent circuits are shown in Figure 4 and the relationship between the current reaching the receiving circuit, and the noise current or open-circuit voltages are given in each case. Since the noise currents flow through the same length of coaxial cable as the calibrating currents, any attenuation due to this cable need not be considered. A 75-ohm insertion unit was used with signal generator to extend the calibrated output range to a smaller value. The relationship between the noise current and receiver current as given in Figure 4a was experimentally determined.

Since the frequency spectrum of random interference must be essentially established on an energy basis and all currents and voltages must therefore be expressed in effective or root-mean-square units, some question may arise as to the accuracy of using the avc voltage as a comparison index between an impulsive type of radio interference and a continuous calibrating signal. This problem has been completely treated in appendix VII, and it suffices to say here that, provided the receiver is sufficiently selective so that the high-frequency audio response is limited by the RF and IF selectivity characteristics and not by the detector and audio system; the rectified, diode current will be proportional to the envelope of the shock oscillation at the second detector. The envelope of this oscillation may be calculated from data obtained from the selectivity measurements; and from this calculated data, the ratio between the effective and average values of the oscillations may be determined. As is shown in the appendix dealing with this problem, the measure of the noise current as obtained by the substitution of a steady-state signal is actually a measure of the average diode current rather than its effective value. If, however, the average number of interference bursts per second is known, the ratio of effective current to average current may readily be calculated and the effective value of the interference current thus obtained. On the basis of certain relationships to be derived later, it is possible to determine this ratio experimentally. The satisfactory agreement between the calculated and experimental values of this ratio as a function of the number of disturbances per second not only verifies the theoretical determination of this ratio, but also serves as conclusive evidence proving the validity of the radio-interference theories to be developed later.

Current and Voltage Measuring Equipment

A vacuum-tube-operated measuring circuit was devised which used a large 0-500 microammeter as the indicating instrument, and which gave full-scale deflection for current values of 0.5, 5, 50, 500, and 5000 microamperes, and for voltage values of 0.5, 2, 5, 20, 50, and 200 kilovolts, depending upon which range had been selected on a multi-button range-selector switch.

The discharge currents were measured in terms of the voltage developed by this current when flowing through a resistance of known value. The range-selector switch simply inserted resistors of different sizes into the circuit, and the voltage developed across this resistor was then indicated on a vacuum-tube voltmeter. The output voltage is, the dc-power supply was also determined by the voltage developed across a resistor connected between ground and a 400-megohm resistance tower connected to the output terminal of the high-voltage power supply. By inserting different resistors, six voltage ranges could be obtained. These various resistors were mounted in the box with the range selector switch which, being connected to the rest of the measuring circuit through a long flexible cable, could be placed conveniently at the operator's fingertips and near the indicating instrument.

The vacuum-tube voltmeter was designed to give a full-scale deflection with an input voltage of 5 volts on a large 0-500 microampere instrument. A reversing switch was inserted between the indicating instrument and the vacuum-tube circuit so that voltage up to 5 volts of either polarity could be measured. At first there was difficulty in obtaining a vacuum-tube voltmeter circuit which would have an extremely low, input

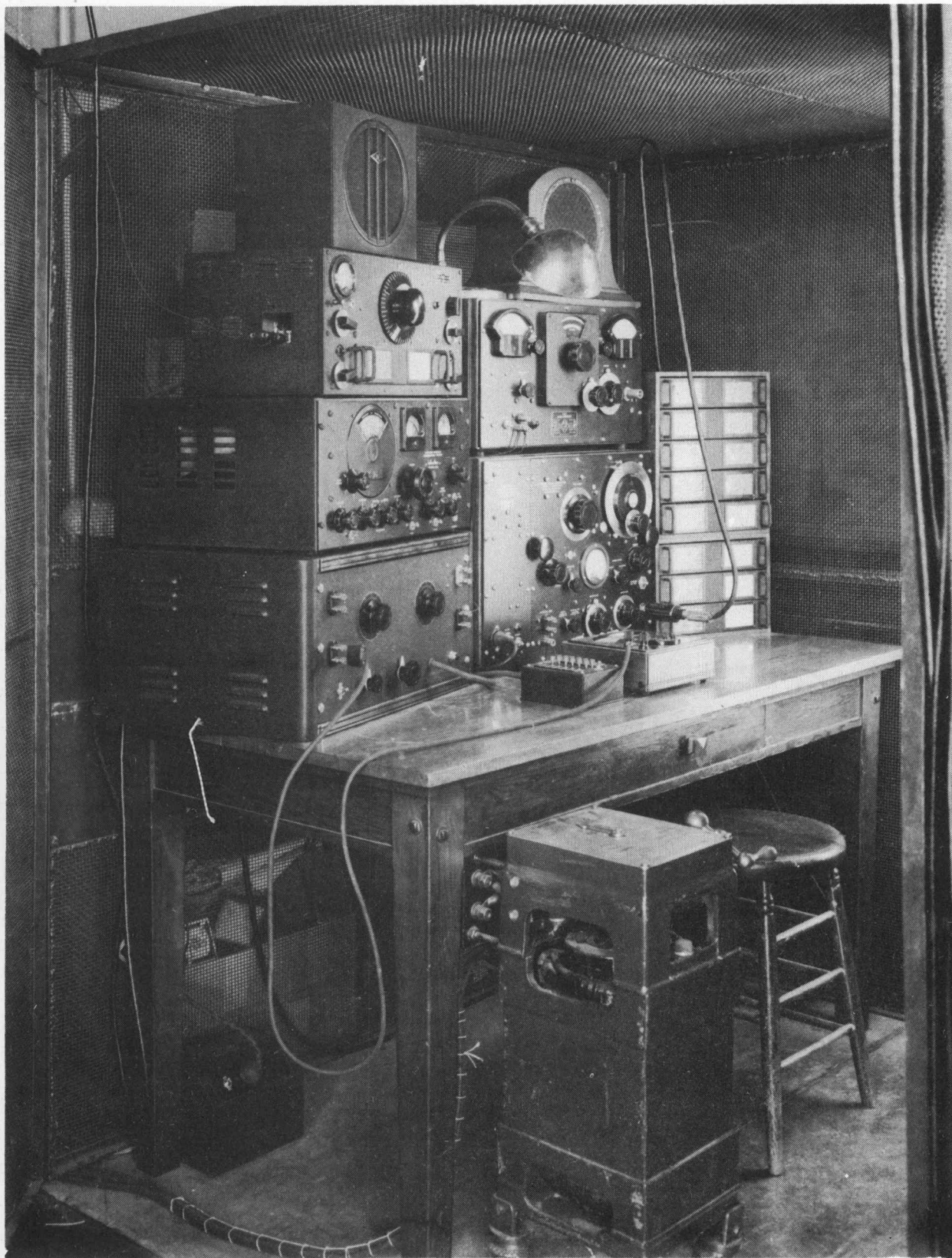


Figure 6. Radio-Interference Measuring Equipment.

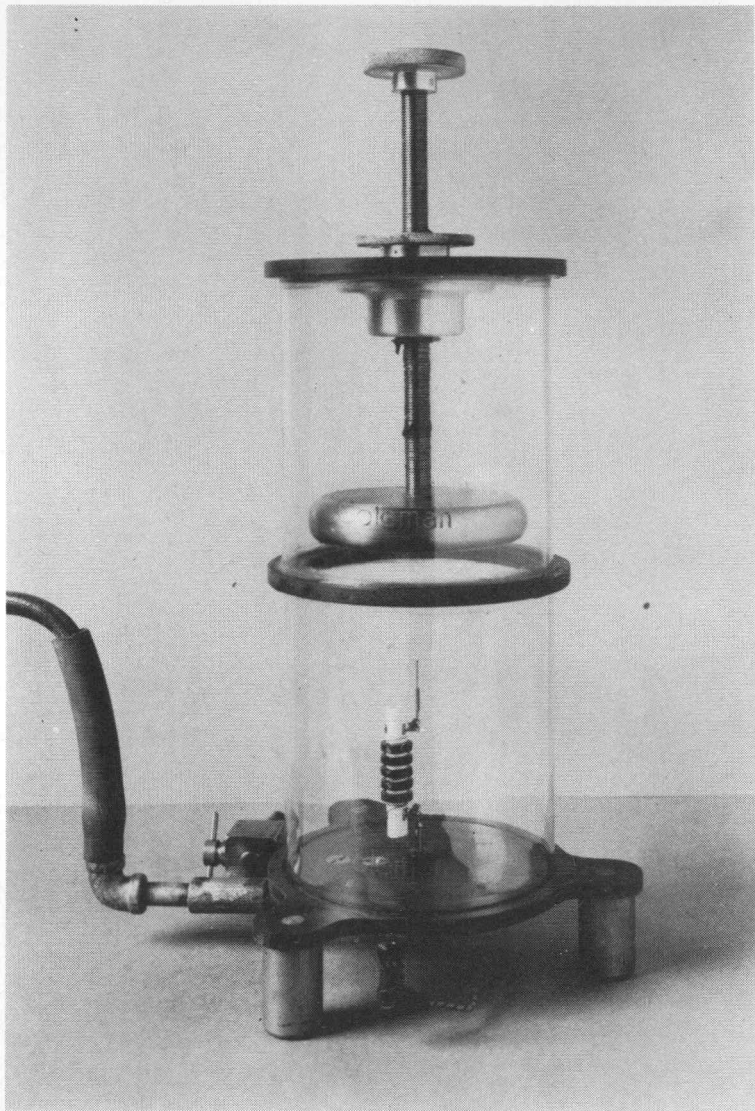


Figure 7a. Low-Pressure Test Chamber showing High-Q Inductor and Gold Point used in obtaining data of Figure 21.

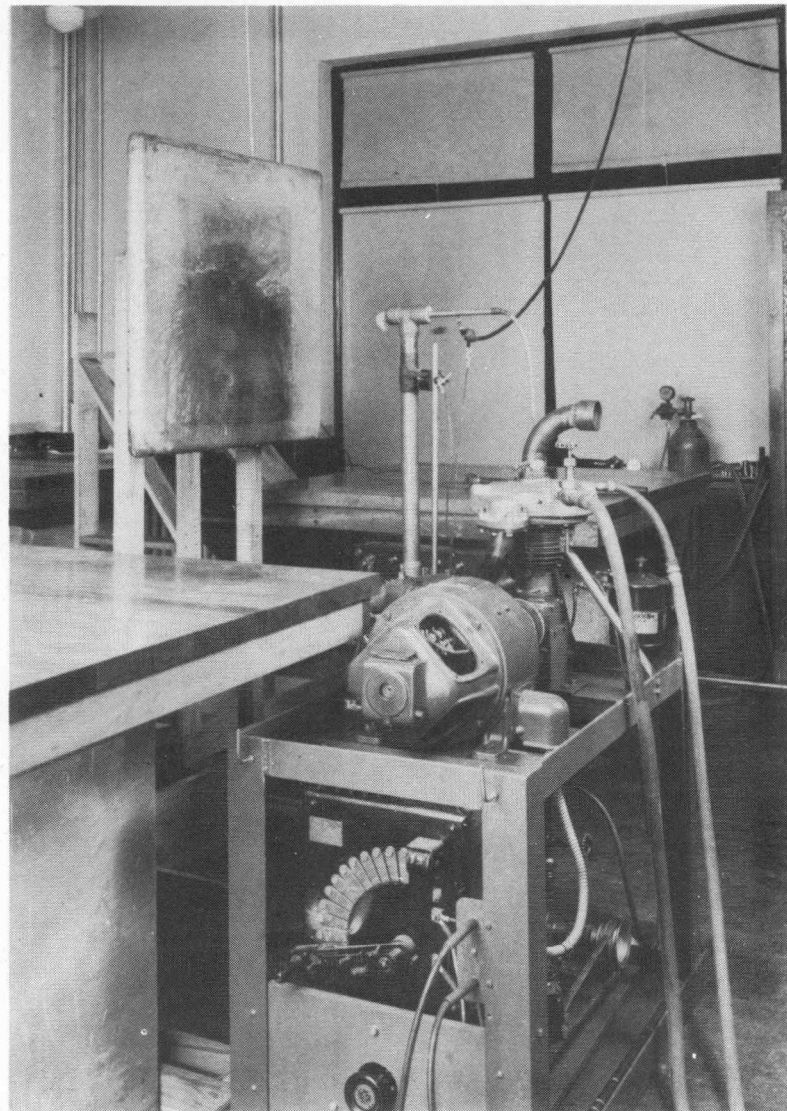


Figure 7b. High-Velocity Wind Set-up showing Supercharger, Exhaust Nozzle, Wick Discharger, Coaxial Line, and High-Voltage Plane Electrode.

RADIO-INFLUENCE CHARACTERISTICS

admittance (obtained by connecting the input voltage directly to a negative grid) and still be sufficiently linear over the operating range of +5 to -5 volts. The circuit which was finally devised is shown in Figure 5. This circuit was found not only to be linear within less than one-tenth of one percent over the operating range, but also to have a maximum overload characteristic well within the range of the indicating instrument. The indicating instrument was accurate to within one percent of full-scale deflection and all range-selector resistors were selected to within plus or minus one percent of their ideal value.

Also shown in Figure 5 is the power supply used to furnish the direct voltages for operation of the vacuum-tube voltmeter. A series-vacuum-tube regulator was used here to maintain a constant output voltage. The circuit is conventional except for the 14 megohm resistance connected from the plate of the 2A3 to the screen of the 6SJ-7. By adjustment of this resistance, the direct-voltage delivered by the power supply could be made completely independent of normal power-line voltage fluctuations.

Other Equipment

In addition to the equipment already described, a small test chamber, shown in Figure 7a was used to investigate the discharge characteristics of various electrodes at pressures less than atmospheric. This chamber could be evacuated by means of a rotary oil pump to an absolute pressure of less than one millimeter of mercury.

Also, shown in Figure 7b, is the equipment loaned by the Department of Mechanical Engineering at Oregon State College for making studies of electrical discharges at atmospheric pressure in a wind stream moving with a high velocity. This equipment consists essentially of an automotive-type supercharger driven by a variable-speed, 5-hp, d-c motor. Wind velocities through a 1½" diameter nozzle sufficient to carry away much of the space charge for either polarity were obtainable with this device. Also under construction, but not completed because of lack of funds, is a much larger, low-pressure test chamber which will provide a high velocity airstream at pressures depending only upon the capacity of the exhausting equipment. It is hoped that these studies at low pressure and high velocity may be continued.

III. HIGH-VOLTAGE DISCHARGE PHENOMENA

Electric Field around a Point

It is well known that the geometry and shape of the discharge point greatly influence the type of corona discharge at the point, and therefore also affect the radio interference produced. Fine wires and sharp, slender points, in general, produce much less radio interference than larger wires or blunt points. Since electrical discharges from a sharp point are perhaps more common than those occurring from any other type of electrode geometrical shape, it would be desirable to establish for study some type of point geometry for which the potential and gradient formulas are not too complicated.

The only type of point geometry which can be made to resemble a needle and still be treated mathematically in a simple way is that composed of confocal paraboloids of revolution in which the surface of the point and the "plane" electrode must be considered as confocal paraboloidal surfaces of widely different size. This representation is surprisingly good. A No. 0 needle, when enlarged some 30 times, resembles the point shown in Figure 8 very closely.

The derivations of the expressions for the potential and gradient around a paraboloidal point are given in appendix I. From Figure 8 it is seen that the equipotentials and the surface of the point and plane electrode are specified by the coordinate "u." The significance of this coordinate is that it is the actual distance from the focus to the tip of the paraboloidal surface which the coordinate represents.

Figure 8

CROSS-SECTION OF PARABOLOIDAL POINT
USED IN CALCULATIONS

EQUIPOTENTIAL SURFACES: $y^2 = 4u(u+x)$ (solid)
LINES OF FLOW: $y^2 = 4v(v-x)$ (dotted)

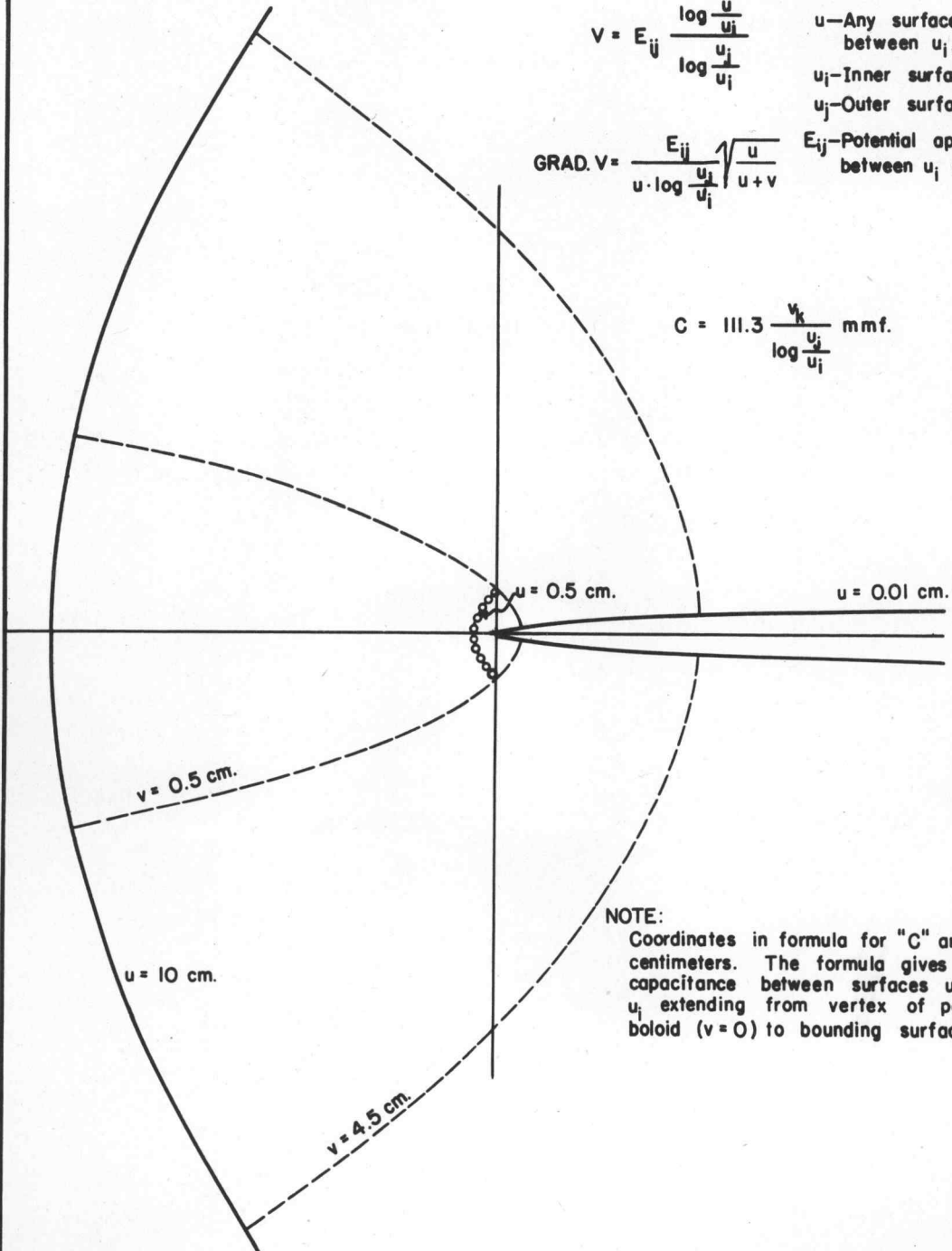
$$V = E_{ij} \frac{\log \frac{u}{u_i}}{\log \frac{u_j}{u_i}}$$

u —Any surface between u_i, u_j
 u_i —Inner surface
 u_j —Outer surface

$$\text{GRAD. } V = \frac{E_{ij}}{u \cdot \log \frac{u_j}{u_i}} \sqrt{\frac{u}{u+v}}$$

E_{ij} —Potential applied between u_i and u_j

$$C = 111.3 \frac{v_k}{\log \frac{u_j}{u_i}} \text{ mmf.}$$



NOTE:
Coordinates in formula for "C" are in centimeters. The formula gives the capacitance between surfaces u_i and u_j extending from vertex of paraboloid ($v = 0$) to bounding surface v_k .

It is also the radius of curvature of that particular surface at the vertex. The lines of flow between these paraboloidal surfaces are represented by an orthogonal family identical in every respect with the first, except that the surfaces extend toward the left in Figure 8. Each surface of flow is determined by the parameter "v" which is numerically equal to the distance between the vertex of that surface and the focus.

Referring again to Figure 8, it will be seen that any point lying in the cross section of the figure may be expressed in terms of the "u" and "v" parameters which represent curves intersecting at that point. For this reason the parameters u, v and w (where w is the angle through which a cross-section of Figure 8 must be rotated to also pass the given point) are called the "paraboloidal coordinates" of the point in space.

It is interesting to compare these coordinates with the more common rectangular coordinates, x, y and z. For example, the equation $x = a$ defines a plane surface normal to the x-axis and of distance "a" from the origin. In an analogous manner for paraboloidal coordinates, when u is equal to the constant "a," a surface formed by revolution of a parabola having a vertex-to-focus distance of "a" is defined. This surface may be bounded by specifying values of v and w over its boundary.

Positive-point Discharge Mechanism

The positive and negative point-discharge mechanism will now be discussed in order that the equivalent circuit used to simulate the voltage-induction effect of corona streamers will be better understood, and also to provide a rational basis for the assumed avalanche-current wave-shape, which will be used in predicting the current-frequency spectrum equivalent to the positive-point type of discharge.

When a positive potential is applied to a point electrode, the negative ions always present to some extent in the air will be attracted toward it. For simplicity, consider what happens to only one of these many ions.

If the anode (point) potential is sufficient to produce a corona discharge, it will be found that, as the ion moves toward the point, it moves through an increasingly intense field which eventually tears the electron from the negative ion. The electron, free of its former mass, hurtles toward the point, but in so doing collides with other gas molecules from which are knocked, by collision, additional electrons which join in the avalanche. In this manner, a single electron in falling toward the point can produce up to 10^7 secondary electrons.^{1*}

The avalanche produces two different phenomena, burst pulses or streamers, depending on whether the positive-ion space-charge left behind the avalanche inhibits or enhances further avalanche formation along the same channel.

Burst pulses ordinarily occur when a normal positive potential is applied to a very small point. The avalanche described above leaves a column of positive ions behind, which reduces the field in that particular region, thus inhibiting the formation of a new burst. However, the photoelectrons created by the ionization in the original avalanche will have created new bursts on all sides. These in turn set off further bursts which spread over those parts of the point surface possessing voltage gradients sufficient to produce ionization. In the meantime, the space charge blocking the original channel will have been swept away by the electric field, and as a result, many little bursts will cover the tip of the point but will be inhibited from extending into the gap because of the combined effects of positive space charge and rapidly decreasing field intensity as they progress outward. It is this type of discharge which Starr² found to produce but little radio interference and termed "Type 1."

If now a blunter point and/or higher voltages are used, the space charge no longer completely inhibits the immediate formation of further bursts along a channel.

*Numbers refer to reference list at end of report.

Instead the "tube" of positive ions in effect acts as a sharp projection of the point itself, and accordingly attracts additional avalanches into its tip. When this repeatedly occurs a long streamer is formed which may extend for several centimeters into the gap. This is Starr's "Type 2" discharge. If a still blunter tip is used, the streamers plume out from the point, giving the "Type 3" discharge reported by Starr.

The time required for the gap to clear itself of the positive space charge resulting from the microscopic bursts is around 10^{-5} seconds, whereas to clear the gap after a streamer has propagated and left a much greater cloud of ions requires around 10^{-3} seconds.¹

Furthermore, once the burst pulses have commenced, a streamer rarely forms (unless the voltage gradients are nearly those required for spark formation). A streamer, on the other hand, can instigate a long series of small burst pulses. An experimental method of measuring the division of the corona current into that due to streamers, and that due to burst pulses, is described in appendix VIII of this report. By using equations (8) and (9) of this appendix, the fraction of the total current occurring as noise-producing streamers was calculated for various streamer rates and the experimental results are given in Figure 8a. At the low streamer rates, the high-voltage-electrode potential was just enough to produce a discharge from the conical point. However, to increase the streamer rate it was necessary to increase the voltage, with the result that burst pulses then followed each streamer. When the voltage was increased still further, the streamer rate increased at first but eventually began to decrease until the streamers ceased and all discharge was in the form of comparatively noise-free burst corona. A wind past the point, however, would disturb the space-charge "blanket," causing streamers and radio interference.

Further evidence that the effect of an increase in polarizing voltage is to decrease the streamer-current/total-current ratio is also found in Figure 8a. The frequency of the streamer discharges was maintained at each value by a synchronizing voltage supplied by a calibrated audio oscillator and amplifier. The high-voltage-electrode polarizing potential could be varied over a small range without destroying the synchronism of the streamer discharges. However, such a small variation in applied voltage should affect the streamer-current/total-current ratio. It will be observed in Figure 8a that just this effect was present, for at certain frequencies where the voltage was set a little higher than was the trend (such as at $n = 800, 2000, 3000$, streamers per second), the streamer current formed a smaller part of the discharge current than one might expect from the trend, indicating that the burst-corona current had been increased by a somewhat greater proportion because of the higher applied voltage. Similar deviations from the smooth curve are observed at $n = 1250, 1500, 2250, \text{ and } 3500$, where for each case the voltage was set a little lower than the trend would require.

Negative-point Discharge Mechanism

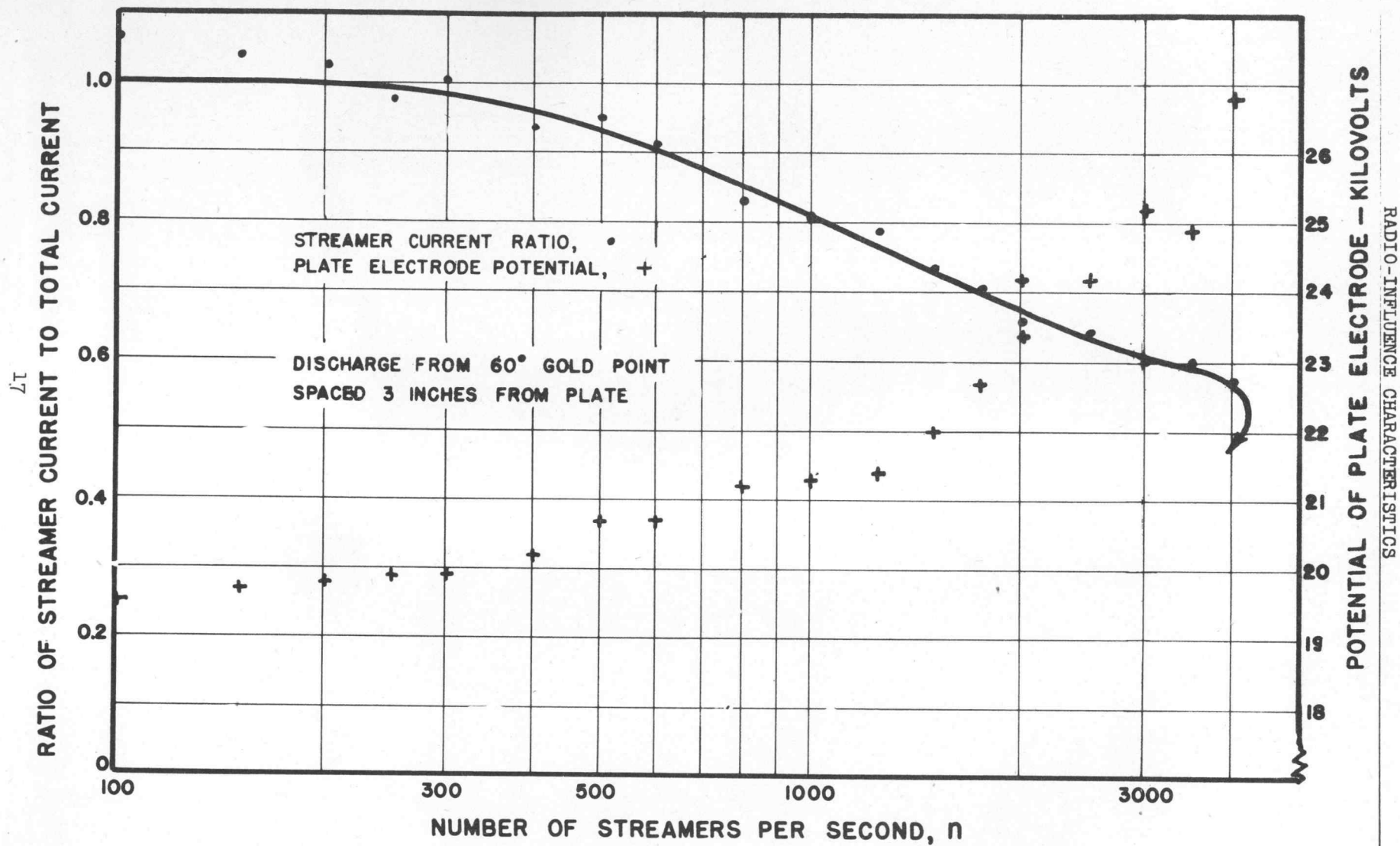
Although the negative-point corona discharge resembles the "Type 1" positive discharge in that it is very localized, actually the mechanism is distinctly different.

When the voltage on the point reaches a value sufficiently negative that a positive ion upon reaching the point produces a secondary electron by impact, that electron will travel outward from the point producing an electron avalanche by collision. The positive ions produced by the avalanche move inward to the point where they liberate new electrons which form additional avalanches. In the meantime, the electrons produced by the first avalanche have moved outward into a weak field (which has been further reduced because of the positive space-charge left behind), where they attach to molecules of oxygen to form slow-moving, negative ions which eventually reach the positive electrode.

The positive space-charge surrounding the point rapidly builds up until it effectively neutralizes the field and the voltage gradient is reduced to a value no longer

FIGURE 8A. STREAMER-CURRENT/TOTAL-CURRENT RATIO

FOR A POSITIVE-POINT DISCHARGE



sufficient to cause additional ionization. At this time the conduction has practically ceased, but as the positive ions are swept into the point, the field again increases until the last ions which reach the point can start new electron avalanches, and the entire process repeats.

Because the positive space-charge is concentrated in the very intense field near the point and must therefore travel but a small distance to be swept away, the frequency with which the negative bursts occur is very much greater than in the case of the positive discharge. Loeb and Kip have reported pulse frequencies up to 200,000 impulses per second,³ and this laboratory has extended these measurements up to five million corona bursts per second by frequency-spectrum studies to be described in a later section of this report.

Comparison of Positive- and Negative-point Discharges

There are, of course, certain characteristics which are common to both positive and negative-point discharges. Electron avalanches play a basic part in both mechanisms. Also, the many photons released during the de-ionizing processes produce photo-ionization in the surrounding gas and also aid in the extraction of electrons from the point and plane surfaces through photoelectric emission. In fact, the discharge of both polarities are known to produce copious amounts of ultra-violet light, a phenomenon which has to date been overlooked with respect to the possibility of employing it to reduce the radio interference produced by such discharges. Loeb states that a Pyrex tube surrounding a point discharge will glow brilliantly and that there is a considerable photo-emission of electrons from the plane electrode if the intervening gap is not too large.¹

A basic difference between the positive and negative discharges is to be found in the behavior of the positive space-charge. The positive space-charges, in the case of a positive point, move outward producing long streamers and in effect extend the point into the gap. On the other hand, a negative point attracts the positive charges resulting in a very intense but localized type of discharge. The positive space-charge so effectively neutralizes the field produced by the negative point that spark breakdown can never extend outward from the negative point but must always advance toward the point from the positive electrode.

Effect of Air Movement and Radiation on Point Discharge

An electrical discharge from a point located in a rapidly moving stream of air may differ materially in its voltage-current characteristics from that obtaining in still air. However, this difference is more superficial than fundamental. Larger discharge currents will obtain in a moving air stream because the space-charge effects will be reduced. This removal of space-charge should have very little effect on the fundamental discharge mechanism described above because streamer formation is so rapid that the movement of the air is negligible during the active period of the corona-burst cycle. For example, if the air stream were moving past the discharge point with a velocity of 360 miles per hour, the air molecules would have moved but 0.0008 inch during the time that the streamer current was flowing. It seems reasonable, therefore, that the principal effect of air movement past a discharge point is simply to increase the magnitude of the electron avalanches, and perhaps their number, without materially altering their shape and other characteristics.

The effect of radiation from radio-active material upon the corona discharge is perhaps more fundamental. Radiation of the air around the discharge point produces many initial ions, each of which, in the case of a positive point, is capable of starting a small electron avalanche. As a consequence many small avalanches are formed, producing a heavy space charge such that long streamers are inhibited and do not occur. The effect of radiation, combined with that of the rapidly moving wind stream, has not yet been investigated, but it is possible that the two effects would neutralize and the

movement of the air stream would again allow streamers to occur, together with the resulting radio interference.

Because of the bearing on the equivalent circuit to be discussed in the next section, it should be emphasized that, for either polarity of discharge, immediately after a streamer or succession of electron avalanches has occurred, a space-charge sheath is formed around the point. It is this sudden change of potential in the region of the space charge, together with the avalanche current, that produces the radio interference.

On the basis of the mechanisms just described, an equivalent circuit yielding induced voltages nearly identical to those actually observed can be constructed.

Equivalent Circuit for Voltage-Induction Effects

In setting up an equivalent circuit to represent a point-discharge phenomena, it will be assumed that the space charge is formed in a shell-like layer surrounding the point. The various distributed capacitances and gap conductances can then be considered as lumped circuit parameters as illustrated in Figure 9.

When an electron avalanche occurs, the outermost space charge tends toward the polarity of the point almost instantaneously because the avalanche requires but 10^{-7} to 10^{-9} seconds to propagate. (A method of indirectly measuring the time required for the build-up of space charge will be discussed in later sections.) The establishment of an ionized channel along the path of the avalanche is in effect equivalent to a sudden increase at the point-to-space-charge conductance Y_s , by ΔY_s . The problem therefore becomes simply one of network analysis: To find the changes in currents and voltages when Y_s is suddenly increased by ΔY_s . Appendices II and III give this analysis for the circuit shown in Figure 9.

The induced-voltage changes resulting when a streamer is assumed to short out completely the "space-charge shell" to the point (i.e. $\Delta Y_s = \infty$) are shown graphically in Figure 10.

Although the circuit parameters indicated in Figure 9 were, with but one exception, calculated directly from the point geometry and other estimated data (see appendix II), it is remarkable that the calculated data agree almost within the limits of measurement with Starr's² oscillographic records reproduced at the top of Figure 9. (Starr's oscillograms are actually records of the voltage induced on the plane electrode. The actual point currents are of much shorter duration as will be shown later.)

The voltage shown in Figure 10 are all measured with respect to that part of the circuit to which the discharge point is connected, and would be, therefore, the voltages as measured with respect to the body of an aeroplane if the equivalent circuit were to be applied in the study of discharges from aircraft.

The two curves at the bottom of Figure 10 represent the voltages across the point resistance. It should be noted that at the instant of streamer formation the same voltage will appear across the discharger regardless of its resistance. For the values shown, the peak current through the low resistance would be 10,000 times that which would flow through the high resistance. The reason that the 10-megohm discharge resistance does not eliminate the sudden discontinuity in the space-charge build-up is that the distributed capacitance of the point is sufficient to supply almost all of the charge that is needed. Thus, even for the extremely small capacitances shown in Figure 9, about 90 percent of the charge needed to establish the space charge can come from this point capacitance alone. This clearly shows that, if dischargers employing series resistors are to function properly, the capacitance shunting the series resistor must be limited to an extremely small value. This would require that all conducting surfaces on the point side of the discharge resistor must be limited to as small a total area as mechanically feasible.

FIGURE 9A. EQUIVALENT CIRCUIT FOR VOLTAGE-INDUCTION EFFECTS

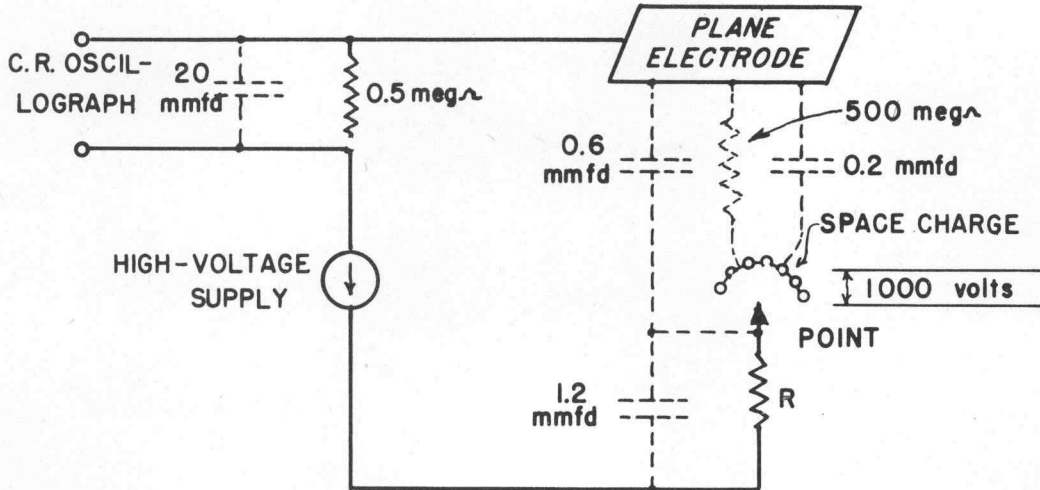


FIGURE 9B. STARR'S OSCILLOGRAMS OF VOLTAGES INDUCED BY A POSITIVE-POINT STREAMER

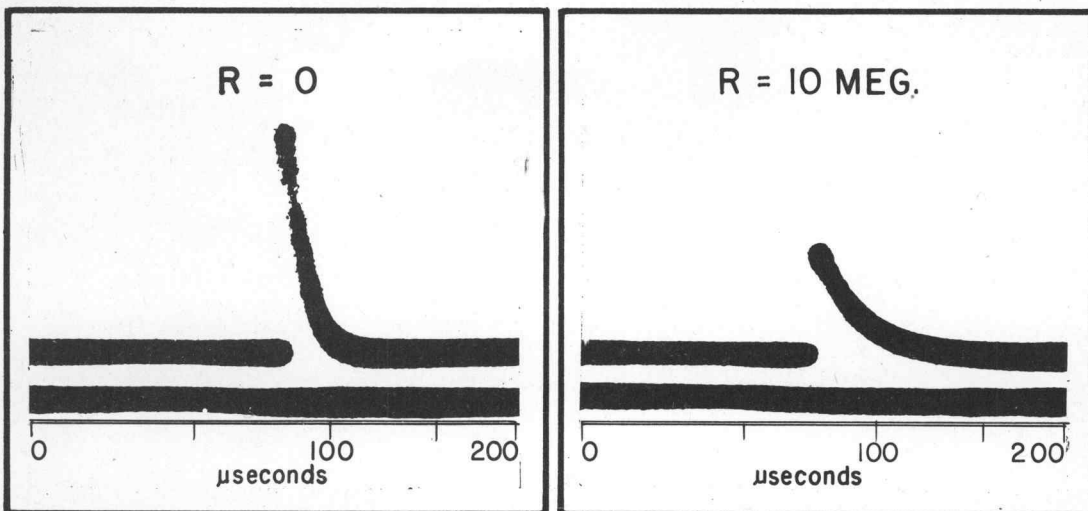
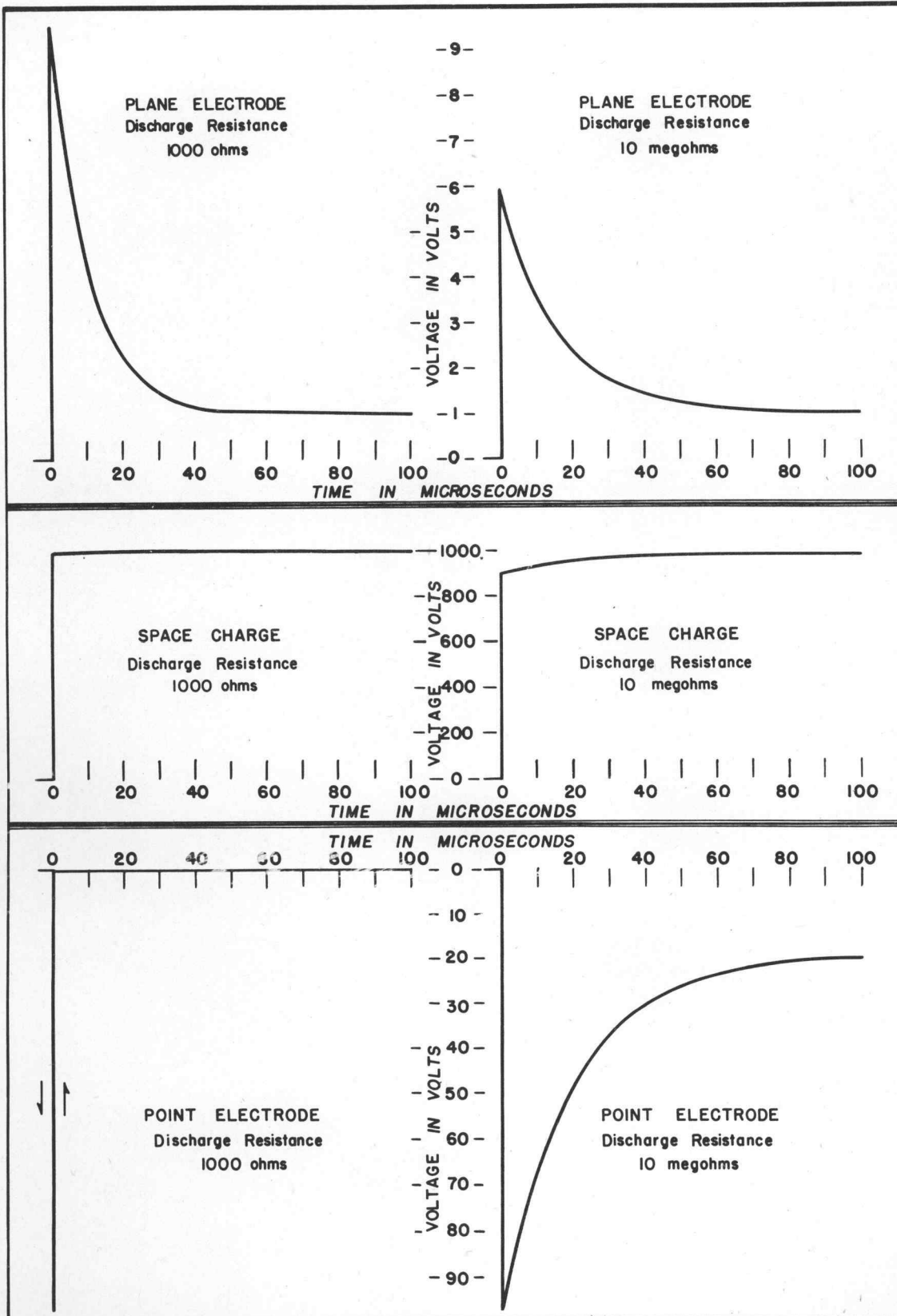


Figure 10

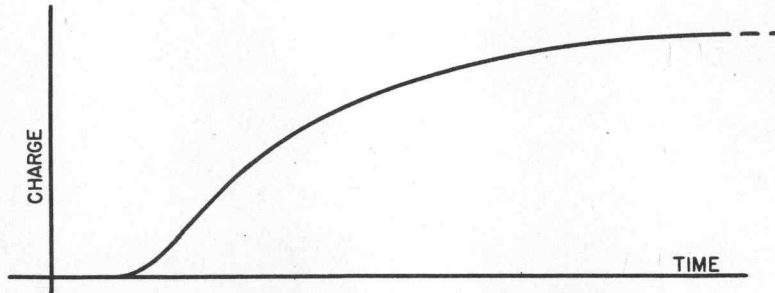
CALCULATED INDUCED VOLTAGES CAUSED BY POINT DISCHARGE



When a high resistance is placed in series with the discharge point, a corona streamer will produce a change in point potential of opposite polarity to the potential change in the space-charge shell. It would seem, therefore, that there might exist around the point and resistor combination, loci along which the change in potential due to the space-charge shell would exactly counterbalance the change in potential arising from the point and resistor. This has been strikingly demonstrated in the laboratory by connecting a small spherical probe through a shielded cable to a radio receiver and then exploring the constant-noise-pickup contours surrounding the point, resistor combination. It was observed that there existed around the point, resistor combination an imaginary surface on which the induction effects did actually cancel. If the probe were moved either toward or away from the point and resistor, the radio interference became very great, but on this surface, which was explored to within an inch of the point, the noise pickup was negligible.

Limitation of the Equivalent Circuit

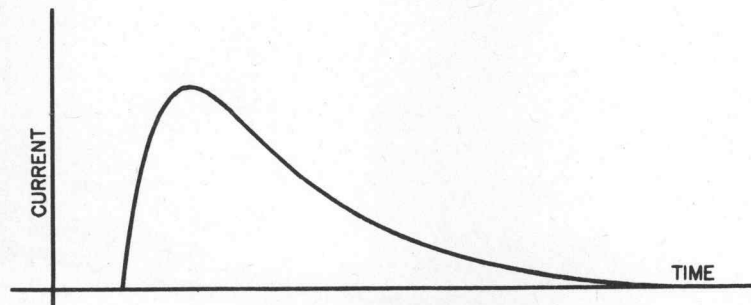
Even though the calculated induced voltages agree almost perfectly with Starr's oscillograms, an instantaneous build-up of space charge as indicated by the equation is a physical impossibility. Instead, if an ideal oscilloscope were available so that the voltage might be plotted on a greatly expanded time-scale, the build-up of space charge would probably appear as in the following sketch.



Assumed Space-Charge Build-Up Characteristic

Since the space charge can build up in about 1/10,000 the time required for it to decay, it may be assumed to approach a constant value during the time intervals of interest in this study.

But since the current flow in the avalanche is given by $\frac{dQ}{dt}$, on the basis of the first assumption, the current would be of the form as shown below:



Probable Shape of Discharge Current

When the voltage across a 150 ohm resistor connected in series with a positive discharge point was examined with a wide-band oscilloscope, all that could be observed was a series of small whisker-like traces very similar to that shown in the lower left-hand part of Figure 10. Because of the extreme rapidity, the shape of these whisker-like impulses could not be observed on the oscilloscope even when using the fastest sweep speed available. A method was therefore developed whereby the shape of the current impulses could be obtained indirectly from measurements made of their frequency spectrum. This phase of the study will be discussed in the next chapter.

IV. STATISTICAL CURRENT FREQUENCY SPECTRUM OF POSITIVE AND NEGATIVE
ELECTRICAL DISCHARGES

Summary of Theory

Perhaps the greatest analytical discovery of all time is that due to Fourier. In his classical work, "Analytical Theory of Heat," Fourier argued that a function $f(x)$, of period, $2\pi\lambda$, could be represented by the series

$$f(x) = \frac{\alpha_0}{2} + \sum_{n=1}^{\infty} \left(\alpha_n \cos \frac{nx}{\lambda} + \beta_n \sin \frac{nx}{\lambda} \right)$$

which series is now known as the Fourier series in honor of its inventor.

Fourier's basic concept has been of great value to the electrical engineer who has learned to think of a distorted electrical wave as equivalent to a sinusoidal wave of fundamental frequency plus sinusoidal waves having frequencies which are integral multiples of the fundamental frequency. The concept is particularly useful in the study of network response to a periodic driving force. In this case, the periodic driving force is considered to be equivalent to the sum of the various harmonic sinusoidal or cosinusoidal components. Now if the network be linear, the response to the periodic driving force is equivalent to the sum of the responses to each of the components of that driving force, so that the network response is also expressible as a sum of sinusoidal and cosinusoidal oscillations of the various frequencies. This application is well covered in the literature.

On the other hand, if the driving force is "quasi-systematic," it can be shown that the sinusoidal and cosinusoidal oscillations are no longer limited to definite frequencies such as the fundamental, second harmonic, third harmonic, etc., but that, instead, oscillations of any frequency may be found. The magnitude of these component oscillations at every frequency from zero to infinity form what is known as the frequency spectrum of the function.

It would perhaps be well to examine the limiting types of disturbances, the frequency spectra of which are to be defined. In general the disturbances may be divided into three types: (a) a single disturbance existing only during a comparatively small interval of time and being zero or non-existent for all other values of time; (b) an aggregate of disturbances of type (a) each occurring in an entirely random fashion with regard to the other elemental disturbances, but extending over a period of time very much greater than the longest time interval between the elemental disturbances; (c) a truly periodic type of disturbance in which the period of the disturbance is the same throughout its regime, and the variation of the disturbance within each period is identical to that occurring within any other period.

As a guide in classifying radio-interference phenomena, type (a) radio interference would be that resulting from a single, transient electrical disturbance; type (b) interference would be that arising from thermal agitation and Schroteffekt noise; and type (c) radio interference would be that resulting from some device producing a regularly reoccurring disturbance, such as that produced by a relaxation oscillator.

Most man-made radio interference would be classified intermediate to the limiting types (b) and (c). Examples of such interference would be that arising from the commutator of d-c motor, an electric razor of the vibrator type, or automotive ignition systems.

Calibration of Noise-measuring Equipment by Shot-effect Noise Currents

In view of the theoretical developments of appendices IV, V and VI, it appeared that an experimental method of measuring the equivalent frequency spectrum of high-voltage electrical discharges would be a very valuable development and, in fact, a necessary one if the phenomenon of radio interference arising from high-voltage electrical discharges were to be studied in a quantitative as well as qualitative manner. It remained, therefore, to determine the relationship between the radio-interference measurement, obtained as outlined in Chapter 2, and the actual, spectral noise intensity discussed in these appendices.

Furthermore, it was necessary to establish with certainty that the shape of the frequency spectrum thus obtained was actually due to the inherent shape of the electrical discharge rather than the electrical transmission characteristics of the measuring circuit. Fortunately both of these objectives could be achieved simultaneously by calibrating the noise-measuring equipment against the "shot-effect" noise produced by a temperature-limited diode.

In appendix V, equation (23), it is shown that the mean-square fluctuation noise in a temperature-limited diode as measured by an amplifier having an effective band width of Δf is $i_n^2 = 2eI\Delta f$. This equation is valid for all frequencies having a corresponding period considerably greater than the transit-time of the electron flow in the diode. Accordingly, by using a diode with a small spacing between the cathode and plate, a noise source is obtained which is acknowledged to have a uniform spectrum over a frequency range somewhat greater than here studied.

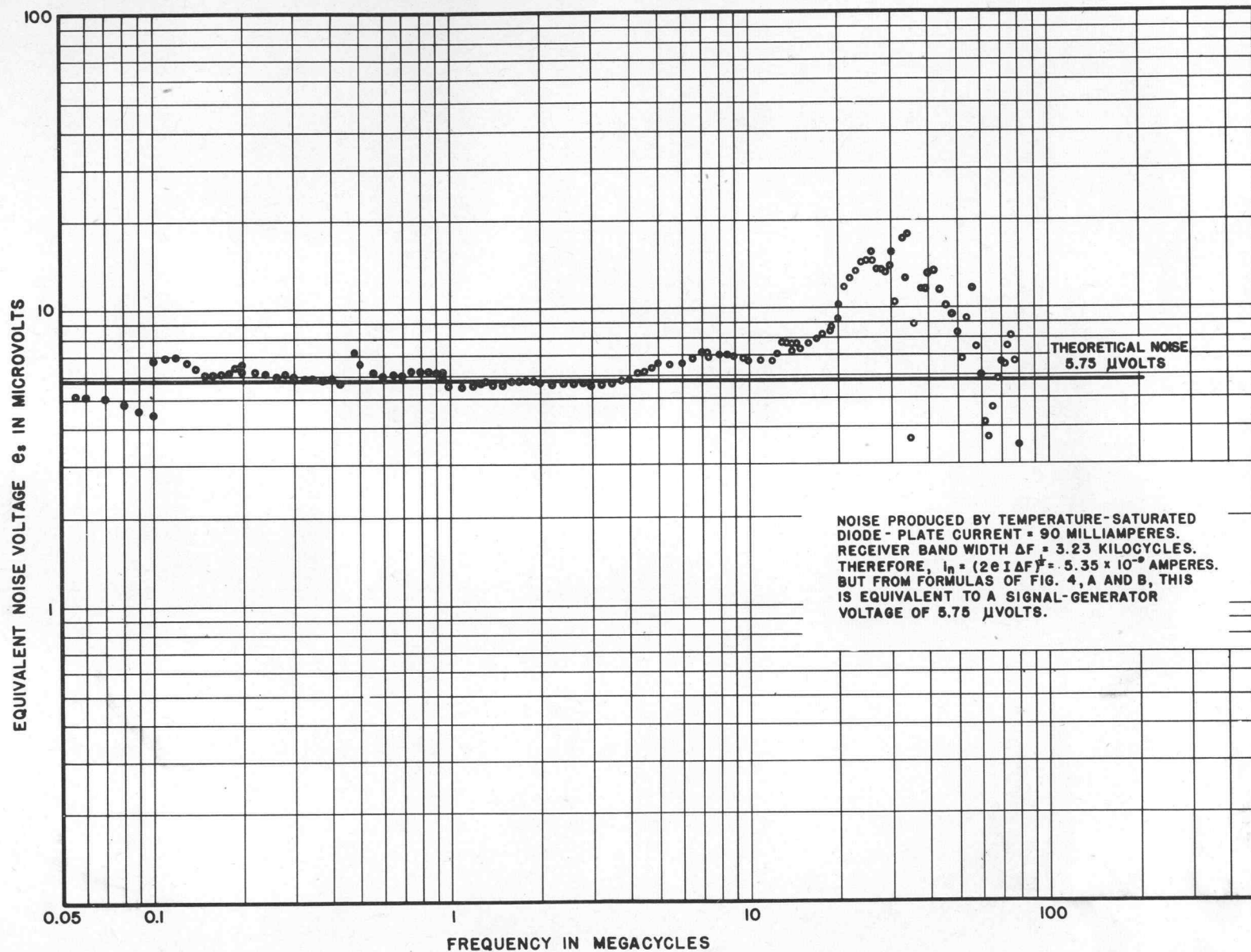
For the reasons discussed above, the radio interference resulting from a large diode passing a temperature-limited current of 90 milliamperes was then measured. The magnitude of the radio interference resulting for frequencies from 50 kilocycles to 80 megacycles is shown in Figure 11. Shown also in Figure 11 is the theoretical spectrum as calculated from the above expression assuming $I = 0.09$ amperes, $e = 1.59 \times 10^{-19}$ coulombs, and $\Delta f = 3.23$ kc. As this fluctuation current produced a voltage drop in the low-resistance measuring circuit of only six microvolts approximately, the noise measurements at the higher frequencies were possibly subject to certain errors because of the very small value of the noise itself. The discontinuities in the spectrum are due to changes in the r.f. coils of the radio receiver. The reason for the reduced radio interference as measured with the 50-100 kc. coils is that these r.f. coils were extremely selective so that they decreased the effective band width of the radio receiver. The differences between the theoretical and actual noise spectrums at the higher frequencies are no doubt due to slight unbalances between the noise and standard-signal comparison circuits.

If it is now assumed that the theoretical noise spectrum is the actual noise spectrum and that differences therefrom in the measured values indicate an error in the measuring circuit; a correction factor obtained by forming the ratio of the theoretical noise to the actual noise at every frequency can be calculated. Since the network is linear, this same correction factor, (or function, as the correction factor itself is dependent upon the frequency,) can be applied to all other noise measurements to correct for errors in those measurements due to variations in the transmission characteristics of the measuring circuit.

Effect of Diode Detector on Noise Measurements

It will be recalled that the magnitude of radio interference producing a given receiver AVC voltage was measured by substituting for the noise a standard signal of

FIGURE II. STATISTICAL NOISE-FREQUENCY SPECTRUM OF "SHOT-EFFECT" NOISE.



frequency to which the receiver was tuned and of magnitude such as to produce the same avc voltage obtaining for the noise. It is shown in appendix VIII that this noise reading is not the true effective value of the noise. This is because the avc voltage is proportional to the average value of the oscillations at the second detector rather than the effective value of those oscillations. For this reason, it is necessary to multiply the standard-signal current value by the form factor, Γ , where Γ is the ratio of the effective to average values of the oscillation impinging upon the second detector. For a "smooth" type of noise such as thermal agitation or shot effect, the form factor, Γ , is unity for all practical purposes. It is shown in appendix VIII that impulsive disturbances occurring at a slow rate will result in shock oscillations at the second detector which have a form factor considerably greater than unity and for such disturbances as "singing corona" a correction factor must be applied to the standard-signal-generator measurement.

Fortunately, it is possible to calculate the form factor which would result from impulse disturbances occurring at various rates. Following the method outlined in appendix VIII the theoretical form-factor as a function of interference bursts per second was calculated and the results are presented in Figure 12. The discrepancy between the observed and calculated values of form factor at the higher burst frequencies is due to the fact that the experimental values of the form factor were determined by assuming that all of the corona current was due to noise-producing streamers. Such an assumption is valid at the lower burst rates, but is known to be incorrect for the higher burst rates. The fact that the experimental and theoretical values do agree over the range where the assumptions made are valid is felt to be ample proof of the accuracy of the method.

Frequency Spectrum of Positive Corona Streamers

From the discussion at the end of chapter 3 it seems reasonable that, to at least a first approximation, the positive streamer-current wave shape should be that of a double-exponential form given by

$$i(t) = I[\exp(-\alpha t) - \exp(-\beta t)]$$

On the basis of this assumption it is shown in appendices IV and V that the equivalent mean-square noise current due to a series of such corona streamers occurring at an average rate of n each second and measured by a radio receiver having an effective band width of Δf , may be calculated in terms of ω , the radian frequency, by the relation

$$i_n^2 = 2nI^2 \frac{(\beta - \alpha)}{(\alpha^2 + \omega^2)(\beta^2 + \omega^2)} \cdot \Delta f$$

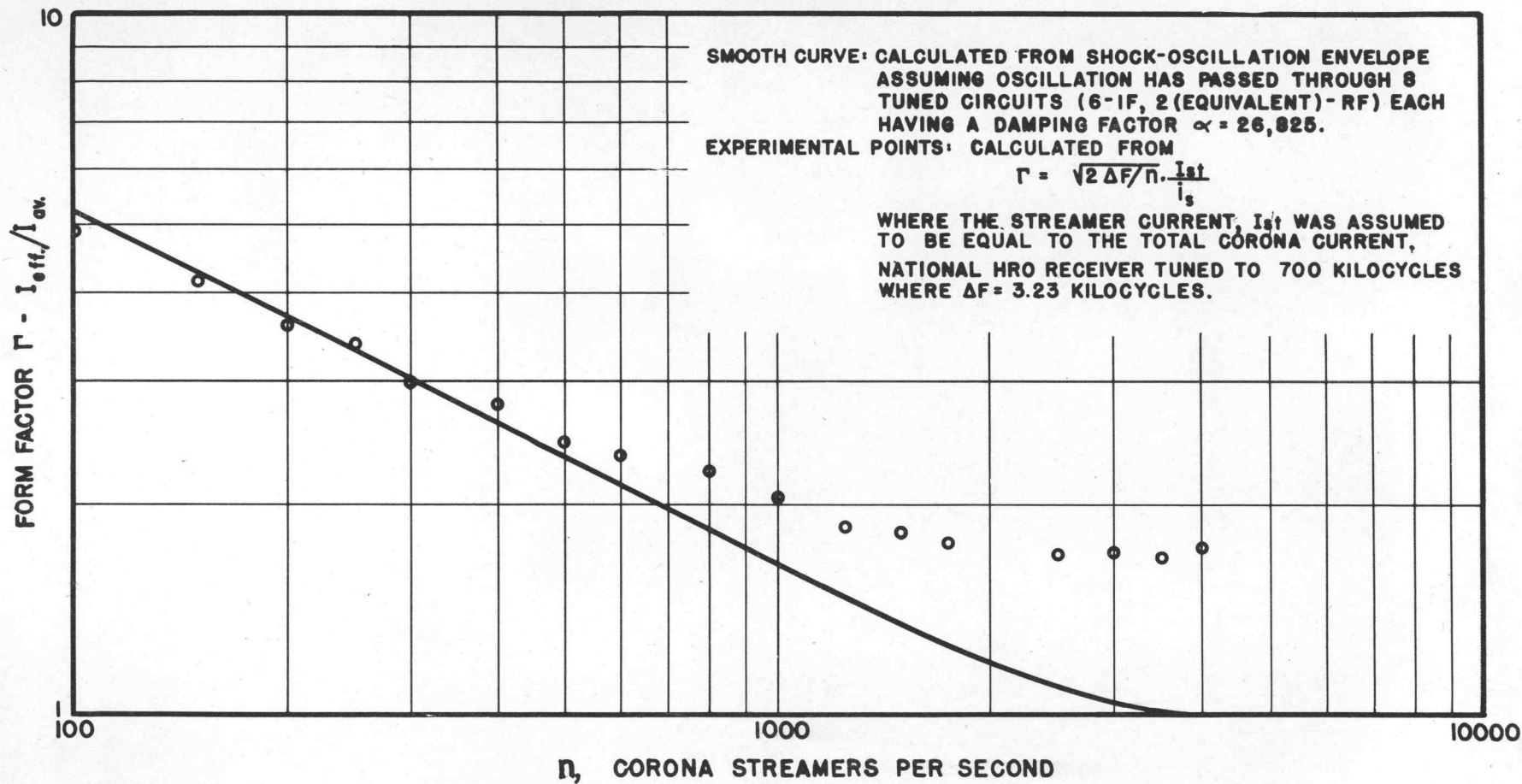
Now, a procedure for experimentally measuring the effective radio interference resulting from positive-point-streamer currents has already been described. The equation given above therefore provides a method of determining the shape of these streamer-current impulses, for it is only necessary to find by trial and error, values of α and β which yield a calculated noise spectrum in closest agreement with that experimentally measured.

Effect of Variations in Wave Shape of Elemental Disturbances

A question may be raised as to the validity of measuring the wave shape of the individual streamer-current impulses by indirectly measuring the noise-frequency spectrum of those impulses. It might be argued, since the streamers are essentially of a very erratic nature, that not only the amplitude of the individual streamers will be different but that the shape of the successive streamers may also vary quite markedly.

The effect of random variation in the amplitudes of the successive streamer currents (the shape of each remaining unchanged, however) is studied in appendix IV,

FIGURE 12. CALCULATED AND EXPERIMENTAL FORM FACTORS OF SHOCK-OSCILLATIONS AT SECOND DETECTOR OF RADIO RECEIVER.



and it is concluded that the shape of the frequency spectrum will not be affected if only the amplitudes of the various current bursts vary.

Appendix IV also gives a general method of determining the effect on the frequency spectrum of variations in the shape of the elemental disturbances as well as the amplitude of each. As an example of this method, there is derived in that appendix the equation giving the noise-frequency spectrum resulting from a series of single exponential transients in which the exponents of the individual impulses are not all identical but are equally distributed over the range $\bar{\alpha} - \Delta\alpha$ to $\bar{\alpha} + \Delta\alpha$, where $\bar{\alpha}$ is the average value of the exponent for the series of transients. A further restriction was also made in that it was assumed that the charge of each streamer impulse was the same.

The calculated results based on these equations are shown in Figure 13. The solid curve of this figure shows the noise-frequency spectrum of the single-exponential transients, all of which have the same shape but are random with respect to time of occurrence. The dotted line shows the frequency spectrum resulting from a series of single-exponential transients in which the exponents of the individual impulses are equally distributed between zero and twice their average value and the amplitudes vary in such a manner as to make the charge involved in each impulse the same for all impulses. This is a much greater variation in exponent than one would expect to find in an actual series of transients such as corona streamers. It should be noted, however, that the general shape of the noise-frequency spectrum in this latter case does not differ materially from that obtained when all transients were identical. It may be concluded, therefore, that a small variation in the shape of the impulses will not alter the frequency spectrum appreciably from that obtaining for the average-shaped impulse.

The noise-frequency spectrum resulting from a series of identical double-exponential impulses will depend upon the steepness of the wave-front as well as the rate of decay of each impulse. The frequency spectrum resulting for several different ratios between the exponents is shown in Figure 14. It will be observed that the two values of ω at which the slope of this curve is changing most rapidly are approximately $\omega = \alpha$ and $\omega = \beta$. This rather interesting relationship is very helpful in determining the exponent of the double-exponential transient which best fits an experimentally-measured frequency spectrum. Thus, after the noise-frequency spectrum has been measured by methods previously described, the data are plotted on log paper and the resulting curve is examined for points at which the slope is changing the most rapidly. The experimental noise-spectrum curve may then be compared with those of Figure 14 and the most probable values of α and β thus determined.

Experimental Results

Following the method previously outlined, the noise-frequency spectrum of positive corona streamers synchronized to occur at the rate of one thousand per second was measured over the frequency range of 50 kilocycles to 80 megacycles. The experimental data thus obtained were corrected for variations in the transmission and selectivity characteristics of the measuring circuit by applying correction factors obtained from the shot-effect calibrating data given in Figure 11. The form-factor correction Γ (which in this case for $n = 1000$ is 1.65) was also applied to the experimentally-determined noise values. These experimental values are shown in Figure 15 as points. Shown also in Figure 15, as a solid line, is the calculated frequency spectrum for the double-exponential impulse which was found to most resemble and fit the experimental data. The best fit was obtained when $\alpha = 23.56$ and $\beta = 94.25$ (both in megaradians per second).

The agreement between the theoretical and experimental noise values is truly remarkable. The theoretical noise spectrum was calculated from

$$i_n^2 = \frac{I_{st}^2}{[1 + (\omega/\alpha)^2][1 + (\omega/\beta)^2]} \cdot \frac{2\Delta f}{n}$$

where, for the case under consideration, $\Delta f = 1000$, $n = 1000$, α and β are as given above, and I_{st} may be found as follows:

FIGURE 13. EFFECT OF RANDOM VARIATION IN THE
IMPULSE SHAPES ON NOISE FREQUENCY SPECTRUM

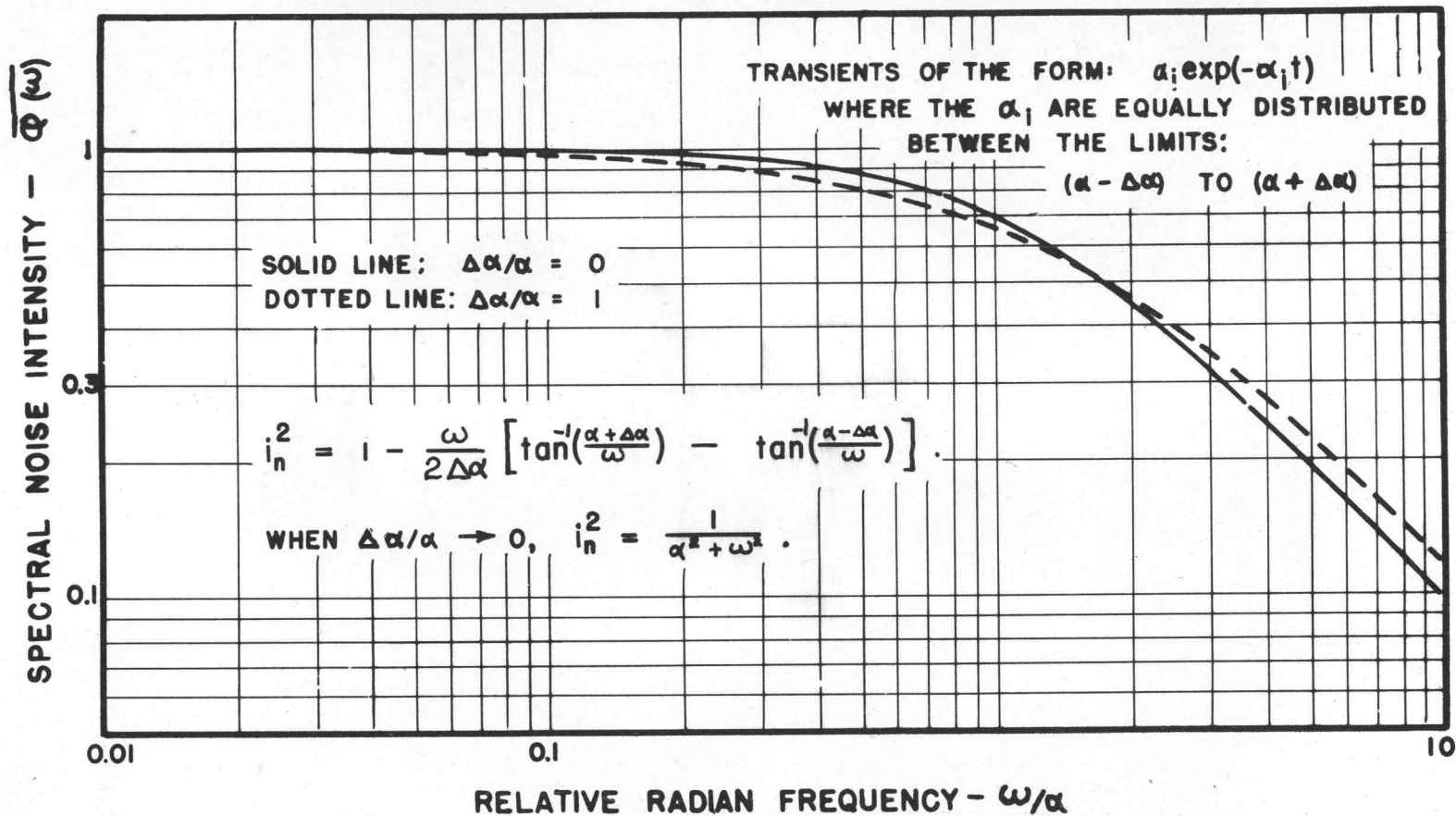
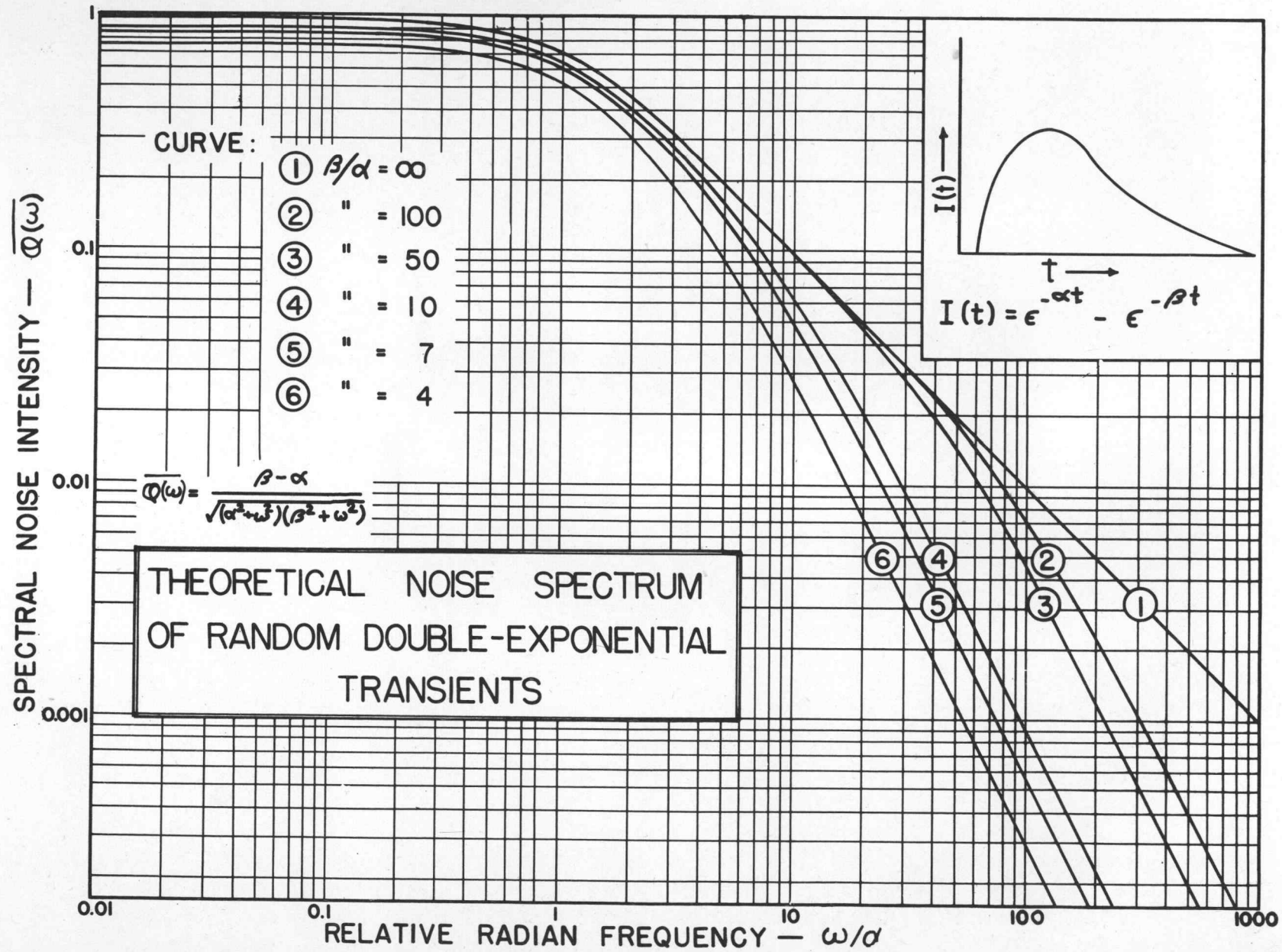


FIGURE 14.



30

RADIO-INFLUENCE CHARACTERISTICS

The measured value of corona current which was maintained constant during the noise measurements was 1.74 microamperes. However, from the data presented in Figure 8A, it is estimated that 0.813 of the total current is due to streamers, the rest being due to burst pulses which produce relatively little noise. Accordingly the actual streamer current is 1.74 times 0.813 or 1.414 microamperes.

These values when substituted into the above noise equation give the theoretical noise-frequency spectrum shown in Figure 15. It should be emphasized that not only is the shape of the theoretical noise-frequency spectrum the same as the shape of the observed frequency spectrum, but that there is also an excellent agreement between the magnitude of the measured and calculated interference where the calculated interference is based on the measured value of the d-c corona current.

With regard to the practical application of the data of Figure 15, one must keep in mind that the noise values given are for a receiver bandwidth of one kilocycle and a unity coupling between discharge point and radio receiver (i.e., all corona current passes through receiver antenna coil). For a typical radio-receiver installation on aircraft, both the bandwidth of the receiving equipment and the coupling between corona discharge and the radio receiver will depend upon the operating frequency. The ultra-high-frequency receiver would have a much broader bandwidth than a medium-frequency receiver. Accordingly, the data of Figure 15 must be converted to that pertaining to the particular receiver under consideration by multiplying the noise values given on the curve by the square root of the effective bandwidth of the receiver. Because these variations in bandwidth and coupling were overlooked, other investigators have obtained "unreferred" noise frequency spectrums which indicate an actual increase in radio noise at the higher frequencies.

Probable Positive-Streamer-Current Wave Shape

Once the exponents α and β have been determined, an equation giving the streamer current as a function of time may be immediately written. It is

$$i(t) = I[\exp(-23.56 \times 10^6 t) - \exp(-94.25 \times 10^6 t)]$$

where the coefficient, I , may be found from

$$I = \frac{\alpha\beta}{n(\beta - \alpha)} \cdot I_{st}$$

This equation is in accord with the known fact that streamer-propagation time lies between 10^{-7} to 10^{-8} seconds. Figure 16 shows the streamer current-flow when plotted as a function of time. The manner in which the space charge also forms is shown in Figure 16.

It is significant that the results obtained above agree with those given by other investigators who have used other methods of measurement. As an example, for the particular positive corona discharge considered here, the streamer current was 1.414 microamperes. But since 1000 streamers were occurring each second, the electrical charge involved in each streamer was 1.414×10^{-9} coulombs, which is equivalent to 8.84×10^9 uni-valent ions. This is in accord with Loeb's statement that, "This number varies from 10^9 to 10^{10} ions."¹

Further experimental evidence of the correctness of these results is to be found in reference (7). Figures 17 and 18 are reproductions of oscillograms taken from this reference, and the captions on these figures are self-explanatory. These figures are oscillographic records of the voltage developed across a resistance in series with the discharge point. Because of the distributed capacitance shunting this series resistor, the voltage developed thereacross was not exactly proportional to the streamer current. The error resulting from this distributed capacitance, however, would be less the lower the value of series resistance, so that, in the limiting case of zero

FIGURE 15. NOISE FREQUENCY SPECTRUM OF POSITIVE STREAMERS.

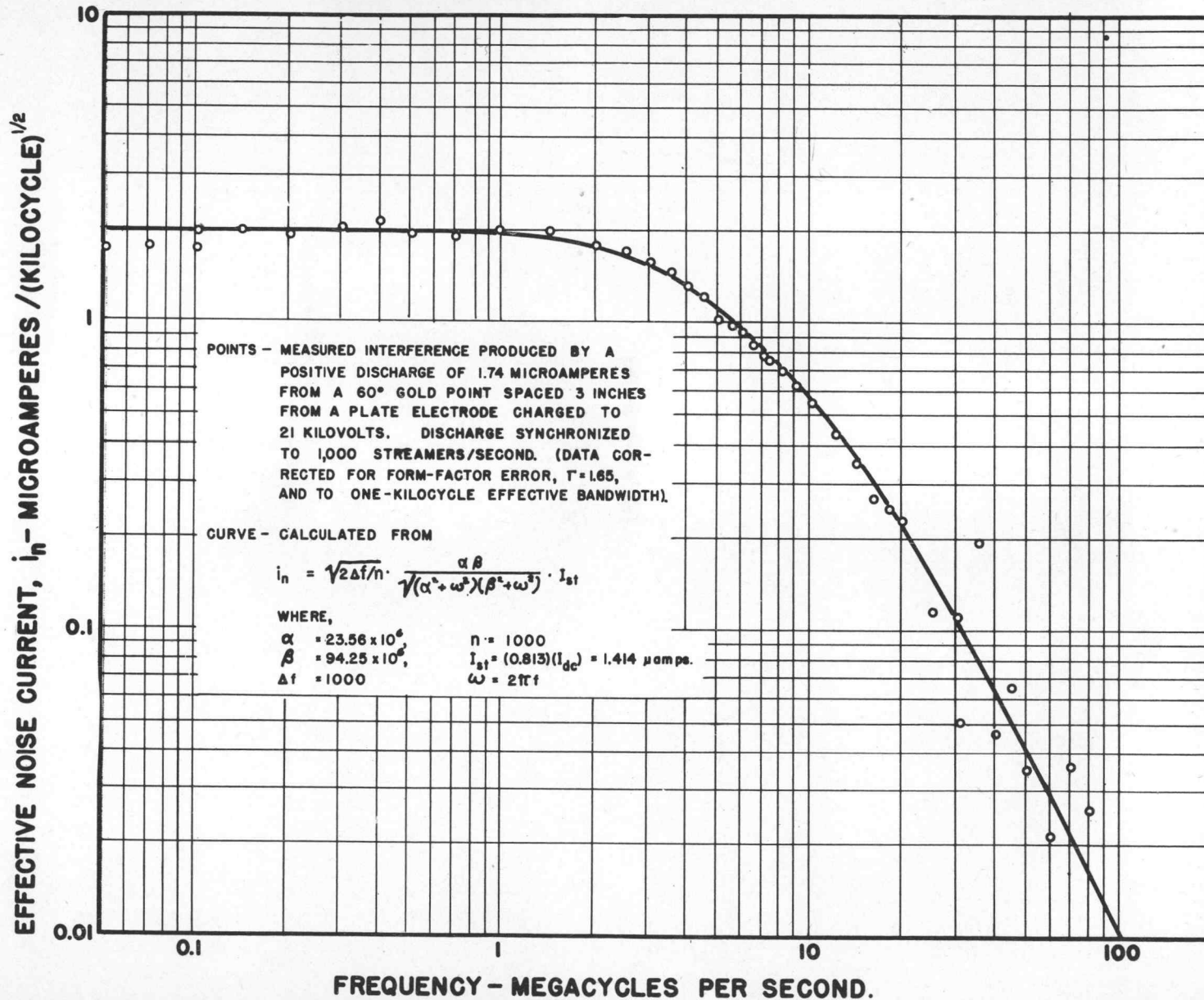
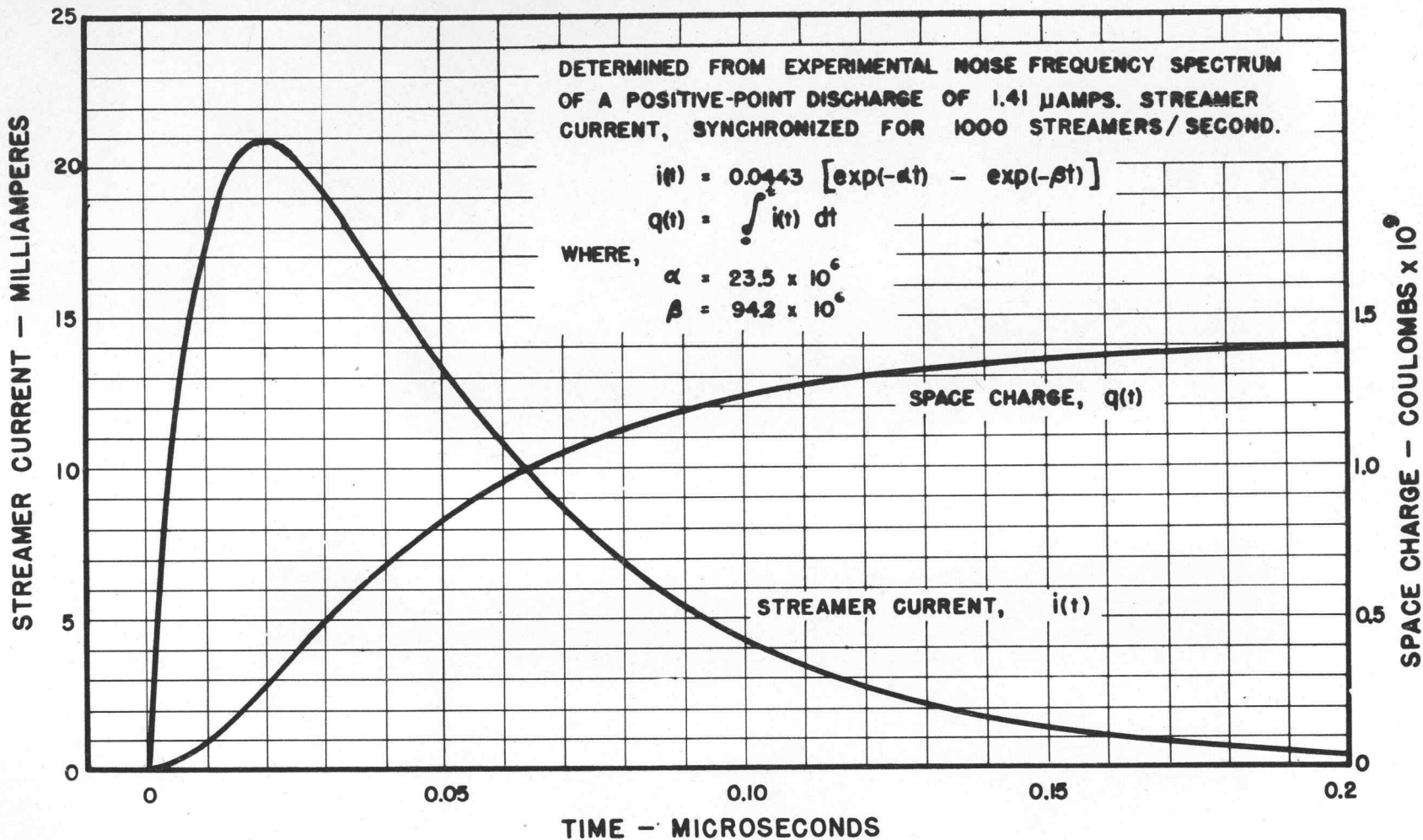


FIGURE 16. PROBABLE STREAMER CURRENT WAVE FORM
AND SPACE CHARGE DEVELOPMENT.

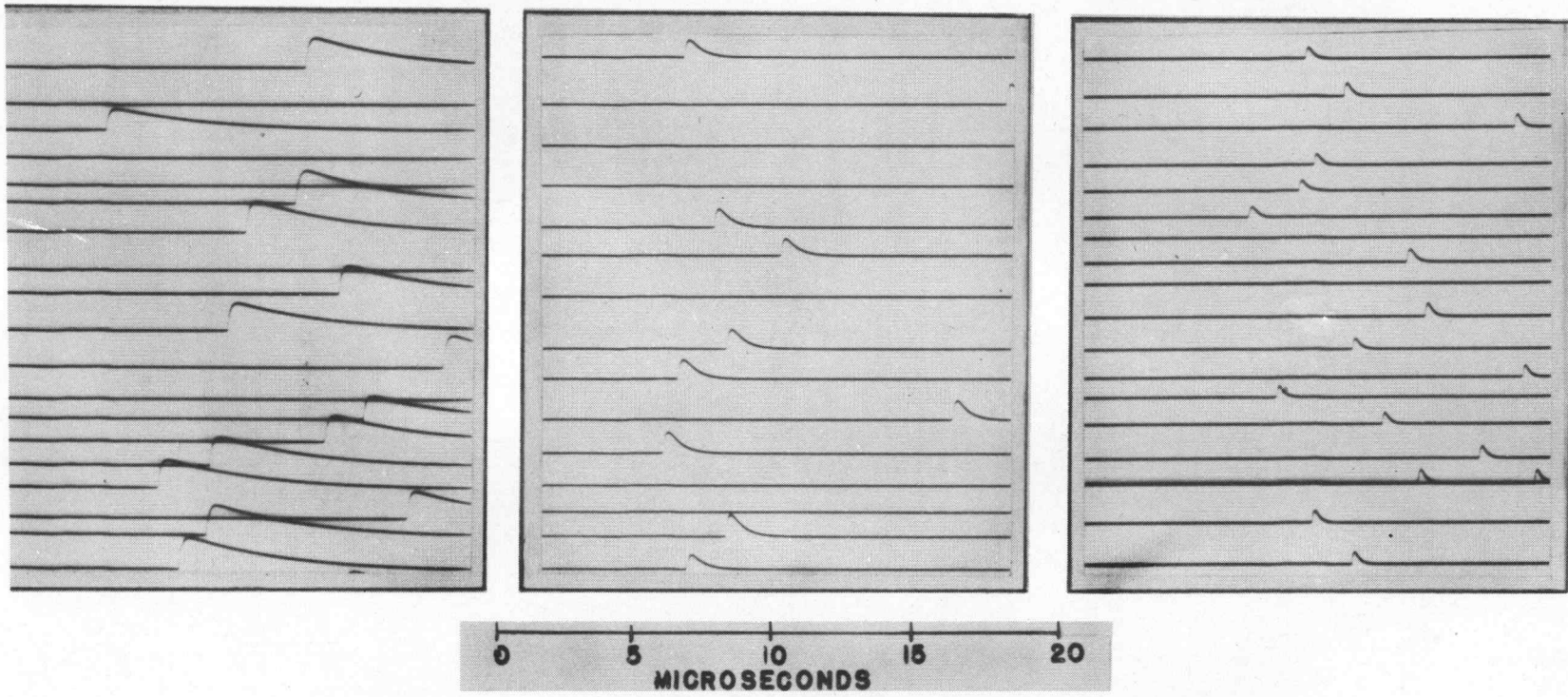
33



R = 100,000 Ohms.

R = 10,000 Ohms.

R = 2,500 Ohms



34

Figure 17. Voltage across a resistance R in series with a 44 Kv. positive needle-point discharge of 150 microamperes in a 150-mph. Wind Stream.

resistance, all of the streamer current would pass through the conductor and none would be diverted through the distributed capacitance shunting the conductor. It will be observed that the trend of the streamer-current pulses shown in Figure 17 and the enlarged oscillogram of Figure 18 indicates that for the limiting case of zero point resistance, a streamer-current wave shape such as shown in Figure 16 is entirely possible.

Frequency of Negative-Point Corona Pulses

Other investigators¹ have reported very rapid corona pulses from a negative point. Their oscillographic observations of the negative-point corona current indicated pulses occurring as frequently as 200,000 times a second. Frequencies higher than this could not be ascertained because of limitations in the response of the oscillograph. A new method of measuring these frequencies of discharge has been developed by the writer and it is now definitely ascertained that from a very fine needle-point at least three million and perhaps more corona bursts per second can occur. The method of measuring this burst frequency is extremely simple and gives as accurate results as desired.

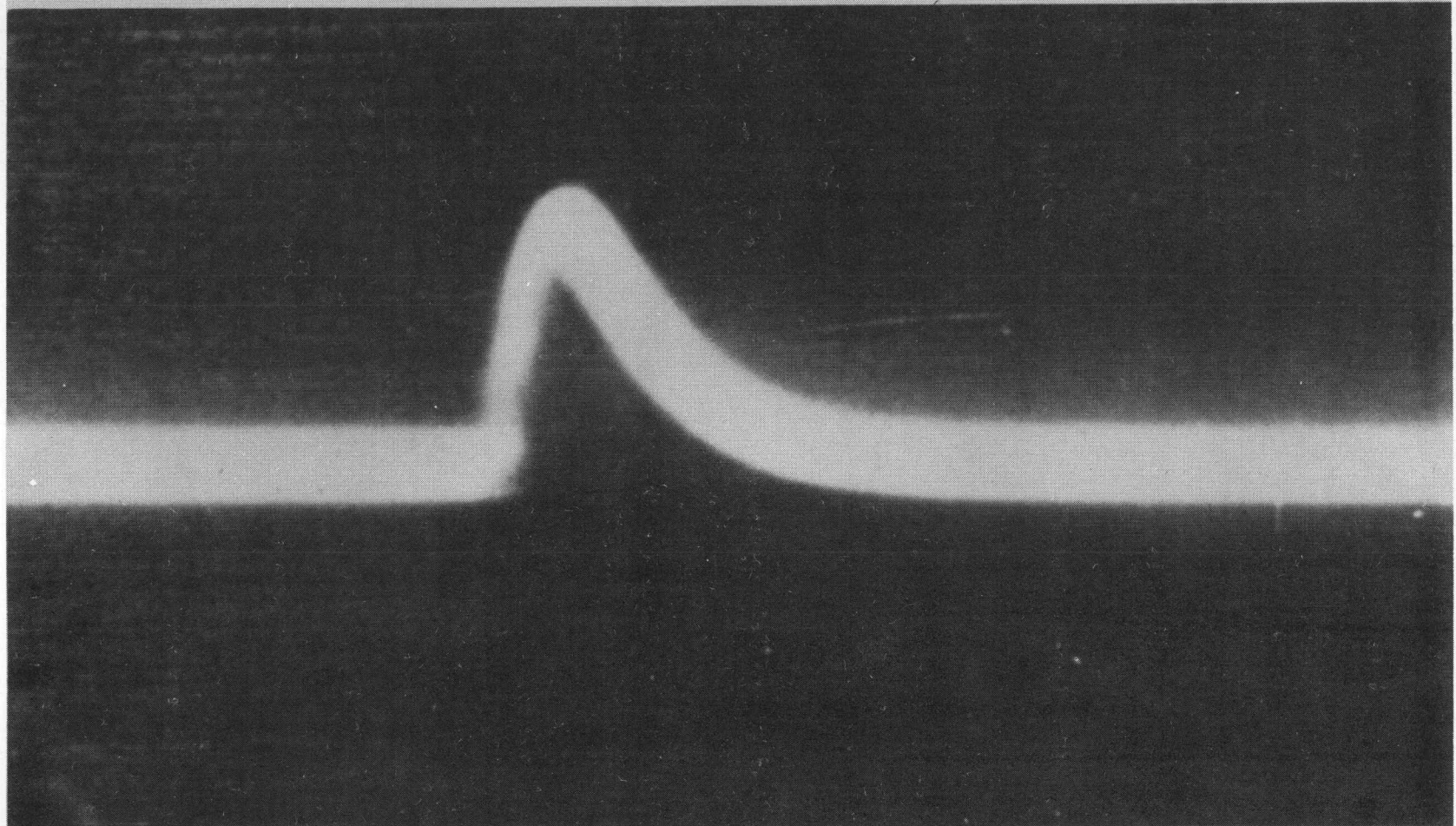
In measuring the noise-frequency spectrum of negative-point needle discharges it was observed that carrier-like bands of intensified noise existed at certain frequencies. Certain characteristics of these bands might well be summarized here.

First, it was observed that the frequency of the maximum noise in the center of each band depended to a very great extent upon the corona-discharge current, and if the current should be increased slightly, the frequency of all the noise bands would likewise increase. Furthermore, it was observed that the frequency intervals between all of these noise bands were more or less equal to each other. These observations could receive but one explanation, viz., the radio interference was being produced by some regularly reoccurring phenomena having a frequency of occurrence equal to the frequency difference between successive noise bands. For example, at a discharge current of about 52 microamperes a very strong, noisy region occurred in the immediate frequency band around 2 megacycles. The strength of the noise was so strong in this immediate frequency band that the receiver was overloaded even with the rf-gain control set at the minimum. For frequencies less than 2 megacycles, very little noise was observed. Likewise, for frequencies greater than 2 megacycles only slight noise was measured until the receiver was tuned to about 4 megacycles. At this frequency again considerable noise was found, but to a lesser degree than in the first band mentioned. Similar noisy bands were measured at 6, 8, 10, and 12 megacycles; the relative strength of the noise bands at the higher frequencies becoming proportionately less and their width greater until at 14 megacycles and higher the background noise (that is, the noise existing between noise bands) made it difficult to continue further with the measurements. Similar measurements were made for a wide range of different discharge currents. The results of these measurements are given in Figure 19.

One of the more interesting conclusions that may be drawn from these experimental data is that apparently each corona pulse must constitute some definite electrical charge for a given-size needle point. This is apparent because there is a direct proportionality between the discharge current and the frequency of the pulses. This constant of proportionality represents "Coulombs-per-burst" and the number of ions involved in each corona burst may thus be readily determined. Additional studies with needle points of various sizes indicate that there is a direct relationship between the charge-per-burst and the bluntness of the needle point, the charge being approximately 10 micro-micro-coulombs for the sharpest point studied and 80 micro-micro-coulombs for a blunter needle point.

The phenomenon described above accounts for the extreme difficulty experienced by other investigators in obtaining smooth, reliable, negative-point, corona-noise data. For example, in reference (2), Figures 41 and 42, extreme radio interference for the negative point was observed at certain voltages and very little interference at voltages intermediate to these. At the time this was thought to be due to "erratic" nature of

FIGURE 18. VOLTAGE ACROSS 2,500 OHM RESISTOR IN SERIES WITH A
44-KILOVOLT POSITIVE-NEEDLE-POINT DISCHARGE

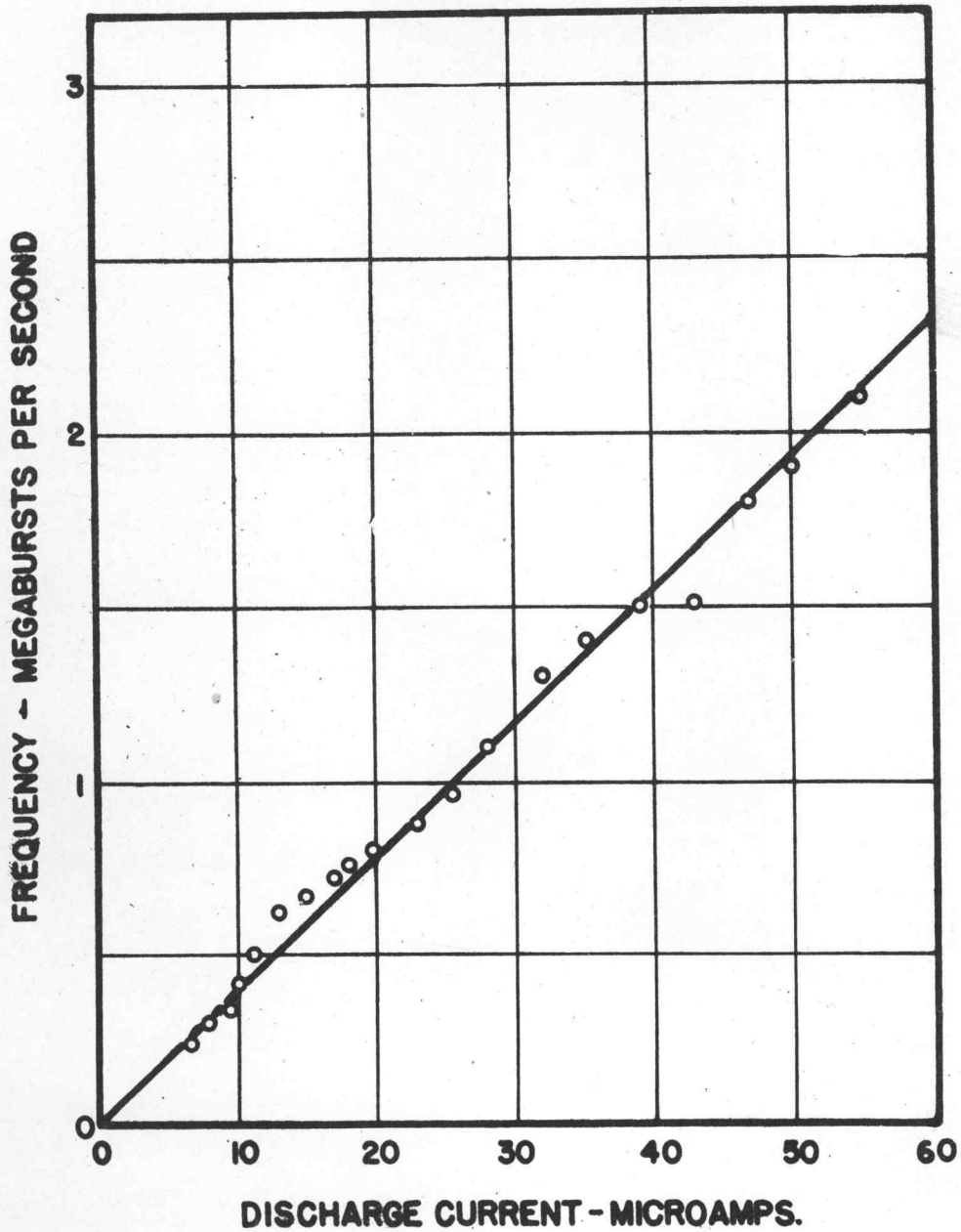


(From Reference 7)

0 0.5 1.0

TIME IN MICROSECONDS

FIGURE 19.
FREQUENCY OF CORONA DISCHARGES
FROM A NEGATIVE SLENDER
NEEDLE POINT



the negative-point discharge. In the light of the recent observations, however, these peaks are seen to be due to the very "regular" nature of the negative-point discharge and noise peaks may be expected to occur whenever the voltage is of such magnitude as to give a frequency of corona discharge that is some sub-multiple of the frequency to which the radio receiver is tuned. Similarly, noisy bands of radio interference are reported in Figures 76 and 77 of reference (7) where, for example, in Figure 77, maximum interference was measured at 0.4, 0.8, 1.25, 1.7 megacycles, thus indicating a burst-frequency rate of approximately 400,000 bursts each second.

For this reason it is practically impossible to make satisfactory noise measurements on a negative-discharge electrode if the corona bursts present are occurring at a very high frequency. It cannot be emphasized too strongly that, in this case, radio-interference measurements made at one frequency are absolutely meaningless, and in fact, may be extremely misleading. For this reason before recording negative-discharge radio interference, a rapid survey of the noise-frequency spectrum should always be made to determine whether or not these noise bands referred to above are present. If such interference bands are present, the comparative noise measurements must be made at a frequency sufficiently great, (many times the pulse frequency), that the carrier-like bands of interference will overlap to give a noise spectrum which is fairly uniform.

It has been suggested that a frequency-modulated communication system could be made relatively insensitive to precipitation static. There is a very definite possibility that such would be the case if the precipitation static were produced by positive-point corona, which from its very nature occurs at an audible rate. However, for corona occurring from sharp, negative points it is possible that there may be no improvement gained through the use of a frequency-modulated communication system. The frequency with which the negative-corona bursts occur is continuously shifting very slightly above some mean value in a most erratic manner. This means that all of the harmonics are also shifting around, so that, in effect, the noise produced by this type of corona discharge is both a frequency-modulated and amplitude-modulated noise, and would possibly produce severe interference in a frequency-modulated radio receiver.

The presence of these carrier-like interference bands explains the report often made by pilots that their "radio would suddenly go dead." Exactly this effect has been observed in the laboratory and has been due to the intensely strong, carrier-like interference actuating the AVC circuit of the radio receiver thus blocking it against all other signals.

V. RADIO INTERFERENCE IN COMPLICATED NETWORKS

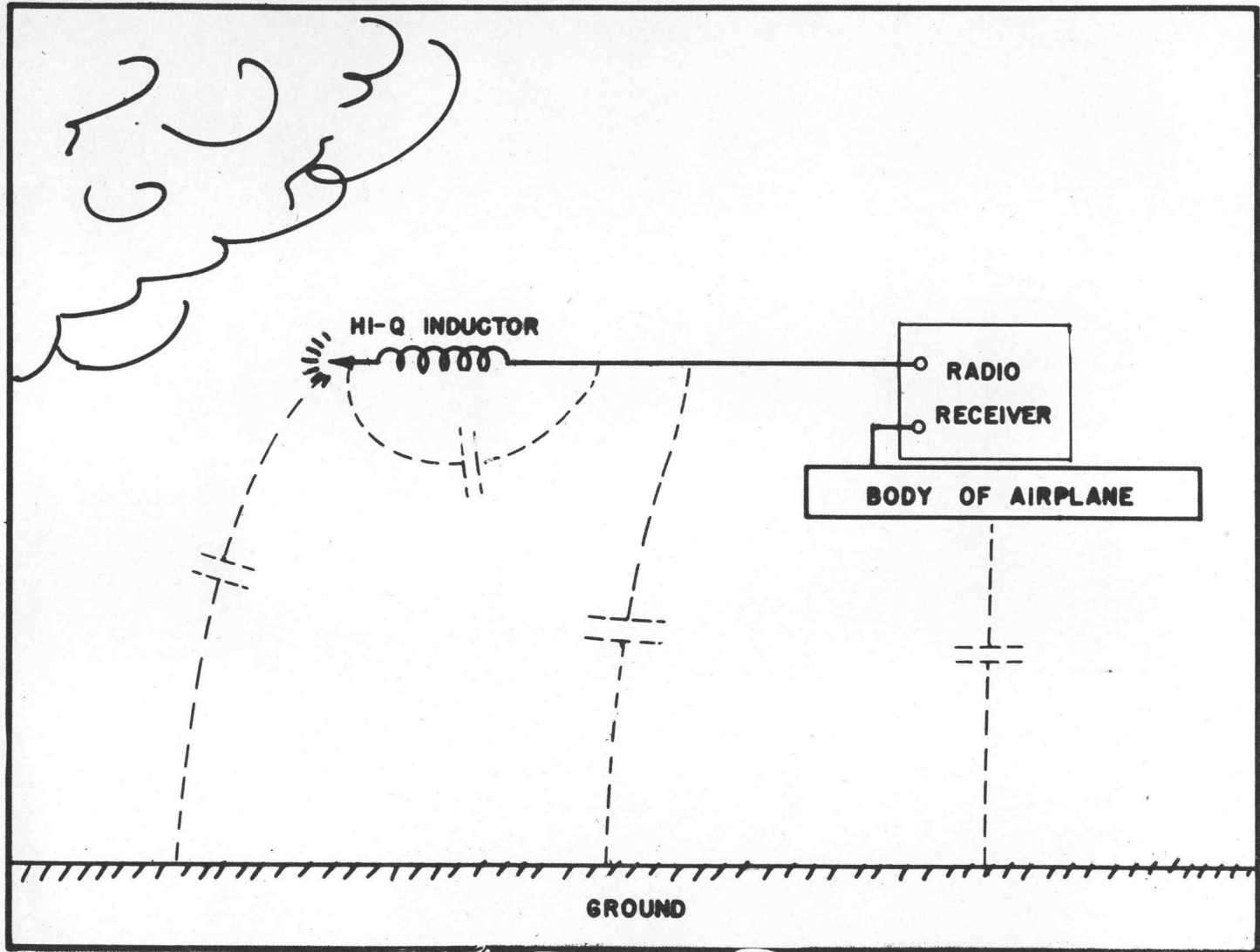
Theory

The studies made in the previous chapter of radio interference arising from high-voltage electrical discharges were somewhat idealized in that it was assumed that all of the corona currents reached the radio receiver. Actually this is not the case, for there is always an exterior circuit lying between the point in corona discharge and the antenna circuit of the radio receiver. For this reason the currents reaching the antenna coil of the receiver will differ considerably from the actual corona-streamer current.

In order to estimate the radio interference resulting at any frequency, it is first necessary to determine either experimentally or theoretically the fraction of a sinusoidal current of frequency ω which, when impressed at the point of corona, would reach the antenna coil of the receiver. Obviously this fraction or ratio will depend upon the frequency of the current and, being a function of the frequency, will hereafter be designated by $H(\omega)$. It is shown in appendix VI, equation (1), that the radio interference at any frequency may be calculated from

FIGURE 20.

PROPOSED RESONANT CIRCUIT FOR TERMINATION OF TRAILING-WIRE ANTENNA.



$$i_n = \sqrt{\Delta f} \cdot \sqrt{2I_{st}/n} \cdot \frac{1}{\sqrt{[1 + (\omega_0/\alpha)^2][1 + (\omega_0/\beta)^2]}} \cdot H(\omega_0)$$

The first factor takes into consideration the band width of the radio receiver; the second, the rate at which the disturbances are occurring and their amplitude; the third, their shape; and the last, the transmission characteristic of the network over which the noise currents must flow to reach the radio receiver. Two examples of noise-radio-interference calculations in complicated networks are given in appendix VI. Because of their practical importance they will now be discussed more fully.

Effect of an Inductor in Series with a Discharge Point

One of the inherent disadvantages of the trailing-wire antenna is that, because of its small size and exposed position, electrical discharges are apt to occur from its end and along its length in even mild precipitation-static conditions. This disadvantage prohibits the use of the trailing-wire antenna in certain instances where otherwise its use would be highly desirable.

On the other hand, the end of the trailing-wire antenna is an ideal location for a discharge electrode because it is in such a position as to produce maximum voltage-gradient conditions. The question, therefore, is whether there might not be some method of isolating a discharge electrode at the end of a trailing wire antenna in such a manner that the radio interference resulting from the electrical discharges could be prevented at one or more frequencies. The simplest circuit which might be used here is a trailing-wire antenna terminated in a discharge point which is fastened to the antenna through a high-Q inductor, such as shown in Figure 20. This circuit was studied in the laboratory for the case where the antenna wire proper was very short. The experimental noise data obtained therefrom are plotted as points in Figure 21. Shown also in Figure 21 as the solid curve is the calculated noise-frequency spectrum as obtained from the equation given in the preceding section. Here again, the agreement between experimental and calculated results is satisfactory.

The most interesting feature of these measurements is the minimum radio interference observed at 3 megacycles. This minimum occurs at the frequency for which the inductance and its distributed capacitance form a parallel resonant circuit. If the corona-discharge current is considered as an equivalent frequency spectrum the explanation of this effect is simple; e.g., the inductance and its distributed capacitance form a very high impedance at a certain frequency so that only a small fraction of the noise currents of that frequency reached the radio receiver. But in terms of the actual physical currents and voltages involved, the operation of this circuit is not so apparent. In this case the noise currents reaching the radio receiver may be considered as consisting of two components, the first component being that which reaches the radio receiver through the inductance alone, and the second component of the current being that which reaches the radio receiver through the distributed capacitance which shunts the inductor. Both of these noise components can be shown to produce shock oscillations in the receiving circuits. However, at some particular frequency the shock oscillations due to the impulsive current reaching the receiver through the inductor are for the most part exactly equal and opposite in phase to the shock oscillations produced by the impulsive current flowing through the distributed capacitance around the inductor. Accordingly at that particular frequency the two oscillations cancel and a minimum of noise results.

Effect of a Resistor in Series with a Discharge Point

Figure 22 gives the experimental noise frequency spectrum for a discharge from a positive needle in series with a 15 megohm resistor. Figure 23 gives the noise frequency spectrum for a 5 megohm resistance in series with the discharge point. Also shown on both figures are the equivalent circuits for each case and the theoretical

FIGURE 21.

RADIO-INTERFERENCE SPECTRUM FOR INDUCTANCE IN SERIES WITH POSITIVE POINT DISCHARGER.

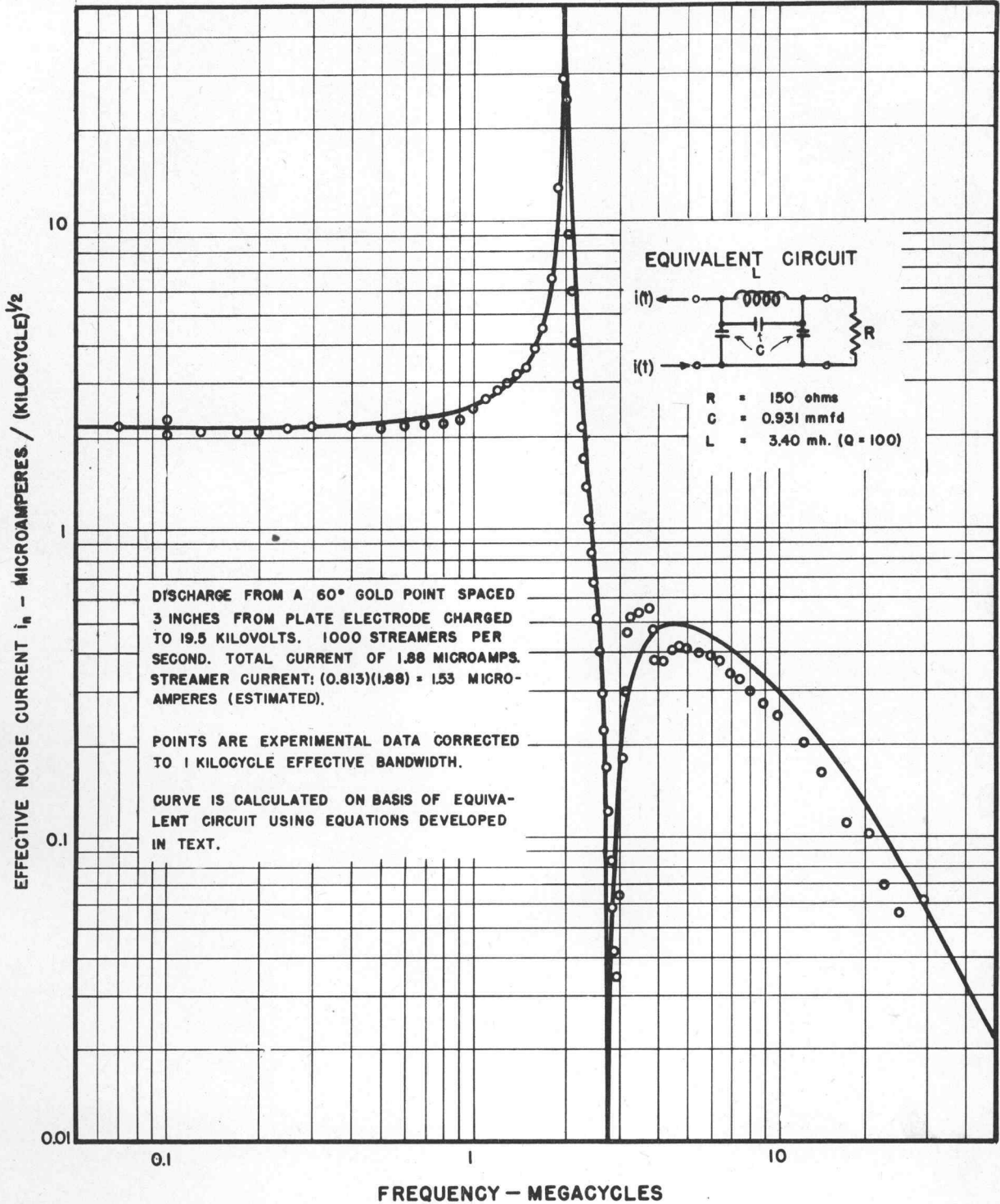
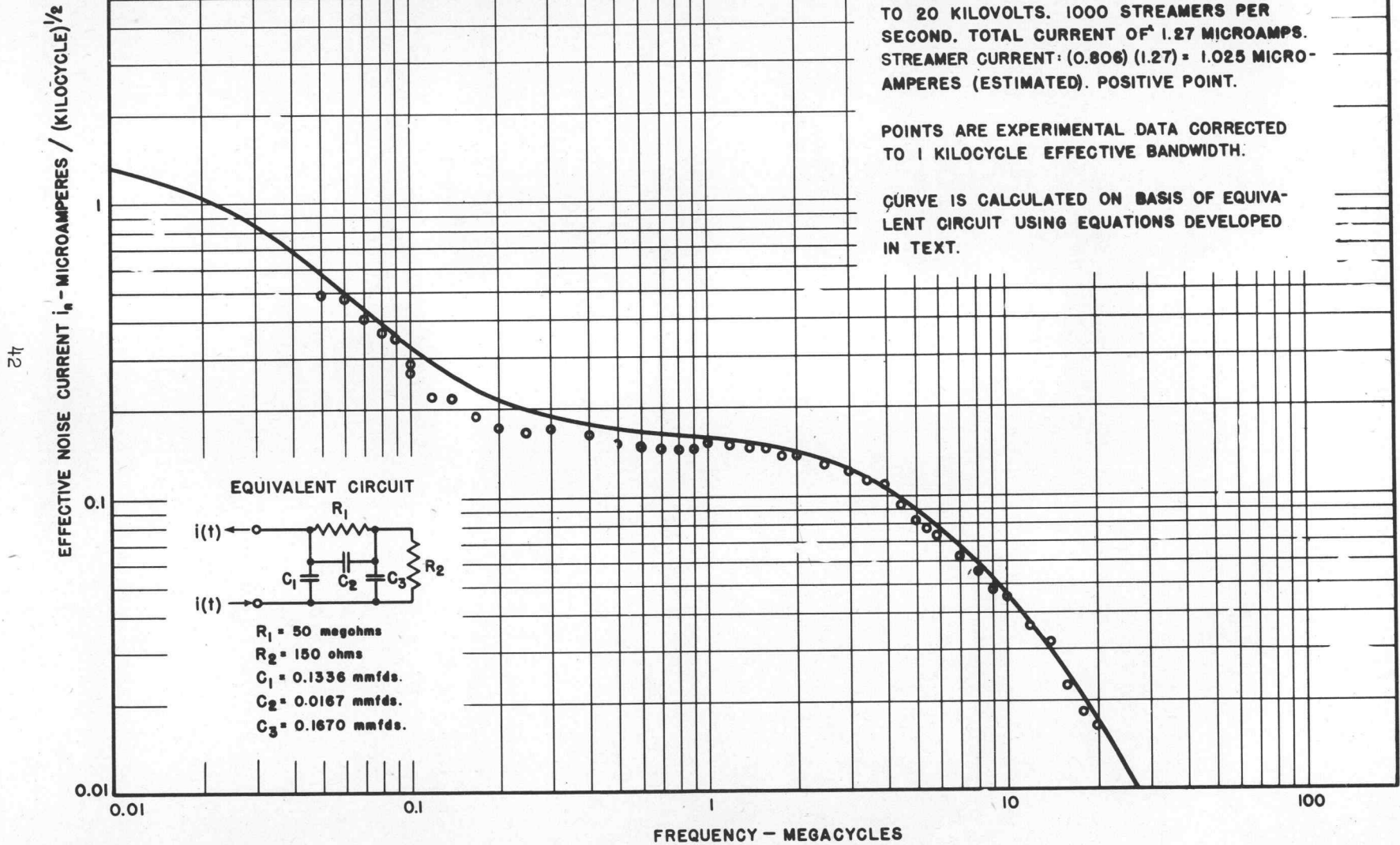


FIGURE 22.

RADIO-INTERFERENCE SPECTRUM FOR 50-MEGOHM RESISTOR IN SERIES WITH POINT DISCHARGER.



noise spectrum as determined on the basis of the equivalent circuit by the methods described in appendix VI. Here again a close agreement between experimental and theoretical results obtained.

It should be noted that although some reduction in radio interference was achieved by the use of a series resistor, a considerably greater reduction at any one frequency could be obtained by means of the series inductor described in the previous section. This is because the resistor can in no way reduce the effect of the shunting capacitance, whereas an inductor can effectively eliminate the effect at one frequency.

It is feasible that perhaps an isolating network of inductors, capacitors, and resistors could be used in place of a single inductor so that by proper design, marked reduction in radio interference could be obtained at several different frequencies. It is hoped that this interesting possibility may be investigated further.

Measurement of Noise-Induction Characteristic of a Discharge Device

All of the noise measurements discussed hitherto have dwelt with the inherent noise-producing properties of the corona current from the discharge electrode and not necessarily with the voltage which would be induced in a nearby antenna by the corona discharge. Emphasis was placed on the former properties because they are the only ones which can be measured with any degree of absolute accuracy. Noise induction by the electrostatic field surrounding a corona discharge depends upon so many factors (such as the shape of the discharge device and its resistance to ground; the shape of the antenna pickup electrode and its position with respect to the discharge device; and the proximity of the ground plane, high-voltage electrode, and other objects) that noise-induction measurements can hardly be other than relative.

However, discharge devices which incorporate isolating resistors, chokes, etc., cannot be studied by direct influence methods. In such instances an induction method of pickup must be used if the effect of the isolating element is not to be overestimated. A method which has proven to be satisfactory for testing such isolated discharge devices is to use for the noise pickup electrode a small probe electrode which may be located in a standard position with respect to the discharger under test.

This laboratory has used a brass sphere 2.5 inches in diameter and connected to the receiver through an unterminated coaxial cable as a noise-induction pickup electrode. The placement of this pickup probe should be such that all active parts of the discharge device are as nearly equidistant as possible from the probe.

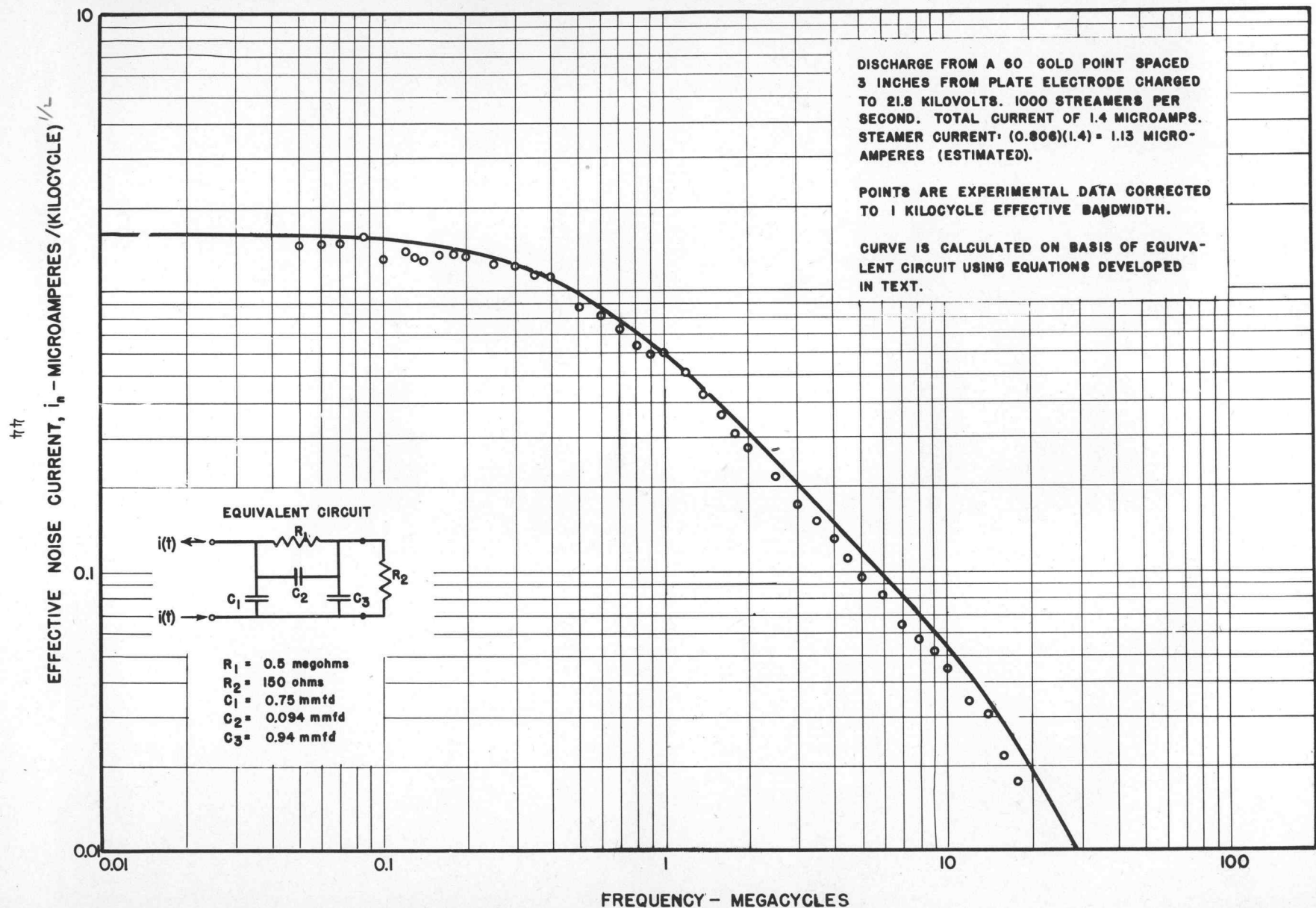
As a typical comparison between the noise-induction and noise-influence effects, the following data were obtained on the effect of a high resistance in series with a positive, conical discharge point. The point discharge current was 1.8 microamperes, point-to-plane spacing was 19 inches, and the induction pickup electrode was located in a position which was 3 feet from the tip of the point and perpendicular to the axis of the point.

	<u>Noise in Microvolts</u>	
	Direct	Induction
No series resistance.....	1200	160
10 megohm series resistance.....	130	65

Thus, whereas the direct, noise-influence measurements would indicate that the series resistance would reduce the noise by a factor of 10.8%, the more likely reduction insofar as noise pickup by nearby antennas is concerned would be only 65/160 or 40%.

It is suggested that the induction pickup values be standardized by replacing the discharge device under test by a standard positive point which, by application of equation 22, appendix V, can be made to produce a known amount of radio interference at the lower radio frequencies.

FIGURE 23
RADIO INTERFERENCE SPECTRUM FOR 0.5 MEGOHM RESISTOR IN SERIES WITH POINT DISCHARGER.



Equation (3) is a basic relationship yielding the transform of the secondary voltage in terms of the transform of the primary voltage. The secondary voltage may be calculated as a function of time by

$$e_s = \frac{1}{2\pi j} \int_{Br} \tilde{e}_s e^{pt} dp \quad \dots \dots \dots (5)$$

(See reference 5 for details and methods of evaluating this integral.)

Response of Tuned Circuit to Double-Exponential Impulse

It will now be assumed that a voltage impulse, such as that developed by a single, positive-streamer current in flowing through a 100 ohm resistor, is impressed upon the antenna coil. Then,

$$e_p = E[\exp(-\alpha t) - \exp(-\beta t)] \quad \dots \dots \dots (6)$$

The Laplace transform of e_p will be,

$$\begin{aligned} e_p &= \int_0^{\infty} e_p \cdot \exp(-pt) dt \\ &= E \frac{\beta - \alpha}{(p + \alpha)(p + \beta)} \quad \dots \dots \dots (7) \end{aligned}$$

Accordingly, by equation (5) the voltage appearing across the secondary will be,

$$e_s = \frac{M}{L_p} \omega_0^2 (\beta - \alpha) \cdot E \cdot \frac{1}{2\pi j} \int_{Br} \frac{pe^{pt} dp}{(p - p_1)(p - p_2)(p - p_3)(p + \alpha)(p + \beta)} \quad (8)$$

where $p_1, p_2,$ and p_3 are the three roots of the characteristic equation,

$$p^3 + a_1 p^2 + a_2 p + a_3 = 0 \quad \dots \dots \dots (9)$$

Impedance measurements on a Meissner, individual r-f coil, 14-7688, (132 kc to 405 kc), gave the following values:

$r_p = 186$ ohms	$r_s = 40$ ohms
$L_p = 25.4$ mh	$L_s = 3.53$ mh
$M = 0.78$ mh.	

For these values, the five poles of equation (8) occur at

$$\begin{aligned} p_1 &= -7.32 \times 10^3 \\ p_2 &= -5.727 \times 10^3 + j 1.257 \times 10^6 \\ p_3 &= -5.727 \times 10^3 - j 1.257 \times 10^6 \\ p_4 &= -\alpha = -23.56 \times 10^6 \\ p_5 &= -\beta = -94.25 \times 10^6 \end{aligned}$$

and evaluating the integral by forming the sum of the residues at each of these poles gives, for $E = 4.43$ volts,

$$\begin{aligned} e_s &= [-31.7 e^{-7.32 \times 10^3 t} + 5,430 e^{-5.73 \times 10^3 t} \sin(\omega_0 t - 0.0608) \\ &\quad + 386 e^{-23.56 \times 10^6 t} - 24.2 e^{-94.25 \times 10^6 t} \text{ microvolts.}] \quad \dots \dots (10) \end{aligned}$$

The first two terms of (10) are the "transient" components of the voltage, and the last two terms are exponentials of the same decrement as the two components of the applied double-exponential impulse.

The first transient component is due to the "inductive-discharge" transient in the primary winding. The second transient component is due to the capacitive-inductive energy interchange in the secondary circuit and will hereafter be called the "shock-oscillation." This oscillating component is of extreme importance because all of the other components are negligible as compared to it.

Perhaps the most interesting characteristic of the shock oscillation is the very slow manner in which it dies away. Whereas the original impulse applied to the antenna winding had decayed to one-tenth of its peak value in 0.13 microseconds, the oscillation requires 0.41 milliseconds to decay to the same extent. That is, the phenomenon of resonance has converted a very rapid disturbance into a disturbance lasting some 3,000 times as long. Furthermore, most of the energy of this shock-oscillation lies within the frequency band of the signal being received and is therefore extremely objectionable.

Impulse Excitation of Cascade Tuned Circuits

The preceding numerical example illustrates that the effect of the corona-streamer currents on a low-frequency radio receiver is primarily one of "impulsive" excitation; that is, the "driving force" has expended itself before the system has scarcely begun to respond. This is apparent in Figure 24 which shows that the impressed disturbance has subsided by the time the voltage across the secondary winding has built up to only about one-fifth of the peak value it will ultimately reach during the first half-cycle of the oscillation.

The calculation of network response to truly impulsive disturbances is simplified because, for such disturbances, it can be shown that the shape of the impulse is unimportant and that the network response will be determined by the "area" under the impulse instead. This property will be utilized in the next chapter to investigate the possibilities of "limiters" in the r-f and antenna circuits of a radio receiver.

In appendix VII the shock oscillations produced in a series of unilaterally coupled tuned circuits by a unit impulse, (i.e. an impulse, usually designated by $S_0(t)$, lasting an infinitesimally-short period but having a unit area) are studied and formulas are developed for the amplitude (upper envelope) of the oscillation after any number of tuned circuits.

An approximate expression for the relative amplitude, $\frac{E}{\omega Q^{n-1}}$, of the shock oscillation after "n" tuned circuits, each tuned to the frequency ω_0 and having identical Q's, is

$$\frac{E}{\omega_0 Q^{n-1}} = \frac{e^{-\alpha t}}{(n-1)!} (\alpha t)^{n-1} \dots \dots \dots (11)$$

where

$$\alpha = r/2L = \omega_0/2Q$$

In the case of the single tuned circuit analyzed in the previous section, there results for $n = 1$,

$$E/\omega_0 = e^{-\alpha t}$$

where $\alpha = r/2L = (40)/(7.06 \times 10^{-3}) = 5,660$. This compares favorably with the value, 5,730, obtained in the exact analysis (equation 10) for the exponent of the "damping" factor.

The upper envelopes of the shock oscillations appearing at the first, third, and sixth tuned circuits are shown in Figure 25. The most interesting characteristic of the envelopes shown is the lengthening of the oscillations by the additional tuned circuits. It should be noted that each oscillation reaches its peak magnitude when $\alpha t = n - 1$.

FIGURE 24.

IMPULSE EXCITATION OF A 200-KC ANTENNA TRANSFORMER

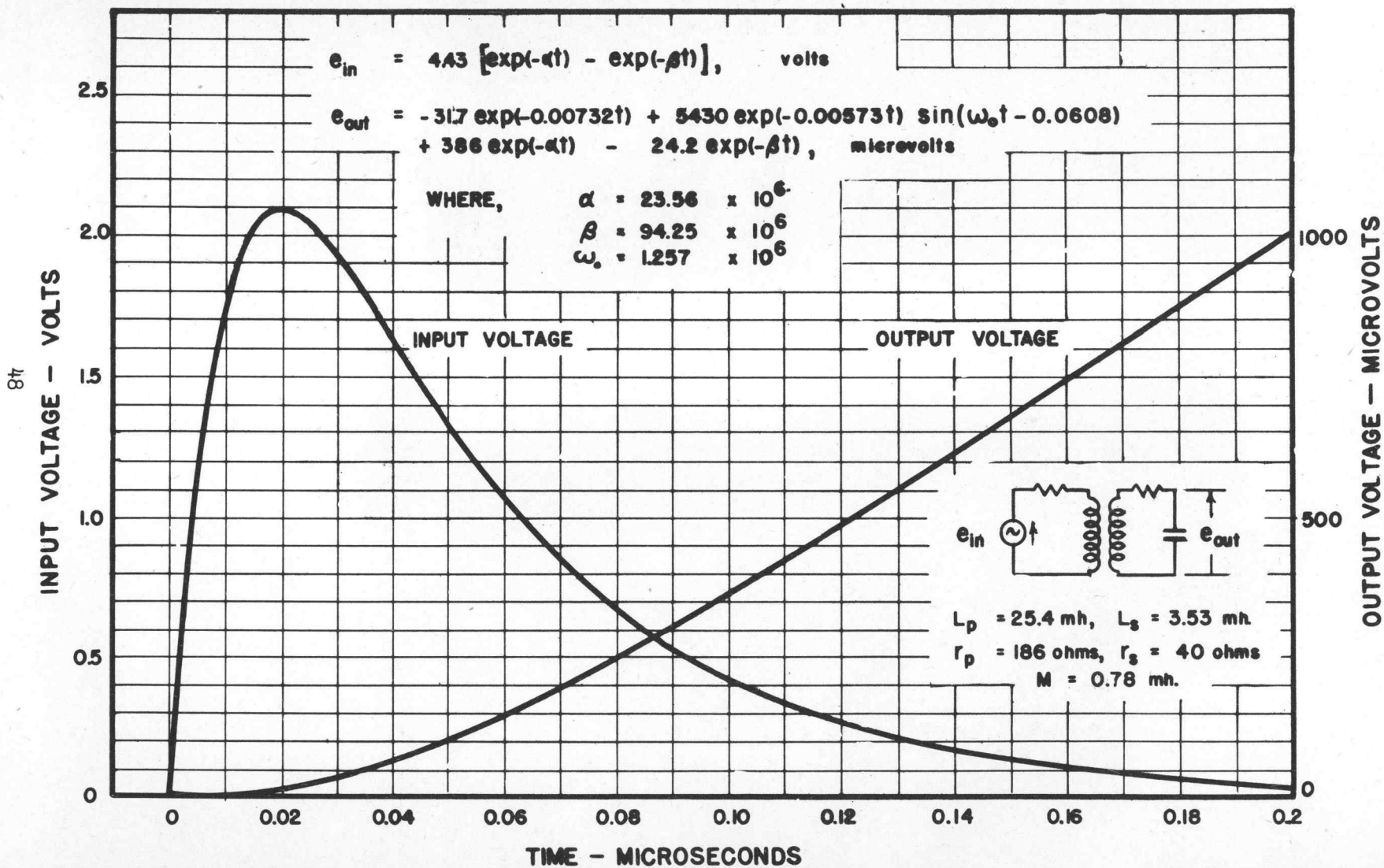
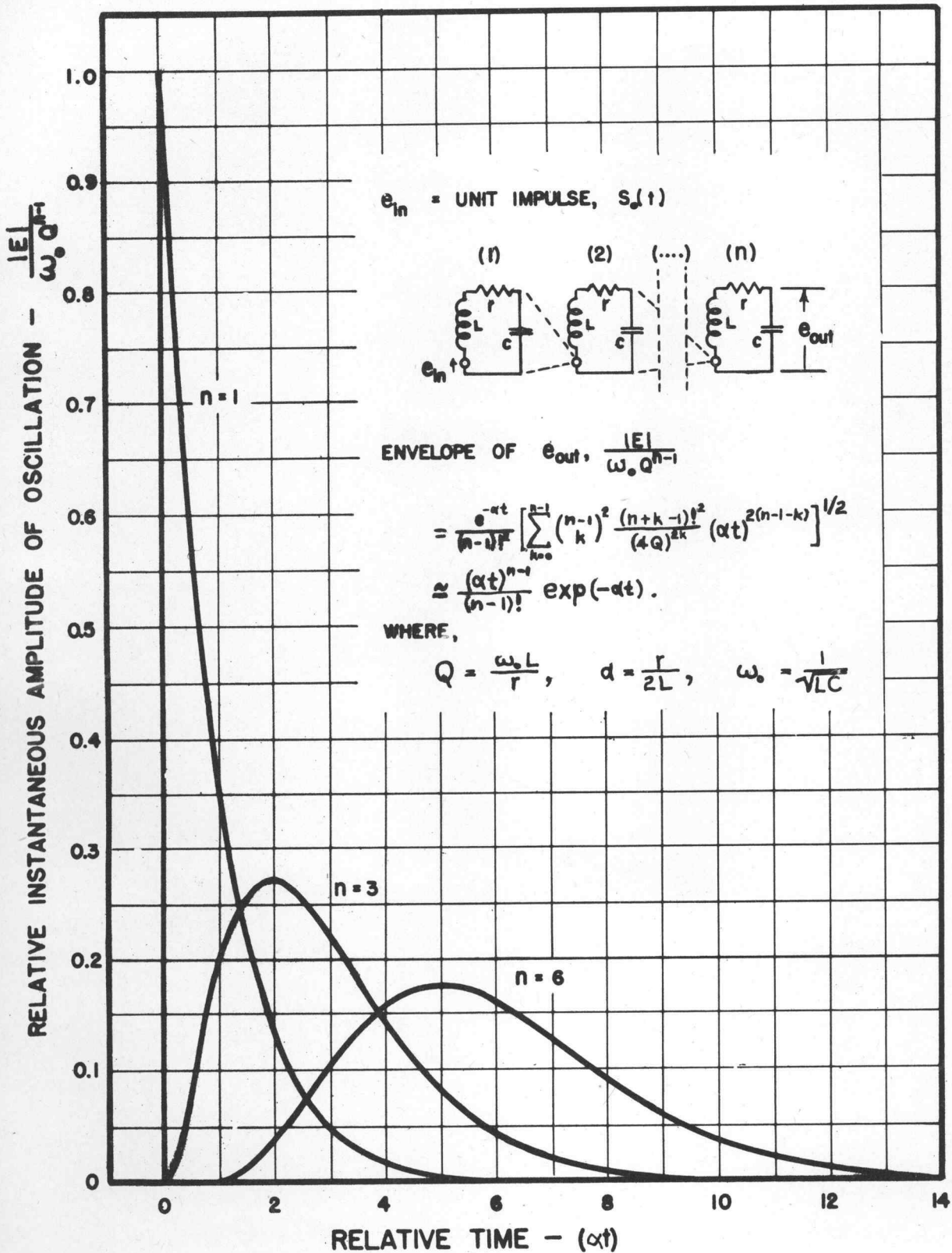


FIGURE 25. ENVELOPE OF SHOCK OSCILLATIONS AFTER FIRST, THIRD, AND SIXTH TUNED CIRCUITS.



It should also be noted that the peak amplitude of the oscillations is somewhat reduced by the additional tuned circuits. This peak amplitude has been calculated as a function of the number of additional tuned circuits beyond the first, and the results are presented in Figure 26. Because of the units in which the quantities are expressed the ordinates represent the "peak-noise-to-peak-signal ratio," expressed as fraction of that ratio obtaining for a single tuned circuit. This figure shows quite clearly that additional tuned circuits beyond 4 or 5 contribute little toward reducing the noise-to-signal ratio, and in fact they may do more harm than good because of the "sluggishness" which they produce.

VII. NOISE REDUCTION BY NONLINEAR CIRCUIT ELEMENTS AND OTHER SCHEMES

Noise Reduction by Detuning

In the previous chapter it was shown that for all practical purposes the shock oscillations in the first tuned circuit are of the frequency to which the secondary is tuned. Hence, they are of the same frequency as the received signal and severe radio interference results.

It has been suggested that if this first circuit were tuned to a frequency slightly different from that of the signal, the frequency of the shock oscillations would no longer be that of the signal, and consequently the interference would be less. Except for two effects which will now be discussed, this idea would have some merit.

First, it should be pointed out that the energy of a damped oscillation is distributed over the entire frequency spectrum, most of the energy, however, being at those frequencies near the frequency of the oscillation. Following the method outlined in Appendix V, it is easily shown that the frequency spectrum of the time function, $i(t) = e^{-\alpha t} \cos \omega_0 t$, ($t > 0$), is

$$\overline{\varphi(\omega)} = \frac{\omega_0}{\sqrt{[\alpha^2 + (\omega + \omega_0)^2][\alpha^2 + (\omega - \omega_0)^2]}}$$

This spectrum is shown in Figure 27.

It must be emphasized that the noise spectrum shown in Figure 27 is expressed on a "per cycle" band-width basis. If random damped oscillations such as that shown were impressed at an average rate of "n" each second upon a radio receiver (selective circuit) having an effective band width of Δf and tuned to ω , the equivalent mean-square interference current produced in the receiver would be, by equation (18) of appendix V,

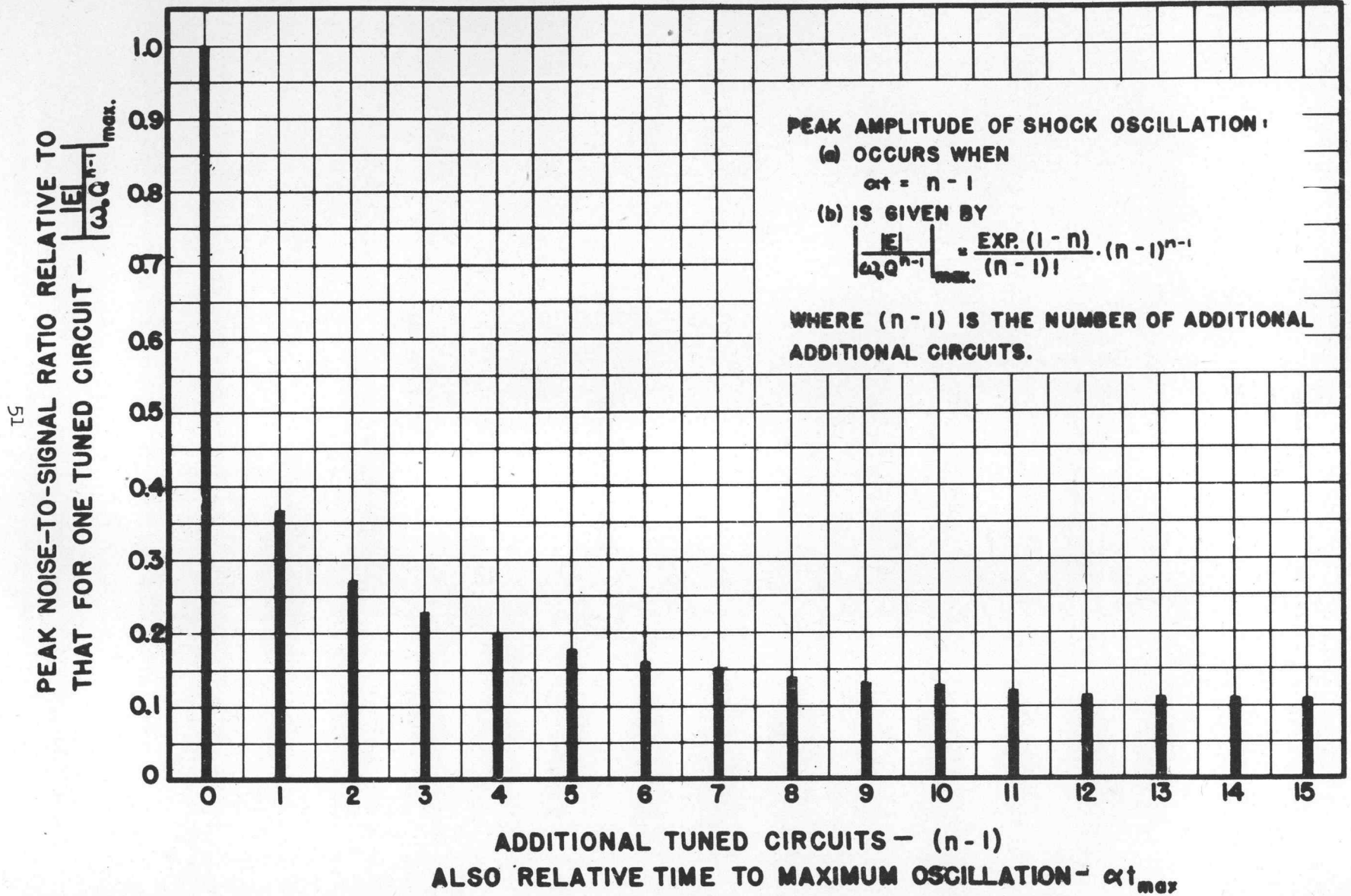
$$i^2 = 2n \cdot \overline{\varphi(\omega)^2} \cdot \Delta f$$

However, for the most part, the selectivity characteristic of the first-tuned circuit is nearly identical to the frequency spectrum of the shock oscillations produced in that circuit. In fact, the aggregate frequency spectrum of the shock oscillations plus other transient components produced by a true impulse (of zero duration) would be identical to the selectivity characteristic of that circuit. Accordingly, while it is true that detuning the first-tuned circuit would produce less disturbance in the following circuits of the receiver, the loss of signal strength due to the detuning would for all practical purposes be the same as the reduction in the interference so that nothing would be gained by this method.

The second "hitch" in the detuning scheme is that although both signal and oscillations produced in the subsequent radio circuits are reduced, there are other exponential components of the noise (transient and impulse terms) which are not reduced by the detuning. Consequently it is most likely that the signal-to-noise ratio would actually be impaired and reduced by the detuning scheme.

FIGURE 26.

IMPROVEMENT IN IMPULSE NOISE-TO-SIGNAL RATIO BY ADDITIONAL TUNED CIRCUITS.



Carson's "Irreducible Minimum of Interference"

By considering any static disturbance in general as being equivalent to a frequency spectrum, it is apparent that the ideal selectivity characteristic of the radio receiver would be of rectangular shape and of width just equal to the band width of the signal to be received.

However, even for this ideally selective circuit, there exists an irreducible minimum of interference which is produced by those noise-frequency components lying within the signal-frequency band. It was the observance of this minimal interference which led Carson to conclude that "representative circuit arrangements and schemes designed to reduce static interference--are incapable of reducing, in any substantial degree, the mean interference as compared to what can be done with simple filters and tuned circuits. The underlying reason lies in the nature of the interference itself."

Nevertheless Carson overlooked one thing! While it is true that there is a limit to the discrimination against static on the basis of frequency alone, it is possible to reduce this "irreducible minimum" still further by introducing a nonlinear characteristic into the receiver (provided the amplitude of the interference is materially different from the amplitude of the signal). A necessary condition that Carson's conclusions be valid is that the network must be linear in its characteristics so that the principle of superposition may be invoked. By introducing a nonlinear device, such a limiter, this condition would no longer be satisfied, and Carson's pessimistic "minimum interference" can be reduced still further. Because of this fact, it would seem that the engineer's last best hope for greatly improved radio reception must lie in a more universal adoption and wise application of nonlinear circuit elements incorporated in radio design.

Nonlinear Circuit Elements for Further Noise Reduction

The nonlinear circuits may be roughly divided into two types, "limiters" and "dampers," depending upon their behavior. Most nonlinear circuits successfully used to date have been of the "limiter" type, which commonly depend on the saturable characteristic of an under-voltaged vacuum tube. The proposed "damper" type of nonlinear circuit will be discussed in a later section.

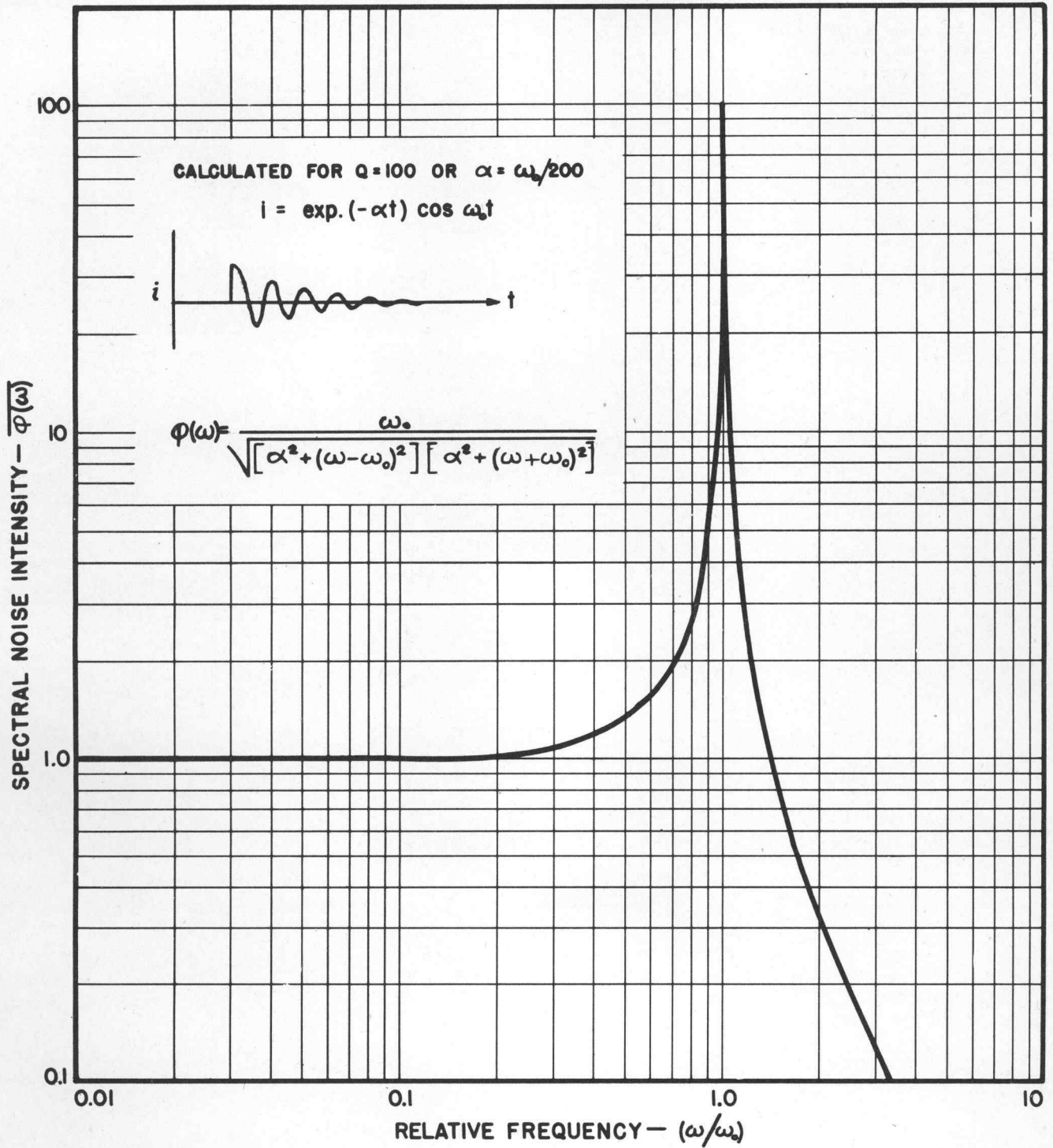
Limiter circuits have been applied in the audio and i-f circuits of the radio receiver with considerable success. The application of limiters in r-f and antenna circuits is somewhat doubtful. The results of studies made in each of these applications will now be given.

Noise Reduction by Audio Limiters

Audio limiters are of two general types: They may be manually adjusted in threshold so that any signal, steady or transient, which exceeds this threshold will be limited; or they may be of an automatically-adjusting type which limits sudden bursts but does not affect the steady signal. The Halicrafter's ultra-high frequency receiver, previously described, was equipped with an audio noise limiter of this latter type and tests were accordingly made upon this receiver to determine the effectiveness of an audio limiter in reducing precipitation-static interference.

Since the threshold of this limiter was dependent upon the avc voltage, it was realized that the noise bursts occurring at a slow rate would be successfully limited by the circuit, whereas very rapidly reoccurring bursts would produce an increase in the avc voltage which in turn would reduce the effectiveness of the limiting action. By the method described in a previous chapter, the corona disturbances were made to occur at several different rates, and the improvement in signal-to-noise ratio resulting was measured over a wide range of signal strengths. The experimental results of these measurements are shown in Figure 28. Although the improvement is not very great for a rapidly reoccurring noise, the increase in signal-to-noise ratio for an intermittent

FIGURE 27.
FREQUENCY SPECTRUM OF DAMPED OSCILLATION.



noise is rather significant. In view of the simplicity of the limiter circuit it would seem that a limiter of this type should be included in all receivers subject to interference arising from random electrical discharges.

Intermediate-Frequency Limiters

Nonlinear circuit elements may also be incorporated in the i-f amplifiers of the radio receiver. For example, in the ordinary amplitude-modulated receiver, the Lamb noise-silencing circuit has been used to some advantage. For proper operation of this circuit, the limiting threshold must be very sharp and abrupt if serious clipping of the modulation envelope is to be avoided. This usually requires at least two additional tubes to obtain the necessary sharpness of cutout. Actually the Lamb circuit is not a "limiter" in the true sense, but being more in the nature of a "damper," will be discussed later under that heading.

Some of the difficulties encountered in applying i-f limiters to amplitude-modulated receivers do not occur when incorporating the limiter tube in a frequency-modulated receiver. Here, the limiter tube is purposely designated to operate on the signal as well as the interference in order to remove any vestigial amplitude modulation which might be present. Disturbances greater than the signal are accordingly reduced considerably in their effect. On the other hand, disturbances somewhat smaller than the signal can only affect the "phase" of the oscillation reaching the discriminator, and that but slightly. Accordingly the frequency-modulated receiver is relatively insensitive to disturbances having peak values less than that of the steady signal¹⁰. It should be emphasized that the noise reduction in the f-m receiver as compared to the a-m receiver, for both large and small disturbances relative to the signal strength, is directly attributable to the nonlinear limiter tube which forms the very heart of the f-m receiver.

It was most fortunate that a receiver was available which combined both the f-m and a-m detection circuits, for by making tests on a receiver of this type the relative merits of both a-m and f-m detection circuits are directly comparable since the rest of the receiver remains unchanged.

This receiver was the Halicrafter's ultra-high frequency, f-m a-m receiver, model S-27, serial number 150851. The test signals were generated by two signal generators: a General Radio UHF signal generator, type 804-B, serial number 332, used to generate the unmodulated and amplitude-modulated signals and also to calibrate, by substitution, the f-m signal generator; and a Hickok model 188, all-wave signal generator, used to generate the frequency-modulated signals. In addition a General Radio, peak vacuum-tube voltmeter, was used to measure the audio output voltage of the receiver.

The interfering noise was produced by corona streamers from a platinum wire 0.040 inches in diameter with its end ground to a 60° conical point (generating angle). The point was maintained at an average potential of 7 kv. positive with respect to a plate surface three inches away. A 1000 cycle per second synchronizing voltage was then superimposed upon the direct voltage, resulting in 1000 corona bursts per second at an average current of 1 microampere. The discharge point and the two signal generators were then connected directly to the antenna terminals of the receiver. The signal-to-noise ratio at various signal strengths was measured as follows:

The peak voltage at the output terminals of the receiver produced by the interference when superimposed upon a steady unmodulated signal to which the receiver was tuned was measured for various values of signal strength ranging between 1 microvolt and 10,000 microvolt intensity. Then, with the interference reduced to zero and the signal modulated by some constant amount, the audio-output voltage resulting from this modulated signal was measured over the same range of signal strength. If it is assumed that, for a given signal strength, the noise-output voltage will be the same whether the standard signal is modulated or not, then the signal-to-noise ratio is simply obtained by

FIGURE 28.

EFFECT OF AUDIO LIMITER ON
SIGNAL-TO-NOISE RATIO

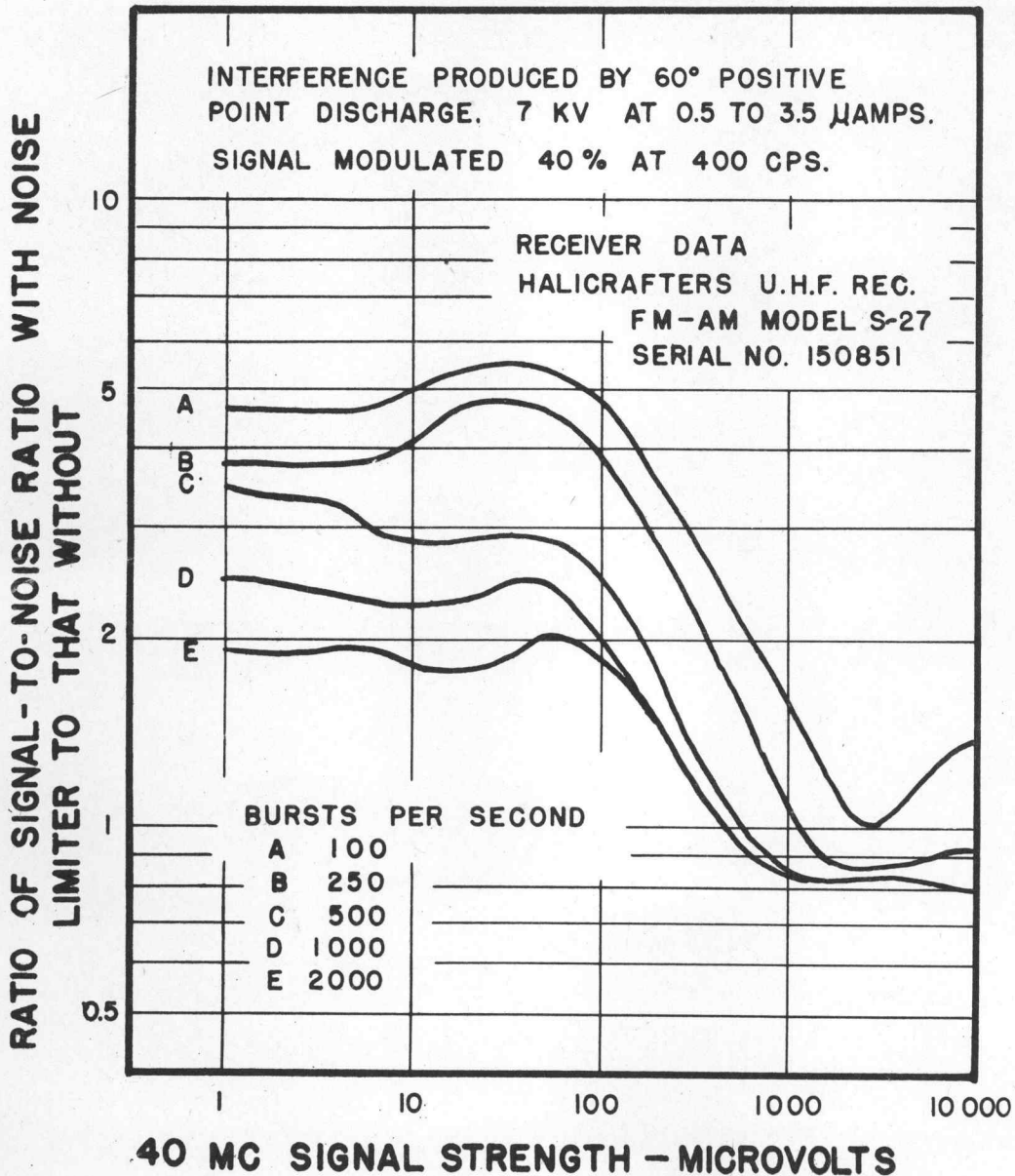
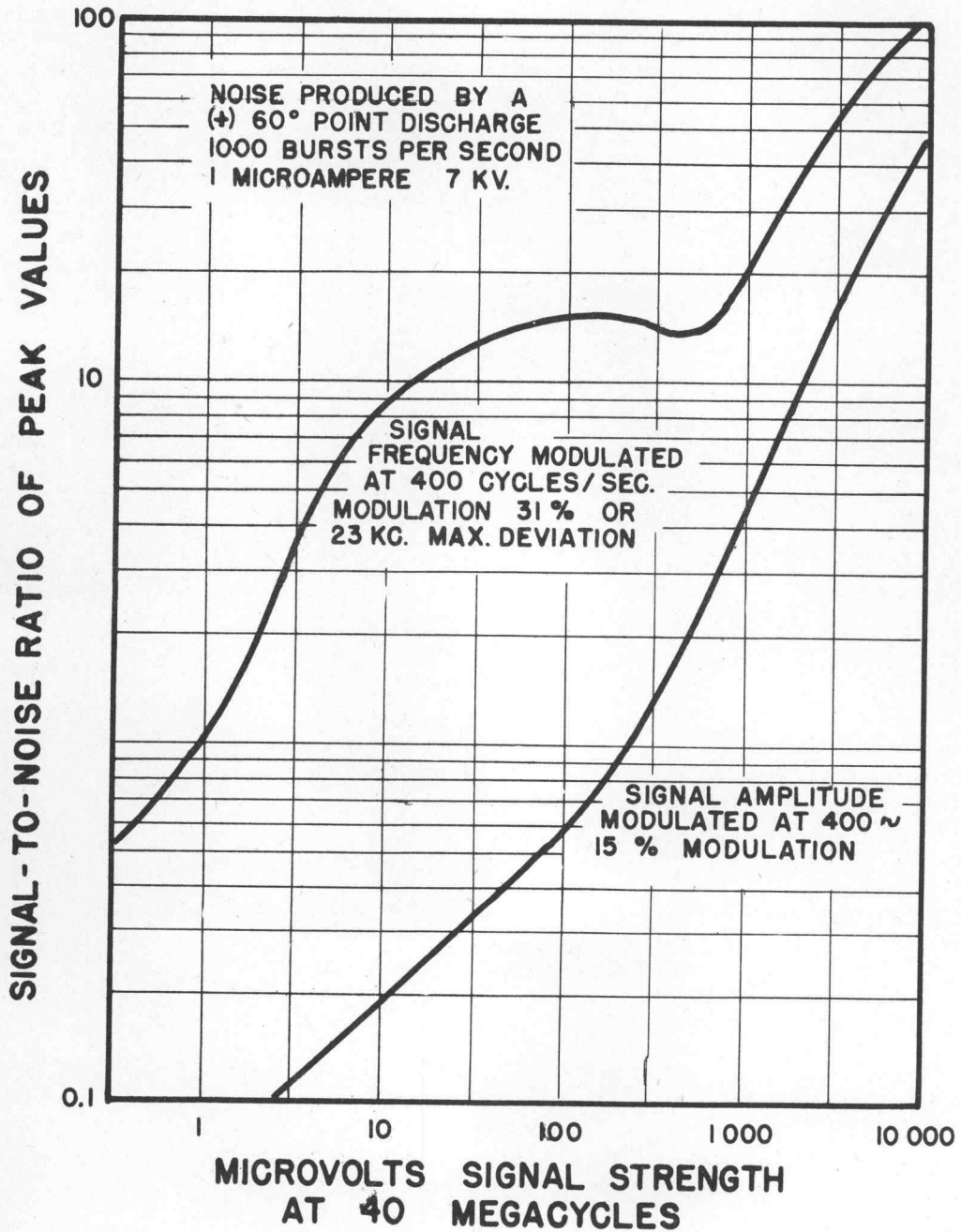


FIGURE 29.
SIGNAL-TO-NOISE RATIO OF AMPLITUDE
AND FREQUENCY MODULATED SYSTEMS



dividing the noise-output voltage at that particular signal strength by the modulated-output voltage in the absence of noise. In this manner the signal-to-noise ratio curves shown in Figure 29 were obtained. The amplitude modulation was purposely kept very low to avoid undesirable, simultaneous frequency modulation.

Actually the tuning of the receiver was such as to make the impulse noise a minimum. It was observed that detuning the receiver slightly from the frequency of the steady signal resulted in a sharp increase of interference. Accordingly, the interference resulting in the case of a modulated signal would be somewhat greater than that which was measured because the frequency modulation in effect would be equivalent to momentary detuning. Nevertheless, the improvement in reception during the idle periods of modulation would be very worth while.¹⁰

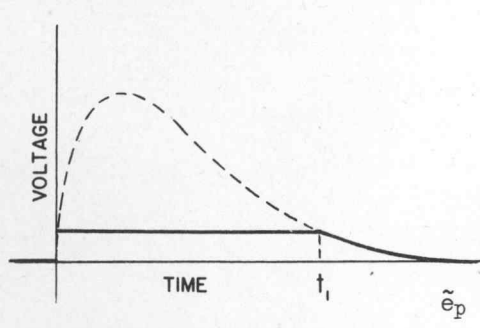
Limiters in the Antenna Circuit

In Chapter VI calculations were given showing that a very short impulse would set the first-tuned circuit into an oscillation of duration three thousand times as long as the causative impulse. Because of this effect, it might seem well to attempt to limit the impulse itself since it is the cause of all the disturbance.

From the results of other studies it is estimated that the peak value of the impulse impressed upon the antenna winding of the input transformer would ordinarily be several volts. If now a nonlinear resistor, possessing a very high resistance for all impressed voltages less than some threshold value and a relatively low resistance for all impressed voltages greater than threshold were connected across the antenna coil, the voltage applied to the antenna coil of the receiver would at all times then be limited to the threshold value of the nonlinear resistor.

The writer knows of no nonlinear resistance material which would be operative at the very low voltages encountered in this application. While it is impossible at present to test the idea experimentally, its performance may be investigated analytically and conclusions may be reached as to whether it would be worthwhile to search for a nonlinear device which might be used for this purpose. An investigation such as this has been made and the important results will now be outlined.

The circuit shown in Figure 24 was analyzed. It was assumed, however, that a nonlinear-resistance element connected across the terminals of the antenna coil limited the input voltage to one-tenth of its original value or 0.21 volts. Examination of Figure 24 would show that for the first 0.13 microseconds the applied primary voltage would be then limited to 0.21 volts, after which time it would decay exponentially exactly as shown in the figure. The peak of the impulse would thus be eliminated and the voltage applied to the antenna winding would be



$$t_1 = 0.13 \text{ } \mu\text{secs.}$$

$$e_p = 0.21 \text{ volts for } 0 < t < 0.13 \text{ } \mu\text{secs.}$$

$$= 0.21 e^{-\alpha(t - t_1)} \text{ for } t > 0.13 \text{ } \mu\text{secs.}$$

In a manner similar to that used in obtaining equation (7) of Chapter VI, the transform of the impressed voltage may be shown to be

$$\tilde{e}_p = \frac{0.21[p + \alpha(1 - e^{-pt_1})]}{p(\alpha + p)}$$

where t_1 equals 0.13 microseconds.

Then by an analysis similar to that given in Chapter VI it can be shown that

$$e_{out} = - 8.13 e^{-7.32 \times 10^3 t} + 1,394 e^{-5.73 \times 10^3 t} \sin(\omega_0 t - 0.113) + \\ + 18.3 e^{-23.56 \times 10^3 t} \text{ microvolts,}$$

giving the components of voltage appearing across the secondary winding for all values of time greater than 0.13 microseconds.

Notice that the initial amplitude of the shock oscillation is 1394 microvolts. By comparison with the amplitude of the shock oscillation calculated in Chapter VI, it is found that even though the impulse was limited to a peak value one-tenth of its original value, the shock oscillations were reduced only by the ratio $1394/5430 = 0.2566$. Apparently the peak values of the impulses are not related directly to the amplitudes of the shock oscillations which they produce.

The important quantity which does determine the amplitude of the shock oscillation is the "area" of the driving impulse.* In the example above, the area of the non-limited impulse was found to be 0.1410×10^{-6} volt-seconds; the area of the limited impulse to be 0.03621×10^{-6} volt-seconds; thus giving a ratio between the impulse areas of $0.03621/0.1410 = 0.2568$. This is for all intents and purposes equal to 0.2566, which is the ratio between the amplitudes of the shock oscillations described above.

The general conclusion to be reached from this numerical example is that for a single impulsive type of disturbance, the amplitude of the shock oscillations resulting will be directly proportional to the "area" under the impulse.

In the light of this conclusion, it seems doubtful that a large reduction in radio-interference would ever be achieved through application of antenna limiters. If cross-modulation and other types of related interference were to be avoided, the limiter threshold could certainly not be much less than that given in the numerical example. Accordingly, it would seem that, very roughly, little more than a five-fold reduction in radio interference could be secured by an antenna limiter.

Noise Reduction by "Damper" Circuits

The preceding studies have all illustrated that the long drawn-out shock oscillations produced in the various tuned circuits of the radio receiver are the outstanding noise-producing phenomenon. It has been shown that, although the shock oscillations produced in the first tuned circuit commence with a maximum amplitude and die away rapidly, the oscillations become more and more sluggish and drawn-out as they proceed through the successive tuned circuits.

This suggests that considerable noise reduction might be obtained by damping the oscillations in the first i-f circuit before they have had time to produce an appreciable oscillation in the following tuned circuit. The damping action could be produced by a nonlinear-circuit element, the resistance of which would depend upon a control voltage, shunted across the grid tuned circuit of the first i-f amplifier. If the control voltage were properly correlated with each static burst, it might then be possible to vary the resistance of the "damper" element in such a manner as to damp out the shock oscillation resulting from a static burst and yet not interfere with the reception of a steady signal in any manner whatsoever.

There are two major difficulties which will have to be overcome if this idea is to be made to work satisfactorily. First, the action of the variable-resistance element (probably a biased vacuum tube) must produce very little radio interference when its resistance varies suddenly. Second, the control voltage must be derived from the noise in sufficient time to operate the "damper" element before the oscillation has begun.

*By "area" is meant the area under the impulse curve formed by plotting instantaneous values of voltage as a function of time.

RADIO-INFLUENCE CHARACTERISTICS

The first difficulty could be overcome by carefully balancing the damper circuit so that, for example if vacuum tubes were here employed, the sudden changes in the plate currents would cancel and not produce a transient disturbance. The necessary fineness of balance should be attainable in a fixed-frequency amplifier such as the first i-f stage.

The second difficulty might be solved by using a separate noise amplifier operating at a fixed frequency considerably greater than that of the signal being received. The noise amplifier being coupled directly to the antenna would also pick up the static bursts, but since the time delay of tuned circuits is roughly inversely proportional to their frequency, the noise amplifier would deliver a rectified control voltage, setting the "damper" into action well before the first i-f circuit is set into oscillation. Furthermore, since the noise amplifier need operate but at one frequency, the circuits may be made to have a very high gain, efficiency, and simplicity. This method of control-voltage pickup could also be used to improve the performance of the Lamb noise silencer.

Even though an improvement in signal-to-noise ratio of only several times is obtainable by means of a damper alone, it is entirely possible that dampers used in conjunction with antenna, i-f and audio limiters and other devices could effect a very material improvement in radio reception under adverse conditions. This possibility should be studied more completely by both analytical and experimental investigation. In the application of various nonlinear devices to this problem there lies an unexplored field offering tremendous possibilities.

PART II

THE DEVELOPMENT OF A PRACTICAL CHARGE DISSIPATOR

THE DEVELOPMENT OF A PRACTICAL CHARGE DISSIPATOR

VIII. INTRODUCTORY SUMMARY

Electrical discharges have been found to occur from aircraft in flight for two reasons: either the airplane is traveling through regions of high electric stress, or an electric charge has accumulated on the airplane by any of the known mechanisms. In either case, the effect is to produce high electric gradients at the extremities of the plane and other sharp sections which are unshielded. These electric gradients may easily exceed by several times the dielectric strength of the air surrounding these extremities, and as a result corona discharges occur, producing through the mechanisms described in Part I of this report impulsive currents which result in much radio interference.

Obviously the straight forward procedure for eliminating the radio interference would be to eliminate the corona discharges. The only practical method of eliminating or reducing corona discharges from aircraft passing through regions of high electric field intensity is to "clean up" the surface of the plane--perhaps eliminating insofar as possible all sharp corners, edges, etc., at which high gradients might appear.

If, however, the corona discharges are due to an accumulation of an electric charge on the airplane, they may only be eliminated by dissipating the excess charge in a manner which does not produce radio interference. This part of the report deals with tests which have been made on various types of charge dissipators which have been proposed for this application.

All dischargers may generally be classified as either "self-ionized" or "pre-ionized" types. The "self-ionized" type of discharger is that on which ordinary corona discharges occur, but through proper selection of physical construction and shape, the resulting radio interference may be kept to a minimum. Under this type of discharger would be classified the Bendix discharger, where the noise is reduced by an isolating resistor, and other fine-point and wire dischargers, which because of their fine size produce a relatively noise-free type of corona.

There seems to be no self-ionized discharger available today capable of dissipating without producing objectionable radio interference the charge which accumulates on the large, high-speed aircraft now in service. There are, however, several kinds of pre-ionized dissipators which show considerable promise of being able to dissipate large quantities of electricity with little or no radio interference whatsoever resulting. Examples of such preionized dissipators are the radioactivated, fluid, r-f excited, and flame dischargers. Of all dissipators tested by this laboratory, the only kind capable of discharging large currents in a rapidly moving airstream with absolutely no measurable radio interference resulting is the "pre-ionized" flame discharger.

The chapters to follow will discuss the characteristics of these various dischargers with particular emphasis upon the pre-ionized radio-activated and flame types.

IX. POINT AND FINE-WIRE DISCHARGERS

In this and the following chapters it must be understood that all tests described were made under still-air conditions at atmospheric pressure and normal room temperature unless specified to the contrary. For this reason the practical value of much of the data is limited because it is definitely known that the discharge characteristics in a moving air stream may be radically different from those obtained in still-air

conditions. However, it is felt that comparative results between two dissipators of the same kind would be of the same trend whether made in still or moving air conditions, and that accordingly the data obtained are of sufficient value to be presented here.

A study was made to determine the relative noise produced by very small wires as compared to the noise produced by blunt objects such as a projecting rivet on an extremity of an airplane. The blunt discharge electrode used in these tests was a No. 16 copper wire, cut at one end with a pair of side cutters at an angle of 45 degrees with the axis of the wire. Fine tungsten wires studied for comparison were 0.00053, 0.0012, and 0.00246 inches in diameter. Each discharge electrode under test was mounted at a spacing of three inches and normal to a high voltage plane electrode. It was observed that for a given potential on the high-voltage electrode the discharge current resulting for each of the three fine wires was substantially the same. The electrode potential required to produce the same discharge current from the larger copper wire was approximately two kilovolts greater than that needed for the small tungsten wires, the difference undoubtedly being due to the dissimilarity in size rather than material.

The radio interference produced by the high-voltage discharges from these wires for various discharge currents is shown in Figure 30. When the discharge wire was positive the size of the discharge wire had a great influence upon the radio interference. The electrical discharge from the small tungsten wires was of the minute burst type (Starr's Type 1), whereas the positive discharge from the copper wire was in the form of long streamers which, because of the mechanisms discussed in Chapter III, are known to produce severe radio interference.

When the discharge electrode was negative, the radio interference resulting for a given discharge current was substantially the same for all electrodes tested. For this reason, Figure 30 shows only the average radio interference characteristic for the negative electrode.

Comparison of Fine-Wire Discharges with the Bendix Discharger

In view of the results of the foregoing section, it was felt that perhaps a discharger employing very fine wires might yield even better results than the standard Bendix trailing-wire discharger. In the still-air conditions of the laboratory this actually proved to be the case. Shown for comparison in Figure 31 is the noise produced at the various currents by positive corona discharges from a Bendix wire, a tungsten wire 0.0034 inches in diameter, and a multiple, ring discharger consisting of approximately 15 small tungsten wires each 0.0012 inches in diameter and mounted in a circular block of plastic resistance material. Although no fatigue or other strength tests were made on the small tungsten wire, it seems in all outward appearances to be a very tough and durable material that might be substituted for the regular standard Bendix wire. Perhaps even a smaller wire could be used with additional reduction in radio interference obtaining. Only mechanical limitations would be the determining factor in this direction.

Interesting phenomena were noticed in the interference produced by the positive Bendix wire due to the particular placement of the wire with respect to the high-voltage electrode. Because of this particular placement, corona would begin first at the far end of the wire and then with increasing voltage would gradually extend over its entire length. However, due to certain kinds and irregularities in the wire, this spread of corona was not at all uniform but would occur suddenly over intervals of several inches in length.

It has repeatedly been observed that maximum radio interference from a positive point occurs at corona onset because, then, the inductive kinks or long streamers are formed. At higher voltages, the inductive kicks are superseded by a more or less continuous burst corona which inherently produces but little radio interference. Apparently then as each section of the Bendix wire would successively go into corona, it

FIGURE 30
POINT AND FINE-WIRE NOISE CHARACTERISTICS
AS A FUNCTION OF CURRENT

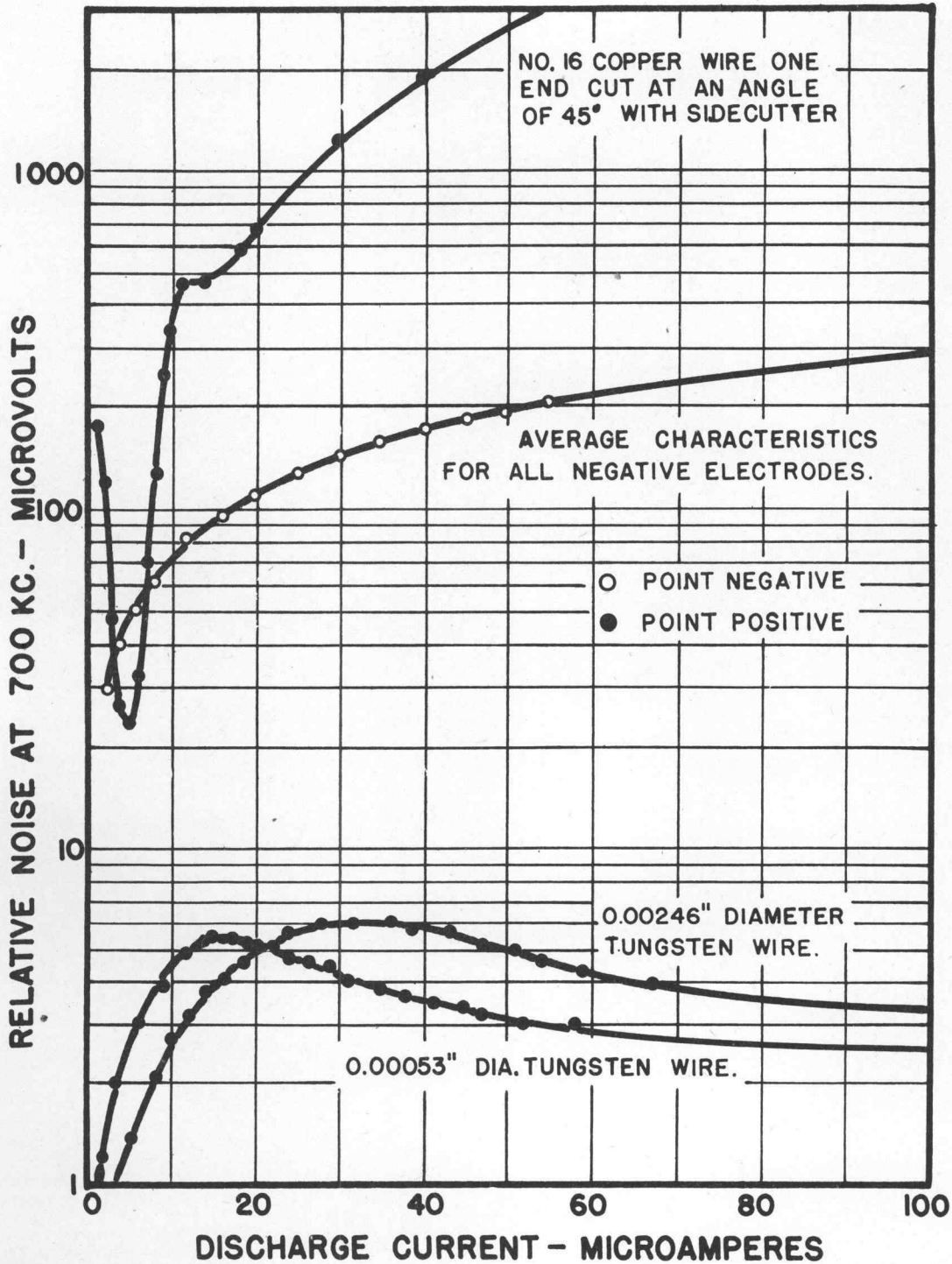


FIGURE 31
EXPERIMENTAL COMPARISON OF
POSITIVE DISCHARGES

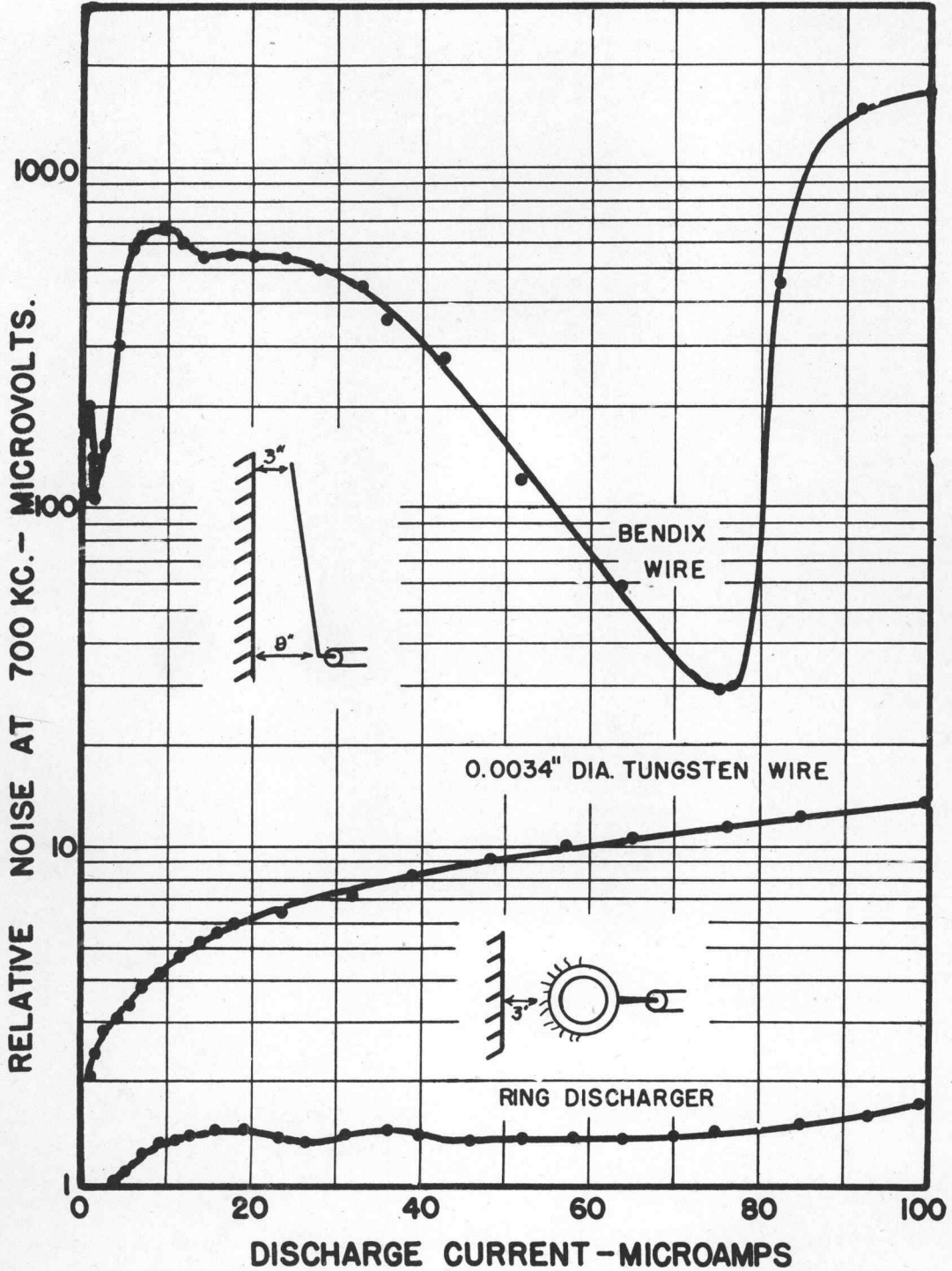
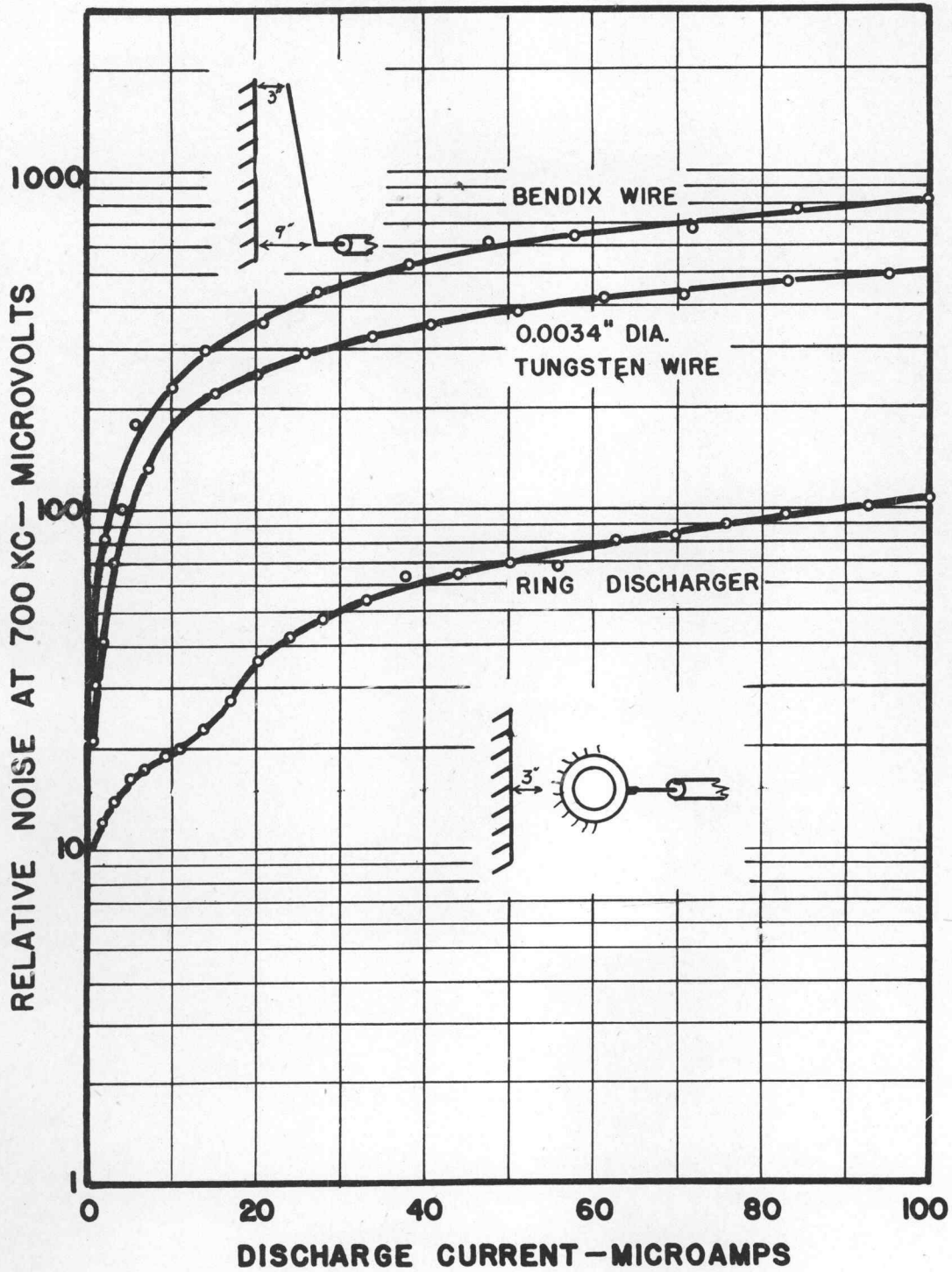


FIGURE 32
EXPERIMENTAL COMPARISON OF
NEGATIVE DISCHARGERS



would first produce the streamers mentioned above with an accompanying large radio interference, and then with increasing voltage the interference produced by that particular section would gradually decrease until the next section would go into corona with its inductive kicks. This process would repeat itself in a similar fashion along the wire until the entire wire was enveloped in corona and the end nearest the high-voltage electrode would spark over.

In the case of the negative discharge electrode, the small tungsten wire 0.0034 inches in diameter offered some improvement over the Bendix wire. A marked improvement over the Bendix discharger was achieved by the ring electrode, as is shown in Figure 32. Although the small tungsten wire shows but slight improvement over the Bendix wire insofar as the noise at any particular current is concerned, there was a marked reduction in the voltage required to produce that current. Thus, to produce a given current, the small tungsten wire required only about two-thirds the voltage needed by the Bendix wire.

It may be concluded from these experimental comparisons that the special discharger using the very fine tungsten wires in multiple is far superior to the Bendix type of discharger insofar as electrical characteristics are concerned. Mechanical characteristics may, however, prevent the use of a wire any smaller than that now used. The measurements used with the 380,000 ohm Bendix flexible resistor in series with the various discharge electrodes indicated that the results were still proportional, so the experimental data obtained without the resistor would apply equally well if it were used.

It is admitted that extremely small wire such as that used in the ring discharger would be too fragile and delicate to be used aboard an aircraft in its present form. However, the important conclusion to be reached from these studies is that all points and wires should be made as small as mechanically practical.

X. RADIOACTIVATED DISCHARGE DEVICES

Theory of Operation

A type of pre-ionized discharge device which has definite possibilities is the radioactivated discharger containing radioactive salts of sufficient strength to produce ionization of the surrounding atmosphere. When this discharger is subjected to an electric field, the ions produced in the air by the radiation will move in such a direction as to neutralize the electric field. For example, if the discharger is positively charged with respect to the surrounding space, the negative ions formed in the atmosphere immediately adjoining the discharger by the alpha radiation will be attracted to the discharger whereas the positive ions will be repelled, thus eventually neutralizing the charge accumulation on the discharger. The same neutralizing action would occur if the polarity of the discharger were reversed, since then the positive atmospheric ions formed by the radiation would be attracted to the discharger neutralizing the negative charge thereon.

The maximum current which could be discharged through this mechanism would be realized when all of the ions of one polarity were removed by the discharge device. The general problem, therefore, in the design of the radioactive type of discharger has been to utilize the radium salts in the most efficient manner so that the largest possible saturation current can be obtained from a given amount of radium.

It has been suggested by Dr. Victor F. Hess, of Fordham University, and others that thin sheets of radium alloy could be fastened to the outer surface of the aircraft in such position that the ions produced would best be able to reach the metal parts of the airplane and thus neutralize any charge bound thereon. Very thin foils have been developed by the United States Radium Corporation which reportedly show an alpha radiation efficiency of 70 percent of the theoretical value. That is, a saturation discharge current of between 1.4 and 1.7 microamperes per milligram of radium might be obtained

from such foils. The United States Radium Corporation has recently supplied this laboratory with samples of this foil but unfortunately time has not allowed us to make these tests in time to be reported upon here. These gold sheets will, however, be studied as soon as possible and the experimental results will be given in a later report.

The major objection to the use of the radioactivated foil for charge-dissipating purposes is that relatively large quantities of radium salts would be required to discharge satisfactorily the currents of roughly 100 microamperes which are known to charge present-day aircraft. The Canadian Radium and Uranium Corporation has championed the use of radioactivated point and wire dischargers as it is their opinion that devices of this type can be made to discharge the necessary current without producing radio interference and with a considerable saving in the quantity of radium salts required. Tests were made in this laboratory on dischargers of this type which were generously supplied by Mr. Boris J. Pregel, president of the Canadian Radium and Uranium Corporation, and the results will be presented in the following sections.

No final conclusions should be drawn from these rather preliminary tests as to the ultimate success, or failure of the radium dischargers for two reasons. First, the tests described are for static air conditions--a strong blast of air past the radium cup may feasibly change the entire performance. Second, the physical shape of the dischargers was in a very early state of development, and alterations in their design may change their performance considerably. Nevertheless, it is felt that the phenomena observed in the study of these devices will be common to a greater or lesser extent to all radium dischargers utilizing the same principle.

Description of Radioactivated-Cup Discharger

The essential feature of the two dischargers furnished by the Canadian Radium and Uranium Corporation was the brass cup, containing the radium salts, which could be fastened to the discharge needle point and locked in place by a set screw as is shown in Figure 38. Two activated cups were supplied, the smaller cup having an outside diameter of 1.245 cm and the large cup having an outside diameter of 1.807 cm. The inner surface of each cup was treated with approximately 1 mg of radium salts and then covered with a thin coat of lacquer for protection. The trajectory of the alpha particles from the larger cup was estimated to be from 1.5 to 2 cm whereas for the smaller cup, the trajectory was from 2 to 2.5 cm.

Preliminary tests made at atmospheric pressure indicated that the larger cup possessed current and radio interference characteristics which, for all practical purposes, were identical to those of the smaller cup. Accordingly all tests described hereafter were made on the small cup only, since it was felt that detailed tests made on both cups would be unnecessarily repetitious.

Summary of Tests Made

The small discharge cup was mounted on its needle in a Pyrex vacuum chamber constructed especially for the purpose, and the spacing between the high-voltage plate electrode and the needle point adjusted to three inches. Internal pressures ranging from 1 atmosphere to 1/2 mm. of Hg were obtainable, and the high-voltage plate electrode could be supplied with direct potentials of either polarity up to 50 kilovolts.

The tests may be classified into three groups: first, the performance of the radioactive cup alone; second, the performance of the cup with a needle projecting 5 mm. beyond its surface; and third, the performance of a needle alone. In all groups, the relationship between the current, voltage, and radio interference at 1, 1/2, and 1/4 atmosphere was observed. Additional measurements were made of the effect of pressure on the discharge current for the cup only, and data are given showing that for a given plate-to-cup voltage there exists some pressure at which the ionization current is a maximum.

Discharge Characteristic of Radioactive Cup Only

From previous studies, the discharge characteristics of a needle point were fairly well known. It was, therefore, thought advisable to investigate rather fully the behavior of the radioactivated cup in the absence of a needle point. The small activated cup was therefore placed on the needle so that the surface of its rim was flush with the needle point giving a spacing between the activated cup and the high-voltage plate electrode of 3 inches. A fixed potential was then impressed across the discharger cup and plate electrode, the pressure varied from 1 atmosphere down to approximately 1/2 cm of Hg, and readings of the current and radio-interference voltages taken. The data obtained from these tests are shown in Figure 33 for both polarities of discharge as well as for plate-to-cup voltages of 5, 2, and 1 kv.

It is interesting that, at the higher pressures, there exists a pressure at which the discharge current becomes a maximum. This is, apparently, the optimum pressure for field-intensified ionization by electrons found by Stoletow.* Stoletow observed that the pressure at the current maximum varied directly with the electric field. However, tests made on the radioactive discharger, the results of which are shown in Figure 37, indicated that the optimum pressure varied approximately as the cube root of the applied voltage. The lack of agreement with Stoletow's observations is probably due to space-charge alterations of the non-uniform electric field around the discharger cup.

Negligible radio-interference existed at the higher pressures where the discharge current was chiefly that due to radioactive ionization; but as the pressure was further reduced, the current was found to increase quite rapidly if the discharge were of positive polarity. Simultaneously with this increase in current, radio-interference was observed. This rapid increase in current was apparently due to field-intensified ionization by electrons, for, after the current had increased to several microamperes, a pale ring of burst corona could be observed around the rim of the cup, appearing much as indicated in the photograph of Figure 39 (b).

When the cup was negative, the increase in current with decreasing pressure occurred very suddenly. When the potential difference between the discharger and the plate was 5 kv, a spark suddenly formed as the pressure was reduced to 22 mm of Hg. This is mentioned because normally, at atmospheric pressures at least, the sparking potential of the negative point is somewhat greater than the sparking potential of the positive point.

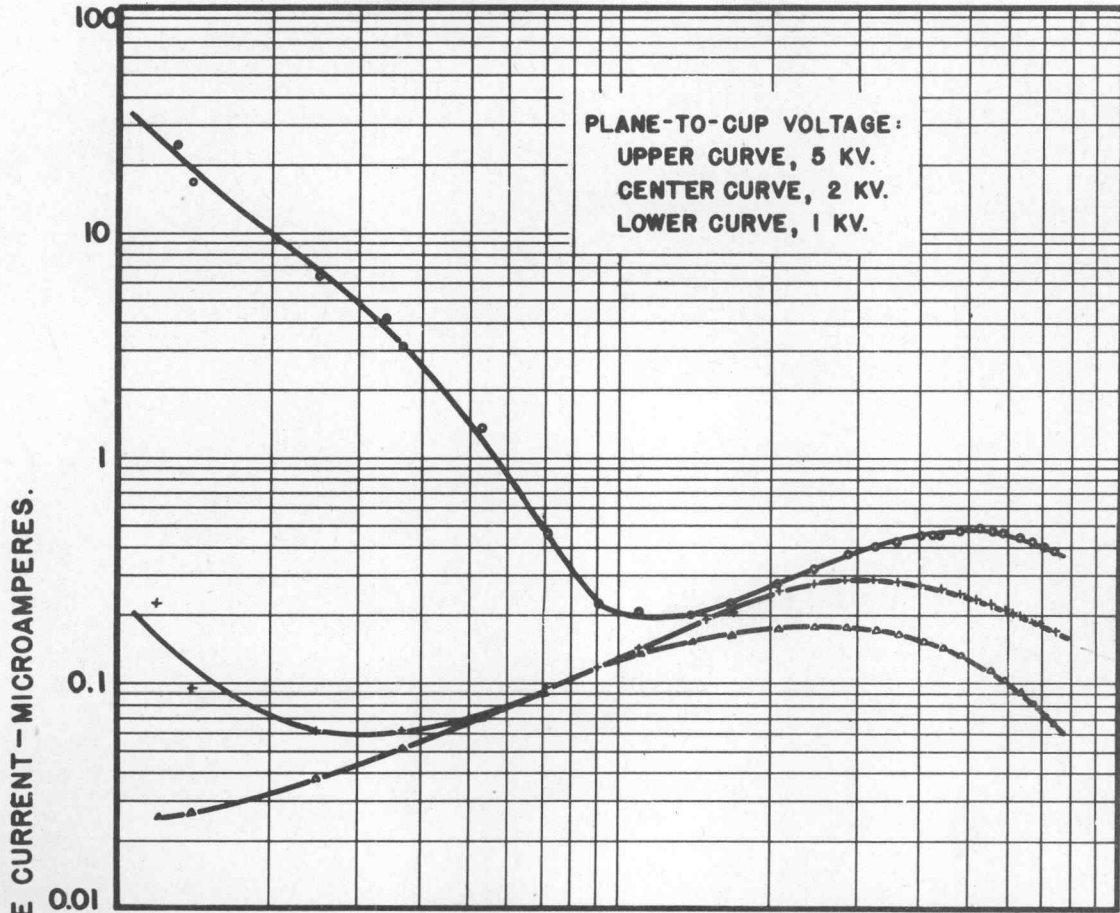
Another interesting characteristic of the data presented in Figure 33, which is worthy of note, is that the radioactive ionization currents (that is, the current for pressures greater than 10 cm of Hg) are nearly identical for both positive and negative polarity. At the lower pressures, however, distinctly different mechanisms of corona discharge account for the differences observed in the discharge characteristics at those pressures. Whereas a burst-corona glow was visible at the rim of the cup for the positive polarity, no visible glow was observed on the negative cup for the data shown in Figure 33.

The next phase in the investigation dealt with the discharge current and radio-interference as a function of the plate-to-cup potential for pressures of 1, 1/2, and 1/4 atmosphere. The data obtained for the positive cup are indicated graphically in Figure 34. It is interesting that the general shape of the discharge curve is not altered materially but simply displaced in both the horizontal and vertical directions by an amount roughly corresponding to the logarithm of the pressure ratio. It should also be noticed that the slope of the curves for the low potentials is unity which indicates that the gap resistance is constant. Also, if one will examine the curves at an abscissa of 2 kv, he will observe that the discharge current at 1/2 atmosphere pressure is greater than that obtaining at 1 or 1/4 atmospheres pressure. From the behavior of the discharge

*A. Stoletow, J. d. Physique, 9, 468, 1890.

FIGURE 33.
DISCHARGE CURRENT AS A FUNCTION OF PRESSURE

(a) ELECTRODE: RADIUM CUP ONLY TO PLANE. SPACING: 3 INCHES.
 POLARITY: DISCHARGER POSITIVE.



(b) ELECTRODE: RADIUM CUP ONLY TO PLANE. SPACING: 3 INCHES.
 POLARITY: DISCHARGER NEGATIVE.

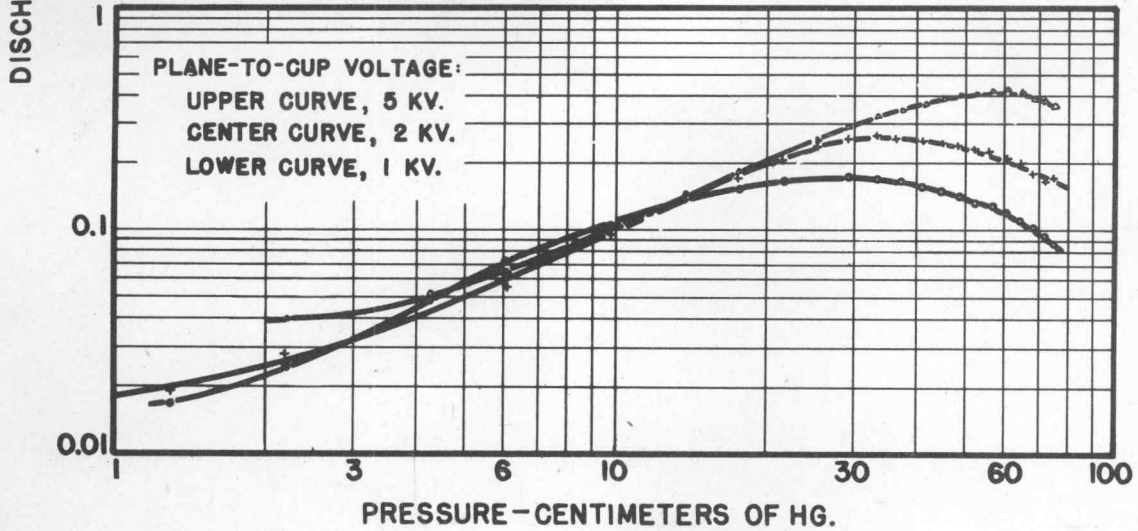
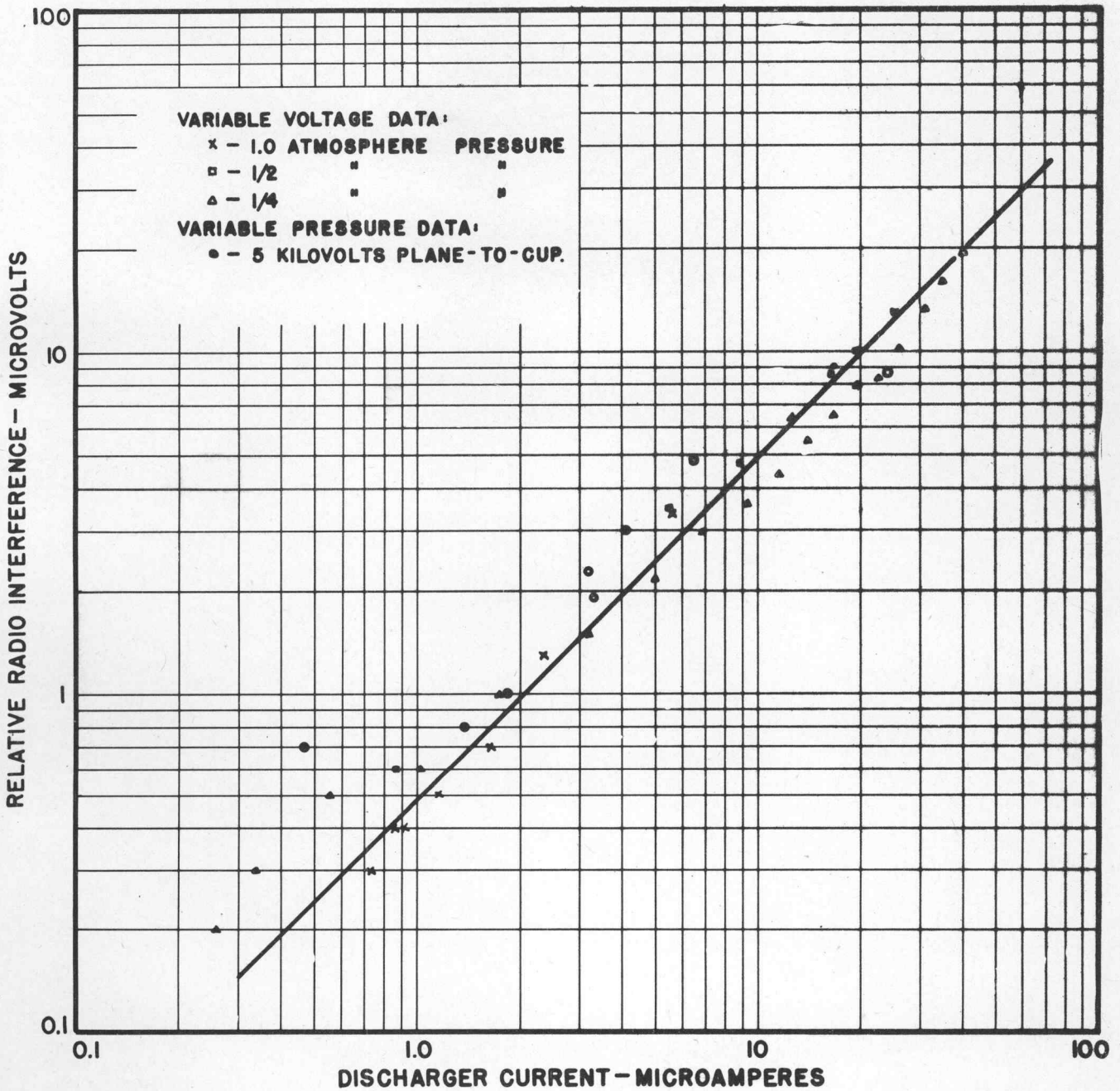


FIGURE 34.
POSITIVE DISCHARGER RADIO INTERFERENCE AS A FUNCTION OF
DISCHARGE CURRENT.



curves in this region, it becomes apparent why a maximal current obtains at some optimum pressure.

It has already been pointed out that no measurable radio-interference was produced by the discharge current until cumulative ionization began to occur as indicated by the very rapidly increasing current characteristic.

The radio-interference data for the same measurements shown in Figures 33 (a) and 34 are plotted as a function of discharge current in Figure 35. The important point to be gathered from this figure is that, for practical purposes, the radio-interference varies directly with the discharge current and is independent of the atmospheric pressure. The radio-interference itself is due to the burst type of corona which, because of the external ionization, can commence immediately at onset without the advent of the more usual corona streamers. Apparently, each corona burst constitutes a definite charge and also produces a more or less definite amount of radio-interference. Further indication that this is the case is found in Figure 42 which shows the radio-interference produced by the burst corona from a radiated needle point.

The negative discharge current as a function of plate-to-cup voltage is shown in Figure 36. Here, because of the effect of space charge and the negative-corona mechanism, the increase in discharge current at onset is found to be much more abrupt than in the case of the positive discharge cup. The sudden increase in current at onset was accompanied both by severe radio-interference and also by corona on the rim of the cup as shown in Figure 38. The radio-interference was, in general, several hundred times as great as the positive-discharge radio-interference obtaining for the same current. Because of the carrier-like behavior of the negative point discharge interference, it is practically impossible to make measurements of the magnitude of the interference which have any meaning. It is sufficient to point out that the appearance of the cathode spot on the cup's rim was accompanied by very severe radio-interference.

The negative-cup corona, three photographs of which are shown in Figure 38, was a fascinating thing to study. At onset, only one cathode spot would appear. With increasing voltages other spots would appear, and, because of the space-charge distortion of the electric field, the spots would space themselves at equal distances around the periphery of the rim of the cup. Figure 38 illustrates not only the equal spacing of these spots under various conditions, but also illustrates the growth of the ionized region as the pressure is reduced. For a given discharge current, the physical dimensions of the corona plume seemed to vary roughly as the inverse of the pressure.

The photographs of Figure 39 illustrate the appearance of the corona when the discharge cup was made positive with respect to the plate electrode. All three photographs show the burst corona completely covering the upper rim of the cup, and, in addition, it will be noted that Figure 39 (a) shows several positive streamers. Streamer formation of this type produces extremely severe radio-interference. The radio-interference factor of 350 microvolts as recorded for this particular condition is an average value; the peak interference would undoubtedly be much greater. Figure 39 also illustrates the growth in the physical size of the burst pulses with a decrease in pressure. At very low pressures, the burst pulses cover most of the surface of the cup.

Characteristics of Radioactivated Needle-Point Discharges

In this phase of the investigation, the cup was adjusted so that the needle point projected 5 mm beyond its surface. The spacing between the needle point and the plate electrode was maintained at 3 inches. Each test was made twice, first using the radioactivated cup, and then using the unactivated cup. Unfortunately, the two cups were not identically shaped so that the results obtained from this series of tests may not be exactly comparable.

Figure 40 compares the activated and unactivated needle-point current-discharge characteristics at 1, 1/2, and 1/4 atmospheres pressure. At voltages below corona onset,

FIGURE 35.
 RADIOACTIVATED CUP DISCHARGER CURRENT AS A FUNCTION OF VOLTAGE.
 POSITIVE POLARITY.

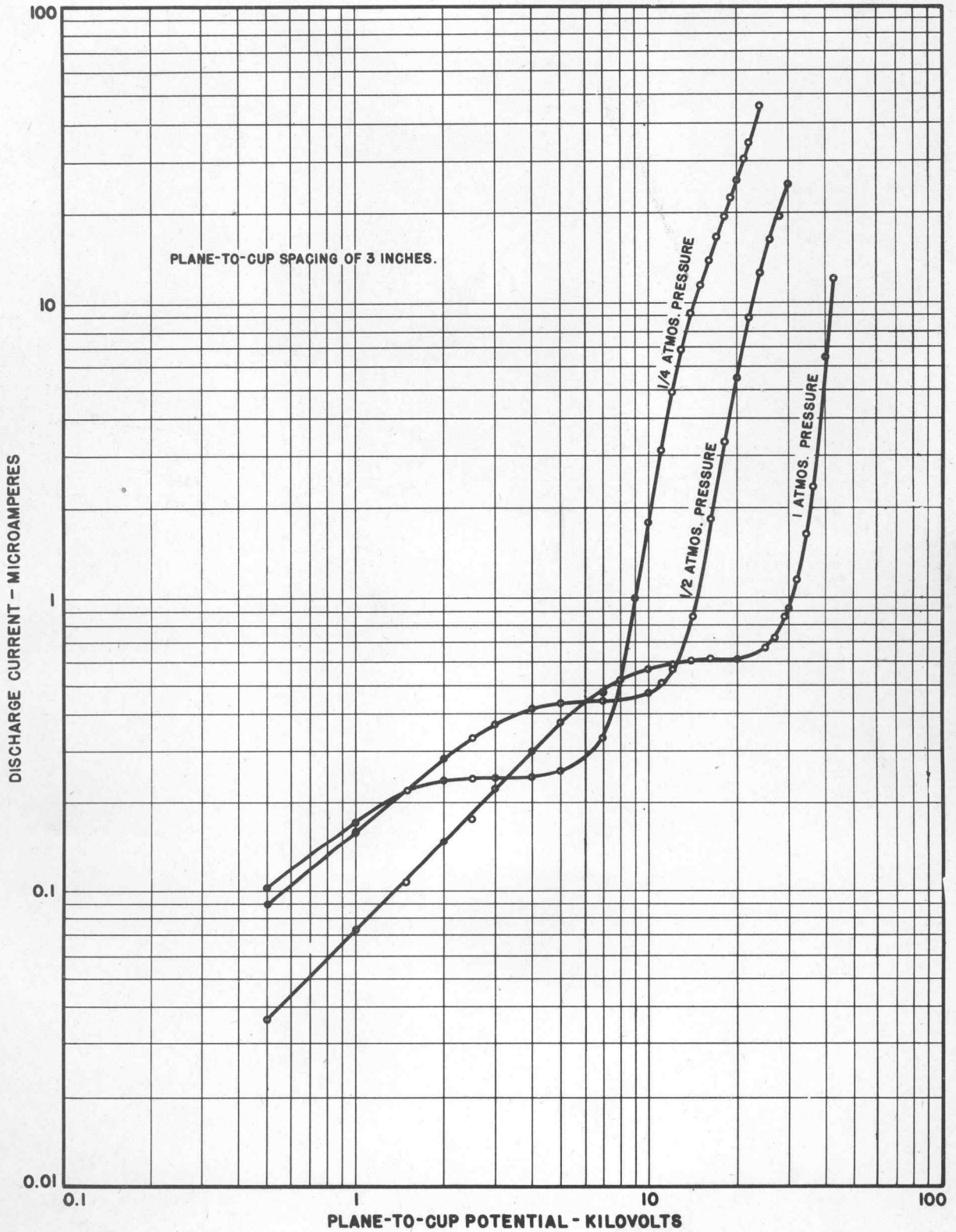


FIGURE 36.
RADIOACTIVATED CUP DISCHARGER CURRENT AS A FUNTION OF VOLTAGE.
NEGATIVE POLARITY.

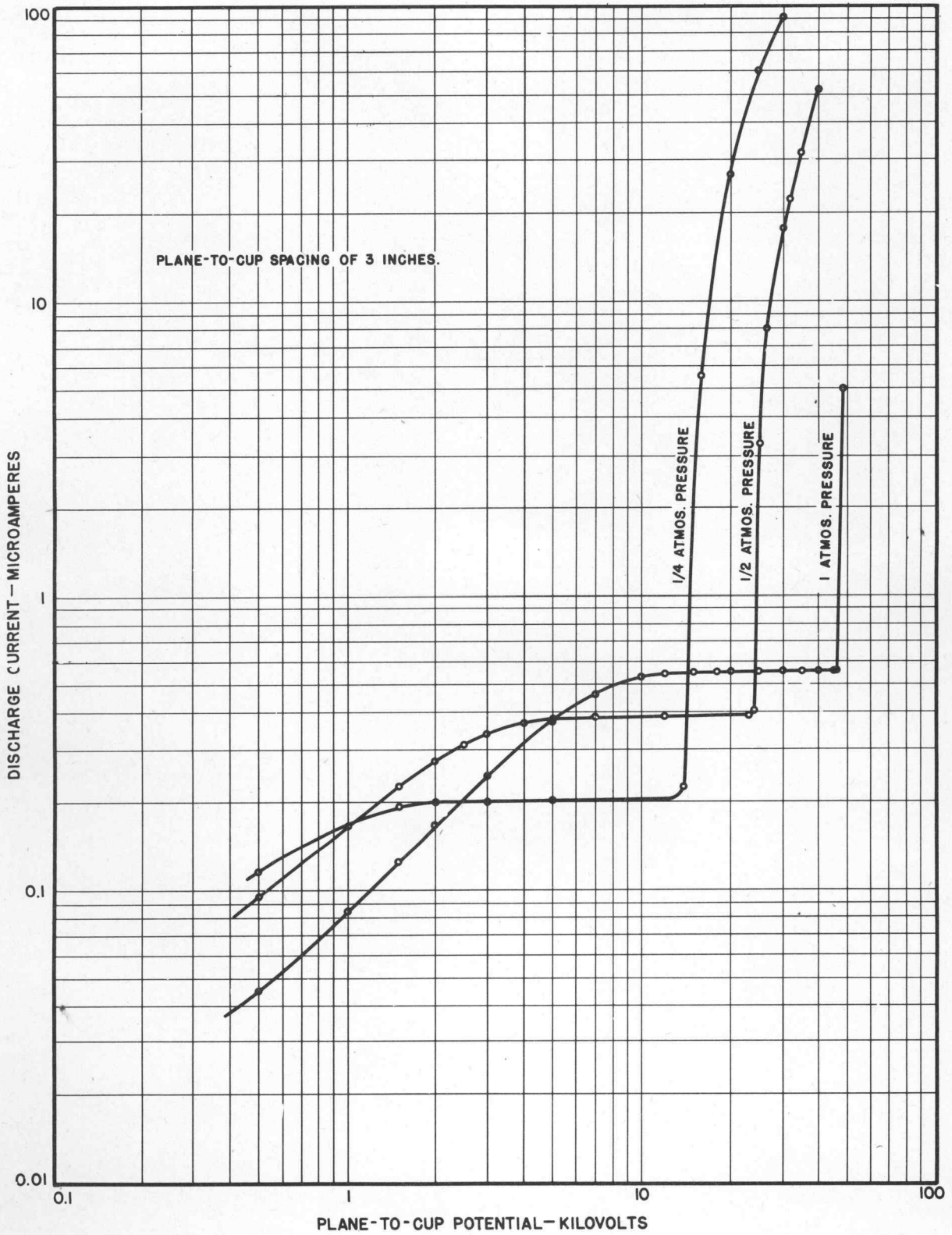
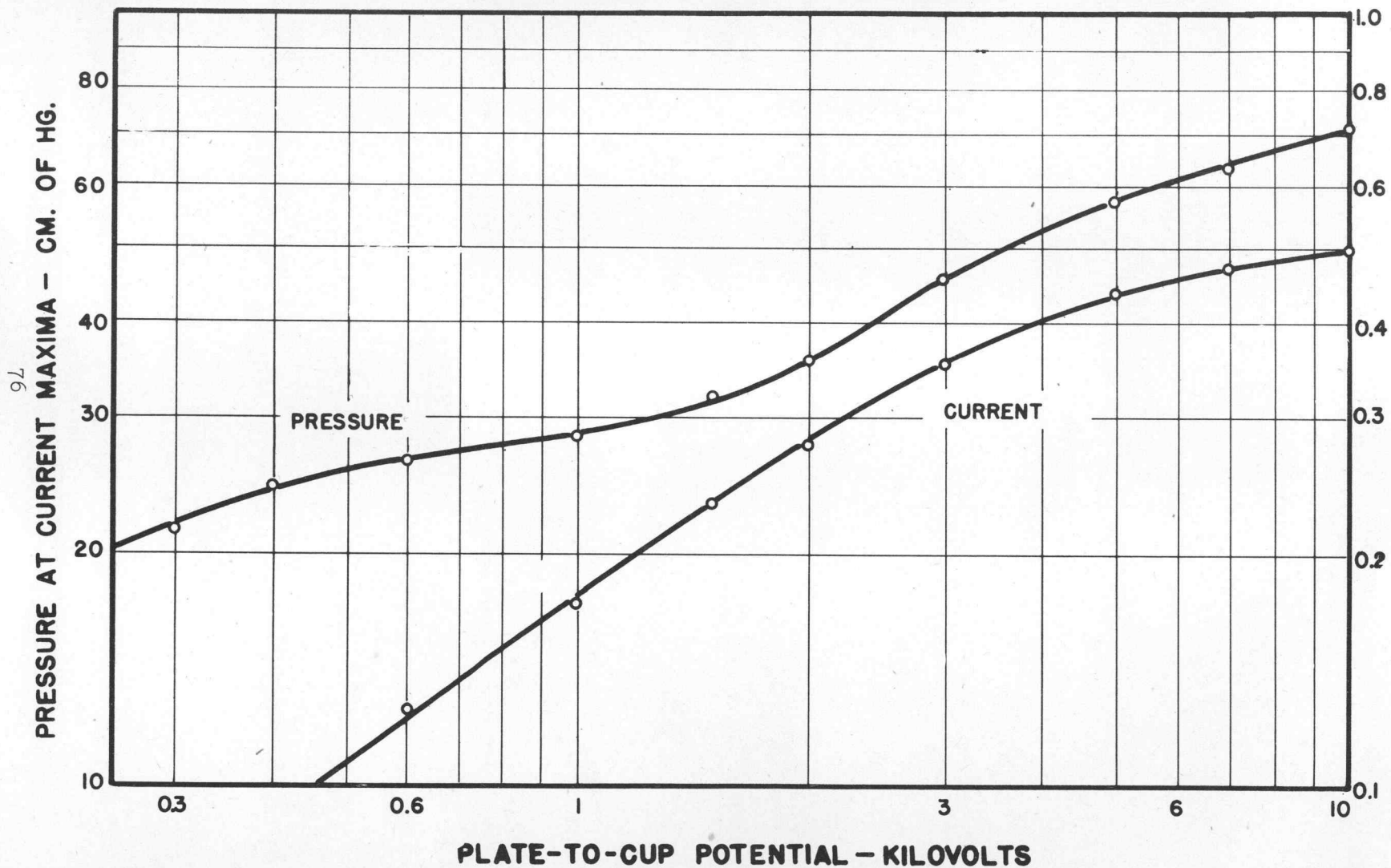


FIGURE 37. PRESSURE AT CURRENT MAXIMA AS A FUNCTION OF PLATE-TO-CUP POTENTIAL.



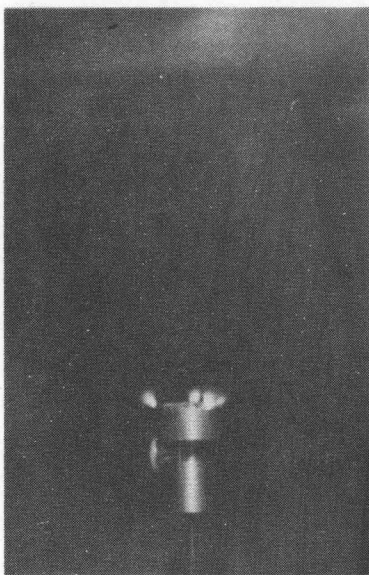
PRECIPITATION-STATIC-REDUCTION RESEARCH

MAXIMUM CURRENT - MICROAMPERES

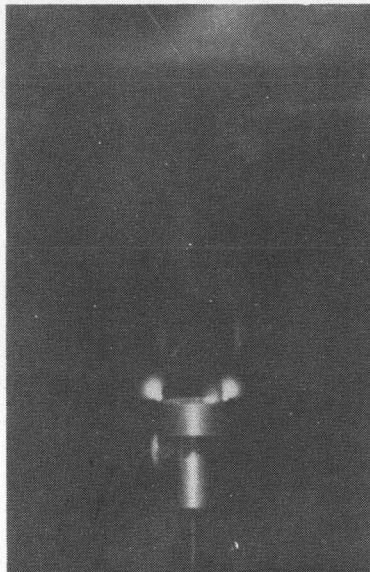
Fig. 38

CORONA ON NEGATIVE DISCHARGER

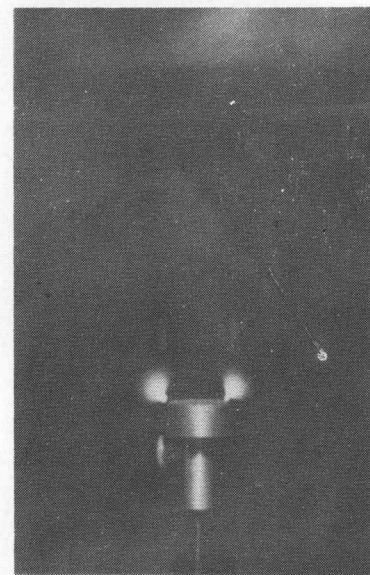
Cup-to-plate spacing: 2.08 inches



(a) Pressure: 1.0 atmos.
Voltage: 45 kv.
Current: 35 microamps.
R.I.F.: 320 microvolts.



(b) Pressure: 0.5 atmos.
Voltage: 25 kv.
Current: 56 microamps.
R.I.F.: 600 microvolts.

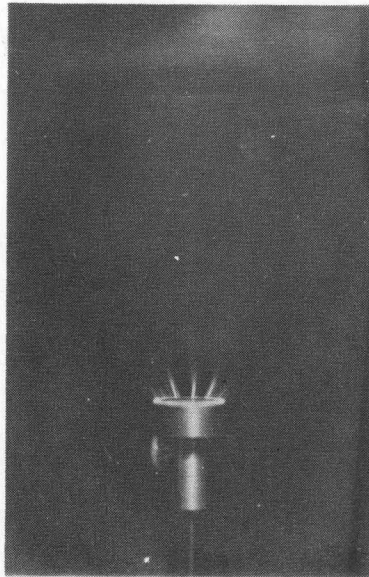


(c) Pressure: 0.25 atmos.
Voltage: 15 kv.
Current: 47 microamps.
R.I.F.: 620 microvolts.

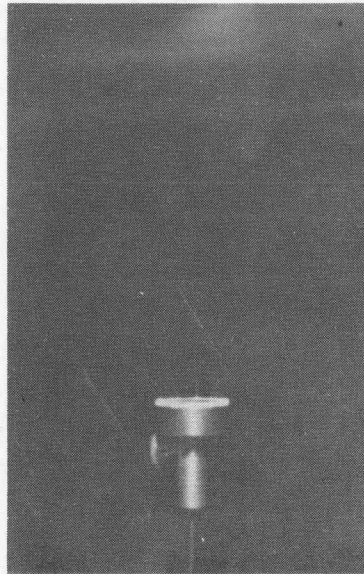
Fig. 39

CORONA ON POSITIVE DISCHARGER

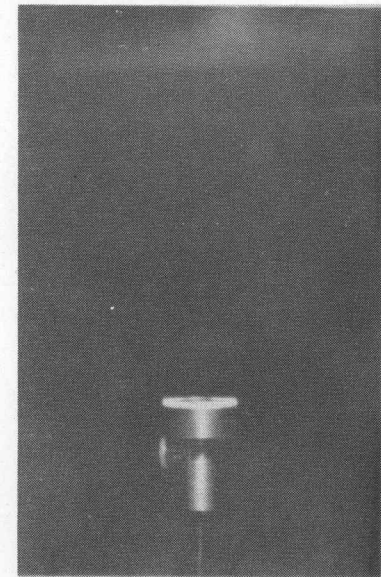
Cup-to-plate spacing: 2.08 inches



(a) Pressure: 1.0 atmos.
Voltage: 38 kv.
Current: 15 microamps.
R.I.F.: 350 microvolts.

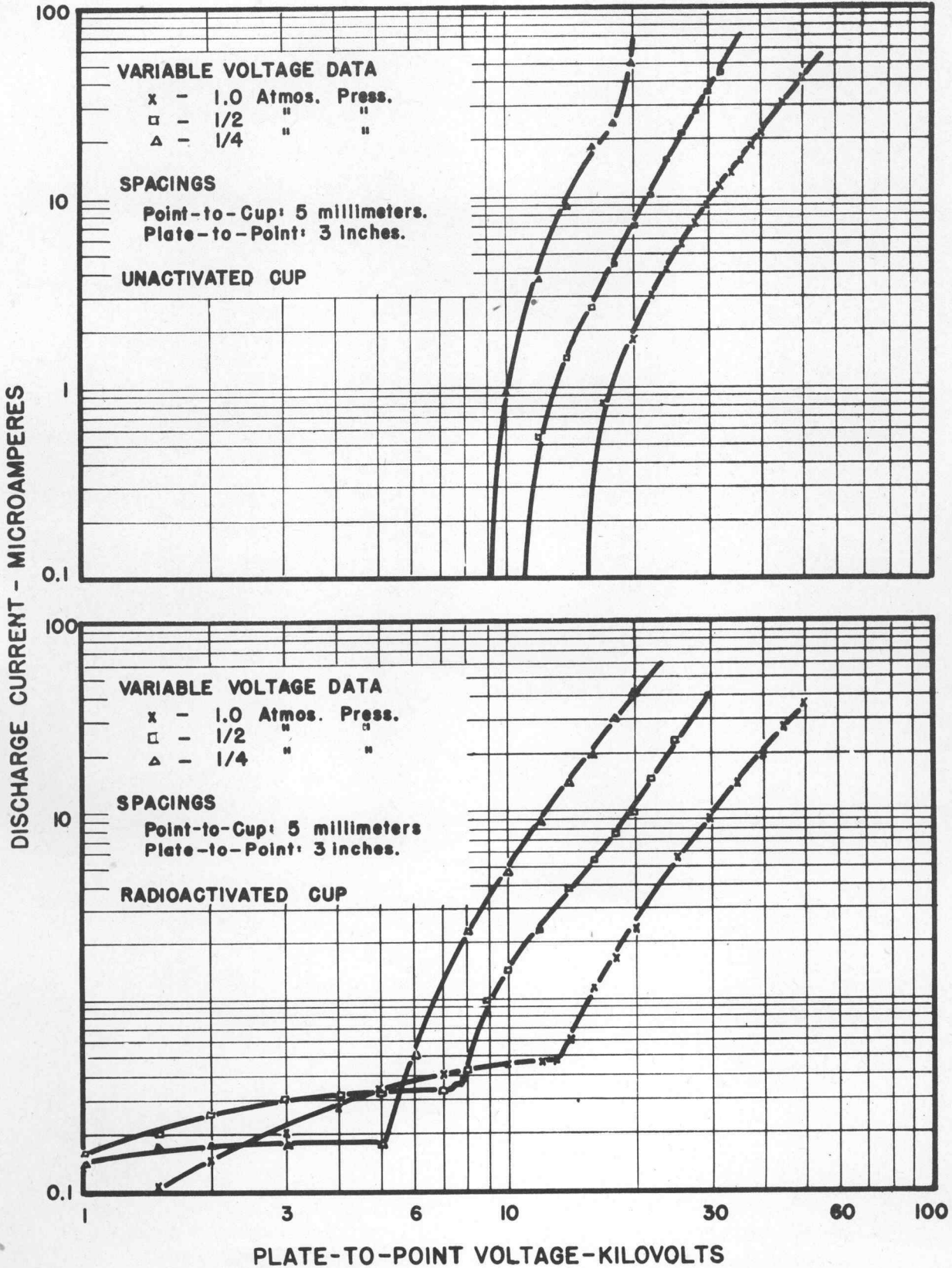


(b) Pressure: 0.5 atmos.
Voltage: 23 kv.
Current: 15 microamps.
R.I.F.: 12 microvolts.



(c) Pressure: 0.25 atmos.
Voltage: 15 kv.
Current: 15 microamps.
R.I.F.: 15.5 microvolts.

FIGURE 40. EFFECT OF RADIOACTIVE MATERIAL ON NEGATIVE NEEDLE-POINT DISCHARGE.



the radioactivated cup could discharge, without radio-interference, a current of from 0.2 to 0.5 of a microampere which would definitely be of some advantage in discharging aircraft. Even after corona onset, the radio-activation of the discharge point materially increases the current. However, at current values greater than 2 microamperes approximately, the effect of the radiation becomes increasingly less until, at the maximum current value studied, the discharge current for both the activated and unactivated points are found to be nearly identical.

When the needle point was made positive, the discharge characteristics as shown in Figure 41 were found to be very similar to those obtaining for the negative points. An important difference, however, is that for the positive point discharges, the radio-activation increases the current to a somewhat greater extent than obtaining for the negative needle point.

Figure 42 shows the radio-interference produced by the radiated-positive-point discharge as a function of discharge current for the three pressures heretofore used. For all noise data shown on this graph, the burst corona existed entirely at the needle point (Starr's Type 1 discharge). It is because of this very localized type of discharge and the resulting strong space charge that the experimental data shown do not follow the dotted straight line. Even so, there is a remarkable correspondence between the data of Figure 42 and the data of Figure 34.

Figure 43 shows the radio-interference as a function of discharge current for the unactivated needle point. The saddle-like shape of these curves has an explanation, but one would not expect to find less radio-interference than occurred in the radiated points. The reasons for this very unusual behavior should be investigated more thoroughly. The explanation of the initial high noise value is that, at corona onset, small positive streamers are formed prior to the more or less steady burst corona occurring at higher currents.

No interference data have thus far been given for the negative point discharge for the simple reason that no single number can be used to designate the radio-interference of the negative discharge because of its discontinuous frequency spectrum. However, certain startling information as to the frequency with which the negative corona bursts occur was obtained. The first negative point data to be taken were those for the unactivated cup at atmospheric pressure as shown in Figure 40. At the maximum current and voltage value recorded the corona bursts were occurring at a rate of 4.3 million bursts per second. This indicated that each corona burst constituted a charge of approximately 10 micro-microcoulombs. Similar data were obtained at 1/2 atmosphere when, for the maximum current value indicated, the burst frequency was found to be 3.9 million bursts per second giving an average charge per burst of approximately 11 micro-microcoulombs. Unfortunately, in reducing the pressure to 1/4 atmosphere, a spark-over occurred which apparently burnt the end of the needle point so that the maximum discharge frequency observed at 1/4 atmosphere was only 2.0 million bursts per second, giving an average charge of 38 micro-microcoulombs per burst.

Similar measurements made on the radioactivated needle point at one atmosphere gave a maximum burst frequency of 660,000 bursts per second at an average charge of 54 micro-microcoulombs per burst; at 1/2 atmosphere pressure of 760,000 bursts per second at an average charge of approximately 55 micro-microcoulombs per burst; and at 1/4 atmosphere pressure a maximum frequency of 670,000 bursts per second at an average charge of approximately 60 micro-microcoulombs per burst.

Other tests have indicated that there is a gradual corrosion of the steel needle point which makes interpretation of the above data rather difficult. We have manufactured a gold needle point and we hope to definitely ascertain whether the radiation of the needle point does decrease the frequency with which the negative bursts occur.

FIGURE 41. EFFECT OF RADIOACTIVE MATERIAL ON POSITIVE NEEDLE-POINT DISCHARGE.

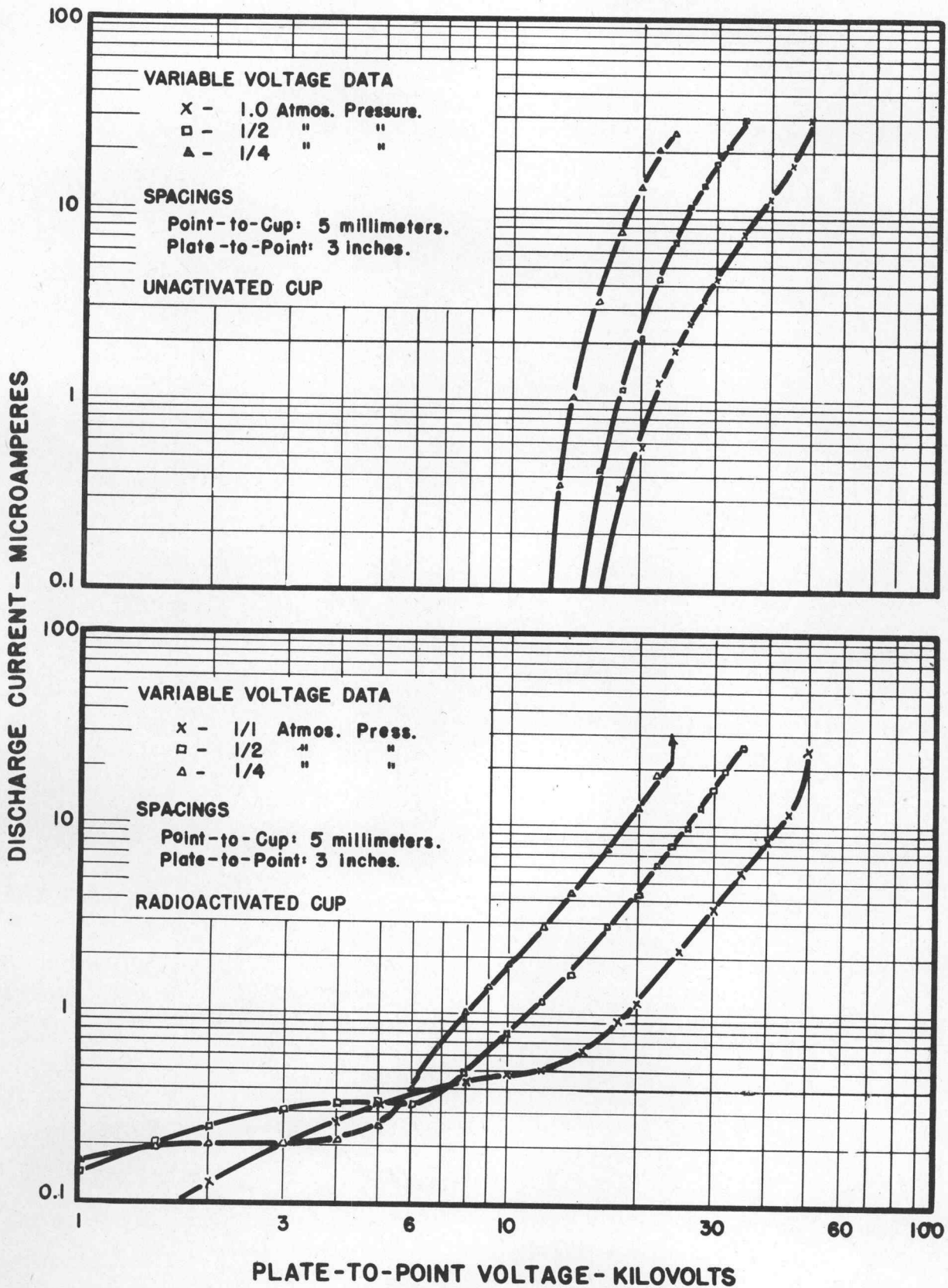


FIGURE 42.
 RADIOACTIVATED-POSITIVE-POINT-DISCHARGE RADIO INTERFERENCE
 AS A FUNCTION OF DISCHARGE CURRENT.

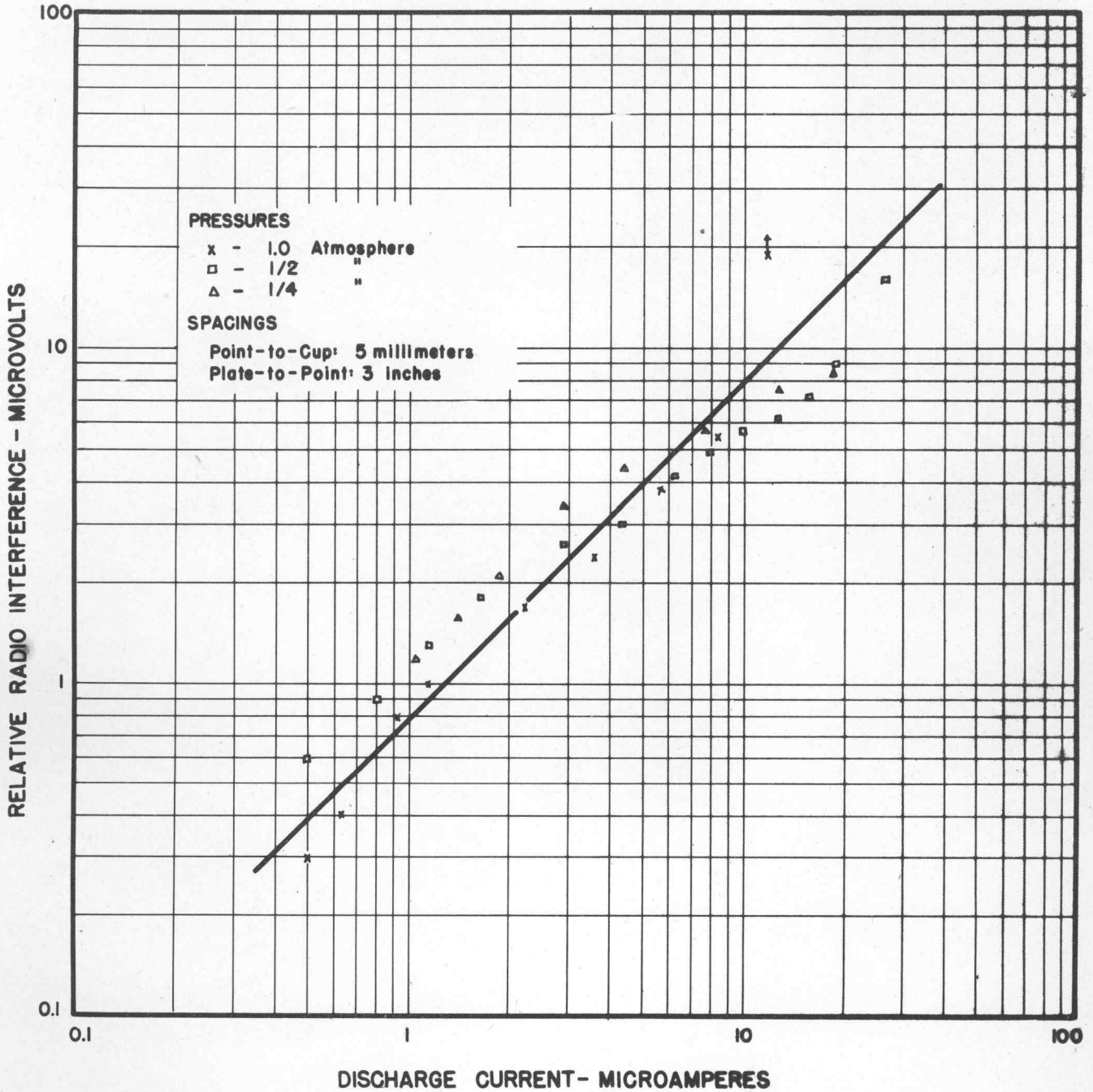


FIGURE 43.
UNACTIVATED-POSITIVE-POINT-DISCHARGE RADIO INTERFERENCE AS A
FUNCTION OF DISCHARGE CURRENT.

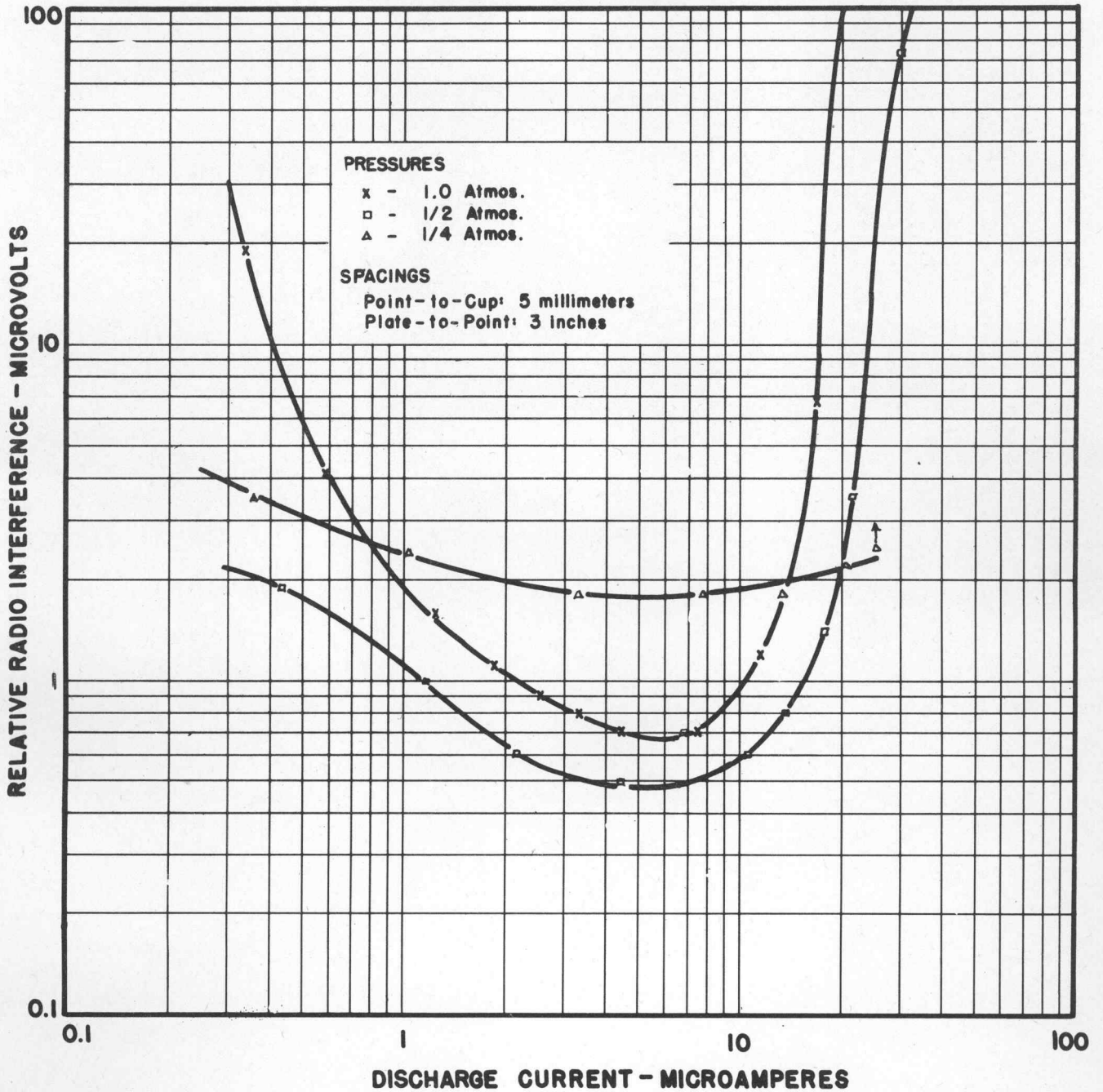
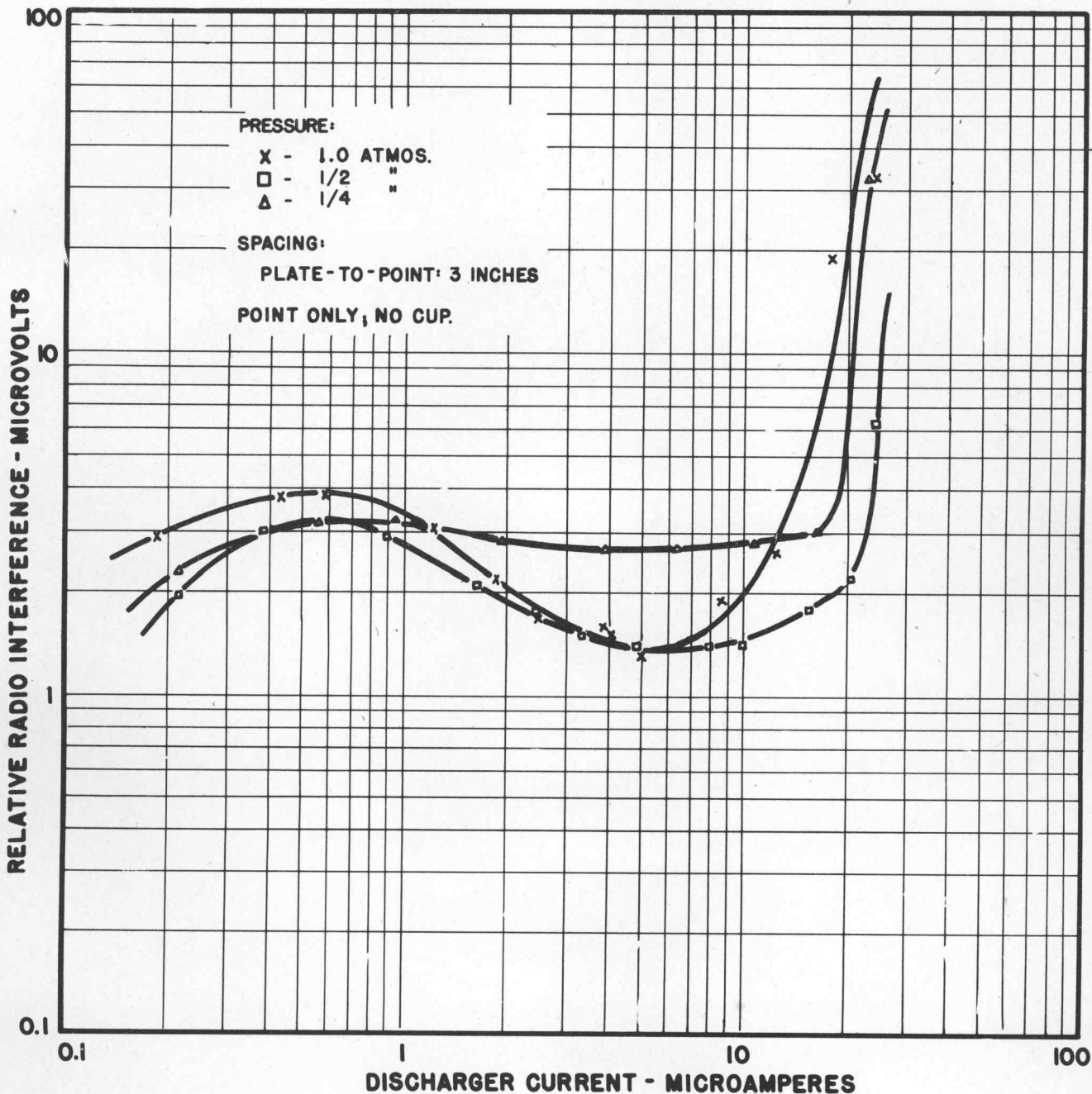


FIGURE 44.
UNACTIVATED-POSITIVE-NEEDLE-POINT-DISCHARGE RADIO
INTERFERENCE AS A FUNCTION OF DISCHARGE CURRENT.



Discharge Characteristics of Needle Point Only

To complete the study, the discharge characteristics of a needle point without a cup backing were studied. The current-voltage characteristics resemble very much those shown for the unactivated cup in Figures 40 and 41, and accordingly are not given here. However, Figure 44 does show the radio-interference produced by a positive needle point discharge. The general shape of these radio-interference curves is quite similar to those given in Figure 43 for the unactivated needle point discharges. Because of the smaller applied voltage necessary to produce corona on the needle point without the large cup backing, the interference at onset is somewhat less. During the time that the data of Figure 44 were being taken, additional corrosion of the needle occurred. Nevertheless, the maximum frequency of discharge observed at 1/4 atmosphere was 630,000 bursts per second giving a charge per burst of approximately 70 micro-microcoulombs.

Conclusions

The most important conclusion to be reached from these investigations is that radiation of a positive discharge electrode results in burst corona which produces a radio-interference proportional to the current but apparently independent of both pressure and discharge-electrode geometry. The radio-interference produced by this positive burst-corona would be negligible for all practical applications.

Except for the field-intensified ionization current of roughly 0.5 microamperes, radiation of the negative discharge electrode did not seem to materially reduce the radio-interference.

A phenomenon which should be verified and studied further is the apparent increase in radio interference resulting from radiation of the space surrounding a sharp, slender positive point. A tentative conclusion to be drawn from this effect is that, for certain types of positive fine-wire discharges operating in a limited current range, radiation of the point by radioactive material can actually increase the radio-interference produced by the discharge.

XI. FLAME DISCHARGERS

Summary

The pre-ionized discharger employing a high-temperature oxyacetylene flame at the end of a long slender conducting electrode has proven to be the best discharge device yet tested. Experiments have indicated that it is capable of discharging currents of 50 microamperes or more at atmospheric pressure and in a high-velocity wind stream without producing measurable radio interference.

Although the theory of a stationary flame produced in a combustible gas mixture issuing from an orifice is discussed, the phenomena of combustion in an electric field is not well understood for the possible reactions and combustion products are very numerous and complex. A clue as to the possible constituents of an oxyacetylene flame in the presence of an electric field is to be found in Table I, which lists the possible ions formed from the flame constituents as arranged in the order of their ionization potentials. It is observed that the ionic constituents are predominately positive, which accounts for the difference in behavior of the positive and negative flame dischargers observed experimentally. It is shown that in still air, where space charge effects become of great importance, the discharge current flowing between the flame and a large plate electrode spaced at some distance from the tip of the flame will vary almost exactly as the square of the potential difference between the flame electrode and the plate electrode--i.e., $I = B \times V^2$. Since B, the second flame-conduction coefficient, is substantially constant for any particular flame-spacing configuration, an entire voltage-current characteristic may be represented by a particular value of B, and accordingly a

study of the effects of flame length, flame spacing, and burner spacing on B shows that there exists an "effective flame center," the spacing to which determines the discharge current at a given applied potential difference.

Data are also given showing the increase in discharge current produced by a wind stream at one-atmosphere pressure past the flame electrode. It is apparent that the high-velocity wind stream greatly reduces the space charge around a positive flame, thus allowing much larger currents to flow at comparatively low potentials.

Theory of the Stationary Flame

The simple Bunsen burner provides a good starting point for a discussion of the physical theory of a flame formation and the various factors which control the shape of the flame. For this type of burner, as well as all others in which we are interested, a combustible mixture of gas escapes from an orifice into the atmosphere where it is allowed to burn. In certain regions the stream of gas leaving the orifice may have a velocity greater than the velocity of propagation of the flame which is consequently carried along with the gas stream. But at the boundary of the stream, where it meets the atmosphere, minute eddies may be formed which decrease the velocity of the combustible gas so that the flame upon reaching these boundary zones may be able to travel back toward the rim of the orifice, providing dilution of the gas at the boundary layer has not rendered the mixture noncombustible. If the gas flow is laminar and steady, the flame will then form a cone of fixed position and shape. Obviously the shape of this cone depends upon the velocity of the various gases in the flame as well as the rate of propagation of the flame front. These relations as given by Mache¹¹ will now be summarized.

It is conceivable that the various factors influencing the shape of the Bunsen cone are identical with those operating in the oxyacetylene flame of a discharger. These factors will, therefore, be considered in some detail and quantitative expressions will be derived for the relations between the various velocities occurring in the flame processes.

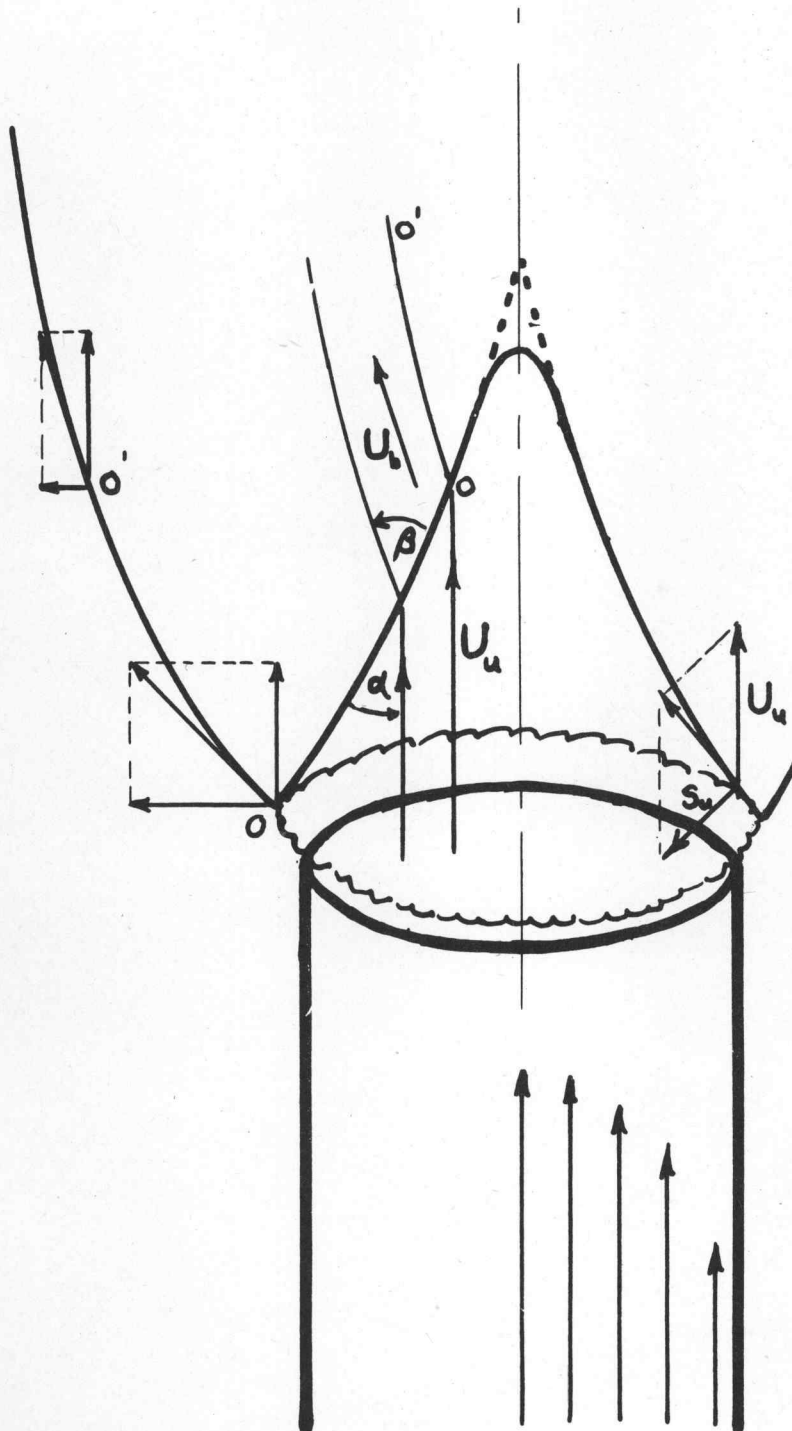
A portion of the Bunsen flame is shown diagrammatically in Figure 45. The shape of the cone is determined largely by the burning velocity at the various points and the distribution of the stream velocity. Upon consideration it is apparent that the cone will assume a shape such that the components of the gas velocity normal to its surface must equal the burning velocity (the velocity of the unburned gases relative to the flame front).

With reference to Figure 45 illustrating the Bunsen flame, the following quantities are defined:

- U_u Velocity of the unburned gas
- U_v Velocity of the burned gas
- S_u The burning velocity (velocity of unburned gas with respect to the flame front)
- S_v The flame speed (velocity of the burned gas with respect to the flame front)
- α Angle of flame front with respect to unburned gas flow
- β Angle of direction of gas flow on burned side with the reaction zone (at flame front)
- ρ_u Density of unburned gas
- ρ_b Density of burned gas

$$\text{Ctn } \alpha = \sqrt{(U_u/S_u)^2 - 1} \dots \dots \dots (1)$$

FIGURE 45.
DIAGRAM OF BUNSEN BURNER FLAME.



A curious reaction of the gas flow in the reaction zone is observed. It is due to the change of density of the gas as it burns and expands. The mass of the gas entering the reaction zone must equal the mass leaving it so that

$$\rho_u S_u = \rho_b S_b \quad (2)$$

Since the reaction zone is very narrow there can be no change of the components of the gas velocity in the plane of the reaction zone, so that $U_u \cos \alpha = U_b \cos \beta$. This may be written as

$$U_u \frac{\sin \alpha}{\tan \alpha} = U_b \frac{\sin \beta}{\tan \beta} \quad (3)$$

$$\frac{\rho_u}{\rho_b} = \frac{\tan \beta}{\tan \alpha} \quad (4)$$

This relation provides a method whereby the density of the flame of various interior points might be measured, for if the paths (O - O' of Figure 45) followed by some fine particles of carbonaceous material were observed after they had become incandescent from passing through the reaction zone, the angle β is easily measured and the relative density at the point in question may then be calculated. As the burned gas moves away from the reaction zone of the flame, it expands and the horizontal velocity component is decreased. The upward velocity component, however, remains almost unchanged for a while and consequently the lines of flow all curve upward.

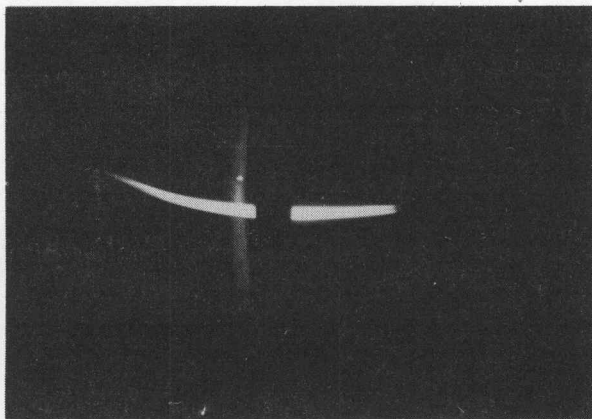
In the above discussion other factors such as the redistribution of flow velocities of the gas upon emerging from the tube and the back pressure exerted by the off-streaming burned gas have not been considered. With regard to this last factor, rough calculations show that the change in pressure occurring over the reaction zone is negligible for burning velocities which are slow when compared to the speed of a sound wave in the same medium. Measurements indicate this back pressure to be roughly one millimeter of mercury in the case of an oxyacetylene flame. It should be realized, however, that where the factors considered are entirely adequate insofar as a regular Bunsen flame of coal gas and air is concerned, it is entirely possible that other factors of considerable importance may be acting in the oxyacetylene flame.

Combustion Processes in an Electric Field

The chemistry and physics of a flame subjected to an intense electric field are but little understood. Even the process of combustion alone is a very complex phenomenon according to the latest theories involving "material and energy chain reactions with their many complicated and transitory by-products." When the phenomenon is altered by subjecting the flame to an intense electric field, it becomes of such complexity that virtually none but the roughest type of qualitative physical analysis is possible.

However, it is known¹³ that "molecules will lose one or two electrons and form single- and double-charged (positive) ions; they will dissociate into smaller fragments by electron impact; they and their dissociation products will undergo a process of 'building-up' to structures of higher molecular weight. Molecules and their dissociation and aggregation products will add electrons and they will form negatively charged ions."

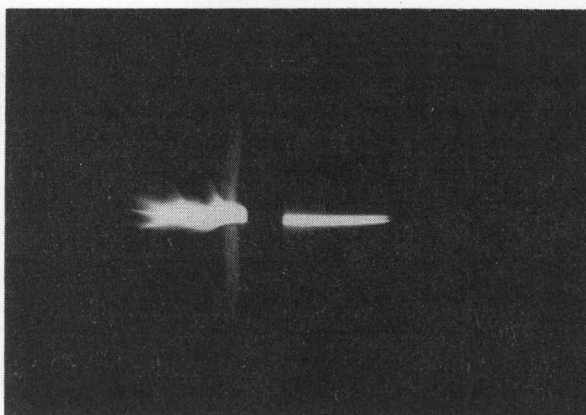
Further experimental evidence that the process of combustion is actually an electro-chemical reaction is seen from the fact that the propagation of the flame is largely dependent upon the positive-ion concentration therein. A flame will usually be attracted toward an electrode which is negatively charged with respect to the flame. If the electric field is sufficiently intense, the positive ions will be drawn away from the reaction zone faster than the flame can follow so that, assuming the positive ion to be favorable to the combustion process, the combustion is limited and the flame becomes, with increasing potential, rather weak and erratic in appearance until it is eventually



Type 4 Acetylene Flame,
Ring-shaped Cathode $2\frac{1}{2}$ "
Internal Diameter. Flame
Directed through Center.

Voltage = 0 KV.

Voltage = 10 KV.



Voltage = 20 KV.

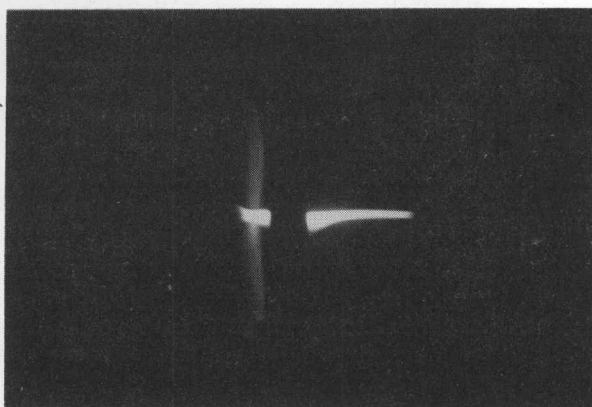


Figure 46. Effect of Electric Field on Positive Flame.

PRECIPITATION-STATIC-REDUCTION RESEARCH

Extinguished. Figure 46 shows the effect of an electric field on a positive, type 4 acetylene flame.*

The anode in this case was a metallic ring $2\frac{1}{2}$ inches in internal diameter, and the flame was adjusted to pass through its center and a normal to the plane of the ring electrode. With no voltage applied, the flame was very long and slender with large quantities of dense carbon smoke and streamers ascending with the heated gases from the pointed tip.

When a negative voltage of 10 kv. was applied to the ring, the smoke almost entirely disappeared and the end of the flame developed a finned appearance. The fins themselves were very thin, and because of the increased surface area seemed to allow rather complete combustion--hence the disappearance of the carbonaceous smoke. At higher voltages the finned appearance became somewhat less, probably because the intense electric field acting on the edges of the fins removed the positive ions so rapidly that the combustion could not follow.

Even without a flame, an electrical discharge is sufficient to produce various ions from the molecules of the constituents of the gas and thus through mass spectroscopy many ions have been observed. Table 1 gives many of the possible ions which may be formed from the products of combustion of the oxyacetylene flame, arranged in order of their ionization potentials.

TABLE I
Possible Ions Formed by Oxyacetylene
Flame and Ionization Potentials

Ionization Potential (Electron Volts)	Ion or Reaction	Source† (see footnotes for meaning of symbols)
64.2	$C + O^{++} + O$	D
58.5	$C + O^{++}$	C
54.5	O^{++}	E
54.2	$CO^{++} + O^{++}$	D
51.2	$C^{++} + O + O$	D
49.7	$CO^{++} + O$	D
48. <u>±</u> 2	$2H^{+} + K.E.$	A
45.5	$C^{++} + O^{++}$	C
43.0	CO^{++}	C
42.7	$C + O^{+} + O^{+}$	D
40.5	$C^{+} + O^{+} + O$	D
37.4	$N^{+} + N^{+}$	E

†Glockler and Lind, "The Electro-Chemistry of Gases and Other Dielectrics," John Wiley & Son, New York, 1939.

Source code is as follows:

- | | | |
|--------------|---------------------|---------|
| A - Hydrogen | C - Carbon monoxide | E - Air |
| B - Water | D - Carbon dioxide | |

* For convenience, the acetylene flames obtained for various amounts of oxygen may be classified into four groups, each determined from certain obvious characteristics. They are:

- (1) Complete combustion at inner cone. This is the welding type of flame (approximately 50 percent oxygen).
- (2) A second cone apparent with just a trace of yellow (approximately 30 percent oxygen).
- (3) A brilliant, white flame (10 percent oxygen approximately).
- (4) A diffusion flame, all acetylene and much smoke (no oxygen).

THE DEVELOPMENT OF A PRACTICAL CHARGE DISSIPATOR

TABLE I (Continued)

Ionization Potential (Electron Volts)	Ion or Reaction	Source [†] (see footnotes for meaning of symbols)
34.7	$C^+ + O^+$	C
34.?	$H_2O \rightarrow H_2^+ + O^-$	B
33.3	$CO^+ + O^+$	D
33.2	$N^+ + N^+$	E
33.0	$O_2 \rightarrow O^+ + O^-$	E
31.4	$2H^+$	A
28.3	$C^+ + O + O$	D
26 ± 1	$H^+ + K.E.$	A
24.0	$C + O$	C
22.9	$N^+ + N$	E
22.2	$C^+ + O^-$	C
20.5	O^+	E
20.5	$C^+ + O$	C
20.4	$CO^+ + O$	D
20.0	$CO_2 + CO_2^+ \rightarrow 2CO + O_2^+$	D
19.6	$CO^+ + O^+$	D
19.2	$H^+ + OH^+$	B
18.8	$H_2^+ + O^+$	B
17.9	H^+	A
17.9	H_3^+	A
17.3	OH^+	B
15.9	H_2^+	A
15.65	N_2^{++}	E
15.5	$CO^{++} \rightarrow C + O^{++}$	C
15.3	$CO_2^+ \rightarrow C + O^+ + O$	D
14.4	CO_2^+	D
14.1	CO^+	C
13.0	H_2O^+	B
12.9	$CO_2^+ \rightarrow C^+ + O + O$	D
12.5	O_2^{++}	E
12.2	$CO_2^{++} \rightarrow C + O^{++} + O$	D
9.5	$CO^- \rightarrow C + O^-$	C
9.4	$CO^+ \rightarrow C + O^+$	C
7.5	$N_2^+ \rightarrow N^+ + N$	E
7.5	$O_2^+ \rightarrow O^+ + O$	E
7.1	$CO^+ \rightarrow C^+ + O$	C
6.6	$H_2O^- \rightarrow OH^+ + H^-$	B
5.8	$CO_2^+ \rightarrow CO^+ + O^+$	D
4.2	$CO_2^+ \rightarrow CO^{++} + O^+$	D
2.5	$CO^{++} \rightarrow C^{++} + O^{++}$	C
2.2	$CO_2^{++} \rightarrow CO^+ + O^{++}$	D
-0.8?	$CO_2^{++} \rightarrow C^{++} + O + O$	D
-2.3?	$CO_2^{++} \rightarrow CO^{++} + O$	D
-9.3	$CO_2^{++} \rightarrow C^+ + O^+ + O^+$	D
-11.5	$CO_2^{++} \rightarrow C^+ + O^+ + O$	D
-17.3	$CO^{++} \rightarrow C^+ + O^+$	C
-18.7	$CO_2 \rightarrow CO^+ + O^+$	D

It is seen from the above that many different kinds of ions may be formed from the constituents of the acetylene flame. The ease with which they are formed is indicated by the ionization potential given in each case. Although expressed in volts, the ionization potential actually represents an energy being equal to the work acquired by an electron in falling through that potential difference. If inelastic collisions are assumed, it is apparent that for considerable ionization the electric gradient must be such that the potential drop over a distance of one mean-free-path of the ionizing particle possessing one electronic charge, must be roughly equal to the ionization potential required for that reaction.*

It should be kept in mind, however, that mass spectrography measurements are necessarily made at very low pressures and that the ionic production may not be directly comparable to that occurring for the pressures at which the flame discharger would operate. Nevertheless, the mass spectrographic analysis is the best that is available at the present and should serve as a satisfactory working guide.

Desirable Properties of the Discharger Flame

Now, whereas the ions discussed above could be produced as a result of an intense electric field literally tearing the molecules to pieces, just the opposite should obtain if a flame is to discharge silently large quantities of electricity; that is, a copious supply of ions should be present to neutralize any intense field which might tend to develop. In the reference by Glockler and Lind is found the statement that, "flames undoubtedly are conducting and a separation of electrical charges accompany the reaction taking place in the flame. But ionization occurring in flames is most probably produced indirectly by the high temperature of the process, and it is not necessarily a primary act related to the intrinsic chemical change."

Even so, there seems to be some relationship between the electric field and the temperature of the flame. Other investigators† have found that the effect of the field was to reduce the flame temperature in all cases investigated. The greatest effect was found for lean mixtures and the smallest for rich mixtures. Thus, for ethylene the temperature lowering for a lean mixture was 116° and for a rich mixture only 12° . These same investigators found that a low-temperature flame of carbon-disulfide vapor was unaffected by an electric field, but that a high-temperature flame of the same combustible vapor was deflected toward the negative electrode as were the flames of all other combustibles investigated.

From the foregoing it seems fairly evident that the best type of discharger flame would be one possessing a very high flame temperature. The flame temperatures of several different combustibles as given by Lewis and Von Elbe are tabulated in Table 2.

The hottest flame shown in Table 2 is the oxygen-diluted 44 percent acetylene flame. Nevertheless, there are certain advantages to be gained if an air-diluted flame could be made to perform satisfactorily, since the need for oxygen storing and regulating equipment is then obviated. Butane and isobutane fuels seem particularly desirable because of the very small ratio of fuel-to-air that may be used to give the desired flame temperature. The chief objection to an air-diluted flame that has been observed so far is the inherent slow-burning velocity of the flame which leaves it susceptible to the motion of the surrounding atmosphere. The velocity of propagation of the flames suitable for discharge use is, therefore, one of their most important properties and will now be briefly considered.

It should perhaps be pointed out at this time that the most likely source of radio interference from a flame discharge electrode is the very thin layer of unburned gas between the flame proper and the metal tip of the burner electrode. This narrow

*Actually, because of cumulative ionization and excitation, the necessary potential drop may be obtained over several mean free paths.

†Lewis and Krentz, Journal of American Chemistry Society, Vol. 55, p. 934, 1933.

TABLE II
Flame Temperatures of Combustibles

Combustible	Dilutent	Percent Combustible	Flame Temperature °C.
Hydrogen	Air	31.6	2045
	O ₂	67.0	2487
		78.0	2660
Hydrogen atoms			3760*
Carbon monoxide	Air	20.0	1650
		32.0	2100
		55.0	1560
	O ₂	20.0	1850
		70.0	2925
Methane	Air	10.0	1875
Ethane	Air	5.8	1895
Propane	Air	4.15	1925
Butane	Air	3.2	1895
Iso-butane	Air	3.2	1900
Acetylene	Air	9.0	2325
	O ₂	18.0	2927
		44.0	3137
		50.0	2927
Ethylene	Air	7.0	1975
Propylene	Air	4.5	1935
Butylene	Air	3.4	1930
Mixed coal gas	Air	17.6	1918

*Estimated for hydrogen torch by Langmuir. Included here only for comparison.

region of gas serves somewhat as an insulator, and if it is sufficiently thick will suffer dielectric breakdown when the flame is subjected to an electric field. Accompanying this breakdown is radio interference of great severity. This effect was observed for slow-burning fuels in air. Fortunately, it was found that the oxyacetylene flame burned with such a high velocity (1,100 feet per second) that apparently intimate contact between the flame and burner tip results. Furthermore, because of the very high burning velocity the speed of the gases leaving the orifice may be made very great with the result that the motion of the surrounding atmosphere has but little effect upon the inner cone of the flame.

It was felt that an experimental determination of the external wind velocity required to extinguish the acetylene flame would be of much more significance than the more theoretical determinations based on the burning velocity of the mixture. Through the generous assistance of the Department of Mechanical Engineering of this college, an automotive-type supercharger driven by a variable-speed d-c motor was made available to supply very large quantities of air with a high velocity. The velocity of the air-stream at the exhaust nozzle was calculated from measurements made on the rate of air intake as well as traverse readings taken with an impact tube.

When the burner electrode was placed in line with the air stream, air velocities

of greater than 300 miles per hour (maximum speed available) did not extinguish the flame because of the shielding effect exhibited by the electrode itself. Attention was then focused upon the velocity of the cross wind required to extinguish the flame, and it was found that velocities of more than 300 miles per hour could be successfully withstood provided the oxygen content of the flame was increased slightly above that of a neutral mixture.

Observations were also made with the flame directed into the air blast. In several cases the flame was extinguished with an air velocity of approximately 150 miles per hour. Inasmuch as the torch was operating at only three or four pounds pressure in each of these cases, it was thought that the flame was perhaps being extinguished by the large impact pressure of the high velocity air striking the burner tip and literally preventing the gas from leaving the orifice. This was definitely shown to be true, for when the oxygen and acetylene pressure feeding the torch was doubled, the blowout velocity increased to 254 miles per hour.

This completes the discussion of the physical features of the flame discharger. The results of studies made of its electrical characteristics under still and moving air conditions will now be given.

Still-Air Characteristics of Flame Discharger

In the discussion to follow, the following terms will be used:

- Flame length: The visual length of the flame from the burner tip to the flame tip when examined in a darkened room against a black background.
- Flame spacing: The perpendicular distance between the plane electrode and the flame tip when viewed in a darkened room against a black background.
- Burner spacing: The perpendicular distance between the plane electrode and the burner tip.

In an effort to determine which part of the flame was most effective in contributing to the current discharge, an extensive series of tests was made on the discharge characteristics of flames of various length, each at several spacings. Voltage-current characteristics of neutral (Type 1) flames 2.5, 5.0, 7.5, and 10.0 inches in length were measured, each over a similar range of plane-to-flame spacings.

Typical characteristics for a positive and negative 2.5-inch flame are shown in Figures 47 and 48, respectively. Since, as shown in the next paragraph, each characteristic can be represented with sufficient accuracy by a single number, B, the many other characteristics taken for flames of other lengths will not be given here as they are identical in form to those of Figures 47 and 48.

An outstanding property of all voltage-current characteristics obtained for both positive and negative flames is that all characteristics when plotted on rectangular paper formed almost perfect parabolas. Furthermore, since the vertex of the parabola was at the origin, the same curves plotted on logarithmic curve paper become a straight line having a slope of two. Because of this rather unexpected property, all voltage-current characteristics could quite accurately be represented by the relation

$$I = AV + BV^2$$

where I is the discharge current and V is the voltage difference between the plate and the burner electrodes.

If now, the flame conductance is defined by $G = I/V$, it follows that

$$G = A + BV$$

and it is seen that the flame conductance is composed of two components; one component

FIGURE 47.
 CHARACTERISTIC V-I CURVES FOR 2.5-INCH POSITIVE FLAME.
 NO. 1 ACETYLENE WELDING HEAD

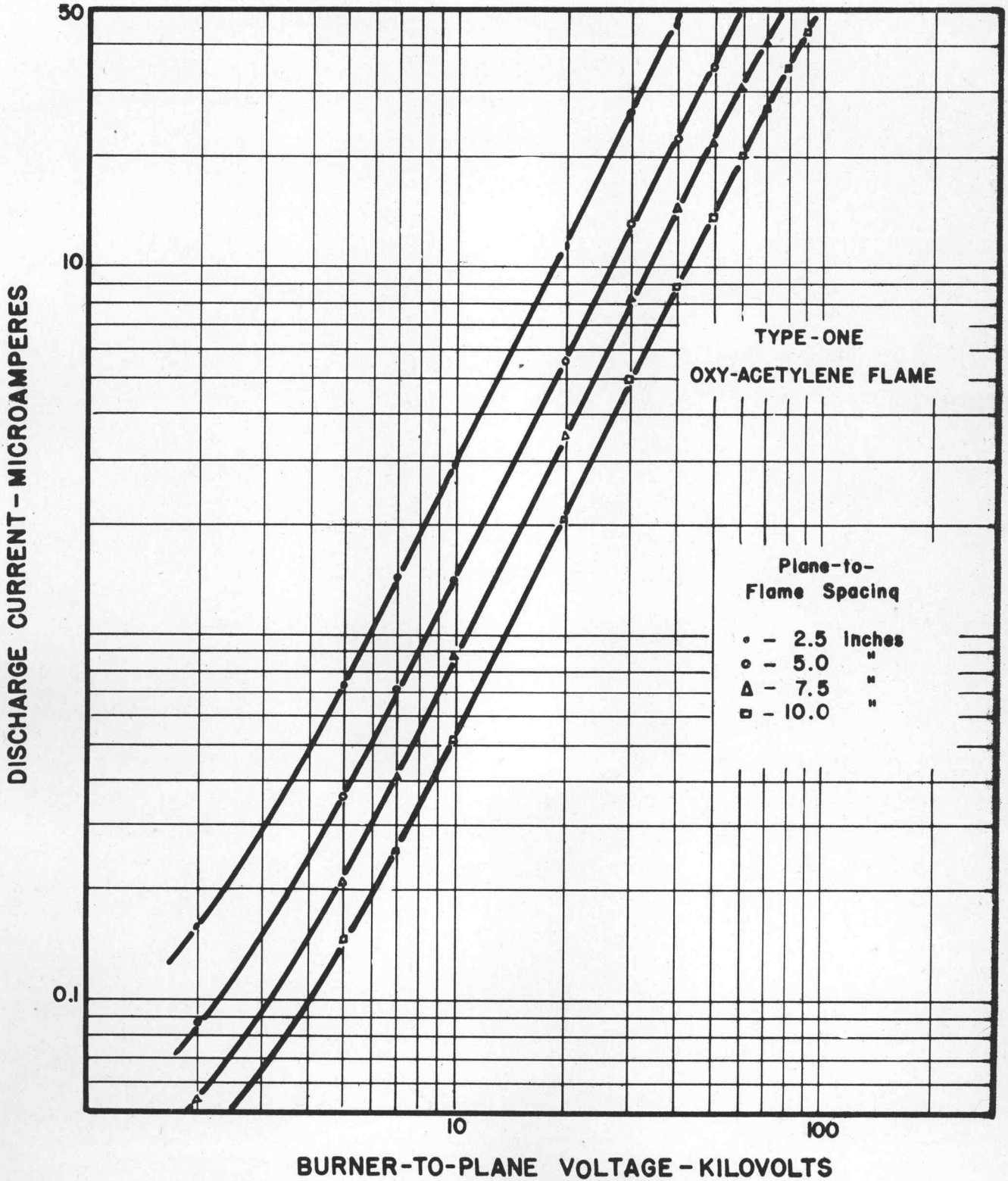
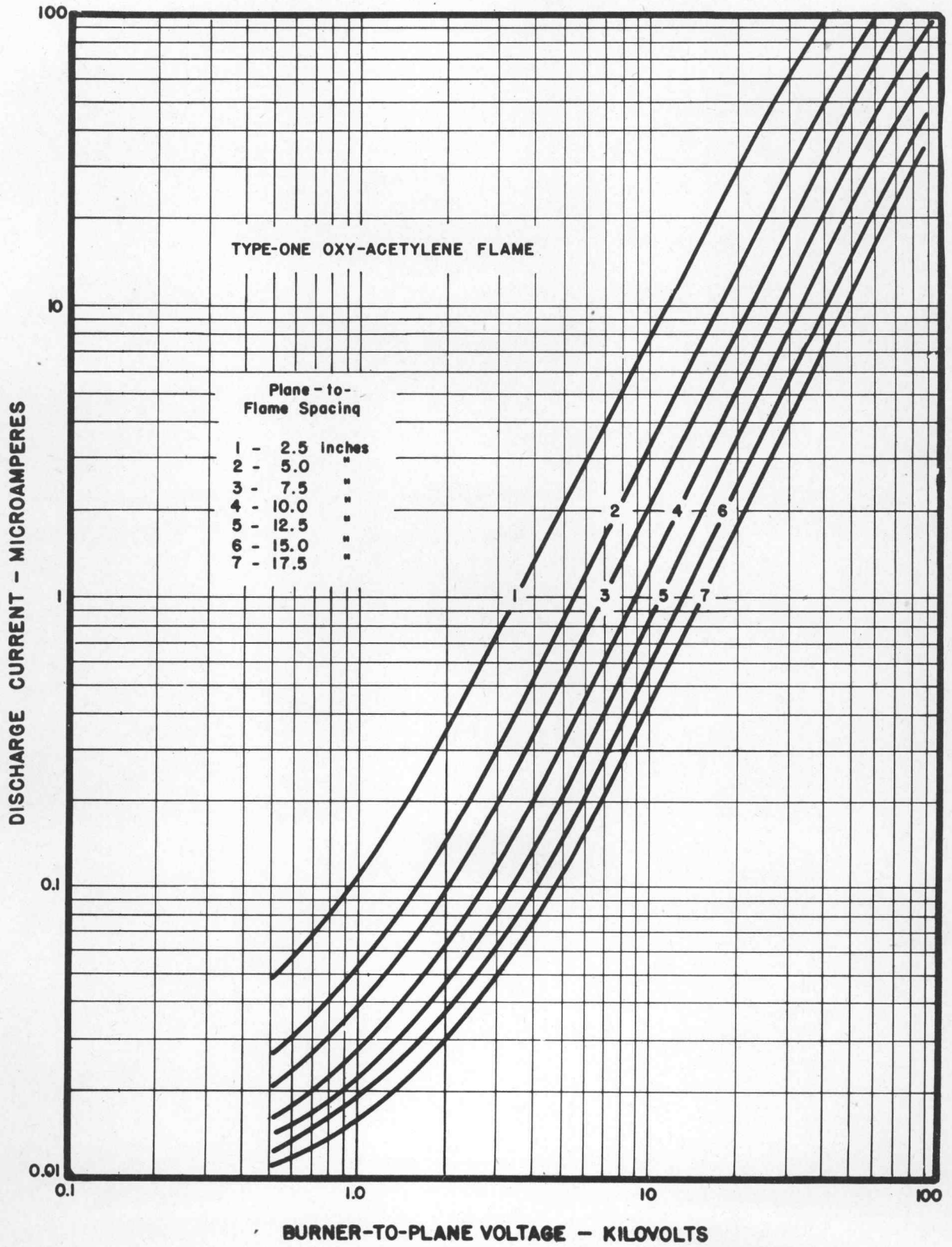


FIGURE 48
CHARACTERISTIC V-I CURVES FOR 2.5-INCH NEGATIVE FLAME.
NO. 1 ACETYLENE WELDING HEAD



which is constant, and a second component which varies directly with the applied voltage.

The A and B which best represent the G's obtaining for a given current-voltage characteristic may be calculated from the formulas,

$$A = \frac{\Sigma G \cdot \Sigma V^2 - \Sigma I \cdot \Sigma V}{N \Sigma V^2 - (\Sigma V)^2} \quad (5)$$

$$B = \frac{N \Sigma I - \Sigma G \cdot \Sigma V}{N \Sigma V^2 - (\Sigma V)^2} \quad (6)$$

where N is the number of experimental points taken along the characteristic. The values of A and B given by the above equations are those which yield the least error in the sense of least squares in predicting G. The same coefficient may be used in the equation predicting the current from the voltage, but in this case, the error in the current prediction will be weighted inversely as the voltage.

It was discovered that at the time these data were taken, there existed, unfortunately, a small leakage current through the insulation of the measuring equipment so that all current values recorded were consistently high by approximately 0.01 microamperes. It was observed that in most cases this correction would serve to straighten the voltage-current characteristics, such as those shown in Figures 47 and 48. This would indicate that the constant conductance, A, was needed only to account approximately for this leakage current, and that for all except the highest values of voltage, the true flame discharge current may quite accurately be represented by

$$I = BV^2 \quad (7)$$

where B may be calculated from the formula already given, and will hereafter be referred to as the second flame-conduction coefficient.

Effective Flame Center of Positive and Negative Flames

The use of the second flame-conduction coefficient, B, facilitates considerably the study of the effect of flame length, spacing, etc. In Figures 49, 50 and 51 these coefficients are shown as the function of flame length, flame spacing and burner spacing for the case of a positive flame. It is rather surprising that for the positive flame, the flame length, flame spacing and flame size have comparative little effect on the discharge currents. Indeed, it is found that the discharge current at a given voltage is determined chiefly by the spacing between the burner tip and the plate electrode. In other words, it is the apparent voltage gradient near the burner tip which determines the discharge current. On the other hand, the negative-flame conduction coefficient shown in Figures 52, 53 and 54 show definitely that for the negative polarity it is the flame spacing which is instrumental in controlling the discharge current.

By trial and error it was found that an effective flame center could be located such that the B's, when plotted as a function of the spacing between the high-voltage electrode and this effective flame center, would all group themselves into two curves, one for each polarity of flame. For the positive flame, this effective center was about 0.2 of the flame length from the burner tip, whereas for the negative flame the effective center was 0.6 of the flame length from the burner tip. The second flame-conduction coefficient as plotted against these effective spacings are shown in Figure 55.

From these data it may be deduced that the positive flame itself is rather a poor conductor, so that it is the electric field at the burner tip which determines the curve. In the case of the negative flame, the flame itself is a good conductor and it is therefore the spacing to the off-streaming gases which determines the discharge current. This is exactly the effect which would be expected if the ions in the flame are truly those listed in Table 1.

FIGURE 49.
 POSITIVE FLAME-CONDUCTION COEFFICIENT AS A
 FUNCTION OF FLAME LENGTH

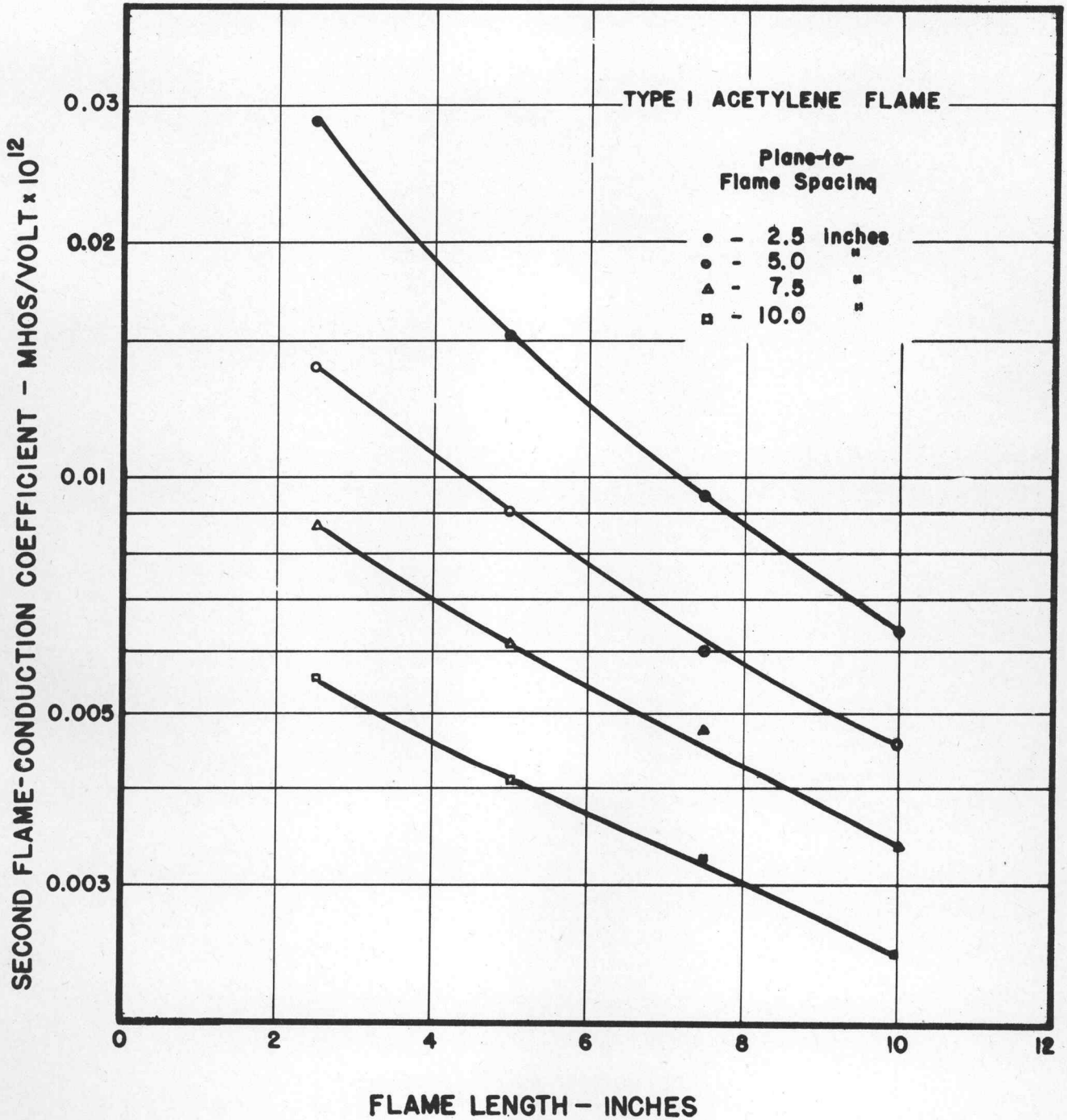


FIGURE 50.
 POSITIVE FLAME CONDUCTION COEFFICIENT AS A
 FUNCTION OF BURNER SPACING

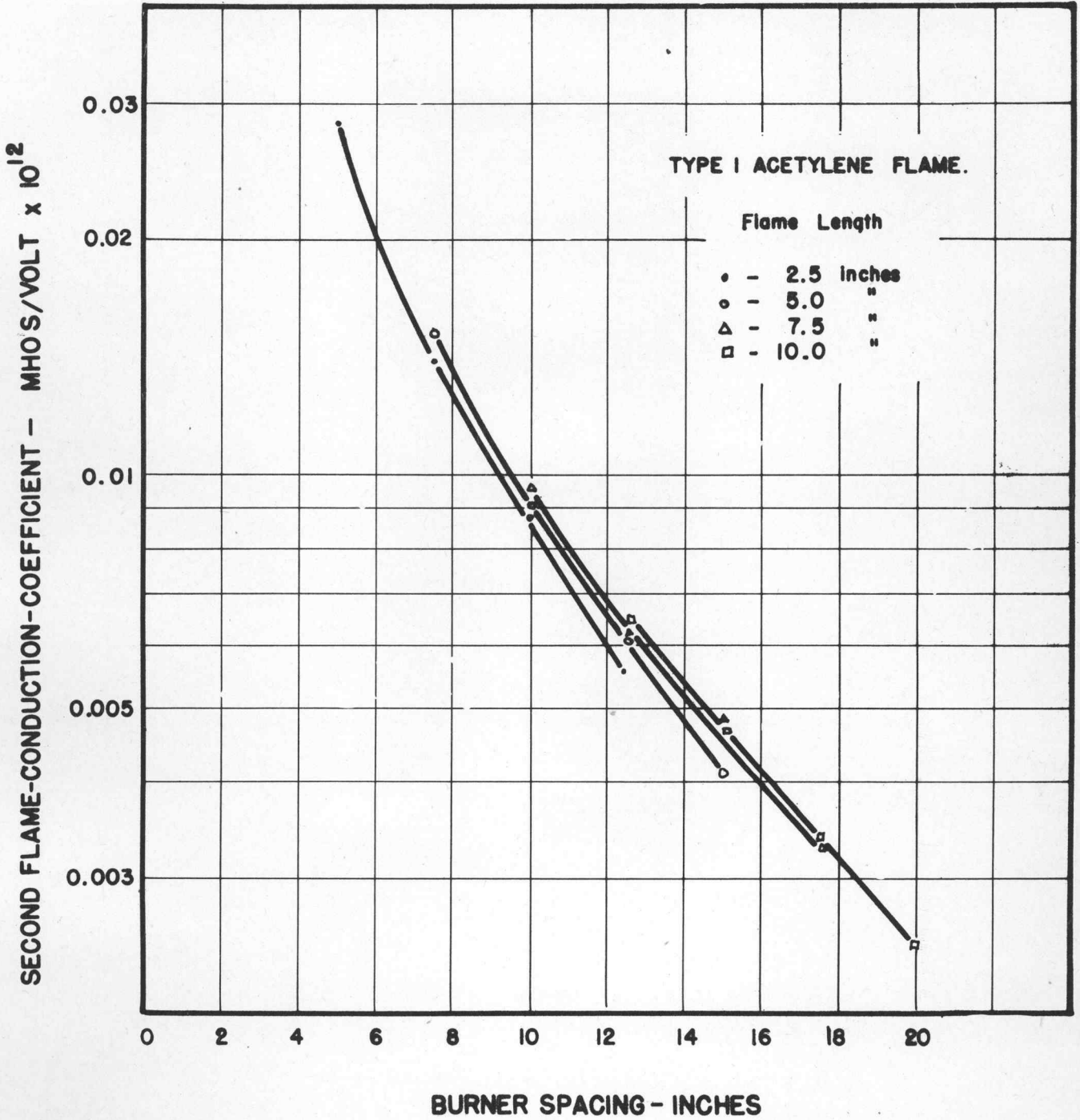


FIGURE 51.
 POSITIVE FLAME-CONDUCTION COEFFICIENT AS A
 FUNCTION OF PLANE-TO-FLAME SPACING

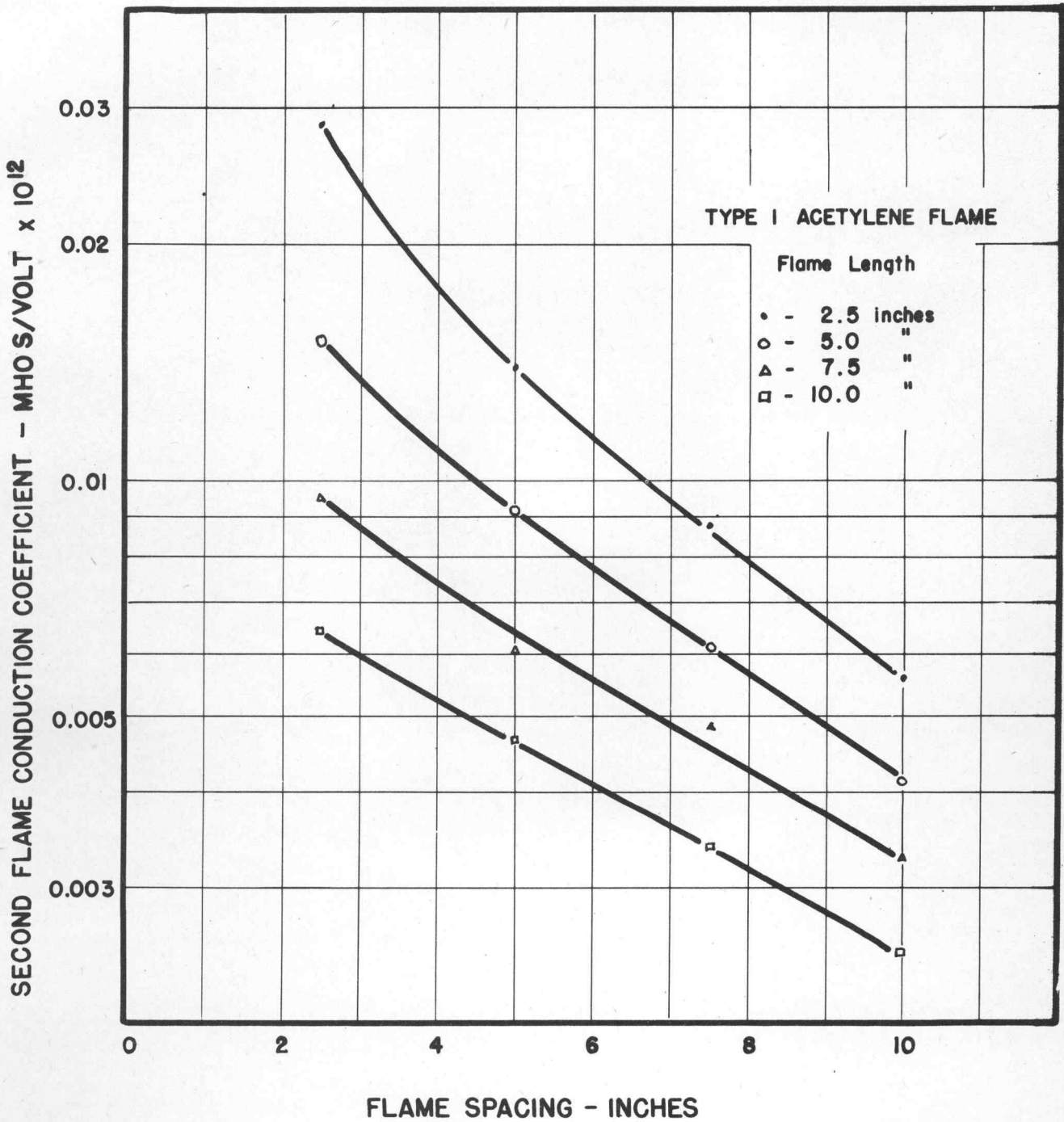


FIGURE 52
NEGATIVE - FLAME-CONDUCTION COEFFICIENT AS A
FUNCTION OF FLAME LENGTH

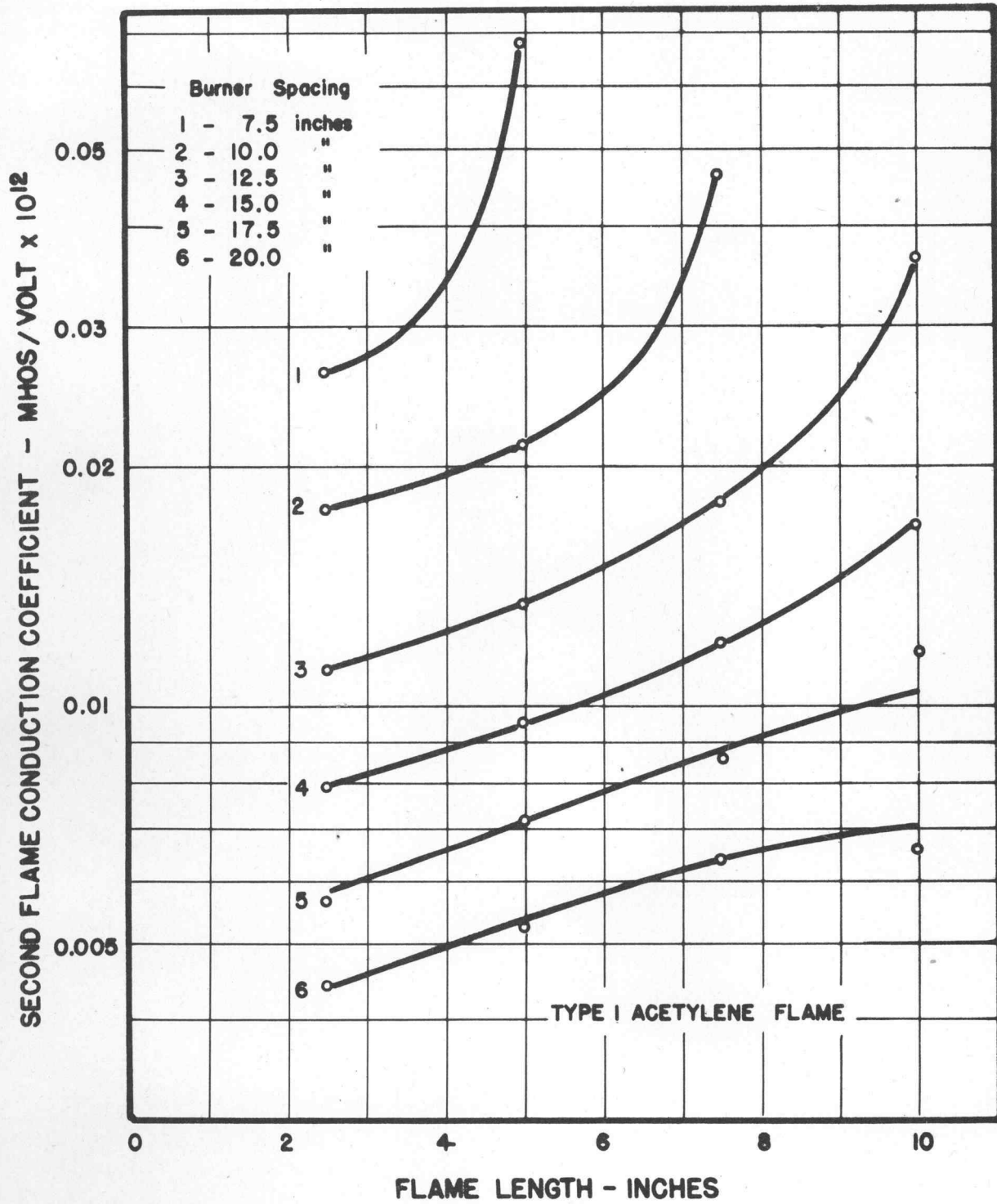


FIGURE 53
NEGATIVE-FLAME-CONDUCTION COEFFICIENT AS A
FUNCTION OF BURNER SPACING

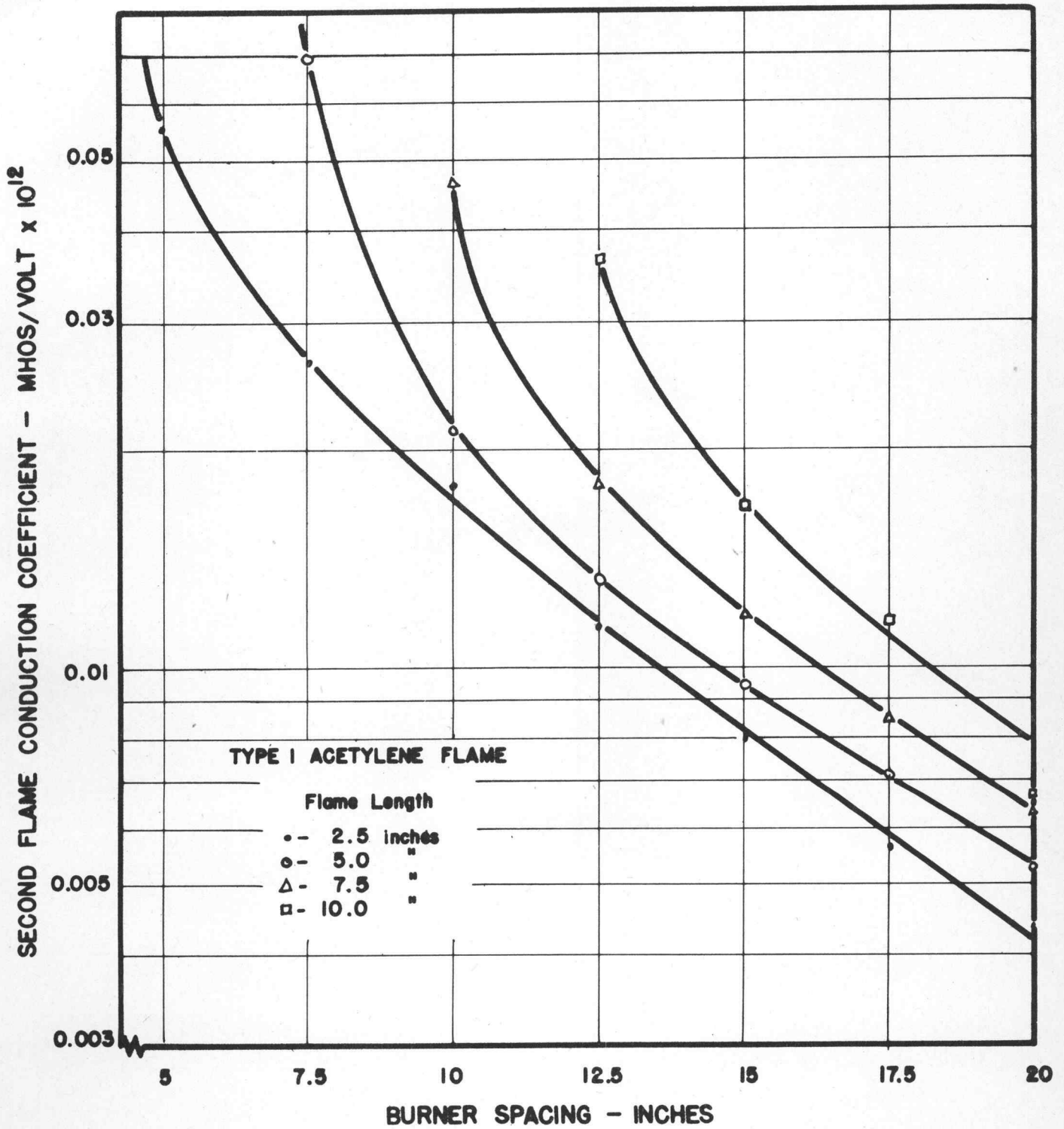


FIGURE 54
NEGATIVE-FLAME-CONDUCTION COEFFICIENT AS A
FUNCTION OF FLAME SPACING

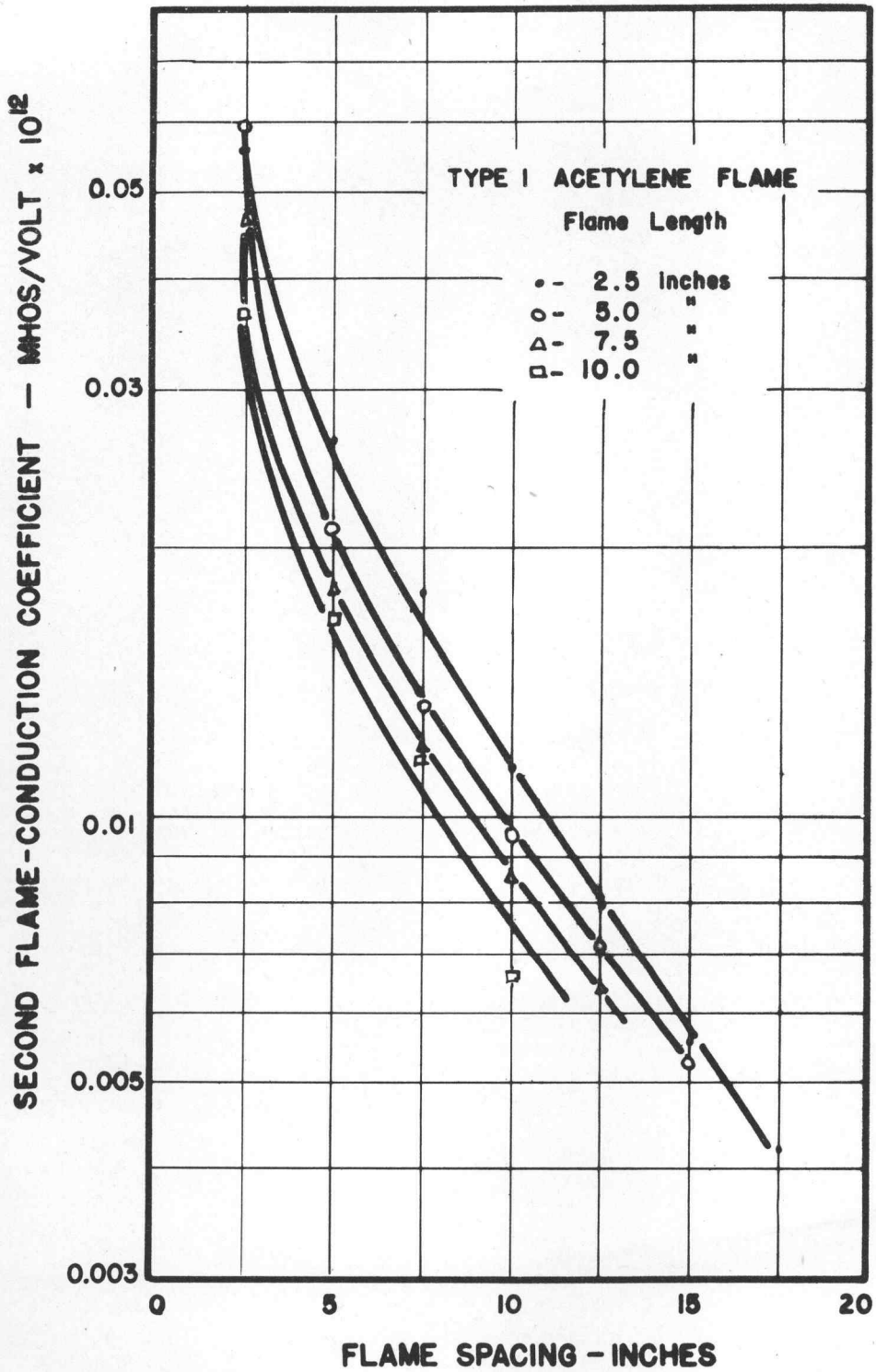
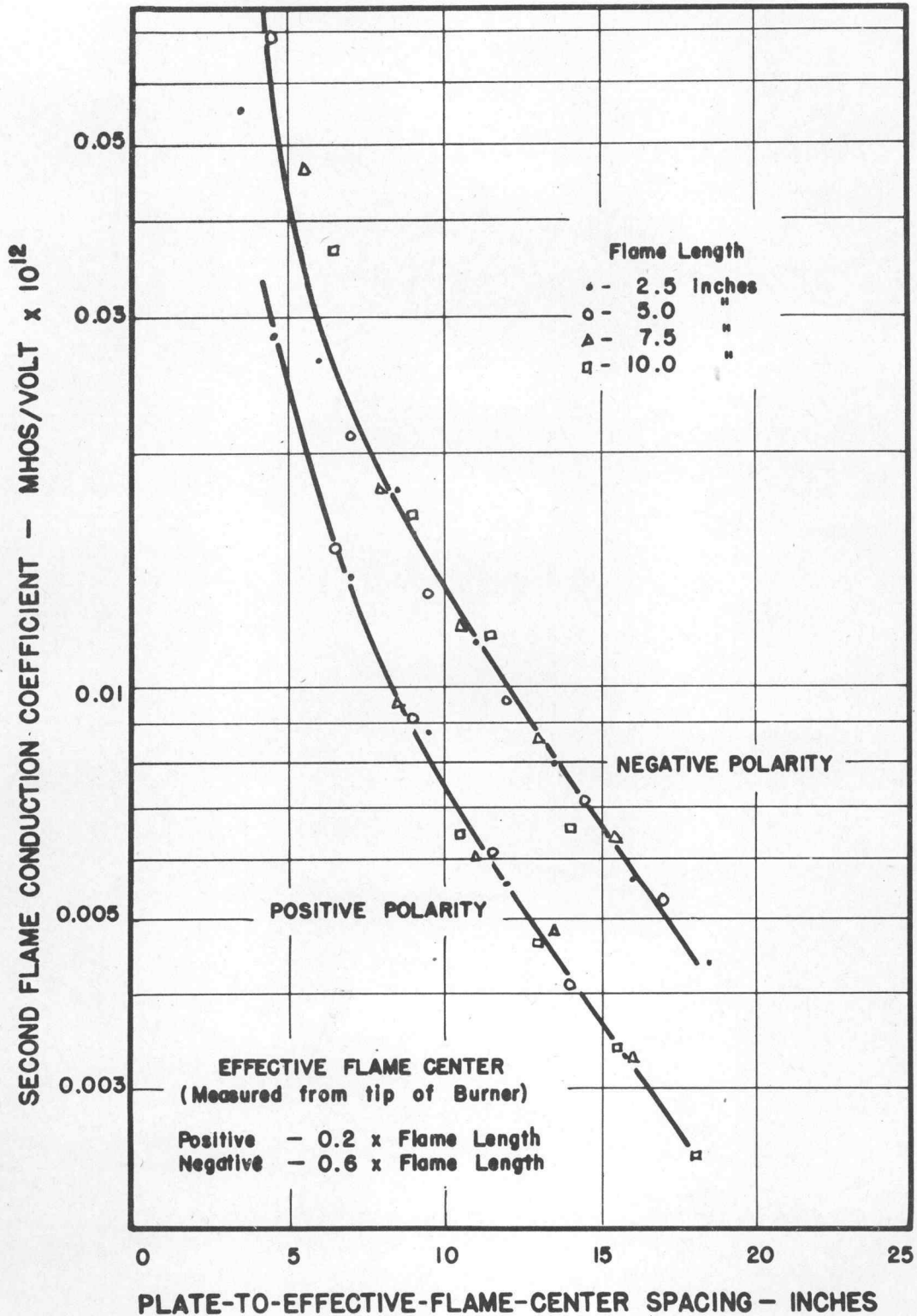


FIGURE 55
SECOND-FLAME-CONDUCTION COEFFICIENTS AS
FUNCTIONS OF EFFECTIVE-FLAME-CENTER SPACING FOR
TYPE I OXY-ACETYLENE FLAME



Effect of Space Charge on Flame Discharger

From the foregoing discussion, it is very apparent that the ionic space-charge must be of considerable importance in controlling the discharge from the flame. Accordingly an attempt will be made in this section to investigate the effect of the space charge on the flame V-I characteristic. While it is openly admitted that the analysis to follow is not exact, it is believed that it leads to results which resemble, however approximately, those actually obtaining and, provided its limitations are considered, it is of interest and value in understanding the basic factors influencing the flame-discharge phenomena.

Since the motion of all charges through space is comparatively slow, the problem is essentially one in electrostatics. It is known that the potential at any point in space around the flame must satisfy Poisson's equation

$$\nabla^2 V = \frac{\rho}{k_0} \quad (8)$$

where V is the potential in volts, ρ is the charge density in coulombs per cubic meter, and k_0 is the permittivity of free space equal to $1/(36\pi \times 10^9)$ farad/meter.

To set up the problem, it will be assumed that the flame and burner electrode may be represented by a paraboloidal surface of revolution, as may also the high-voltage electrode. Accordingly, by equation (17) of appendix I, equation (8) may be written as,

$$\frac{1}{2(u+v)} \left[\frac{\partial}{\partial u} \left(2u \frac{\partial V}{\partial u} \right) + \frac{\partial}{\partial v} \left(2v \frac{\partial V}{\partial v} \right) + \left(\frac{1}{2u} + \frac{1}{2v} \right) \frac{\partial^2 V}{\partial w^2} \right] = \frac{\rho}{k_0} \quad (9)$$

Some radical assumptions must now be made. First, it will be assumed that $\frac{\partial V}{\partial v} = 0$ and

$\frac{\partial V}{\partial w} = 0$, so that paraboloidal equipotentials and lines of flow will be maintained. Then,

$$\frac{\partial}{\partial u} \left(2u \frac{\partial V}{\partial u} \right) = \frac{2\rho(u+v)}{k_0} \quad (10)$$

But if $\frac{\partial V}{\partial v} = 0$, $2\rho(u+v)$ must be a constant in v. Therefore, as a second radical assumption let $2\rho(u+v) = q$, a constant, giving as a solution to (10) the equation,

$$V = \frac{q}{2k_0} u + C_1 \ln u + C_2 \quad (11)$$

Now, it is necessary to satisfy the boundary conditions. Let the flame reaction zone have an inner boundary u_0 and an outer boundary u_s , and let the high-voltage electrode be represented by the parabolic surface u_p . It will be assumed that for ionization to occur, the potential at the outer surface of the flame reaction zone must be ΔV greater than that of the inside surface. If the potential of the inside surface is taken as zero, there then exists the following conditions:

$$\begin{array}{ll} \text{For } u = u_0, & V = 0, \\ u = u_s, & V = \Delta V \\ u = u_p, & V = V_p \end{array}$$

where V_p is the voltage applied to the high-voltage electrode. If the arbitrary constants of (11) are determined to satisfy the first and last of the above boundary conditions, there results:

$$V = \frac{q}{2k_0} (u - u_0) + \frac{\ln(u/u_0)}{\ln(u_p/u_0)} \left[V - \frac{q}{2k_0} (u_p - u_0) \right] \quad (12)$$

The condition for ionization must now be incorporated. It is that V must equal ΔV when $u = u_s$. If the potential is less than this amount, there will be no ionization and consequently $q = 0$ so that the potential at any point will be

$$V = V_p \frac{\ln(u/u_0)}{\ln(u_p/u_0)} \quad (13)$$

In particular, at the bounding condition just before ionization begins,

$$\Delta V = V_{p,s} \frac{\ln(u_s/u_0)}{\ln(u_p/u_0)} \quad (14)$$

where $V_{p,s}$ indicates the potential of the high-voltage electrode at the instant ionization commences. But when the space charge has established itself, by equation (12),

$$\Delta V = \frac{q}{2k_0} (u_s - u_0) + \frac{\ln(u_s/u_0)}{\ln(u_p/u_0)} \left[V_p - \frac{q}{2k_0} (u_p - u_0) \right]. \quad (15)$$

Equating these two expressions gives, after some rearrangement,

$$V_p - V_{p,s} = \left[\frac{q}{2k_0} (u_p - u_0) - (u_s - u_0) \frac{\ln(u_p/u_0)}{\ln(u_s/u_0)} \right]. \quad (16)$$

The charge density q must now be estimated. Consider a paraboloidal surface lying between the flame and the high-voltage electrode. At any point, the current density through this surface would be $K \text{ grad}(V)$, where K is the mobility of the ions forming the space charge. Accordingly, $di = K \text{ grad}(V) \cdot dA$, or in terms of the paraboloidal coordinates,

$$\begin{aligned} di &= \frac{K q}{2(u+v)} \cdot \frac{\partial V}{\partial u} \frac{u}{u+v} \cdot 2\sqrt{u(u+v)} \, dv \, dw \\ &= \frac{K q u}{u+v} \cdot \frac{\partial V}{\partial u} \, dv \, dw. \end{aligned} \quad (17)$$

In evaluating $\frac{\partial V}{\partial u}$, the effect of the space charge will be neglected. This approximation, which unfortunately may produce considerable error in the result, is necessary to avoid a complicated quadratic expression in q . Also, it will be assumed that all space charge flows within the paraboloidal boundary, v_0 . The total current flow will therefore be

$$\begin{aligned} I &= K q \frac{V_p}{\ln(u_p/u_0)} \int_0^{v_0} \int_0^{2\pi} \frac{1}{u+v} \, dw \, dv \\ &= 2\pi q K V_p \frac{\ln(1+v_0/u)}{\ln(u_p/u_0)}, \end{aligned}$$

$$\text{or } q = \frac{I \ln(u_p/u_0)}{2\pi K V_p \ln(1+v_0/u)}. \quad (18)$$

From (18), if q is to be independent of u and v , it is apparent that v_0/u must be constant. That is, as one recedes from the flame (source) the outer boundary of the area through which all space charge is assumed to pass increases in such a manner to maintain the ratio v_0/u constant. Although this conclusion is inconsistent with the original assumption that $\frac{\partial V}{\partial v} = 0$, such a spreading action very likely occurs due to the mutual repulsion between the ions in the space charge. By combining equations (18) and (16) there is obtained,

$$V_p(V_p - V_{p,s}) = \frac{I \ln(u_p/u_0)}{4\pi k_0 K \ln(1+v_0/u)} \left[(u_p - u_0) - (u_s - u_0) \frac{\ln(u_p/u_0)}{\ln(u_s/u_0)} \right]. \quad (19)$$

Equation (19) might be used to represent the discharge characteristic from any paraboloidally shaped object. For example, a steel needle can be represented quite accurately by a small- u_0 paraboloidal surface. The surface u_s would then be at its closest point a known number of ionizing free paths from the tip of the needle, and $V_{p,s}$ would be the onset potential needed to produce a potential ΔV along u_s , this being the necessary condition for self-sustaining corona. Obviously, the equation is only valid for potentials V_p greater than $V_{p,s}$.

However, in the case of current discharge from an oxyacetylene flame, no onset potential could be observed because current flow would commence for even the smallest of applied voltages. This would indicate that for a flame, $V_{p,s}$ was zero, so that equation (19) can be written as

$$I = \frac{4\pi k_0 K \ln(1 + v_0/u)}{\left[(u_p - u_0) - (u_s - u_0) \frac{\ln(u_p/u_0)}{\ln(u_s/u_0)} \right] \ln(u_p/u_0)} \cdot v_p^2 \quad (20)$$

But the empirical relationship, $I = BV^2$, was observed in the foregoing section, so that now by comparing this relationship with equation (20), an equation for the second flame-conduction coefficient B is obtained.

If furthermore, it is assumed that within the limits of accuracy of the expression, both u_s and u_0 are negligible as compared to u_p , there results

$$B = 11.11 \times 10^{-12} K \frac{\ln(1 + v_0/u)}{u_p \ln(u_p/u_0)}$$

Although this equation is far from being exact because of the many approximations involved in its derivation, it is interesting that it gives results which are at least of the same magnitude as those obtained experimentally.

This equation indicates that the second flame conduction coefficient should be proportional to the mobility of the ions forming the space charge around the flame. Typical ion mobilities for air are $K_- = 2.25$, and $K_+ = 1.46$ cm²/volt-sec, giving a ratio of the negative to positive mobilities of 1.54. From the data Figure 55 it is observed that for a given effective spacing (i.e., the spacing between the equivalent flame center and high voltage electrode) the ratio of negative to positive flame-conduction coefficient is roughly 1.7. The presence of the CO₂ and water vapor in the air surrounding the flame could perhaps account for the greater ratio should the theoretical value be of sufficient accuracy to be significant. Even though the many approximations made during the development of this equation prevent it from being a truly accurate expression for B, a numerical example will now be given to show that the expression at least checks in magnitude with the experimental results. The equation will be used to estimate the B for a positive, 2.5-inch oxyacetylene flame, with a burner spacing of 7.5 inches.

Physical considerations lead one to believe that most of the space-charge flow occurs within a very definite, bounded region outside of which very little space charge would be found. Thus, an ion leaving the flame would normally travel straight to the high voltage electrode along the shorest route possible; that is, the flame axis. However, due to diffusion of the ions and the nonlinearity of the electric field and space-charge gradient, the ions upon reaching the high-voltage electrode will have spread out into a circle of diffusion.

Now, although no effort was made to measure the circle of diffusion for the ions, a similar effect was observed during the study of a fluid-spray discharger in which minute particles of fluid were sprayed from a nozzle toward a high-voltage plane electrode, 20 inches away. By examining the condensation of the fluid upon the high-voltage electrode it was observed that apparently all the fluid particles struck the high-voltage electrode within a circle of one-foot radius. Furthermore, it appeared that the radius of the circle of diffusion was directly proportional to the spacing between the nozzle and high voltage electrode. This being the case, the radius of the circle of diffusion for a spacing of 7.5 inches would be approximately 4.5 inches. In the absence of other information it seemed entirely reasonable to accept this radius of 4.5 inches as that which would also result from ion flow. Then, if the effective flame center is taken as the origin, from the relations derived in appendix 1, the physical configurations may be represented by

$$\begin{aligned} \frac{v_p}{u_p} &= \frac{-1 + \sqrt{1 + (y_p/u_p)^2}}{2} \\ &= \frac{-1 + \sqrt{1 + (4.5/7)^2}}{2} = 0.0944 \end{aligned}$$

where u_p is the spacing of the plane electrode, y_p is the radius of the circle of diffusion at the plane electrode, and v_p is the paraboloidal surface passing through this circle of diffusion.

It is estimated that the shape of the flame and particularly the burner electrode is equivalent to the paraboloidal surface, the u of which is equal to 0.1 cm. Substitution of these values into the equation for B gives

$$\begin{aligned} B &= 11.11 \times 10^{-12} \cdot \frac{(1.46) \ln(1.0944)}{(17.78) \ln(17.78/0.1)}, \quad (22) \\ &= 0.016 \times 10^{-12} \text{ mhos/volt.} \end{aligned}$$

In comparing this value with 0.014×10^{-12} , which was observed experimentally for the same conditions as that calculated, it is seen that a reasonable agreement is obtained between theory and experiment.

Fortunately, it is possible to estimate the charge density and space potential even though $K \ln\left(1 + \frac{v}{u}\right)$ is not known. By combining equations (18) and (21) there may be derived the relation

$$q = 2k_0 \frac{V_p}{u_p} \quad (23)$$

But since $q = 2(u + v)\rho$, the space-charge density is

$$\rho = \frac{0.884 \times 10^{-12}}{u + v} \cdot \frac{V_p}{u_p} \text{ coulombs/cc.} \quad (24)$$

Finally, by combining equations (12), (23), and (7), there results

$$V = V_p \left[\frac{u - u_0}{u_p} + \frac{u_0}{u_p} \cdot \frac{\ln(u/u_0)}{\ln(u_p/u_0)} \right], \quad (25)$$

$$\text{Grad } V = \sqrt{\frac{u}{u + v}} \cdot V_p \left[\frac{1}{u_p} + \frac{1}{u} \cdot \frac{u_0}{u_p \ln(u_p/u_0)} \right]. \quad (26)$$

The potential distribution for $V_p = 50$ kilovolts as calculated from equation (25) is shown in Figure 56 for comparison with the space charge free distribution. The uniformity of the gradient resulting from space-charge accumulation should be especially noted.

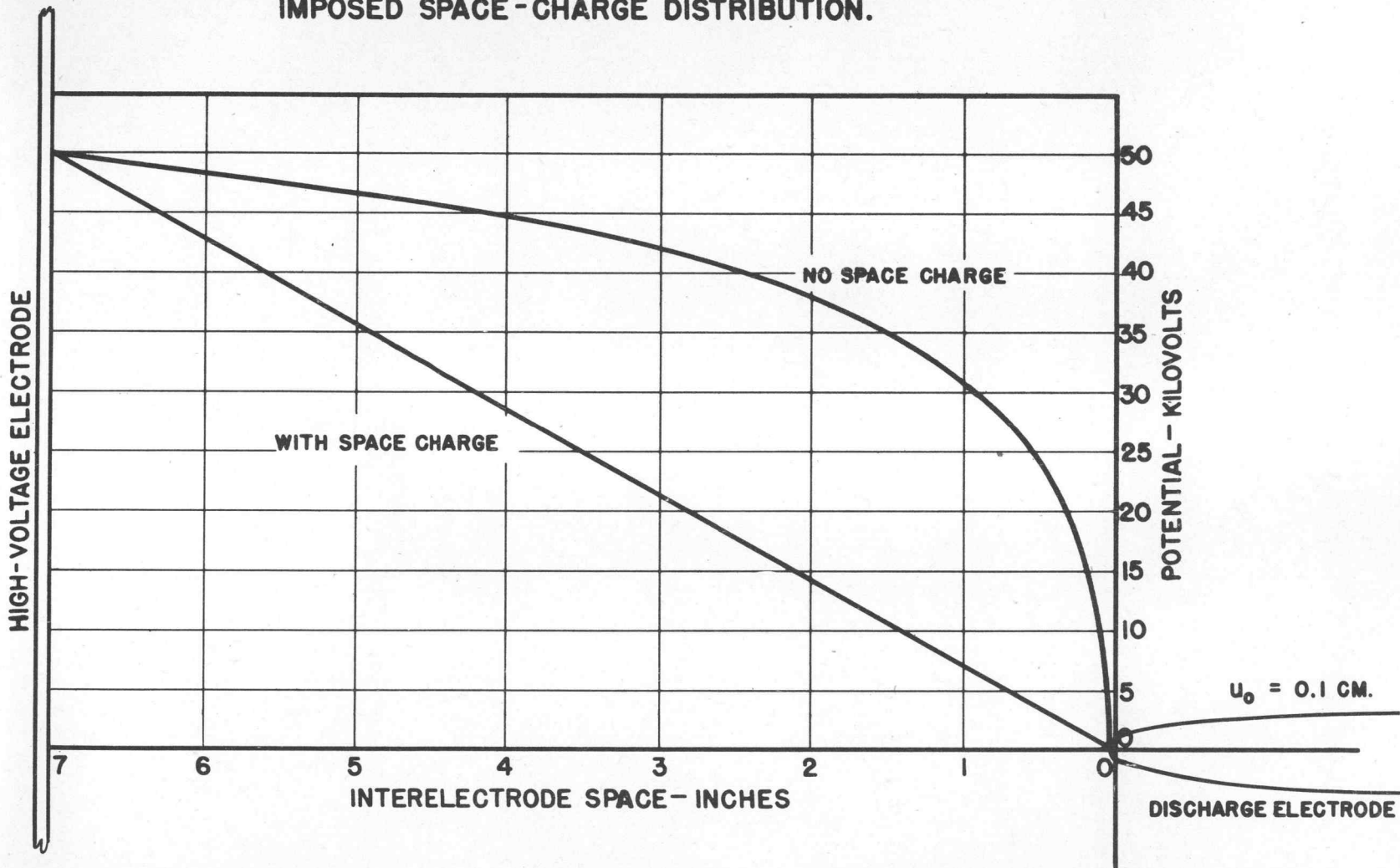
Thermal Ionization

In previous chapters, ionization by electron collision has been emphasized. However, in the flame discharger, other sources of ionization must be present for the analysis of the preceding section indicates that space gradients near the flame are most likely quite small. This, together with the absence of an onset potential, indicates that a supply of ions must exist independently of the electric field. It might be well to review, then the other possible mechanisms of ionization in the oxyacetylene flame.

Ionization by positive ion collision is very unlikely because of the very large energies necessary. However, positive-ion bombardment of the metal electrode may release electrons from the surface.

A much more likely mechanism is ionization by radiation or so-called photoionization. The radio activated discharger discussed in Chapter X utilized this source of

FIGURE 56.
CALCULATED POTENTIAL ALONG CENTRAL AXIS FOR
IMPOSED SPACE-CHARGE DISTRIBUTION.



preionization. Ionization will occur if the $h\nu$ of the photon is greater than the ionization energy, eV_1 , of the gas molecules. Furthermore, the probability of the photoionization is proportional to the intensity of the light and also depends upon its frequency. When it is recalled that the oxyacetylene flame burns with an intensely blue light, it would seem very probable that photoionization must be an important source of ions in the flame.

The term "thermal ionization" is applied to the general processes of ionization occurring in a high-temperature flame. It includes all of the aforementioned processes as well as the ionizing action of molecular collisions. At the high-flame temperature, all particles move with greatly increased velocity, some particles or atoms gaining sufficient velocity to produce ionization or at least excitation by inelastic collision with other particles.

Saha¹² has made the most successful analysis of these complex phenomena by assuming a completely reversible, thermo-dynamic process involving a homogeneous gas of monatomic molecules each capable of becoming only a singly ionized atom. If p is the total pressure in atmosphere, V_1 is the ionization potential in the volts, T is the temperature of the gas in degrees Kelvin, and x is the relative concentration of singly ionized atoms expressed as a fraction of the original concentrations of atoms in the gas; then the relative ionization may be calculated from

$$\log_{10} \left[\frac{x^2}{1-x^2} p \right] = - \frac{5,050}{T} V_1 + 2.5 \log_{10} T \quad (27)$$

where V_1 is the ionization potential of the gas in volts.

In Figure 57 are shown curves calculated from equation (27) for $T = 3,137^\circ \text{C}$, temperature of the oxyacetylene flame. These curves give the relative ionization produced in a gas having an ionization potential V_1 when heated to $3,137^\circ \text{C}$. It is tacitly assumed in equation (26) that the electron density is equal to the positive ion density. In the presence of an electric field, space charges would form so that this equality is not strictly justified. However, in view of the other approximations which have been made thus far, the assumption of equal positive ion and electron densities in the flame reaction zone is probably acceptable.

Fortunately, by using the formulas developed in the preceding section, the ion concentration needed to supply the discharge currents observed experimentally may be calculated and conclusions may be reached as to whether or not thermal ionization is of major importance in the flame discharger.

To use a 2.5 inch flame with a 7.5 inch burner spacing as an example, it was observed that for a positive, high-voltage-electrode potential of 50 kilovolts, a discharge current of 35 microamperes obtained. By equation (24)

$$\rho = 0.884 \times 10^{-12} \frac{V_p}{u_p (u + v)} \text{ coulombs/cc.}$$

Here, $u_p = 17.78 \text{ cm}$ and $V_p = 50 \text{ kilovolts}$. At the reaction zone of the flame, it is estimated that $u = 0.2$ so that at the very tip of the cone (i.e., $v = 0$)

$$\rho = 0.884 \times 10^{-12} \frac{50 \times 10^3}{(17.78)(0.2)}$$

$$\rho = 0.01243 \times 10^{-6} \text{ coulombs/cc.}$$

But each ion ideally carries a charge of 1.6×10^{-19} coulombs. This represents a charge density of 7.768×10^{10} ions per cubic centimeter. Since by the perfect gas laws, the number of gas particles per cc at $3,137^\circ \text{C}$ is estimated to be 2.165×10^{18} particles per cc, the relative ion concentration is $77.68 \times 10^9 + 2.165 \times 10^{18}$ or 35.9×10^{-9} .

Substitution of this value of x in equation (27) and solution of the resulting expression for V_1 indicates that if the ionization potential of the gas were 11.6 volts,

FIGURE 57.
THERMAL IONIZATION IN OXY-ACETYLENE FLAME.

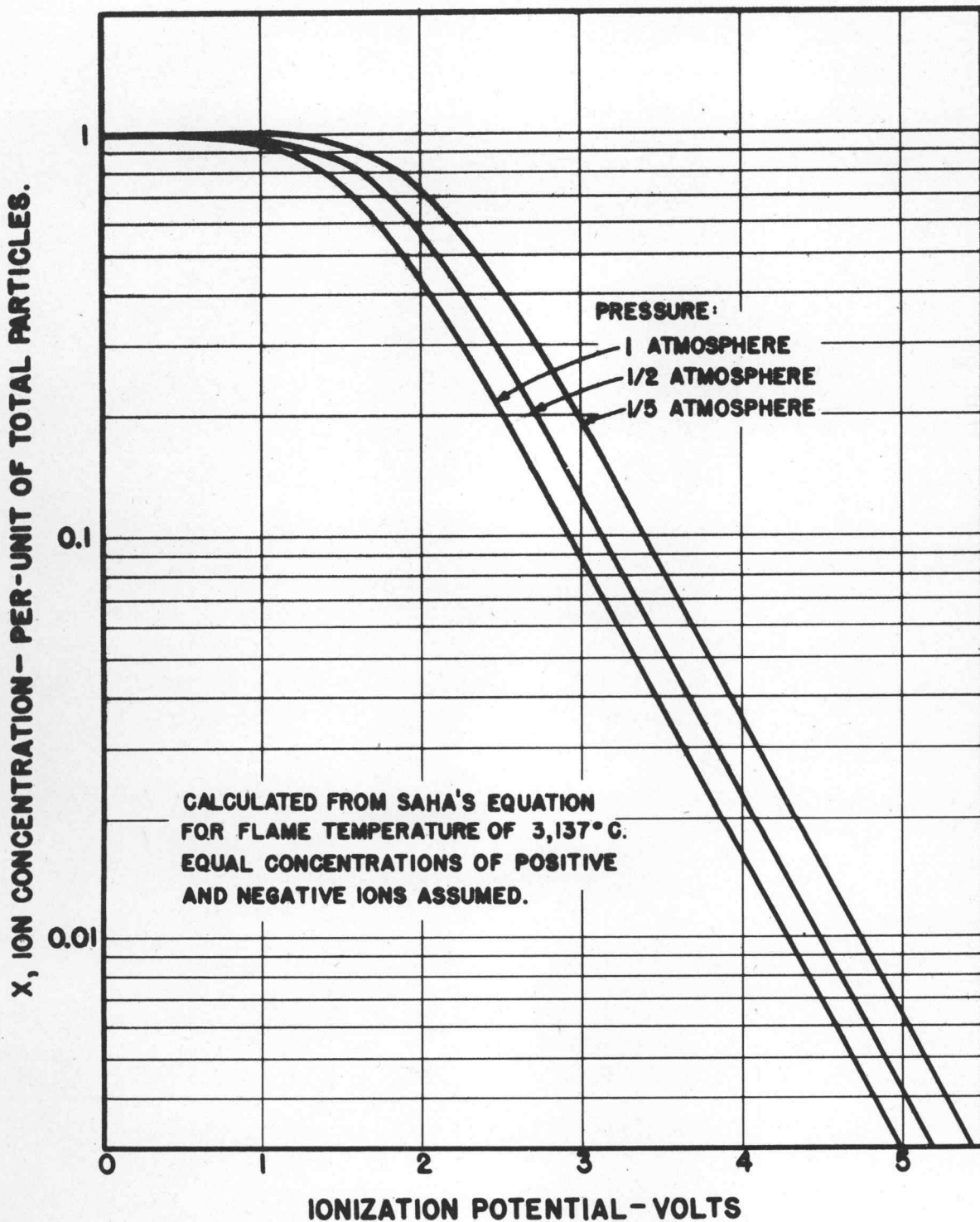


FIGURE 58.
 POSITIVE FLAME DISCHARGE CHARACTERISTIC IN WIND STREAM.

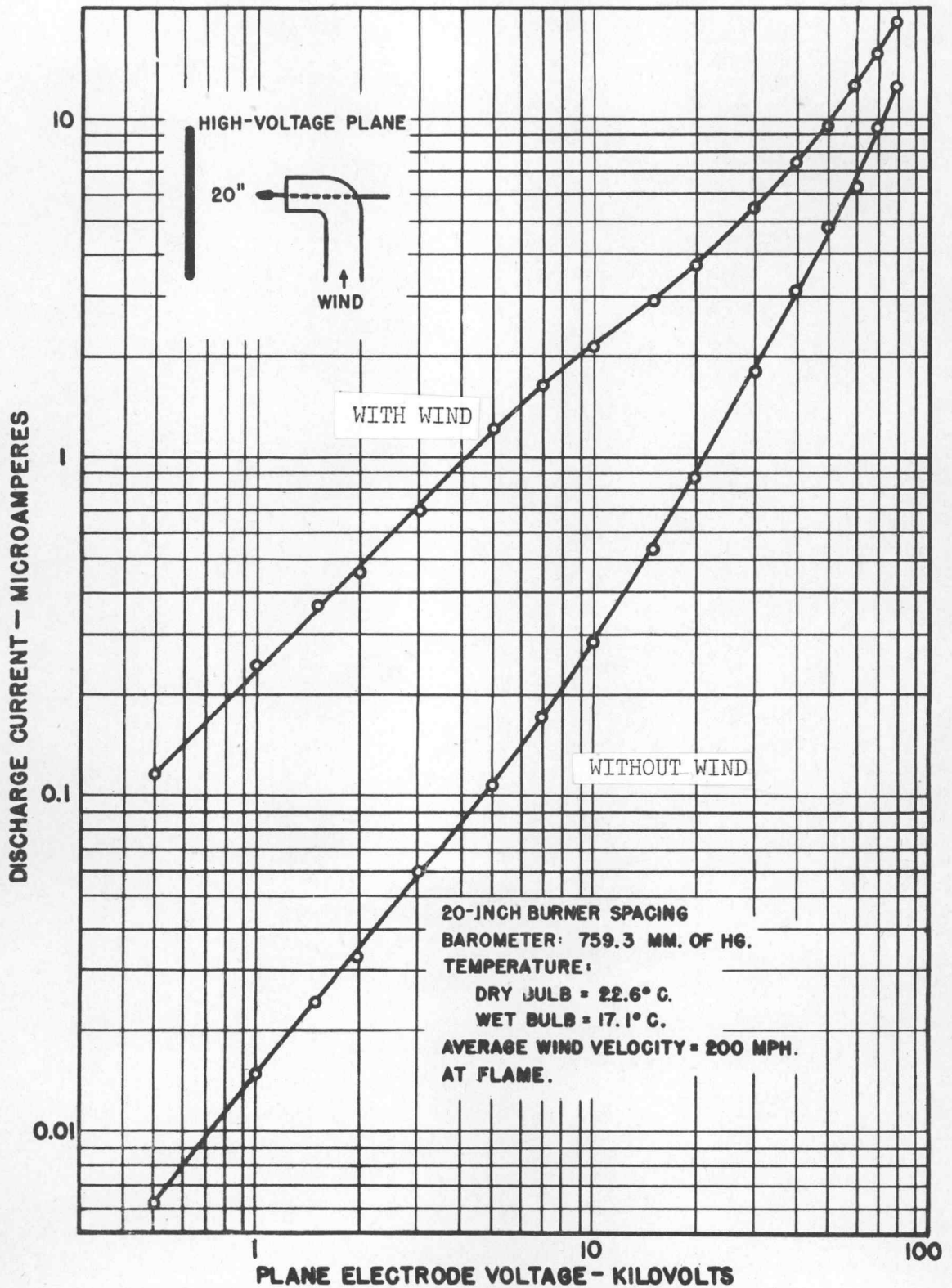
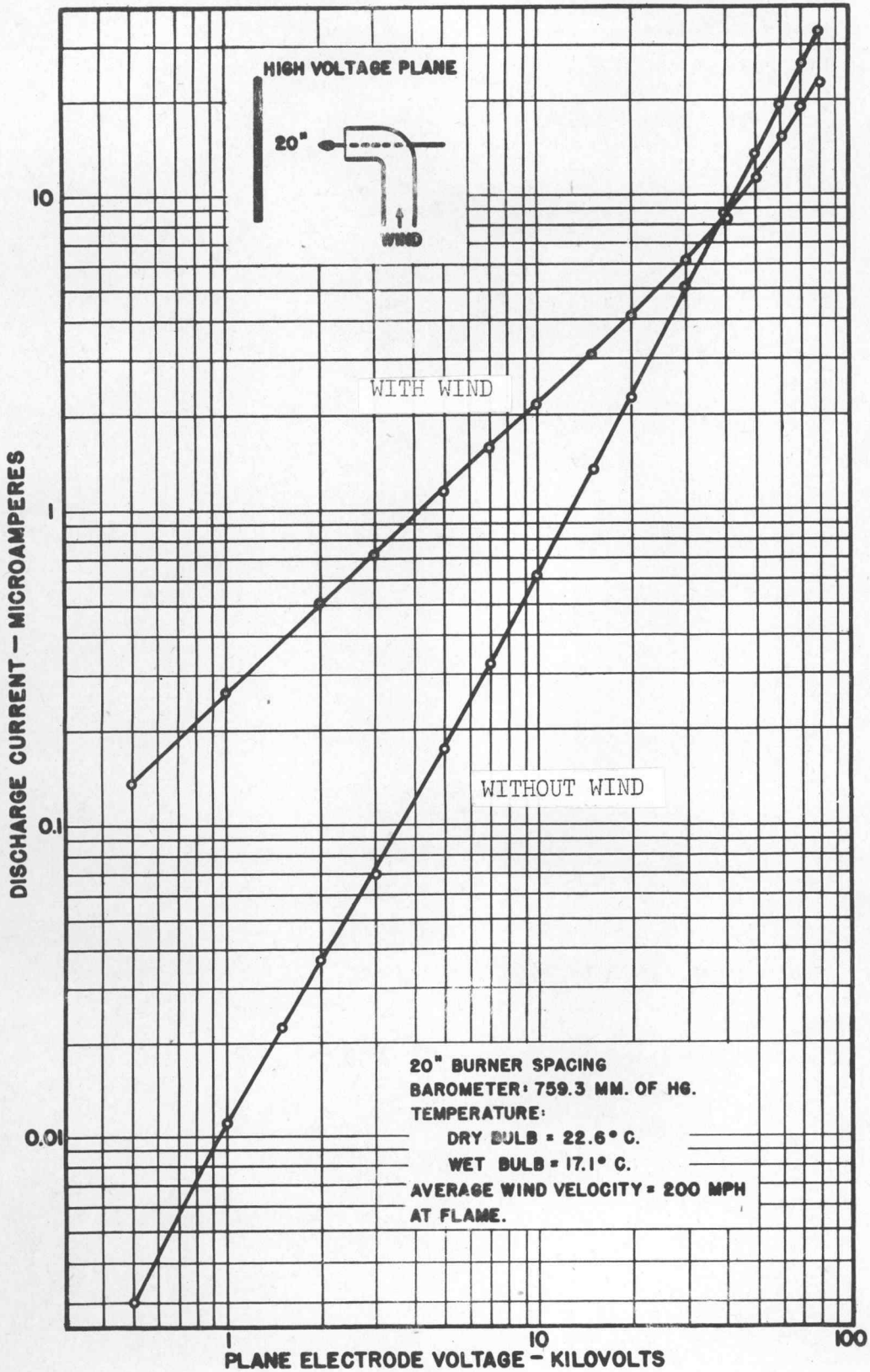


FIGURE 59.
NEGATIVE FLAME DISCHARGE CHARACTERISTIC IN WIND STREAM.



thermal ionization alone could provide sufficient charge to account for the observed discharge currents.

From Table 1 it is observed that the initial ionization of the various gas constituents occurs as follows:

O_2^+	-	12.5 volts
H_2O^+	-	13 volts
CO^+	-	14.1 volts
CO_2^+	-	14.4 volts
N_2^+	-	15.6 volts

In view of these data, it is almost certain that thermal ionization is the outstanding ionization process in the oxyacetylene flame discharger. It is indeed unfortunate that a gas mixture of higher flame temperature is not available. On the other hand, flames of a lower temperature, such as might be obtained from a mixture of acetylene and air, are all probably incapable of discharging a large amount of current without suffering high voltage gradients with resultant dielectric breakdown, corona, and radio interference.

Flame Discharge Characteristics in Moving Air Streams

If the discharge current from the flame is truly limited by a space-charge accumulation in the air around the flame, a moving air stream flowing through the region of space-charge accumulation should tend to reduce the space charge concentration and consequently increase the discharge current from the flame electrode.

The supercharger described in Chapter II was equipped with fittings whereby a wind stream of roughly 200 miles per hour could be directed past the burner electrode toward the high-voltage electrode which was located downstream at a distance of 20 inches from the burner tip. The oxygen and acetylene gas pressures were then adjusted to give a small flame of approximately 5 inches in length in still air the supercharger set into operation, and readings taken of the discharge current for a wide range of high-voltage-electrode potentials. The data resulting from these measurements are shown in Figures 58 and 59.

The high-velocity wind stream has two very interesting effects upon the discharge characteristics: first, the differences between the positive and negative discharge characteristics which were observed under still-air conditions are almost completely eliminated by the moving air stream. Exactly this effect would be expected on the theory developed in the preceding section because, for example, an electrode potential of 10 kilovolts would produce ion movements of roughly 80 miles per hour and negative ion movements of roughly 120 miles per hour, both with respect to the surrounding air molecules. But when the air molecules themselves are moving with an average velocity of 200 miles per hour, the positive and negative ion velocities with respect to the stationary electrode are 280 and 320 miles per hour respectively, and the difference in velocities due to the relative mobility of each is then negligible for all purposes.

The second interesting effect of the moving windstream upon the discharge characteristic is that the current varies directly with the high-voltage potential over the low-current range. No explanation for this effect is offered at this time.

APPENDICES

APPENDIX I

ELECTRIC FIELD AROUND A PARABOLOIDAL POINT

Derivation of Paraboloidal Coordinates

The form equation for the parabolas shown in Figure 8 is

$$y^2 = 4p(p + x) \quad \dots \dots \dots (1)$$

Let p be a variable u. Then

$$y^2 = 4u(u + x) \quad \dots \dots \dots (2)$$

or

$$2yy' = 4u$$

so the primitive differential equation representing all possible sets of parabolas is simply,

$$\begin{aligned} y^2 &= 2yy' \left(\frac{yy'}{2} + x \right) \\ &= y^2 y'^2 + 2xyy' \quad \dots \dots \dots (3) \end{aligned}$$

The differential equation for the orthogonal family is that having a slope everywhere the negative reciprocal of that appearing in (3), i.e.

$$y^2 = \frac{y^2}{y'^2} - \frac{2xy}{y'}$$

Upon rearranging,

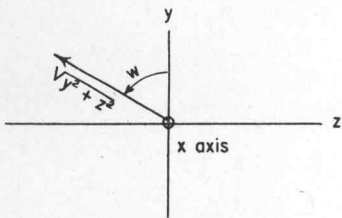
$$y^2 = y^2 y'^2 + 2xyy' \quad \dots \dots \dots (4)$$

But (4) is identical to (3). The difference between the two is that in (3), p is a positive quantity, while in (4) p is a negative number. Therefore, in order that all parameters will be essentially positive, for the solution of (4), let -p = v, so that

$$y^2 = 4v(v - x) \quad \dots \dots \dots (5)$$

Equations (2) and (5) constitute the two orthogonal families of parabolas.

To make surfaces of revolution from these curves, revolve them through an angle w about the x axis. Then,



$$y^2 + z^2 = 4u(u + x) \quad \dots \dots \dots (6)$$

$$y^2 + z^2 = 4v(v - x) \quad \dots \dots \dots (7)$$

Equating (6) and (7) gives,

$$u^2 + ux = v^2 - vx$$

or

$$x = v - u \quad \dots \dots \dots (8)$$

Substituting this into (6) and (7) and setting $y = \sqrt{(y^2 + z^2)} \cos w$, and $z = \sqrt{(y^2 + z^2)} \sin w$, gives:

$$x = v - u$$

$$y = 2\sqrt{(uv)} \cos w \quad \dots \dots \dots (9)$$

$$z = 2\sqrt{(uv)} \sin w$$

Equations (9) are the fundamental equations connecting the conventional Cartesian coordinates with the paraboloidal.

The Differential Geometry of Paraboloidal Coordinates

The relation between the differentials of the old coordinates and the new, is given by the Jacobian matrix, C.

$$C = \begin{array}{c} x \\ y \\ z \end{array} \begin{array}{|c|c|c|} \hline u & v & w \\ \hline -1 & 1 & 0 \\ \hline \sqrt{(v/u)} \cos w & \sqrt{(u/v)} \cos w & -2\sqrt{(uv)} \sin w \\ \hline \sqrt{(v/u)} \sin w & \sqrt{(u/v)} \sin w & 2\sqrt{(uv)} \cos w \\ \hline \end{array}$$

The covariant metric tensor is then, $g = C_t \cdot C$ or

$$g = \begin{array}{c} u \\ v \\ w \end{array} \begin{array}{|c|c|c|} \hline u & v & w \\ \hline (u + v)/u & 0 & 0 \\ \hline 0 & (u + v)/v & 0 \\ \hline 0 & 0 & 4 uv \\ \hline \end{array}$$

The fact that the g matrix is diagonal verifies the original statement that the paraboloidal coordinates constitute an orthogonal system.

In tensor notation, the elemental distance squared in terms of the new coordinates is,

$$ds^2 = g_{ij} \cdot dx^i \cdot dx^j \quad \dots \dots \dots \quad (10)$$

where summation is implied by the Einstein convention, and, for our case, the indices i and j range through u, v, and w. Similarly, the elemental area is,

$$d(\text{Area}) = \left| \begin{array}{cc} g_{11} & g_{1j} \\ g_{j1} & g_{jj} \end{array} \right|^{\frac{1}{2}} \cdot dx^i \cdot dx^j \cdot \dots \dots \dots \quad (11)$$

and the elemental volume is,

$$dV = \left| \begin{array}{ccc} g_{11} & g_{1j} & g_{1k} \\ g_{j1} & g_{jj} & g_{jk} \\ g_{k1} & g_{kj} & g_{kk} \end{array} \right|^{\frac{1}{2}} \cdot dx^i \cdot dx^j \cdot dx^k \quad \dots \dots \quad (12)$$

As examples of the above, the actual distance along a line of force corresponding to a change in u of du, is

$$ds = \sqrt{(u + v)/u} \, du \quad \dots \dots \dots \quad (13)$$

and the elemental area formed by the differentials dv and dw, is

$$dA = 2\sqrt{u(u + v)} \, dv \, dw \quad \dots \dots \dots \quad (14)$$

and the infinitesimal volume produced by the differentials dv, dw, and du, is

$$dV = 2(u + v) \, du \, dv \, dw \quad \dots \dots \dots \quad (15)$$

The Laplacian for the paraboloidal coordinates may be found from the metric equation,

$$\nabla^2 = |C|^{-1} \left[\frac{\partial}{\partial x^i} \right] |C| \cdot g^{ij} \cdot \left\{ \frac{\partial}{\partial x^j} \right\} \cdot \dots \dots \dots \quad (16)$$

Performing the operations indicated, one obtains

$$\nabla^2 = \frac{1}{u + v} \left[\frac{\partial}{\partial u} \left(u \frac{\partial}{\partial u} \right) + \frac{\partial}{\partial v} \left(v \frac{\partial}{\partial v} \right) + \left(\frac{1}{4u} + \frac{1}{4v} \right) \frac{\partial^2}{\partial w^2} \right] \cdot \quad (17)$$

Solution of Laplace's Equation for Arbitrary Potential Distribution over Point

Assuming space-charge-free conditions, the potential around the point must satisfy Laplace's equation, $\nabla^2 \psi = 0$, where ψ is the potential function. To solve this equation, set $\psi = UVW$ where each factor is a function only of the variables u , v , and w respectively. Direct substitution into (17) gives,

$$\frac{d}{du} \left(u \frac{dU}{du} \right) + \frac{d}{dv} \left(v \frac{dV}{dv} \right) + \left(\frac{1}{4u} + \frac{1}{4v} \right) \frac{d^2W}{dw^2} = 0 \quad \dots \dots \dots (18)$$

Now, when w changes through 2π radians, the potential function must return to its original value, so W must be essentially periodic in nature and of period some integral multiple of 2π . Therefore,

$$\frac{d^2W}{dw^2} = -m^2 \quad (m = \text{an integer}) \quad \dots \dots \dots (19)$$

or
$$W = A \cos mw + B \sin mw \quad \dots \dots \dots (20)$$

Equation (18) may now be written as

$$\left[\frac{d}{du} \left(u \frac{dU}{du} \right) - \frac{m^2}{4u} \right] + \left[\frac{d}{dv} \left(v \frac{dV}{dv} \right) - \frac{m^2}{4v} \right] = 0 \quad \dots \dots \dots (21)$$

But the two bracketed quantities are each independent, being functions of independent variables. Consequently, each bracketed quantity must be a constant. Setting the first bracketed quantity equal to k^2 and the second bracketed quantity equal to $-k^2$, gives the following ordinary differential equations.

$$\frac{d}{du} \left(u \frac{dU}{du} \right) - \left(k^2 + \frac{m^2}{4u} \right) U = 0 \quad \dots \dots \dots (22)$$

$$\frac{d}{dv} \left(v \frac{dV}{dv} \right) + \left(k^2 - \frac{m^2}{4v} \right) V = 0 \quad \dots \dots \dots (23)$$

Now let $4u = (x/k)^2$ and $4v = (y/k)^2$, (where the x and y should not be confused with that used in the earlier part of this analysis). Then the above equations become,

$$\frac{d^2U}{dx^2} + \frac{1}{x} \frac{dU}{dx} - \left(1 + \frac{m^2}{x^2} \right) U = 0 \quad \dots \dots \dots (24)$$

$$\frac{d^2V}{dy^2} + \frac{1}{y} \frac{dV}{dy} + \left(1 - \frac{m^2}{y^2} \right) V = 0 \quad \dots \dots \dots (25)$$

But from the theory of Bessel's Functions, equations (24) and (25) have as solutions,

$$V = C_1 J_m(y) + C_2 Y_m(y) \quad \dots \dots \dots (26)$$

$$U = C_3 I_m(x) + C_4 K_m(x) \quad \dots \dots \dots (27)$$

The physical conditions of the problem must now be examined to determine which of the functions in (26) and (27) may be used. Apparently, if the potential function is to be finite (or zero) as the variables become infinite, both C_2 and C_3 must be zero. Therefore the general form of the solution satisfying some of the requirements of the problem is,

$$\psi = \sum_{m=0}^{\infty} J_m(2k\sqrt{v}) \cdot K_m(2k\sqrt{u}) \cdot (A_m \cos mw + B_m \sin mw) \quad \dots \dots (28)$$

However, if it is further assumed that the distribution is independent of w , all arbitrary constants, except for $m = 0$, must be zero so that the potential will be a function only of u and v . Thus,

$$\psi_k(u,v) = A_k J_0(2k\sqrt{v}) K_0(2k\sqrt{u}) \dots \dots \dots (29)$$

Now, (29) is true for any real positive value of k. Therefore, the sum of any two solutions of the form (29) but having different values of k will also be a solution of (18); or more generally,

$$\psi(u,v) = \int_0^\infty A(k) J_0(2k\sqrt{v}) K_0(2k\sqrt{u}) dk \dots \dots \dots (30)$$

It remains to determine the function A(k) so that the potential boundary conditions are satisfied. This may be done by employing the "Fourier-Bessel Integral."

The Fourier-Bessel integral in the form that we wish to use it can be written as,

$$F(2\sqrt{v}) = \int_0^\infty \int_0^\infty k R F(R) K_m(kR) J_m(2k\sqrt{v}) dk dR \dots \dots \dots (31)$$

Now at the surface of the paraboloidal point, the potential function is assumed to be known and, being a function only of $2\sqrt{v}$, will be represented by $F(2\sqrt{v})$. If the surface of the point is given by $u = a$, the potential at the surface is also given by (30), so that equating the two functions results in,

$$F(2\sqrt{v}) = \int_0^\infty A'(k) J_0(2k\sqrt{v}) dk \dots \dots \dots (32)$$

where $A'(k) = A(k) K_0(2k\sqrt{a})$.

By comparing (31) with (32), one sees that they will be equivalent if,

$$A'(k) = \int_0^\infty k R F(R) J_0(kR) dR \dots \dots \dots (33)$$

and $m = 0$.

That is,

$$A(k) = \frac{k}{K_0(2k\sqrt{a})} \int_0^\infty R F(R) J_0(kR) dR \dots \dots \dots (34)$$

and the unknown function A(k) appearing in (30) has now been expressed in terms of the known potential distribution F(R), where $R = 2\sqrt{v}$, over the surface of the point.

To summarize, while it has been shown that it is possible to solve for the field around the point if the potential distribution over its surface is known, the mechanical difficulties encountered in a numerical solution would be tremendous. It is therefore to our advantage to sacrifice some generality for simplicity in mathematical expression, provided that the restricted solution still applies to the problem on hand. Such a simple solution is actually available and will now be considered.

Solution of Laplace's Equation for Equipotential Point

If the point is a conductor, it will represent an equipotential surface, and the potential becomes a function of u alone, since $\frac{dV}{dv} = 0 = \frac{dW}{dw}$. Accordingly, equation (18) may be written as,

$$\frac{d}{du} \left(u \frac{dU}{du} \right) = 0$$

or

$$U = C_1 \log u + C_2 \dots \dots \dots (35)$$

Equation (35) is the general form of the potential function having paraboloidal equipotentials. Designating the point equipotential by u_0 , and the "plane-electrode" equipotential by u_2 ; and if the potential "V" is zero on u_0 and E on u_2 , then the arbitrary constants appearing in (35) are readily determined to give,

$$V = E \frac{\log(u/u_0)}{\log(u_2/u_0)} \dots \dots \dots (36)$$

The gradient may be found from (36) by differentiation, thus

$$\text{Grad } V. = X = \frac{E}{u \log (u_1/u_0)} \sqrt{\frac{u}{u+v}} \dots \dots \dots (37)$$

The radical factor ($\sqrt{\text{reciprocal of } g_{uu}}$) is introduced to express the gradient in terms of the actual distance rather than the u variable.

Capacitance between Confocal Paraboloidal Shells

The capacitance between two paraboloidal shells given by the surfaces, u_0 and u_1 , which extend from $v = 0$, (the tip of the shell), to $v = v_1$; will next be studied.

Now, the total charge stored in the capacitance may be found from

$$Q = \int_S \sigma dA \dots \dots \dots (38)$$

where σ = surface charge density given by $4\pi\sigma = \epsilon X$, X being the electric field intensity at the surface of the point. By (14) and (37), equation (38) becomes,

$$\begin{aligned} Q &= \int_S \frac{\epsilon X}{4\pi} dA \\ &= \frac{E\epsilon}{4\pi \log (u_1/u_0)} \int_0^{2\pi} \int_0^{v_1} \frac{1}{\sqrt{u(u+v)}} \cdot 2\sqrt{u(u+v)} dv dw \dots \dots (39) \end{aligned}$$

$$= \frac{E\epsilon}{\log_e (u_1/u_0)} v_1 \dots \dots \dots (40)$$

But the capacitance is

$$\frac{Q}{E} = C = \frac{\epsilon v_1}{\log_e (u_1/u_0)}$$

Therefore,

$$C = 111.3 \frac{v_1}{\log_e (u_1/u_0)} \text{ } \mu\text{fds. in air} \dots \dots (41)$$

APPENDIX II

DETERMINATION OF EQUIVALENT-CIRCUIT PARAMETERS

Calculation of Capacitance

The point shown in Figure 8 was assumed to have a radius of curvature of 0.01 cms and to be spaced 9.99 cms. from the "plane" electrode, represented by the parabolic surface, $u = 10$. Furthermore, it was assumed that the space charge (which in reality is distributed) would be equivalent to a layer of charge concentrated on the parabolic surface, $u = 0.5$ cm, extending from the vertex at $v = 0$ to $v = 0.5$ cm. The various surfaces may then be summarized as follows:

$u_0 = 0.01$ cm	Point surface
$u_1 = 0.5$ cm	Space-charge shell
$u_2 = 10$ cm	"Plane" electrode
$v_0 = 0$ cm	Shortest line-of-flow
$v_1 = 0.5$ cm	Line-of-flow passing through edge of space charge
$v_2 = 4.5$ cm	Estimated outer boundary of plane and point, to be equivalent to point-to-plane laboratory set-up.

These values, when substituted into equation (41) of Appendix I, gave the point-to-plane-to-space-charge capacitance values shown in Figure 9. The capacitance (1.2 mmfd) shunting the point resistance was estimated, as was also the plane-to-ground capacitance of 20 mmfd. This latter value includes the input capacitance of the oscilloscope used in obtaining the oscillograms shown on the same page.

Calculation of Conductance

The problem of estimating the gap conductance was a rather difficult one because the conductance is apparently a function of the applied voltage.

Gradient calculations indicated that ample point discharge could be expected by the time the applied voltage had increased sufficiently to give a space-charge-shell-to-point voltage of 1,000 volts. This value was accordingly taken as the corona-point voltage. Since the gradient in the gap was then known, the time required for a positive ion to move from the space-charge shell to the "plane" could be readily estimated.

The gap conductance was then arbitrarily specified as that conductance which in parallel with the space-charge-to-plane capacitance would give a time-constant, (C/G) , equal to the time required for the positive ions to reach the plane electrode. Trial calculations for several conditions indicated that 2×10^{-9} mhos, (500 megohms), was not an unreasonable value for this parameter.

APPENDIX III

ANALYSIS OF EQUIVALENT NETWORK

Classification of Network

The properties of the equivalent network which may be used in studying the inductive effects of point discharges, are as follows:

- (1) All of the circuit parameters are linear and known.
- (2) The network is chiefly electro-static and should therefore be analyzed in terms of admittances on a "junction-pair" basis. The network admittance may be designated by the tensor (matrix), Y .
- (3) One (or more) of the admittances is assumed to change instantaneously by the amount ΔY .
- (4) The network is "orthogonal" in that across some of the junction-pairs, known currents (usually zero) and unknown voltages appear; whereas across others (such as the high-voltage power supply), the voltage is known and the current unknown.

The above 4 properties would be common to almost any equivalent circuit used to study voltage-induction effects. These circuits could be much more complicated; for example, there might be other plane electrodes (some corresponding to radio antennas, clouds, etc.), and several constant-voltage sources (used to represent cloud-to-ground potentials). However, the 4 properties above would be common to all, so it would be very valuable for future use if the general solution for all such networks could be given. This may actually be accomplished through the tensorial (or matrix) methods described by Kron,⁸ and the general invariant solution will now be developed.

Invariant Solution of General Network

The solution of any linear, stationary, junction network may be obtained from the basic, matrix equation

$$I = Y E \quad \dots \dots \dots (1)$$

Across some of the junctions, a known voltage is impressed (with an unknown current resulting). Across the other junctions, a known current (usually zero) is caused by impressing an unknown voltage. The former type of junction-pairs and their associated electrical quantities will be designated by the subscript "1"; the latter type by the subscript "2". Then equation (1) may be divided into two invariant equations according to the above distinction.

$$I_1 = Y_{11}E_1 + Y_{12}E_2 \quad \dots \dots \dots (2)$$

$$I_2 = Y_{21}E_1 + Y_{22}E_2 \quad \dots \dots \dots (3)$$

where I_2 , (usually zero), and E_1 are known.

Now, if Y changes suddenly by ΔY ; I_1 will change by ΔI_1 ; E_2 by ΔE_2 ; and all other currents and voltages will remain unchanged. Thus, equation (3) becomes,

$$0 = (Y_{21} + \Delta Y_{21})E_1 + (Y_{22} + \Delta Y_{22})(E_2 + \Delta E_2) \quad \dots \dots \dots (4)$$

Solving (4) simultaneously with (3), gives

$$\Delta E_2 = - (Y_{22} + \Delta Y_{22})^{-1} \cdot (I_2 + \Delta Y_{21} \cdot E_1) \quad \dots \dots \dots (5)$$

where, from (3),

$$E_2 = Y_{22}^{-1} (I_2 - Y_{21} \cdot E_1) \quad \dots \dots \dots (6)$$

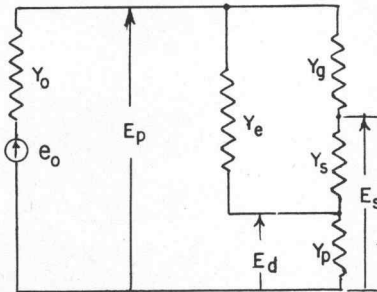
Equation (5) with the help of (6), gives the matrix, operational expression for the changes in the unknown voltages, in terms of known quantities. This is the desired invariant solution for the induced voltages. In a similar manner, the equation for the current changes, is found from equation (2) to be,

$$\Delta I_1 = \Delta Y_{11} E_1 + \Delta Y_{12} E_2 + (Y_{12} + \Delta Y_{12}) \Delta E_2 \quad \dots \dots \dots (7)$$

where ΔE_2 and E_2 are found from equations (5) and (6) respectively.

Solution of Specific Network

The junction pairs selected in the analysis of the network discussed in Chapter III, are indicated by the voltage arrows at the right. The admittance matrix of this network is,



	o	p	s	d
o	Y_o	$- Y_o$		
p	$- Y_o$	$Y_o + Y_e + Y_g$	$- Y_g$	$- Y_e$
s		$- Y_g$	$Y_g + Y_s$	$- Y_s$
d		$- Y_e$	$- Y_s$	$Y_e + Y_s + Y_p$

(8)

where double bars have been used to indicate the division of the axes into types "1" and "2". Here, the only admittance which changes is Y_s so that

$$\Delta Y =$$

	o	p	s	d
o	0	0	0	0
p	0	0	0	0
s	0	0	ΔY_s	$-\Delta Y_s$
d	0	0	$-\Delta Y_s$	ΔY_s

(9)

Also in the specific case under consideration, there are no impressed currents along the p, d and s axes, so $I_2 = 0$. Then, because of the many quantities which are zero, equations (5) and (7) become,

$$\Delta E_2 = - (Y_{22} + \Delta Y_{22})^{-1} \cdot \Delta Y_{22} \cdot E_2 \quad \dots \dots \dots (10)$$

and
$$\Delta I_1 = Y_{12} \cdot \Delta E_2 \quad \dots \dots \dots (11)$$

It will first be necessary to evaluate $(Y_{22} + \Delta Y_{22})^{-1}$. This may be done by first evaluating Y_{22}^{-1} and then replacing all Y_s by $(Y_s + \Delta Y_s)$. Here,

$$Y_{22} =$$

	p	s	d
p	$Y_o + Y_e + Y_g$	$- Y_g$	$- Y_e$
s	$- Y_g$	$Y_g + Y_s$	$- Y_s$
d	$- Y_e$	$- Y_s$	$Y_e + Y_s + Y_p$

(12)

so that, by the usual manipulations,

$$(Y_{22} + \Delta Y_{22})^{-1} = \frac{1}{D} \cdot \begin{matrix} & p & s & d \\ \begin{matrix} p \\ s \\ d \end{matrix} & \begin{matrix} Y_g(Y_e + Y_p) + \\ (Y_s + \Delta Y_s)(Y_e + Y_g + Y_p) \end{matrix} & \begin{matrix} Y_g(Y_e + Y_p) \\ + (Y_s + \Delta Y_s)(Y_e + Y_g) \end{matrix} & \begin{matrix} Y_e Y_g + \\ (Y_s + \Delta Y_s)(Y_e + Y_g) \end{matrix} \\ & \begin{matrix} Y_g(Y_e + Y_p) \\ + (Y_s + \Delta Y_s)(Y_e + Y_g) \end{matrix} & \begin{matrix} (Y_e + Y_p)(Y_o + Y_g) + Y_p Y_e \\ + (Y_s + \Delta Y_s)(Y_o + Y_e + Y_g) \end{matrix} & \begin{matrix} Y_e Y_g + \\ (Y_s + \Delta Y_s)(Y_o + Y_e + Y_g) \end{matrix} \\ & \begin{matrix} Y_e Y_g + \\ (Y_s + \Delta Y_s)(Y_e + Y_g) \end{matrix} & \begin{matrix} Y_o Y_g \\ + (Y_s + \Delta Y_s)(Y_o + Y_e + Y_g) \end{matrix} & \begin{matrix} Y_g(Y_o + Y_e) + \\ (Y_s + \Delta Y_s)(Y_o + Y_e + Y_g) \end{matrix} \end{matrix} \quad (13)$$

where $D = (Y_s + \Delta Y_s)[(Y_o + Y_p)(Y_g + Y_e) + Y_o Y_p] + Y_g[Y_e(Y_o + Y_p) + Y_o Y_p]$. (14)

Now,

$$-\Delta Y_{22} \cdot E_2 = \begin{matrix} p & 0 \\ s & \Delta Y_s(E_d - E_s) \\ d & -\Delta Y_s(E_d - E_s) \end{matrix} = \begin{matrix} p & 0 \\ s & -1 \\ d & 1 \end{matrix} \cdot \Delta Y_s(E_s - E_d) \quad (14)$$

By equation (10),

$$\Delta E_2 = \frac{1}{D} \cdot \begin{matrix} p & -Y_g Y_p \\ s & -Y_e(Y_o + Y_p) - Y_o Y_p \\ d & Y_o Y_g \end{matrix} \cdot \Delta Y_s(E_s - E_d) \quad (15)$$

A special case occurs when ΔY_s becomes infinite. By the theory of indeterminate forms,

$$\Delta E_2 = \frac{1}{(Y_o + Y_p)(Y_g + Y_e) + Y_o Y_p} \cdot \begin{matrix} p & -Y_g Y_p \\ s & -Y_e(Y_o + Y_p) - Y_o Y_p \\ d & Y_o Y_g \end{matrix} \cdot (E_s - E_d) \quad (16)$$

It was this special case which was considered in calculating the curves of Figure 10. To illustrate the method of evaluating the operational expressions in (16), the numerical solution for the case where $R = 1,000$ ohms will be carried to completion.

Evaluation of the Operational Solution

Equation (16) may be evaluated in terms of time functions either by integration in the complex plane, or through use of Heaviside's Expansion Theorem. Since the latter is perhaps the better known, it will be used. It reads, (where M and D are polynomials in p),

$$\frac{M(p)}{D(p)} \cdot 1 = \frac{M(0)}{D(0)} + \sum_{k=1}^n \frac{M(p_k)}{p_k D'(p_k)} \exp(p_k t) \dots \dots \dots (17)$$

where p_k is one of the roots of $D(p) = 0$, and $D'(p_k)$ is the derivative of $D(p)$ with respect to p at the point $p = p_k$. Equation (17) may be considered as a matrix equation in which $M(p)$ represents the one-matrix appearing in (16) have the following numerical values:

$$\begin{aligned}
 Y_o &= (2 \times 10^{-6}) + (20 \times 10^{-12})p \\
 Y_g &= (2 \times 10^{-9}) + (0.2 \times 10^{-12})p \\
 Y_p &= (1 \times 10^{-3}) + (1.2 \times 10^{-12})p \\
 Y_e &= \qquad \qquad \qquad (0.6 \times 10^{-12})p
 \end{aligned}$$

For these values, $D(p)$ becomes

$$D(p) = (2.002 \times 10^{-9}) + (20.8 \times 10^{-15})p + (40.96 \times 10^{-24})p^2 \quad (18)$$

which has the roots, $p_1 = -0.5078 \times 10^9$, and $p_2 = -0.9624 \times 10^5$. Also, $M(p)$ is found to be

$$M(p) = \begin{array}{l}
 \begin{array}{|l}
 p \\
 s \\
 d
 \end{array}
 \begin{array}{|l}
 -2 \times 10^{-12} - (0.2 \times 10^{-15})p - (0.24 \times 10^{-24})p^2 \\
 -2 \times 10^{-9} - (20.6 \times 10^{-15})p - (36.72 \times 10^{-24})p^2 \\
 4 \times 10^{-15} + (0.44 \times 10^{-18})p + (4 \times 10^{-24})p^2
 \end{array}
 \end{array} \quad (19)$$

Performing the operations indicated by (17), one finally obtains,

$$\Delta E_2 = \begin{array}{l}
 \begin{array}{|l}
 p \\
 s \\
 d
 \end{array}
 \begin{array}{|l}
 0.999 - 3.756 \exp(p_1 t) + 8.623 \exp(p_2 t) \\
 999.0 - 93.90 \exp(p_1 t) - 8.898 \exp(p_2 t) \\
 -0.002 - 97.67 \exp(p_1 t) - 0.055 \exp(p_2 t)
 \end{array}
 \end{array} \quad (20)$$

Equations (20) are those from which the curves of Figure 10 were calculated. Similar equations were obtained for $R = 10$ megohms. They are:

$$\Delta E_2 = \begin{array}{l}
 \begin{array}{|l}
 p \\
 s \\
 d
 \end{array}
 \begin{array}{|l}
 0.979 + 1.727 \exp(p_1 t) + 3.1735 \exp(p_2 t) \\
 979.43 - 0.301 \exp(p_1 t) - 82.699 \exp(p_2 t) \\
 -19.59 + 1.355 \exp(p_2 t) - 79.397 \exp(p_2 t)
 \end{array}
 \end{array} \quad (21)$$

where, for this last case, $p_1 = -0.992 \times 10^5$, and $p_2 = -0.5023 \times 10^5$.

APPENDIX IV

FREQUENCY SPECTRUM OF RANDOM IMPULSES

Theory

It has been shown elsewhere⁹ that a time function, $f(t)$, satisfying certain conditions, can be replaced by its frequency spectrum, $\varphi(p)$, by means of the Fourier transforms,

$$f(t) = \frac{1}{2\pi j} \int_{-\infty}^{\infty} \varphi(p) e^{pt} dp \quad \dots \dots \dots (1)$$

where $p = j2\pi f$, and $\varphi(p)$ is "the mate of $f(t)$ " defined by

$$\varphi(p) = \int_0^{\infty} f(t) e^{-pt} dt \quad \dots \dots \dots (2)$$

In the event that the time function may be expressed as the sum of several time functions such as

$$F(t) = f_1(t) + f_2(t) + f_3(t) + \dots + f_N(t) , \quad \dots \dots (3)$$

it follows that

$$\Phi(p) = \varphi_1(p) + \varphi_2(p) + \varphi_3(p) + \dots + \varphi_N(p) \quad \dots \dots (4)$$

and it is seen that the frequency spectrum of the sum of several time functions, is the sum of the frequency spectrum of each.

If now it is assumed that the various time functions in (3) are statistically random impulses, one may evaluate the root-mean-square value of the frequency spectrum when the number of impulses becomes great. If $\varphi(\omega)$ represents the rms amplitude of the component having a radian frequency of ω , by definition it must satisfy the relation,

$$N \overline{\varphi(\omega)^2} = \Phi(p) \cdot \Phi^*(p) , \quad \dots \dots \dots (5)$$

where $\Phi^*(p)$ is the complex conjugate of $\Phi(p)$. Substitution of (4) into (5) gives

$$\overline{\varphi(\omega)^2} = \frac{1}{N} \sum_{i=1}^N \varphi_i(p) \cdot \varphi_i(-p) + \frac{1}{N} \sum_{i=1}^N \sum_{\substack{k=1 \\ i \neq k}}^N \varphi_i(p) \cdot \varphi_k(-p) \quad \dots \dots (6)$$

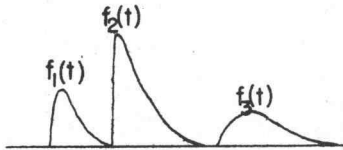
It can be shown on the basis of a few rational assumptions that the average value of the double-summation term should approach zero as N becomes very large, provided $p \neq 0$. Since this exceptional case corresponds to a direct-current component which most certainly would not bother radio receivers, it may be concluded that the meaning-square value of the frequency spectrum of a large number, N , of statistically random, time functions, $f_1(t)$, is

$$\overline{\varphi(\omega)^2} = \lim_{N \rightarrow \infty} \frac{1}{N} \sum_{i=1}^N \varphi_i(p) \cdot \varphi_i(-p) \quad \dots \dots \dots (7)$$

where, as before, $\varphi_i(p) = \int_0^{\infty} f_1(t) e^{-pt} dt$, and $p = j2\pi f$.

Frequency-Spectrum of Double-Exponential Transients

It will be assumed that the radio disturbance is produced by a series of random (but "quasi-systematic"), double-exponential current bursts, a few of which are shown below.



$$f_1(t) = I_1 \left[e^{-\alpha_1(t-t_1)} - e^{-\beta_1(t-t_1)} \right] \underline{S}_1(t-t_1)$$

The subscript, 1, signifies that the parameters, I_1 , α_1 , and β_1 may vary from burst to burst. $\underline{S}_1(t)$ is the Cambell and Foster notation for the functional equivalent of Heaviside's unit step, (i.e., $\underline{S}_1(t)$ is zero for $t < 0$ and is unity for $t > 0$).

Then by (2),

$$\varphi_1(p) = I_1 \left[\frac{1}{\alpha_1 + j\omega} - \frac{1}{\beta_1 + j\omega} \right] e^{-pt_1} \dots \dots \dots (9)$$

After some algebraic reduction, it is found that

$$\varphi_1(p) \cdot \varphi_1(-p) = \frac{I_1^2 (\beta_1 - \alpha_1)^2}{(\alpha_1^2 + \omega^2)(\beta_1^2 + \omega^2)} \dots \dots \dots (10)$$

so that,

$$\overline{\varphi(\omega)}^2 = \lim_{N \rightarrow \infty} \frac{1}{N} \sum_{i=1}^N \frac{I_i^2 (\beta_i - \alpha_i)^2}{(\alpha_i^2 + \omega^2)(\beta_i^2 + \omega^2)} \dots \dots \dots (11)$$

Effect of Variation of Parameters on Energy-Frequency Spectrum

Thus far, no restrictions have been placed on the parameters I_1 , α_1 , and β_1 except to suppose that they vary in a random fashion, which is limited, and tend toward a mean value as N becomes very large; that is, they are "quasi-systematic." In order to specify the variations of these parameters, it is possible to assign to each a "probability distribution function." Thus, for example, if the distribution function of the I_1 is designated by $\psi(I)$, it is implied that out of N bursts, the number having I 's lying within the interval I to $I + \Delta I$ would be expressed by $N\psi(I)\Delta I$. Accordingly, by re-grouping the terms under the summation term in (11), into groups having I 's lying between I_1 and $I_1 + \Delta I_1$, the summation may be written as

$$\overline{\varphi(\omega)}^2 = \lim_{\Delta I_1 \rightarrow 0} \frac{1}{N} \sum_{i=0}^{\infty} \frac{I_i^2 (\beta_i - \alpha_i)^2}{(\alpha_i^2 + \omega^2)(\beta_i^2 + \omega^2)} N\psi(I_1) \Delta I_1 \dots \dots \dots (12)$$

But (12) is the definition of an integral. If it is further assumed that α_1 and β_1 do not vary, then (12) may be written as

$$\overline{\varphi(\omega)}^2 = \bar{I}^2 \cdot \frac{(\beta - \alpha)^2}{(\alpha^2 + \omega^2)(\beta^2 + \omega^2)} \dots \dots \dots (13)$$

where \bar{I}^2 is simply the weighted, mean-square value of the I_1 and calculable from,

$$\bar{I}^2 = \int_{-\infty}^{\infty} I^2 \psi(I) dI \dots \dots \dots (14)$$

The importance of (13) is that it shows that the shape of the frequency spectrum will not be affected if only the amplitudes of the current bursts vary. A similar study may be made to determine the effect of variations in α alone and β alone.

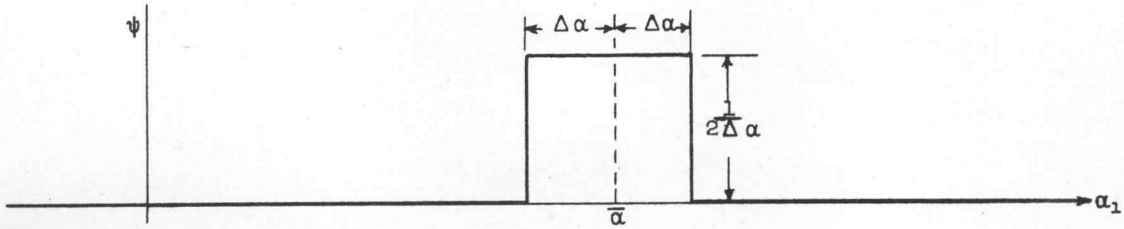
To illustrate the method of determining the frequency spectrum in the case where two parameters vary dependently, the equation for the dotted curve of Figure 13 will be derived. Here, it was assumed that the impulses were single-exponential transients, (i.e. $\beta = \infty$), and that the area under each burst was a constant, Q . This latter restriction simply imposes the condition that the charge involved in each burst would be the same, regardless of the shape of the burst, and requires that

$$I_1 / \alpha_1 = Q \dots \dots \dots (15)$$

For $\beta = \infty$, equation (11) becomes,

$$\overline{\varphi(\omega)^2} = \lim_{N \rightarrow \infty} \frac{1}{N} \sum_{i=1}^N \frac{I_i^2}{\alpha_1^2 + \omega^2} \dots \dots \dots (16)$$

Assuming that the α_1 were distributed as shown below,



the variable summation may be changed so that (16) reads,

$$\overline{\varphi(\omega)^2} = Q^2 \int_{\bar{\alpha}-\Delta\alpha}^{\bar{\alpha}+\Delta\alpha} \frac{\alpha^2}{\alpha^2 + \omega^2} \cdot \frac{1}{2\Delta\alpha} \cdot d\alpha \dots \dots \dots (17)$$

Evaluation of (17) gives,

$$\overline{\varphi(\omega)^2} = Q^2 \left\{ 1 - \frac{\omega}{2\Delta\alpha} \left[\tan^{-1} \left(\frac{\alpha+\Delta\alpha}{\omega} \right) - \tan^{-1} \left(\frac{\alpha-\Delta\alpha}{\omega} \right) \right] \right\} \dots \dots (18)$$

APPENDIX V

RECEIVER BANDWIDTH AND RADIO INTERFERENCE

Receiver Effective Bandwidth

A quantity useful in describing the performance of a selective circuit to random interference, is that known as the "Effective Bandwidth" of the circuit. For a selective radio receiver, this quantity may be described as follows:

Assume that the receiver is tuned to the angular frequency, ω_0 (where $\omega_0 = 2\pi f_0$), and that the steady, sinusoidal current of frequency f which is impressed on the antenna coil must be adjusted to have a magnitude $I(f)$ at each frequency if the output voltage of the receiver is to be maintained at some constant value, E_{out} . Then the "transfer-impedance" expressing the output voltage developed per unit input current of frequency f , is

$$Z(f) = \frac{E_{out}}{I(f)} \dots \dots \dots (1)$$

The output voltage would ideally be that developed by a linear detector, but since the impressed current is adjusted to give the same output voltage for each observation, the exact nature of the detection systems is unimportant and the AVC voltage may be conveniently used.

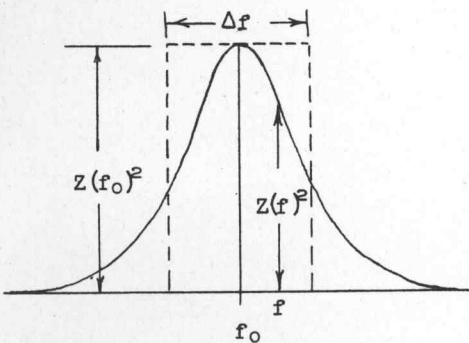
If $Z(f)$ were plotted as a function of the frequency at which it was measured, it would be found very similar in appearance to the ordinary "selectivity characteristic" of the radio receiver. In fact, if the impedance of the antenna coil were constant over the frequency range in question, $Z(f)$ would be identical, within a constant factor, to the selectivity characteristic of the receiver.

Now it has been shown⁴ that noise relationships must be established on an energy basis. Accordingly, we are more interested in the square of the output voltage than the voltage itself, because its square would be proportional to the output power. For a unit input current, this voltage squared would be simply, $Z(f)^2$, and the manner in which $Z(f)^2$ varies with the frequency may be considered as defining the "power-selectivity characteristic" of the receiver.

The effective bandwidth may now be defined as the width, Δf , of an ideal, rectangular, power selectivity characteristic of magnitude $Z(f_0)^2$ over a frequency band, Δf , and zero elsewhere; which would have the same area as the actual power selectivity characteristic, $Z(f)^2$. That is,

$$\begin{aligned} \Delta f \cdot Z(f_0)^2 &= \int_0^{\infty} Z(f)^2 df . \\ \text{or } \Delta f &= \int_0^{\infty} \left[\frac{Z(f)}{Z(f_0)} \right]^2 df \\ \text{or } \Delta f &= I(f_0)^2 \int_0^{\infty} \frac{df}{I(f)^2} \dots \dots \dots (2) \end{aligned}$$

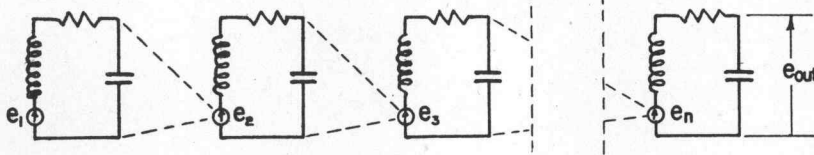
where, as before, $I(f_0)$ is the minimum input current required at the frequency f_0 to which the receiver is tuned, and $I(f)$ is the current required at any other frequency f to maintain the fixed receiver output voltage. The integral may be evaluated graphically by plotting the reciprocal of I^2 as a function of the frequency and measuring the area under the resulting curve



with a planimeter. Obviously, the integral could also be evaluated by employing some method of numerical integration such as Simpson's rule.

Relation between Circuit "Q" and Effective Bandwidth

Consider "n" identical, tuned circuits each formed of an inductor L of effective resistance r, in series with a capacitor, C. The oscillation developed in each circuit is assumed to be introduced in series with the next tuned circuit, either directly by magnetic induction or by means of an intervening vacuum tube.



For circuits having reasonable values of Q (i.e. $Q \gg 10$) it may be shown that the ratio of the voltage induced in any particular coil, to the steady, oscillating voltage applied to the previous coil, can be expressed by the same approximate equation for either vacuum-tube or magnetic coupling between the tuned circuits if the above ratio is expressed as a fraction of the ratio obtaining at the resonant frequency. This ratio may be called the "response ratio" of each circuit and will hereafter be designated by R. It is found that,

$$\dot{R} = \frac{j\omega rC}{(1 - LC\omega^2) + j\omega rC} \quad \text{where } \omega = 2\pi f \quad \dots \dots \dots (3)$$

At the resonant frequency, $(1 - LC\omega_0^2) = 0$ so that

$$\omega_0 = \frac{1}{\sqrt{LC}} \quad \text{and} \quad \dot{R} = \frac{j\omega rC}{j\omega rC} = 1 .$$

As a function of frequency, R resembles a selectivity curve which has a maximum value of unity at the resonant frequency f_0 and which decreases rapidly in value for all frequencies departing from f_0 .

However, R represents a voltage-selectivity characteristic. The power ratio between the two tuned circuits will be proportional to $|R|^2$ or

$$|R|^2 = \frac{(\omega rC)^2}{(1 - LC\omega^2)^2 + (\omega rC)^2} \quad \dots \dots \dots (4)$$

For "n" tuned circuits, the overall "power" response ratio is simply,

$$R_n^2 = \left[\frac{(\omega rC)^2}{(1 - LC\omega^2)^2 + (\omega rC)^2} \right]^n \quad \dots \dots \dots (5)$$

From the discussion and definition of equivalent bandwidth, it is apparent that

$$\Delta f = \int_0^\infty R_n^2 df \quad \dots \dots \dots (6)$$

From (5) and (6), after straightforward but lengthy manipulations, it is found that,

$$\Delta f = \frac{\pi(2n - 2)!}{(2)^{2n-1} (n-1)!^2} \cdot \frac{f_0}{Q} \quad \dots \dots \dots (7)$$

where as usual, $Q = \omega_0 L/r$.

Equation (7), relating the effective band-width of a series of tuned circuits to the Q of each, is actually an approximate expression. However, it is a very good approximation for reasonable values of Q, and is exact for a single tuned circuit in which case, $n = 1$, and

$$\Delta f = \frac{\pi f_0}{2Q} \quad \dots \dots \dots (8)$$

It has erroneously become commonplace to refer to the "overall Q" of a selective network as given by

$$Q' = \frac{f_0}{f_2 - f_1} \dots \dots \dots (9)$$

where f_0 is the resonant frequency, and f_2 and f_1 are the higher and lower frequencies at which the response has dropped to 0.707 of its resonant value. When equation (9) is applied to a single, highly-resonant circuit, it actually gives the true Q of that circuit. However, when applied to a more complicated network, the value of Q' thus obtained has no such dynamical significance, and is highly artificial. A performance index such as Δf has much to be preferred over Q' .

Nevertheless, if the coupling between all "n," tuned circuits is so small that "flat-topping" does not occur, the relationship between Q' and the Q of each circuit may be approximated by

$$Q = Q' \sqrt{(2)^{1/n} - 1} \dots \dots \dots (10)$$

Influence of Effective Bandwidth on Radio Interference

In appendix IV it was shown from an energy standpoint, at least, a static burst can be resolved into an equivalent frequency spectrum of sinusoidal frequencies. This is an important concept because it allows transient phenomena to be treated on the basis of receiver response to steady-state signals.

For example, from the discussion in the first section of this appendix, it is apparent that the "transfer-impedance" of the receiver could also be written as

$$Z(\omega) = \frac{E_{out}}{i(\omega)} = \frac{\text{output voltage}}{\text{input current}} \dots \dots \dots (11)$$

where the current impressed at the input of the receiver is represented by $i(\omega)$ to show that its radian frequency is ω , ($\omega = 2\pi f$), and the transfer impedance is written as $Z(\omega)$ to indicate that this ratio is evaluated at the frequency of ω .

If now a transient current, $I(t)$, having an equivalent current-frequency spectrum $\varphi(\omega)$ were impressed on the antenna coil, the amplitude of the oscillation-component of frequency ω reaching the second detector would be simply,

$$e(\omega) = Z(\omega) \cdot \varphi(\omega) \dots \dots \dots (12)$$

However, we are primarily interested in the amount of energy reaching the second detector, or in, what is practically an equivalent, the mean-square value of the disturbance $E(t)$ at the second detector. Lord Rayleigh was the first to show, some 50 years ago, that there exists a mathematical relation between the mean-square value of a time function and its equivalent frequency spectrum. This relation is that,

$$\int f(t)^2 dt = \frac{1}{\pi} \int_0^{\infty} [\varphi(\omega)]^2 d\omega$$

As applied to our case it gives,

$$n \int [E(t)]^2 dt = \frac{n}{\pi} \int_0^{\infty} [e(\omega)]^2 d\omega \dots \dots \dots (13)$$

where "n" is the average number of times the elemental time-disturbance occurs each second. Equation (13) represents the mean-square value of the oscillations at the second detector. Designating this value by E_n^2 and utilizing the relation (12), one obtains

$$E_n^2 = \frac{n}{\pi} \int_0^{\infty} [Z(\omega)]^2 \cdot [\varphi(\omega)]^2 d\omega \dots \dots \dots (14)$$

But, $Z(\omega)$ is practically zero for all ω except for those in the immediate vicinity of ω_0 . Accordingly, over that narrow region, $\Phi(\omega)$ may be considered a constant equal to its midpoint value, $\Phi(\omega_0)$. Therefore,

$$E_n^2 = \frac{n}{\pi} \overline{\Phi(\omega_0)^2} \int_0^\infty [Z(\omega)]^2 d\omega \dots \dots \dots (15)$$

When the standard signal, i_n , of frequency ω_0 is substituted for the interference and adjusted in magnitude to give the same effective value of oscillation at the diode, ideally

$$E_n^2 = [Z(\omega_0)]^2 \cdot i_n^2 \dots \dots \dots (16)$$

Accordingly, by equating (15) and (16), one obtains

$$i_n^2 = 2n \overline{\Phi(\omega_0)^2} \int_0^\infty [Z(\omega)/Z(\omega_0)]^2 df \dots \dots (17)$$

But from the discussion in the first section, the integral in (17) is nothing other than the effective bandwidth Δf . Hence,

$$i_n^2 = 2n \overline{\Phi(\omega_0)^2} \Delta f \dots \dots \dots (18)$$

Equation (18) is a very important equation giving the mean-square value of the interference current in terms of the bandwidth of the radio receiver; the spectral noise-intensity at the frequency to which the receiver is tuned; and the average number of disturbances per unit of time.

Radio Interference Produced by Corona Streamers

If it is assumed that each corona streamer is expressed by

$$I(t) = I[\exp(-\alpha t) - \exp(-\beta t)] \dots \dots \dots (19)$$

and that the streamers are occurring at the rate of n per second; then by equation (13) of appendix IV and equation (18) of appendix V, the equivalent, mean-square, noise-input current will be

$$i_n^2 = 2n I^2 \frac{(\beta - \alpha)^2}{(\alpha^2 + \omega^2)(\beta^2 + \omega^2)} \cdot \Delta f \dots \dots \dots (20)$$

Now, the average corona current due to the streamers is

$$I_{st} = n \int_0^\infty I(t) dt = nI \frac{\beta - \alpha}{\alpha\beta}$$

Hence, equation (20), when expressed in terms of the average corona-streamer current is,

$$i_n^2 = \frac{I_{st}^2}{[1 + (\omega/\alpha)^2][1 + (\omega/\beta)^2]} \cdot \left[\frac{2 \Delta f}{n} \right] \dots \dots \dots (21)$$

When $\omega \ll \alpha$, the noise current is substantially independent of ω , and accordingly on this "plateau,"

$$i_n = \sqrt{(2\Delta f/n)} \cdot I_{st} \dots \dots \dots (22)$$

Equation (22) is another important equation relating the radio interference on the "plateau" to the average corona current due to streamers. Although in the derivation, a double-exponential impulse was assumed, it can be shown that equation (22) is valid for any impulse shape of comparable duration. In other words, the shape of an impulse of extremely short duration affects only the manner in which the interference varies at the higher frequencies; the interference at the lower frequencies "on the plateau" is determined entirely by the area under the impulse (which in the example just considered is proportional to the average streamer current).

Shot-Effect Noise in Temperature-Limited Diode

Consider the current fluctuations in the plate current of a temperature-limited diode. This noise is known to be due to the fact that the current flow is not continuous but is actually a stream of discrete electrons. However, if the charge on the electron is known, the number of electrons needed to produce any given space current is readily calculated.

If only frequencies of period considerably greater than the transit time of the electrons are considered, the current flow to the plate due to each electron can be considered as truly impulsive and equation (22) developed in the preceding section can be used to estimate the radio interference arising from the "schrotheffekt."

Let

I = Average current due to electron flow

n = Average number of electrons per second reaching plate

Δf = Bandwidth of radio receiver

i_n^2 = Mean-square value of shot-effect current over the bandwidth Δf .

Then, by (22),

$$i_n^2 = (2\Delta f/n) \cdot I^2 .$$

But, $I/n = e$, the charge on each electron. Therefore,

$$i_n^2 = 2eI\Delta f \quad (23)$$

which is the well-known expression for shot-effect "noise."

APPENDIX VI

INFLUENCE OF EXTERIOR CIRCUIT ON RADIO INTERFERENCE

Theoretical Considerations

In the usual case, there is always an exterior circuit between the corona streamer and the antenna circuit of the radio receiver. For this reason, the currents reaching the antenna circuit will differ from the actual corona currents.

To assist in estimating the radio interference at any frequency, the concept of an impulsive noise as equivalent to a frequency spectrum is particularly helpful. It is only necessary to determine either by experiment or theory the fraction of a steady current of frequency ω , impressed at the point of corona, which reaches the antenna coil of the receiver. Obviously, this fraction or ratio will depend upon the frequency, and being a function of the frequency will hereafter be designated by $H(\omega)$.

The effective radio interference produced by a corona discharge in a radio receiver tuned to the frequency ω_0 , in view of equation (21) of appendix V and the above modification, is therefore,

$$i_n = \sqrt{\Delta f} \cdot \sqrt{2I_{st}/n} \cdot \frac{1}{\sqrt{[1 + (\omega_0/\alpha)^2][1 + (\omega_0/\beta)^2]}} \cdot H(\omega_0) \quad (1)$$

The first factor takes into consideration the bandwidth of the radio receiver; the second, the rate at which the disturbance is occurring and its amplitude; the third, its shape; and the last, the transmission characteristic of the network over which the noise currents must flow to reach the radio receiver.

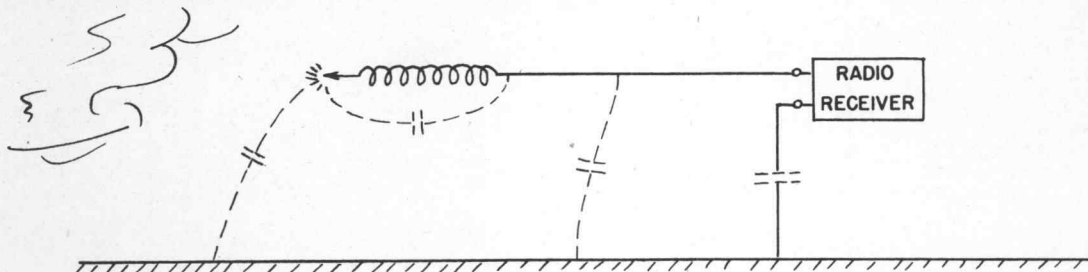
It should perhaps be pointed out that equation (1) is an approximate expression sufficiently exact for practical calculations provided $H(\omega)$ is a slow-changing function. If the exterior circuit should contain resonant circuits so that $H(\omega)$ changes at a rate comparable to that at which the receiver selectivity characteristic changes, the mathematically-exact equation is

$$i_n^2 = \frac{2 I_{st}^2}{n} \int_0^{\infty} \left| \frac{Z(\omega)}{Z(\omega_0)} \right|^2 \cdot \frac{|H(\omega)|^2}{[1 + (\omega/\alpha)^2][1 + (\omega/\beta)^2]} d\omega \quad (1a)$$

However, even in these special cases, the additional work involved in evaluating (1a) offsets the increase in accuracy, so that (1) may be used for all calculations.

Example: Effect on the Radio Interference of a Resonant Circuit Placed between a Discharge Point and Radio Receiver.

Consider a radio receiver in an airplane with a trailing-wire antenna terminated in a highly-resonant circuit and discharge point.



The tuning capacitance across the inductor can just as well be due to that distributed over the high-Q inductor.

The capacitance of the body of the airplane to the ground will be so much greater than the other capacitances in the circuit, that the body of the airplane may be considered at ground potential in this analysis. Accordingly, the approximate equivalent circuit will be:

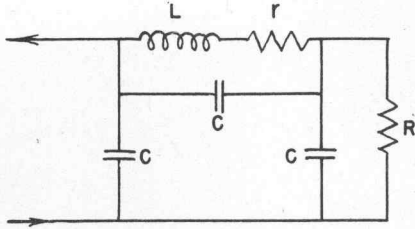


Fig. 2. Actual Equivalent Circuit.

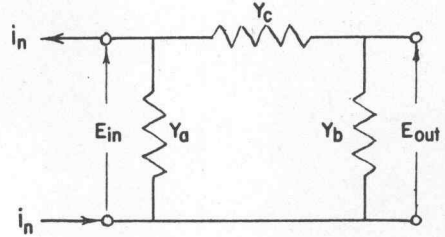


Fig. 3. Operational Admittance Circuit.

The operational-admittance tensor along the junction-pair axes, E_{in} and E_{out} , is

$$\bar{Y} = \begin{matrix} & \begin{matrix} in & out \end{matrix} \\ \begin{matrix} in \\ out \end{matrix} & \begin{bmatrix} Y_a + Y_c & -Y_c \\ -Y_c & Y_c + Y_b \end{bmatrix} \end{matrix},$$

$$\bar{I} = \begin{matrix} in \\ out \end{matrix} \begin{bmatrix} i_n \\ 0 \end{bmatrix}$$

so that,

$$\bar{Z} = \begin{matrix} in \\ out \end{matrix} \begin{bmatrix} Y_c + Y_b & Y_c \\ Y_c & Y_a + Y_c \end{bmatrix} \cdot \frac{1}{\Delta}, \quad \text{where } \Delta = Y_a Y_b + Y_c(Y_a + Y_b)$$

But since $\bar{E} = \bar{Z} \cdot \bar{I}$,

$$E_{out} = \frac{Y_c}{\Delta} \cdot i_n \quad \dots \dots \dots (2)$$

Now, the operational admittances Y_a , Y_b , and Y_c are

$$\begin{aligned} Y_a &= Cp \\ Y_b &= C(p + 1/RC) \quad \dots \dots \dots (3) \\ Y_c &= Cp + 1/Lp + r = C \left[\frac{p^2 + \frac{r}{L}p + \frac{1}{LC}}{p + r/L} \right] \end{aligned}$$

In addition, the current through the receiver is $I_r = E_{out}/R$. Accordingly, by (2) and (3),

$$I_r = \frac{1}{RC} \cdot \frac{p^2 + \frac{r}{L}p + \frac{1}{LC}}{3p^3 + \left(\frac{2}{RC} + \frac{3r}{L}\right)p^2 + \frac{2}{LC}\left(1 + \frac{r}{R}\right)p + \left(\frac{1}{LC} \frac{1}{RC}\right)} \cdot i_n \quad (4)$$

and the operational equation (4) giving I_r in terms of i_n is obtained. This same equation could be used to calculate the actual shape of the static disturbance entering the

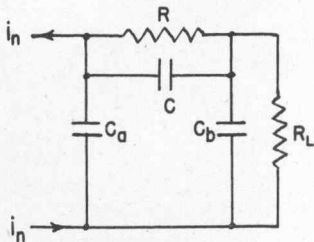
receiver if the operational form of i_n were used. However, for our immediate purpose we wish to evaluate (4) for the steady-state case where i_n is a unit cissoidal oscillation of radian frequency ω and amplitude I_{1n} . To do this, it is only necessary to let $p = j\omega$.

If in the circuit of Figure 2, L is a pi-wound inductor having a natural frequency of 2 mc, a Q of 100, and an inductance of 3.4 millihenrys; and if it is further assumed that the antenna circuit is equivalent to a 150 ohm resistor, equation (4) becomes for the steady-state, where ω is in megaradians per second,

$$\frac{I_r}{I_{1n}} = H(\omega) = 2.388 \cdot \frac{(316 - \omega^2) + j(0.1257\omega)}{(754.5 - 4.78\omega^2) + j\omega(0.8109 - 0.001\omega^2)} \quad (6)$$

By the use of equation (6) together with equation (1), the radio-interference spectrum resulting from positive-corona streamers may be determined analytically. The agreement of these calculated values with the experimental measurements is entirely satisfactory as can be seen from Figure 21 of the body of this treatise.

Example: Effect on the Radio Interference of a High Resistance Placed between a Discharge Point and Radio Receiver.



The analysis of the previous example may be applied to this case where,

$$Y_c = C_p + \frac{1}{R}$$

$$Y_b = C_b p + \frac{1}{R_L}$$

$$Y_a = C_a p$$

Accordingly, by (2)

$$I_r = \frac{[(RC)p + 1] \cdot i_n}{RR_L[C_a C_b + C(C_a + C_b)]p^2 + R[C_a(1 + R_L/R) + C_b R_L/R + C]p + 1}$$

or for the steady-state-cisoidal case,

$$H(\omega) = \frac{1 + jRC\omega}{1 - RR_L[C_a C_b + C(C_a + C_b)]\omega^2 + j[R(C_a + C) + R_L(C_a + C_b)]\omega}$$

This equation, in conjunction with (1), was used to calculate the noise spectrum shown in Figures 22 and 23. Here again, the experimental values agree excellently with those which were calculated.

It is interesting to note that even with an infinite value of R, the maximum noise reduction at low and medium frequencies is

$$\text{Maximum noise Reduction} = C/(C + C_a)$$

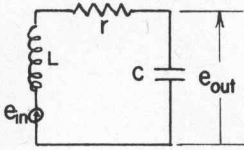
Comparison of this result with the maximum reduction obtainable through use of a series inductor, indicates that for one (or more) frequencies an inductance (or inductive network) can be used to isolate the radio interference much more effectively than can be done with even the highest of resistances.

APPENDIX VII

SHOCK OSCILLATIONS IN TUNED CIRCUITS

General Theory

Consider a series of "n" tuned circuits unilaterally coupled by vacuum tubes so that the voltage impressed in series with each circuit is proportional to the voltage developed across the previous tuned circuit. Then for each circuit,



$$\alpha = \frac{r}{2L}, \quad \omega_0^2 = \frac{1}{LC}$$

$$\tilde{e}_{out} = \frac{\omega_0^2}{p^2 + 2\alpha p + \omega_0^2} \cdot \tilde{e}_{in} \quad \dots \dots \dots (1)$$

where "~" indicates the Laplace transform or operational equivalent of the voltage under consideration. Accordingly, the relation between the input voltage and the output voltage after n circuits, is

$$\tilde{e}_{out} = \left[\frac{\omega_0^2}{p^2 + 2\alpha p + \omega_0^2} \right]^n \cdot \tilde{e}_{in}$$

$$= \left[\frac{\omega_0^2}{(p - p_1)(p - p_2)} \right]^n \cdot \tilde{e}_{in} \quad \dots \dots \dots (2)$$

where $p_1 = -\alpha + j\omega_0$ and $p_2 = -\alpha - j\omega_0$ to a very good approximation for circuits having normal Q's.

Now let a unit impulse (i.e. an impulse lasting an infinitesimally-short period but having a unit area) be expressed in the first tuned circuit. Here, $\tilde{e}_{in} = 1$ so that,

$$\tilde{e}_{out} = \frac{\omega_0^{2n}}{(p - p_1)^n (p - p_2)^n} \quad \dots \dots \dots (3)$$

The actual output voltage as a function of time will be,

$$e_{out} = \frac{1}{2\pi j} \int_{Br.} \tilde{e}_{out} e^{pt} dp \quad \dots \dots \dots (4)$$

$$= \sum \text{Res}(\tilde{e}_{out} \cdot e^{pt}) \quad \dots \dots \dots (5)$$

Now it can be shown⁵ that if $w(p)$ has an m'th order pole at $p = p_0$, then .

$$\text{Res}(w) \Big|_{p_0} = \lim_{p \rightarrow p_0} \left\{ \frac{1}{(m-1)!} \frac{d^{m-1}}{dp^{m-1}} \left[(p - p_0)^m \cdot w \right] \right\} \quad \dots \dots (6)$$

Applying (6) to the evaluation of (5), one obtains,

$$e_{out} = \frac{\omega_0^{2n}}{(n-1)!} \left\{ \frac{d^{n-1}}{dp_1^{n-1}} \left[\frac{e^{p_1 t}}{(p_1 - p_2)^n} \right] + \frac{d^{n-1}}{dp_2^{n-1}} \left[\frac{e^{p_2 t}}{(p_2 - p_1)^n} \right] \right\} \quad (7)$$

If the indicated differentiations are performed and the values $p_1 = -\alpha + j\omega_0$ and $p_2 = -\alpha - j\omega_0$ substituted, equation (7) may be written as

$$e_{out} = \frac{(-1)^n \omega_0^n e^{-\alpha t}}{(n-1)! \cdot 2^{n-1}} \left[\cos \omega_0 t \sum_{m=n/2}^{2n-1} (-1)^m \binom{n-1}{2m-n} \frac{(2m-1)!}{(2\omega_0)^{2m-n}} t^{2(n-m)-1} \right.$$

$$\left. - \sin \omega_0 t \sum_{m=\frac{n-1}{2}}^{n-1} (-1)^m \binom{n-1}{2m-n+1} \frac{(2m)!}{(2\omega_0)^{2m+1-n}} \cdot t^{2(n-m-1)} \right] \quad (9)$$

SHOCK OSCILLATIONS IN TUNED CIRCUITS

where it is understood that each summation is to be performed over all integral values of m lying on and between the limits indicated; and the notation, $\binom{n}{r} = \frac{n(n-1)(n-2)\dots(n-r+1)}{(1 \cdot 2 \cdot 3 \dots r)}$, is that representing the binomial coefficients.

As examples of (9), when $n = 1$,

$$e_{out} = \omega_0 e^{-\alpha t} \sin \omega_0 t, \quad \dots \dots \dots (10a)$$

and when $n = 2$,

$$e_{out} = \frac{\omega_0 e^{-\alpha t}}{2} (\sin \omega_0 t - \omega_0 t \cos \omega_0 t) \dots \dots \dots (10b)$$

Envelope of Shock Oscillation

In the previous section, an expression was derived giving the shock oscillation induced in the last of a series of "n" tuned circuits by a unit impulse applied to the first circuit. This expression gives the instantaneous values of the oscillation. However, the disturbance created in the output of an ideal, linear second detector will be proportional to the envelope of the oscillation. A general expression for this envelope will now be derived.

Starting with equation (7), it can be shown that

$$e_{out} = \text{Real part of } \dot{E}$$

$$\text{where } \dot{E} = \frac{2\omega_0^n}{(n-1)!^2 (2j)^n} \cdot e^{(-\alpha + j\omega)t} \sum_{k=0}^{n-1} (-1)^k \binom{n-1}{k} \frac{(n+k-1)!}{(2j\omega)^k} t^{n-k-1}$$

Accordingly, the "envelope" of e_{out} is simply

$$E = [(\dot{E}) \cdot (\text{conj } \dot{E})]^{1/2} \\ = \frac{\omega_0 e^{-\alpha t}}{(n-1)!^2 (2)^{n-1}} \left[\sum_{k=0}^{n-1} \binom{n-1}{k}^2 \cdot \frac{(n+k-1)!^2}{(4\omega_0^2)^k} t^{2(n-k-1)} \right]^{1/2} \quad (11)$$

But it will be realized that,

$$\alpha = \frac{r}{2L} = \frac{\omega_0}{2} \frac{r}{\omega_0 L} = \frac{\omega_0}{2Q} \quad \dots \dots \dots (12)$$

Furthermore, in the case of impressed steady-state oscillations, the magnitude of the oscillating voltage will be increased by Q times for each additional circuit which is added; that is, due to resonance, each circuit amplifies the signal. Because of this effect, the amplitude of the oscillation should be divided by Q^{n-1} to express it relative to the oscillation occurring in the first tuned circuit. The equation can be still further generalized by also dividing the amplitude by ω_0 . Accordingly, by utilizing the relation $\alpha = \omega_0/2Q$, equation (11) may be written as

$$\frac{E}{\omega_0 Q^{n-1}} = \frac{e^{-\alpha t}}{(n-1)!^2} \left[\sum_{k=0}^{n-1} \binom{n-1}{k}^2 \frac{(n+k-1)!^2}{(4Q)^{2k}} (\alpha t)^{2(n-1-k)} \right]^{1/2} \quad (14)$$

As examples of (14), for $n = 1$,

$$\frac{E}{\omega_0} = e^{-\alpha t} \dots \dots \dots (15a)$$

For $n = 2$

$$\frac{E}{\omega_0 Q} = e^{-\alpha t} [(\alpha t)^2 + (1/2Q)^2]^{1/2} \dots \dots \dots (15b)$$

For $n = 3$

$$\frac{E}{\omega_0 Q^2} = \frac{e^{-\alpha t}}{2} \left[(\alpha t)^4 + \frac{18}{(4Q)^2} (\alpha t)^2 + \frac{(12)^2}{(4Q)^4} \right]^{1/2} \dots \dots \dots (15c)$$

It should be noted that the expressions (15a) and (15b) could have been derived from (10a) and (10b) by forming the square-root of the sums of the squares of the amplitudes of the cosinusoidal and sinusoidal oscillations.

A few trial calculations using equation (14) will show that to a good approximation it may be replaced by a much simpler expression:

$$\frac{E}{\omega_0 Q^{n-1}} = \frac{e^{-\alpha t}}{(n-1)!} (\alpha t)^{n-1} \dots \dots \dots (16)$$

Epoch and Value of Maximum Amplitude of Shock Oscillations

By differentiating (16) with respect to αt , it can easily be shown that the maximum value of (16) occurs when

$$\begin{aligned} \alpha t &= n - 1 \\ \text{or } t &= (n - 1)/\alpha, \dots \dots \dots (17) \end{aligned}$$

which shows that the "sluggishness" of a multi-tuned-circuit amplifier increases linearly with "n", the number of tuned circuits. Furthermore, the maximum amplitude of the oscillation will be

$$\left| \frac{E}{\omega_0 Q^{n-1}} \right|_{\max} = \frac{e^{-(n-1)}}{(n-1)!} \cdot (n-1)^{n-1} \dots \dots \dots (18)$$

Because of the terms in which it is expressed, equation (18) in effect gives the peak-noise-to-peak-signal ratio in terms of the number of tuned circuits, the ratio being expressed as the fraction of the peak-noise-to-peak signal ratio obtaining for a single tuned circuit. Equation (18), therefore, provides a means of estimating the improvement in noise-to-signal ratio obtained by adding additional tuned circuits. Data such as these are shown in Figure 26 of the text.

APPENDIX VIII

COMMENTS ON USE OF AVC VOLTAGE FOR NOISE-MEASUREMENT COMPARISONS

Methodology

The second-detector of a radio receiver ideally produces an output voltage which is proportional to the envelope of the impinging high-frequency oscillation. In the case of a very selective receiver such as was used in making the noise measurements described in the text, the effective value of the envelope of the oscillation is proportional to the effective value of the oscillation itself. Accordingly, a voltmeter which measures effective values could be used to read directly the effective value of the oscillations. A thermocouple could be used here.

However, in measurements of kind discussed in the text, it was not thought advisable to use a thermocouple for this purpose as it would probably leave in a "puff" every time the noise level unexpectedly increased by a large amount. Instead, it was decided to use the avc voltage for comparing the noise with the standard signal. The experimental procedure was as follows:

1. The corona bursts were synchronized to give N bursts per second.
2. With the receiver connected to the noise source, the receiver r.f. gain was adjusted to give a specified a.v.c. voltage of about 2 volts.
3. A standard sinusoidal current of frequency to which the receiver had been tuned, was then substituted for the noise current, and the magnitude of the standard current adjusted to give the same a.v.c. voltage as the noise current. The effective value of the standard signal could then be calculated from the reading of the calibrated attenuator on the signal generator.

From the statement of the procedure, and by consideration of the manner in which the a.v.c. voltage is derived, it is apparent that the standard signal was adjusted to give the same average value as the noise instead of the same effective value. For this reason, it is necessary to determine, by a combination of experiment and theory, the ratio between the effective and average values of the noise envelope. This ratio is also known as the "form factor" and will hereafter be designated by Γ . Also the second detector will be referred to as the "diode."

In order that the problem may be stated more concisely, let

i_n = Effective value of the shock oscillations at the diode.

I_d = The average diode current required to produce the reference a.v.c. voltage.

i_s = The effective value of the steady-state standard signal needed to produce the same a.v.c. voltage as that resulting from i_n .

K = Rectification coefficient (ratio of effective value of oscillation to the effective value of the envelope of the diode-current).

Γ = Envelope form-factor (effective value/ average value).

It seems reasonable to assume that, since the decrement per cycle of the shock oscillation is quite small, the value of K should be the same for the shock oscillation as for the steady signal. Also, the form-factor, Γ , will depend upon the rapidity with which the impulsive disturbances occur but, for a selective receiver, it should be substantially independent of the shape of the initiating impulses.

From the foregoing, it is apparent that

$$i_n = K \cdot \Gamma \cdot I_d \quad \dots \dots \dots (1)$$

Now, when the steady-state calibrating signal is substituted to give the same I_d , the effective value of the envelope is the same as the average value. Accordingly,

$$i_s = K \cdot I_d \quad \dots \dots \dots (2)$$

By eliminating I_d between (1) and (2), there results,

$$i_n = \Gamma \cdot i_s \quad \dots \dots \dots (3)$$

That is, to obtain the true effective value of the noise current, the effective value of the equivalent standard signal (determined on the basis of the same a.v.c. voltage) must be multiplied by Γ .

Theoretical Determination of Γ

For noise impulses occurring at various, known rates, the form factor, Γ , can be determined from the envelope of the shock oscillation. This determination can best be performed either numerically or graphically. The envelope of the oscillation resulting from an impulse every "T" seconds can readily be constructed from the envelope of the oscillations produced by a single impulse, formulas for which are derived in appendix VII. For the usual impulse rates, such as those obtaining for positive corona streamers, each shock oscillation will have died away by the time the next one occurs. so that it is only necessary to obtain the effective value of the envelope over the interval T by the usual methods of graphical or numerical calculations. The average value of the envelope can also be easily determined, and the form-factor thus obtained.

The form factor will depend upon the time interval elapsing between successive impulses. For very short intervals, the successive shock-oscillations may overlap. In this case, the envelope resulting from the sums of two or more oscillations (the instantaneous values of the envelopes of each being known) is found by forming the square-root of the sums of the squares of the envelopes of the component oscillations at every instant. The values thus obtained represent the probable envelope of the composite oscillation from which the probable form-factor may be determined as described in the previous paragraph.

Sample Calculations for HRO Receiver

However, in order to calculate Γ , the shape of the shock oscillations at the detector of the particular receiver used must be determined. Before this can be done, the Q and the number of tuned circuits employed in the receiver used for making the noise measurements must be found.

Inspection of the National HRO receiver circuit revealed that there were 6 i.f. circuits each tuned to 456 kc, and 3 r.f. circuits each tuned to 700 kc. Furthermore, a measurement of the overall selectivity of the receiver when tuned to 700 kc., indicated an effective bandwidth, Δf , of 3.23 kc.

From other measurements it was found that the selectivity of the receiver was contributed mostly by the 6 tuned i.f. circuits. By slight rearrangement of equation (7) of appendix V, an expression may be obtained for the Q of each i.f. tuned circuit in terms of the known quantities: f_0 , Δf , and n. It is

$$Q = \frac{\pi(2n-2)!}{2^{2n-1} (n-1)!^2} \cdot \frac{f_0}{\Delta f} \quad \dots \dots \dots (4)$$

$$= \frac{\pi(10)!}{2^{11} (5!)^2} \frac{456}{3.23} = 54.5$$

Also, from equation (12) of appendix VII,

$$\alpha = \frac{r}{2L} = \frac{\omega}{2Q} = \frac{2\pi(456,000)}{(2)(54.5)} = \underline{26,285} \dots \dots \dots (5)$$

An approximation must now be made with regard to the three r.f. stages. Obviously, as they are tuned to 700 kc, they will each contribute to the shock oscillations of the i.f. system because the frequency-converter stage changes any oscillation in the r.f. system to the i.f. frequency. However, because of the lower i.f. frequency it seemed reasonable to assume that, insofar as the effect on the shock oscillation is concerned, the three r.f. circuits would be equivalent to about two additional i.f. circuits. On the basis of this approximation, the approximate equation for the envelope at the second detector is (equation (16), appendix VII, for n = 8)

$$\frac{E}{\omega_0 Q^7} = \frac{e^{-\alpha t}}{7!} (\alpha t)^7 \dots \dots \dots (6)$$

where, by (5), $\alpha = 26,285$.

From these calculated data, the form-factor for various burst frequencies was determined by the methods just described. The results are given in Figure 12 of the text.

Experimental Determination of Γ

By equation (3) of this appendix and equation (22) of appendix V

$$i_n = \Gamma i$$

$$i_n = \sqrt{(2\Delta f/n)} \cdot I_{st}$$

so that,

$$\Gamma = \sqrt{(2\Delta f/n)} \cdot \frac{I_{st}}{i_s} \dots \dots \dots (7)$$

where, I_{st} = corona streamer current

i_s = effective value of equivalent, standard signal

Δf = effective bandwidth of receiver

n = average number of disturbances per second.

Equation (7) therefore provides a method of experimentally determining Γ by measuring the radio interference obtaining for a given corona-streamer current.

Unfortunately however, the streamer current may not always be directly measurable. It is pointed out in Chapter 3 of the text that the corona discharges from a positive point are of two types which may occur more or less simultaneously, i.e., streamer currents and burst-pulse currents. At corona onset, the corona consists mostly of the streamers. But as the voltage is increased above the onset value, each streamer instigates a series of burst impulses which may continue throughout much of the time period between successive streamers, and the average corona current may be considerably greater than the current due to streamers alone.

Nevertheless, it has been observed that by using a large synchronizing voltage superimposed upon a steady voltage of value somewhat less than the corona-onset value, corona streamers at the rate of 100 to 500 streamers per second could be obtained. Since the electric field at the point would be sufficient to produce corona only during a comparatively small part of each synchronizing cycle, the total current thus measured would be very nearly equal to the streamer current, for the small burst pulses could occur for only a fraction of the time.

On the other hand, to produce streamer discharges at the rate of 800 to 4,000 each second required that the direct-component of the electric field be increased

considerably above that obtaining at onset. As a result, the small burst-corona pulses occurred most of the time and the total corona current was increased beyond that due to actual corona streamers. Accordingly, the experimental values of Γ as obtained from (7), by assuming the corona current to be the same as the streamer current, were accurate only insofar as this assumption is true. From the above discussion, it seems reasonable that the streamer current should be nearly equal to the total corona current for streamer-synchronization rates less than 500 per second. For higher streamer rates, the corona current should be appreciably greater than the streamer current and the experimental values of Γ thus calculated from (7) may be expected to be appreciably greater than the theoretical value. The comparison of the theoretical and experimental value of Γ as presented in Figure 12 of the text, shows that the above expectations are actually true.

It is interesting to note that if the theoretical form factor is accepted as accurate, the above theory provides a method of measuring separately the streamer and burst components of the corona current, for by (7),

$$I_{st} = \Gamma \cdot \sqrt{(n/2\Delta f)} \cdot i_s \quad \dots \dots \dots (8)$$

and

$$I_b = I_{dc} - I_{st} \quad \dots \dots \dots (9)$$

REFERENCES

1. FUNDAMENTAL PROCESSES OF ELECTRICAL DISCHARGES IN GASES, L. B. Loeb, John Wiley and Sons, Inc., New York, 1939. (Contains a critical compilation of the theoretical and experimental knowledge on the subject up to the time that it was written.)
2. PRECIPITATION-STATIC RADIO-INTERFERENCE PHENOMENA ORIGINATING ON AIRCRAFT, E. C. Starr, Bulletin No. 10, 1939, Engineering Experiment Station, Oregon State College
3. ELECTRICAL DISCHARGES IN AIR AT ATMOSPHERIC PRESSURE, L. B. Loeb and A. M. Kip, Journal of Applied Physics, Vol. 10, p. 142, 1939
4. THE THEORY OF THE SCHROTEFFEKT, Thornton C. Fry, Journal of the Franklin Institute, Vol. 199, No. 2, 1925
5. LAPLACIAN TRANSFORM ANALYSIS OF CIRCUITS WITH LINEAR LUMPED PARAMETERS, Jacob Millman, Electrical Engineering, Vol. 61, Apr. 1942, pp. 197-205
6. SPONTANEOUS CURRENT FLUCTUATIONS IN VARIOUS CONDUCTORS, W. Schottky, Ann. Physik., 57, pp. 541-567, 1918
7. REPORT ON A LABORATORY INVESTIGATION ON "PRECIPITATION-STATIC" INTERFERENCE AS ENCOUNTERED ON AIRCRAFT, R. H. George, Technical Development Report No. 29, Civil Aeronautics Adm., U. S. Dept. of Commerce, Apr. 1940
8. TENSOR ANALYSIS OF NETWORKS, G. Kron, John Wiley and Sons, New York, 1939
9. SELECTIVE CIRCUITS AND STATIC INTERFERENCE, J. R. Carson, Bell System Tech. Journ., Apr. 1925
10. SERVICE RANGE OF FREQUENCY MODULATION, Murray G. Crosby, RCA Review
11. DIE PHYSIK DER VERBRENNUNGSERSCHENUNGEN, Mache, Veit and Company, Leipzig, 1918
12. IONIZATION IN THE SOLAR CHROMOSPHERE, M. N. Saha, Phil. Mag., Vol. 40, p. 472, 1920
13. THE ELECTRO CHEMISTRY OF GASES AND OTHER DIELECTRICS, Glockler and Lind, John Wiley and Sons, New York, 1939